WL-TR-95-4008

PROCEEDINGS OF THE MINI-SYMPOSIUM
ON COMPUTATIONAL MATERIALS SCIENCE

RUTH PACHTER
WADE ADAMS
HARDENED MATERIALS BRANCH

BARRY L. FARMER
DEPT OF MATERIAL SCIENCE
UNIVERSITY OF VIRGINIA
CHARLOTTESVILLE, VA   22901

SEPTEMBER 1994

FINAL REPORT FOR 07/15/92–07/16/92

APPROVED FOR PUBLIC RELEASE; DISTRIBUTION IS UNLIMITED.

19950711 021

NOTICE

When Government drawings, specifications, or other data are used for any purpose other than in connection with a definitely Government-related procurement, the United States Government incurs no responsibility or any obligation whatsoever. The fact that the Government may have formulated or in any way supplied the said drawings, specifications, or other data, is not to be regarded by implication, or otherwise in any manner construed, as licensing the holder, or any other person or corporation; or as conveying any rights or permission to manufacture, use, or sell any patented invention that may in any way be related thereto.

This report is releasable to the National Technical Information Service (NTIS). At NTIS, it will be available to the general public, including foreign nations.

This technical report has been reviewed and is approved for publication.

DENNIS S. HAGER, TAM
Hardened Materials Technology Section
Hardened Materials Branch
Electromagnetic Materials and
Survivability Division

PAMELA M. SCHAEFER, Chief
Hardened Materials Branch
Electromagnetic Materials and
Survivability Division

WILLIAM R. WOODY, Chief
Electromagnetic Materials and
Survivability Division

If your address has changed, if you wish to be removed from our mailing list, or if the addressee is no longer employed by your organization please notify WL/MLPJ, Wright-Patterson AFB, OH 45433-7702 to help maintain a current mailing list.

Copies of this report should not be returned unless return is required by security considerations, contractual obligations, or notice on a specific document.

1. AGENCY USE ONLY *(Leave Blank)*	2. REPORT DATE September 1994	3. REPORT TYPE AND DATES COVERED FINAL 07/15/92--07/16/92

4. TITLE AND SUBTITLE	5. FUNDING NUMBERS
MINI-SYMPOSIUM ON COMPUTATIONAL MATERIALS SCIENCE	PE 62102 PR 2422 TA 04 WU 01

6. AUTHOR(S)

R. PACHTER
W. W. ADAMS
B. L. FARMER

7. PERFORMING ORGANIZATION NAME(S) AND ADDRESS(ES)	8. PERFORMING ORGANIZATION REPORT NUMBER
MATERIALS DIRECTORATE WRIGHT LABORATORY AIR FORCE MATERIEL COMMAND WRIGHT PATTERSON AFB OH 45433-7702	

9. SPONSORING MONITORING AGENCY NAME(S) AND ADDRESS(ES)	10. SPONSORING/MONITORING AGENCY REP NUMBER
MATERIALS DIRECTORATE WRIGHT LABORATORY AIR FORCE MATERIEL COMMAND WRIGHT PATTERSON AFB OH 45433-7702	WL-TR-95-4008

11. SUPPLEMENTARY NOTES

12a. DISTRIBUTION/AVAILABILITY STATEMENT	12b. DISTRIBUTION CODE
APPROVED FOR PUBLIC RELEASE; DISTRIBUTION IS UNLIMITED.	

13. ABSTRACT

This technical report documents the WL/MLPJ Mini-Symposium on Computational Materials Science Research held during 15-16 July 1992 at the Materials Directorate, Wright-Patterson AFB. The purpose of the meeting was to inform collaborators of scope of work and ensure complementary nature, reduce direct overlap of work while looking for uncovered subjects, produce cross fertilization of ideas, brainstorm coverage of relevant AF interests, critique our work, and provide students a chance to present current work to a "friendly" audience. The topics discussed included properties determination, for example, as summarized by Dr. W. Wade Adams/MLPJ on the prediction of mechanical properties, structure-to-property relationships, for example for star and oligomeric siloxanes as reported by Dr. Barry Farmer/University of Virginia, biopolymers structure determination and prediction, with aspects of biomolecular structure determination discussed by Dr. Ruth Pachter/MLPJ, macromolecular simulation, for example, for high-temperature properties of PBZT fibers, as presented by Dr. Ken McTurk/Akron University, and algorithms and other modeling applications, with parallel computation discussed by Prof. Gary Lamont/AFIT. Numerous posters were presented, and scientific interactions led to collaborations and fostering of new ideas.

14. SUBJECT TERMS	15. NUMBER OF PAGES
Modeling, Laser Hardened Materials, Computation, Molecular Simulations, Siloxanes, Fibers, Visualization	
	16. PRICE CODE

17. SECURITY CLASSIFICATION OF REPORT UNCLASSIFIED	18. SECURITY CLASS OF THIS PAGE. UNCLASSIFIED	19. SECURITY CLASS OF ABSTRACT UNCLASSIFIED	20. LIMITATION ABSTRACT UL

TABLE OF CONTENTS

TABLE OF CONTENTS (Con't)

FOREWORD

Accesion For		
NTIS CRA&I		☑
DTIC TAB		☐
Unannounced		☐
Justification		
By		
Distribution /		
Availability Codes		
Dist	Avail and / or Special	
A-1		

MLPJ Mini-Symposium on Computational Materials Science Research

15-16 July 1992
Bldg. 653 Cafetorium

PURPOSE

Inform collaborators of scope of work and ensure complementary nature, reduce direct overlap of work while looking for uncovered subjects, produce cross fertilization of ideas, brainstorm coverage of relevant AF interests, critique our work, and provide students a chance to present current work to a "friendly" audience.

July 14

6:00 p.m.	Mixer: Trolley Stop

July 15

8:30-9:40   Introduction and Overview

Chairman:	Dr. Wade Adams MLPJ	
8:30 - 8:50	Registration	
8:50 - 9:00	Dr. Wade Adams MLPJ	Welcome
9:00 - 9:20	Dr. Robert Crane MLPJ	Overview of MLPJ
9:20 - 9:40	Dr. Ruth Pachter MLPJ	Overview of Computational Projects at MLPJ
		Overview of Computational Initiatives in DoD/DARPA/NSF
9:40-10:00		Coffee Break

10:00-12:00   Properties Calculations

Chairman:	Dr. Barry Farmer U. Virginia	
10:00 - 10:20	Dr. Wade Adams	Prediction of Mechanical Properties
10:20 - 10:40	Dr. Peter Haaland AFIT	Properties of C_{60} Molecules
10:40 - 11:00	Dr. Tom Horn AFIT	Strain-Dependence of Normal Mode Frequencies: A "Biased-Hessian" Approach
11:00 - 11:20	Dr. Ruth Pachter	Prediction of Strain-Dependent Properties of Biopolymers
11:20 - 11:40	Mr. Philip Klunzinger U. Akron	Computations of Moduli and Coefficients of Thermal Expansion in Extended Chain Polymers

| 11:40 - 12:00 | Dr. Doug Dudis
MLBP | Cooperative Effects in Rigid-Rod Polymer Dynamics |
| 12:00 - 13:30 | | Box Lunch |

13:30-15:30 — Structure-to-Property Relationships

Chairman:	Dr. Ruth Pachter	
13:30 - 13:50	Dr. Barry Farmer	Simulation of Star and Oligomeric Siloxanes
13:50 - 14:10	Dr. Soumya Patnaik MLPJ	Molecular Modeling of Siloxanes
14:10 - 14:30	Mr. Ed Socci U. Virginia	Calculations of Mesogen Interactions in Cyclic Siloxane-Based Liquid Crystals
14:30 - 14:50	Dr. Harvey Paige MLBT	Computational Chemistry in Liquid Lubricant Research
14:50 - 15:10	Dr. Steven Pollack U. Cincinnati	Ab Initio Studies of Torsional Potentials in Mesogens Exhibiting Conformational Flexibility
15:10 - 15:30	Dr. Don Dorsey MLPO	Application of Computational Chemistry Techniques to Modeling of Semiconductor Thin-Film Epitaxy
15:30 - 15:45	Mr. Chuck Lovett MLPJ	Laser Demo

15:45 - 17:30 — Coffee Break: Poster Session

| 18:30 | | Conference Dinner: Steven Kao's Restaurant |

July 16

8:30-10:30 — Biopolymers Structure Determination and Prediction

Chairman:	Dr. David Martin U. Michigan	
8:30 - 8:50	Dr. Ruth Pachter	Aspects of Biomolecular Structure Determination
8:50 - 9:10	Mr. Ernie Fuentes MLPJ	Molecular Simulation of Beta-Sheet Polypeptides
9:10 - 9:30	Mr. Marc Martin MLPJ	Modeling of Polypeptide-Bound Chromophores
9:30 - 9:50	Mr. David Mahoney U. Akron	Approaches to Spider Silk Modeling
9:50 -10:10	Mr. Philip Anderson U. Michigan	Morphology and Modeling of Genetically Engineered Silk-Like Polypeptides
10:10 - 10:30	Mr. Steven Fairchild MLPJ	Protein Structure Prediction using Artificial Intelligence, Neural Networks, and Modeling Techniques
10:30 - 10:50		Coffee Break

10:50-12:30   Macromolecular Simulation

Chairman:	Dr. Ronald Eby	
10:50 - 11:10	Dr. David Martin	Intermolecular Twist Defects in Extended-Chain Polymers
11:10 - 11:30	Ms. Patricia Wilson U. Michigan	Defects and Defect Modeling in Poly(diacetylenes)
11:30 - 11:50	Mr. Ken McTurk U. Akron	High-Temperature Properties of PBZT Fibers
11:50 - 12:10	Mr. Rafael Ramirez U. Akron	Deformation of Fibers and Birefringence
12:10 - 12:30	Mr. Jaime Ojeda U. Michigan	Atomic Force Microscopy of Poly(imides) Near Surfaces
12:30 - 13:30		Lunch: Flying Pizza

13:30 - 15:10   Algorithms and Other Modeling Applications

Chairman:	Dr. Steven Pollack	
13:30 - 13:50	Mr. Walt Johnson MLPJ	Modeling of Rugate Filters
13:50 - 14:10	Dr. Jim Lupo MLPJ	Nano-Crystalline Silicon: Simulation and Visualization
14:10 - 14:30	Dr. Garry Lamont AFIT	Parallel Computation
14:30 - 14:50	Lt Chris Hasser Armstrong Lab Dr. Ruth Pachter	Modeling of Intermolecular Interactions using a Force-Feedback Arm
14:50 - 15:10	Dr. Steven Leclair MLIM	The Application of Genetic Algorithms to Understanding Protein Structures
15:15 - 15:30		Coffee Break

15:30 - 17:00   Round Table Discussion

17:30		Farewell Dinner: Young's Dairy

Poster Session

Dr. Shashikala Das, MLPO

Semiconductor Surface Atom Energetics by Quantum Chemistry

Mr. Walt Johnson

Reducing the Standing-Wave Field Profile within High Reflection Interference Coatings

Dr. Dan Kost, Ben-Gurion University, Israel

Do Bipolarons or Nitrenium Ions Exist in Doped Polyazines?

Dr. George Medrano, MLBT

Quantum Mechanical Studies of Quasi-Particles in Polyacetylene

Dr. Soumya Patnaik

X-Ray Structure Determination of Poly(di-n-hexyl-silane)

Mr. Ed Socci

Conformation and Packing of Poly(*p*-phenylene)

Dr. Steven Trohalaki, MLBT

Conformational and Dynamical Effects of Pendant Poly(ether ketone) Chains on the Rigid-Rod Polymer PBZT

Dr. R. Venkat, U. Nevada

Stochastic Model for MBE Growth

COMPUTATIONAL MATERIALS SCIENCE RESEARCH

Computational Materials Science Research

• Materials Design: Issues & Approaches Used

• Summary of Projects

• Computational Aspects: Programs and Algorithms in Parallel

• Initiatives for Computational Research in Materials

3

Design of Laser-Resistant $\chi(2)$ and $\chi(3)$ Materials

- **Organic materials and polymers of high intrinsic 3-D order substituted with NLO moieties**

  Biomaterials
  Liquid crystalline macromolecules

- **Carbon-based solutions**

  Carbon clusters

4

Type of Simulation

- **Structure**
  - Electronic Structure
  - Molecular Geometry in Ground and Excited States
  - Potential Energy Surfaces
  - General Topology and Folding
  - Atomistic Simulation: *Intra- + Intermolecular Interactions*
  - Molecular Dynamics
  - Solvent Effects

- **Properties**
  - Diffraction Patterns
  - Optical Properties: Finite Field (semi-empirical and ab initio)
  - Calculation of Oscillator/Rotational Strengths: Absorption / CD Spectra
  - Mechanical Properties
  - NMR Parameters: Coupling Constants(FF at semi-empirical); NOE's: Bloch equations
  - Properties Prediction of Polymers using Single-Chain Statistical Mechanics

- **Visualization**
  - Calculation of intermolecular interactions by using the force-feedback arm

5

Molecular Size: Level of Approximation

- **Molecular Orbital Calculations**

  -ab initio – Gaussian 90, GAMESS, CADPAC

  -Semi-empirical - AM1, MNDO, PM3, I(C)NDO, MOSOL, ZINDO

- **Semi-classical Calculations**

  -Molecular mechanics force-fields: CHARMm; GROMOS; DREIDING; MM2; AMBER

  -Generalized Bloch equations to simulate NOE spectra

- **Search of Conformational Space for Large Bio/Macromolecules**

  -AI and Neural Networks with protein data base of known structures

  -Algorithms which use experimental data

  -Distance and dihedral angle constrains from NMR - PROTEAN

  -Probe conformational space by using the force-feedback arm GROPE

NLO Biomaterials Design

- Predicting Tertiary Structure: Full Exploration of Conformational Space to find the Global Energy minimum

- Study of the Effects of Chromophore Substitution on the Structure of Polypeptides of Defined Secondary Structure

- Solvation and Aggregation Effects

- The Effects of the Biomolecular Backbone on NLO Properties

- Mechanical Properties of Biomaterials

Effects of Chromophore Substitution on the Structure of Polypeptides of Defined Secondary Structure

- Molecular Dynamics Simulation of Poly(Spiropyran-L-Glutamate): Influence of Chromophore Isomerisation

- A Nonlinear Optical Chromophore Containing Polypeptide: Modification of Poly(L-Glutamic acid) with 1-docosyl-4-(4-hydroxystyrl)pyridinium bromide

- Molecular Simulation of Amphipatic Polypeptides

- Application of the Double-Iterated Kalman Filter Technique and Molecular Modeling Simulations to Structure Determination of Nonlinear Optical Polypeptides of Beta-Sheet Conformation

- The Influence of Charged Side-Chains on the Stabilty of Alpha-Helix: Modification of Poly(L-Glutamic Acid) with Congo Red

8

Study of Explicit Solvent Effects

- Parameters to analyze for studying the intrinsic alpha helicity on solvation:

  change in number of hydrogen bonds

  their lengths

  $\phi-\psi$ angles

  hydrogen bonds with water molecules

  - three-center hydrogen bonds which may break the helical structure

- Minimize energy of peptide

- Additional minimization after water insertion

  - this step serves to release any unfavorable vdw contacts

- Molecular dynamics simulation

  Poly(spiro-L-Glutamate) :spiropyran and merocyanine

Properties of Biomaterials

- The Effects of the Biomolecular Backbone on NLO Properties

- Mechanical Properties of Biomaterials poly(L-Ala) and poly(L-Glu)

Future Studies of Biopolymers: Application

- Polypeptide-bound chromophores synthesized in the Lab

  - coiled coil super-helices

- Newly designed polypeptide-bound chromophores to predict candidates for synthesis

- Sequence-dependent secondary structure formation

  - optimal configuration of amino acid building blocks

  - polypeptide simulations of short alanine based peptides which show unususal stable alpha-helix formation in solution

- Systematic study of the influence of side-chains

  - bulky-steric effects

  - D and AC-electronic effects

  - various chromophores

  - side-chain length

- Energetics of intermolecular interactions and self-assembly

  - packing and aggregation

- Solvent effects

Future Studies of Biopolymers: Methods

- Prametrization of empirical potentials

  -ab initio study of chromophore-bound dipeptides

- Optimization techniques for determining *a priori* the global minimum of a polypeptide-bound chromophore

  - comparison of MCM and simulated annealing techniques

- Calculation of CD spectra of chromophores of interest

- Secondary and tertiary structure prediction from PDB data base

- Amphipatic alpha-helices structure prediction

  hydrophobicity character at 100° intervals (360°/3.6 residues /cycle=100°/residue); define mean helical hydrophobic moment: Σ multiplication of unit vector from the center of the wheel to the position of the residue on the wheel by the hydrophobicity of the residue apply methods to detect periodicity (discrete FT): peak at ~100° ⇒ amphipatic α -helix

- Application of theoretical techniques based on experimental data

  - PROTEAN for general topology definition

  - further Refinement

    solution of Bloch equations ⇒more precise distances

    energy minimization/dynamics

Structure-to-Property Relationship in Siloxane-Based Liquid Crystals

- Molecular Structure and X-ray Scattering of Cyclic Siloxane-Based Liquid Crystals (LC{BC})

- Molecular Dynamics of Cyclic Siloxane-Based Liquid Crystals

- Molecular Mechanics, Dynamics, and X-Ray Scattering Calculations for a Cyclic Siloxane Macromolecule (LC{B})

- Individual Mesogen Interactions

- LC{BC} vs. LC{B} Analysis : Individual and Interdigitation

- Initial Study on the Effect of Spiropyran Substitution on Interdigitation

13

Future Studies of Siloxane-Based Liquid Crystals

- Effect of varying the leader or terminal groups

- LC{BC} vs. LC{B} analysis : individual and interdigitation and the effect of application of periodic boundary conditions

- Stress–Strain relationship - ability to form fibers

- Molecular simulation of novel photochromic liquid crystals

- Study of simpler systems where mesogen effects are better discerned: trisiloxane; disiloxane; linear vs. cyclic siloxanes

- A suitable potential energy function to be added to the force-field in order to simulate, for example, a nematic environment modelled by an expression of the type : $Enem = -\Sigma constant(3cos^2\theta - 1)$, summed over all molecular pairs i

- Monte Carlo simulations of LC's represented by empirical potentials, for example, soft ring potential r^{-9} term and backbone Lennard - Jones 6-12 potential

- Parameters estimation for siloxanes using higher-level (quantum mechanical ab initio and semi-empirical) methods

Strain-Dependent Mechanical and Electro-Optical Properties

- Mechanical Properties

  Biopolymer Chains

  Highly Conjugated Systems - e.g. PPP

  Buckminsterfullerene

- Method Development

  New Approach to Calculate Young's Modulus from the Hessian- applied at various levels of theory

  Biased - Hessian Approach

Future Properties Calculations

- **Optical properties**
  -The effects of the biomolecular backbone on NLO properties of polypeptide-bound chromophores
  -Carbon clusters: SOS calculations for gaining insight into the optical limiting phenomenon in C60
  -C60: NLO properties calculations for appropriate derivatives

- **Strain-dependent properties**
  -Biomaterials: poly(L-Ala) and poly(L-Glu)
  -Highly conjugated systems: e.g. diphenyl polyenes
  -Method development: introduce intermolecular interactions

- **Spectroscopic Data**
  - NMR parameters: Coupling constants & NOE's: biopolymers
  - Calculation of oscillator/rotational strengths:absorption /CD spectra for chromophore-bound polypeptides

- **Diffraction patterns**
  - Siloxane-based materials

Visualization

Program for the simulation of 3D arrangements
Interdigitation of L.C.'s and packing of polypeptides

GROPE: runs on MAS-PAR parallel machine

The SG code (no force arm) is available to us

Plan to parallelize and use with force arm

Initiatives for Computational Research in Materials

Materials - by - Design with 'Tailored' Properties
Ultimate Goal: Model and Predict 'Real' Materials Phenomena

Molecular -to - Real (defects)

Electronic Structure

Atomic/Molecular Structure

Microstructure

Quantum Chemistry and Solid-State Physics

ab inito & Semi-empirical; First Principles & LDF

Molecular Mechanics/Dynamics

Monte Carlo

GAP

President's Initiatives

HPCC -High Performance Computing and Communication

AMPP - Advanced Materials & Processing Program:
Modeling and Simulation

Solve Materials Design Problems with High Performance Computation

	Computational Complexity	Current	Goal
MD	$o(N)$	10^4	10^6
LDF	$o(N3)$	10^2	10^4
HF	$o(N4)$	10	10^3

GOALS
Short term

Quantum Chemistry	100's
MD	1million

Five Years

Quantum Chemistry	25Å
MD	1000Å-1 µ

Grand Challenge

- High Performance Computing Systems (HPCS)

  - Development of underlying technology required for scalable high-performance computing systems capable of sustaining trillions of operations per second on large problems

- Advanced Software Technology and Algorithms (ASTA)

  - Development of generic software technology and algorithms

- National Research and Education Network (NREN)

  - Development of national high-speed network

- Basic Research and Human Resources (BRHR)

  - Support for individual investigator and multidisciplinary long term research

Research Thrust

Software Development: DOE, NASA, NSF

NSF: CARM (Computational Approaches to Real Materials)

Participating Divisions: Materials Theory, New Technologies, Computational Mathematics, Theoretical and Computational Chemistry

Interdisciplinary Teams & Collaborative work

"...focused research thrust at NSF which directly affects computational materials science...cuts across divisional boundaries at NSF"

FUTURE Proposals

Deadeline for proposal submission in present fiscal year has passed

Center for Two AFOSR Initiatives: Search of Configurational Space for the Global Energy Minimum of Macromolecular Structures: Polymers, Surfaces and Biomolecules

- Thrust: To develop mathematical models and computer software for the identification of stable structures for complex, extended chemical systems and to correlate these structures with the physical properties of these systems–e.g. genetic algorithms

- Parallelization of new optimization techniques are to be an integral part of the initiative

Computational Materials Science Research Initiatives:
Hardware, Software & Application

HARDWARE

DARPA Consortium

Caltech Delta

Private Collaboration with National Labs

Touchstone at WPAFB

SOFTWARE

Collaborative Work: e.g. GAMESS, GROMOS
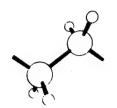
APPLICATION and DEVELOPMENT

NSF & NASA Initiatives
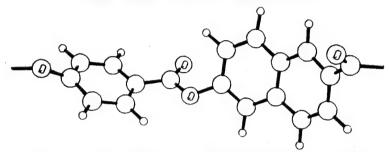
AFOSR

PREDICTION OF MECHANICAL PROPERTIES
Dr. Wade Adams
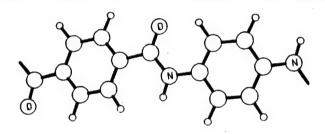
POLYETHYLENE
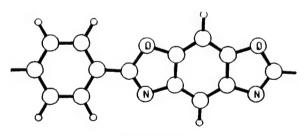
THERMOTROPIC POLYESTER
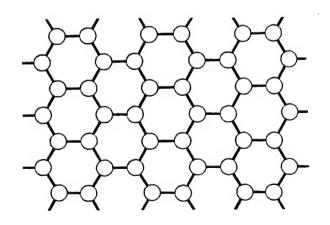
POLY (p-PHENYLENE TEREPHTHALAMIDE)

POLY (p-PHENYLENE BENZOBISOXAZOLE)

CARBON

27

CHAIN MODULUS

MOTION	MODULUS	
	GPa	MPsi
Stretch	740	107
Bend	80	12
Rotate	6	1
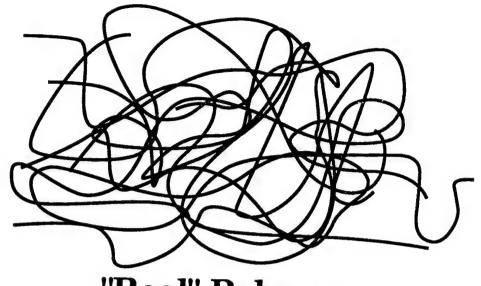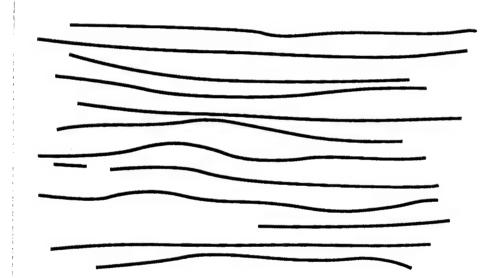
WHY CALCULATE CHAIN PROPERTIES?

1. Figure of merit for processing efficiency

2. Establish upper limit for calculation of (composite) properties, especially molecular properties

3. Insight for molecular design, especially biopolymers

4. Understand molecular nature of deformation

5. Predict temperature dependence

6. Calculate strain dependence of properties
   - mechanical
   - electronic
   - optical
   - vibrational spectra

"Real" Polymer

"Ideal" Polymer
Calculations assume

ZERO ~~DEFECT~~ MATERIAL

TOTAL QUALITY !

Ultimate Polymer Properties
"Continuous Crystal"

Staudinger 1935

But ultimate properties depend on intrinsic chain properties

Perfect Order

Perfect Orientation

Few Defects

SCALE

Small Scale (Molecule)
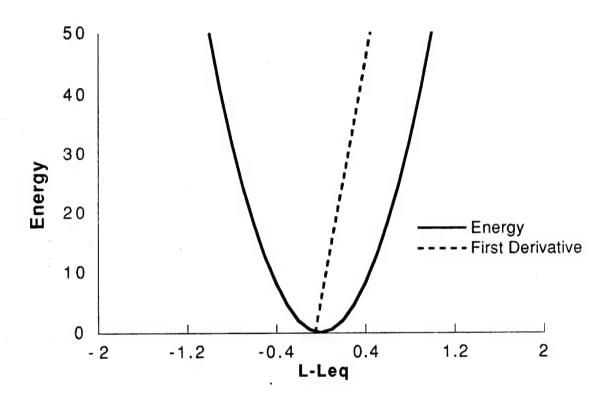
INTERACTIONS

No Intermolecular Interactions

ARCHITECTURE

No Architecture (Single Chain)

Poly-Unobtainium

F ←— Ubu -WWW- Ubu -WWW- Ubu -WWW- Ubu —→ F
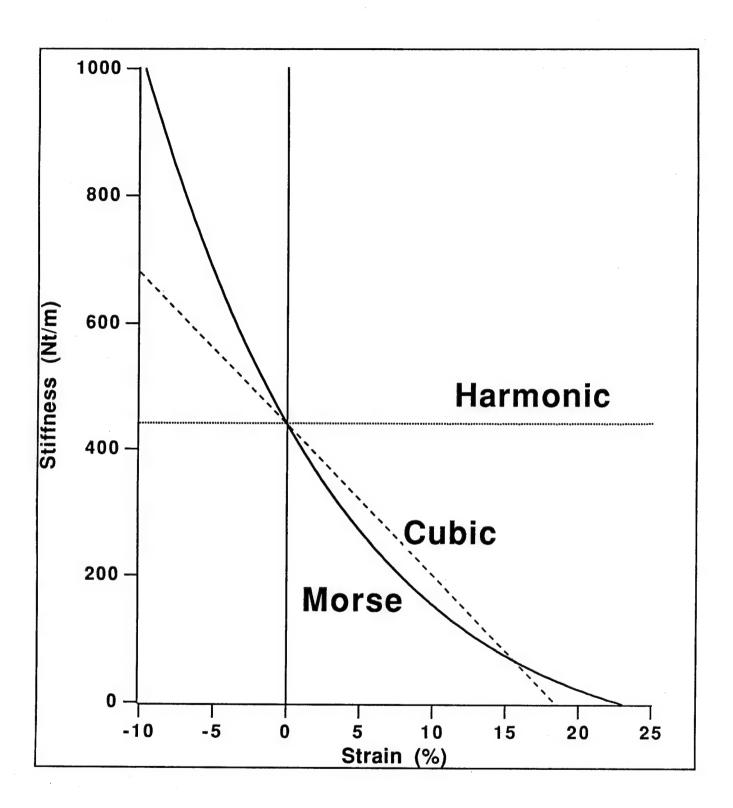
$$U(L) = \frac{k}{2}(L - Leq)^2 \quad \text{Harmonic}$$
(Good Fracture Properties!)

$$F = \frac{dU}{dL} = k(L - Leq) \quad \text{Hooke's Law}$$

$$E = \frac{\text{Stress}}{\text{Strain}} = \frac{\frac{\text{Force}}{\text{Area}}}{\frac{\Delta L}{L}} = \frac{\text{Force}}{\Delta L} \cdot \frac{L}{\text{Area}} = \frac{k \times L}{\text{Area}}$$

MODULUS CALCULATION
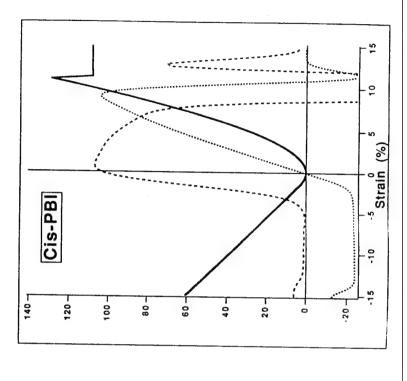
Optimize Geometry at Equilibrium $\Rightarrow \Delta H_f$

Elongate/Compress Unit Cell $\Rightarrow \Delta L$

Optimize Geometry at Different ΔL

$$\Rightarrow \Delta H_f \text{ vs. } \Delta L$$

Rigid Rod Polymers: PBI, PBO, PBZT *

Repeat units: cis-PBI X=Y=N; cis-PBO X=N; Y=O; cis-PBZT X=N; Y=S; a trans derivative--exchange of X and in one heterocylic ring

Cis- PBI energy (kcal/mol) vs. strain (%)-solid curve; fine dashed line-corresponding force curve by numerical derivative); heavy dashed line-second derivative of the energy (N/m)

* Polymer, 33, 3357 - 3368 (1992)
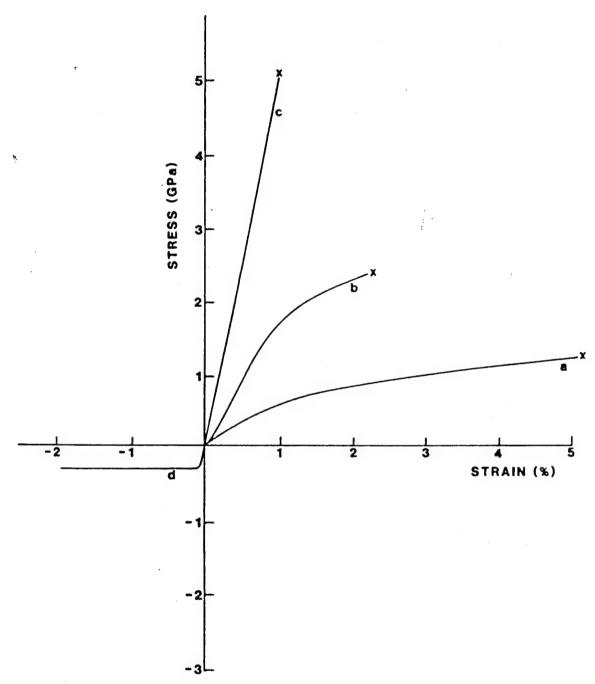
FIG. /3.3/ Typical (a–c) tensile and (d) compressive stress–strain curves of PBO fibers: (a) as-coagulated (wet), (b) as-spun (dried), (c) and (d) heat-treated.
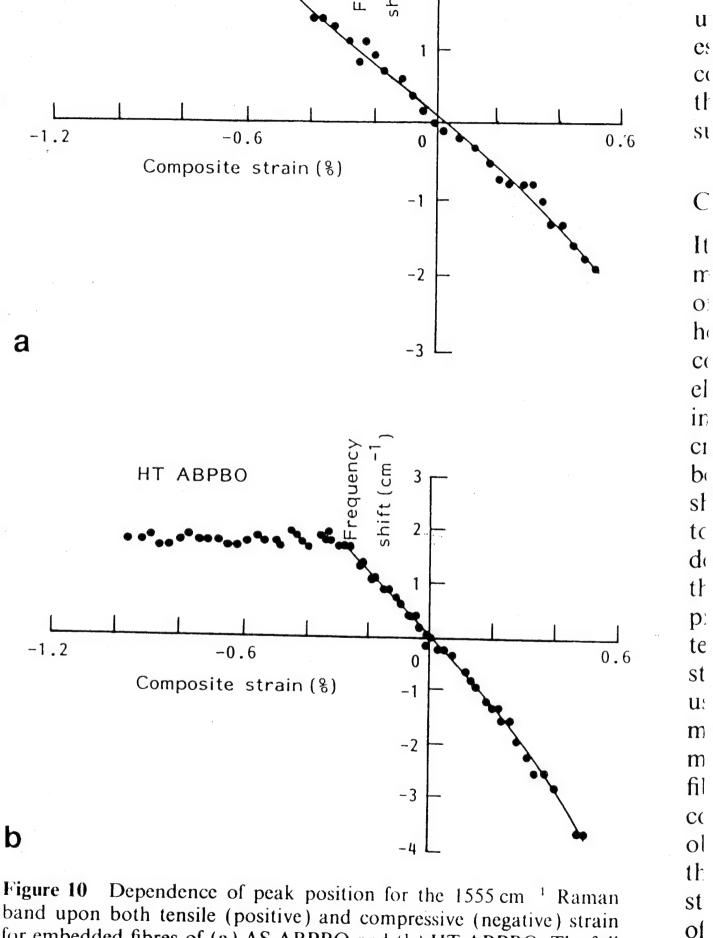
Figure 10 Dependence of peak position for the 1555 cm^{-1} Raman band upon both tensile (positive) and compressive (negative) strain for embedded fibres of (a) AS ABPBO and (b) HT ABPBO. The full curves are fits of the experimental data during elastic deformation to third-order polynomials

49

MOLECULAR INSTABILITY
VS.
MICROSTRUCTURAL INSTABILITY (FIBRILS)
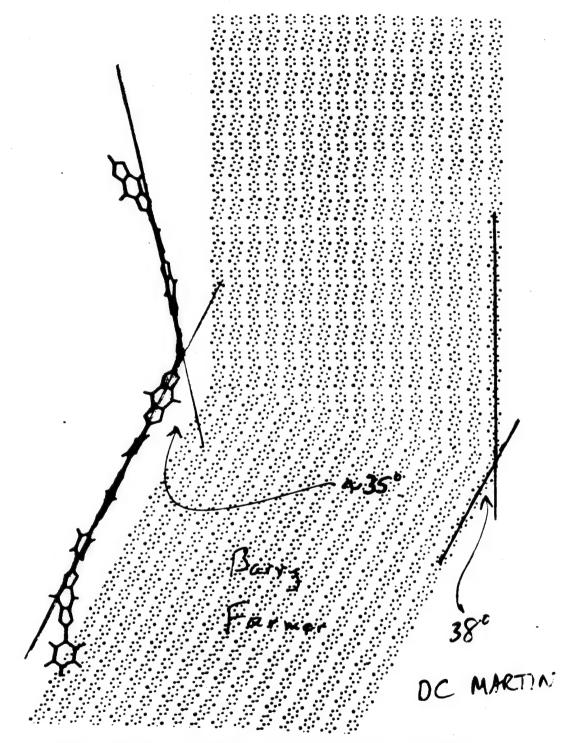
Figure 6.14: Molecular interpreation of Figure 6.13 which is consistent with the experimental HREM contrast. The molecules undergo a sharp bend as they change from one orientation to the other across the boundary. This would require the bending of covalent bonds in each polymer which passes through the ACR boundary.

The electrical conductivity increases linearly with the modulus and tensile strength, with polymer chain orientation as the implicit variable

• Theoretical Relation between E and draw ratio:

$$E = [E_h^{-1} + (3\pi/4)\lambda^{-3/2}(E_u^{-1} - E_h^{-1})]^{-1}$$

E_h axial modulus of perfect oriented polymer
E_u axial modulus of unoriented polymer

• Linear correlation between conductivity and draw ratio

⇒ A direct, linear correlation between the electrical conductivity and mechanical properties (Young's modulus and tenacity) of polyacetylene and PDMPV

S. Tokito, P. Smith and A. J. Heeger, *Polymer* **32**, 464 (1991)
Y. Cao, P. Smith and A. J. Heeger, *Polymer* **32**, 1210 (1991)

PROBLEMS WITH THE METHOD

BOUNDARY CONDITIONS FOR CONJUGATED POLYMERS

OVERESTIMATION OF YOUNG'S MODULUS BY 10-30%

Too far from equilibrium

Force constant too stiff

NO INTERMOLECULAR INTERACTIONS

e.g. Hydrogen bonding

No lateral constraints in compression

57

FUTURE

METHOD

ab initio - including electron correlation

Biased Hessian Correction to SE

INTERMOLECULAR INTERACTIONS

Δ TEMPERATURE

SPECTRA

HYPERPOLARIZABILITY

CONDUCTIVITY

ULTIMATE PROPERTIES OF POLYMER CHAINS
Dr. Wade Adams

ULTIMATE PROPERTIES OF POLYMER CHAINS

W. WADE ADAMS, RUTH PACHTER*, PETER D. HAALAND, THOMAS R. HORN, SCOTT G. WIERSCHKE**, AND ROBERT L. CRANE
Wright Laboratory, Materials Directorate, Wright-Patterson Air Force Base, Ohio 45433
*This work was done while the author held a National Research Council Research Associateship
**Department of Chemistry, U.S. Air Force Academy, Colorado 80840

ABSTRACT

New polymers with exceptional properties are needed for applications in high-performance structures, novel electrical, optical and electro-optical devices, and for multi-functional smart materials. Concurrently, new computational capabilities and methods for properties prediction and analysis have enabled the study of a variety of polymer chain architectures to examine the principles that govern their high-performance properties. By semi-empirical and *ab initio* computational methods, flexible, stiff-chain, rigid-rod, and biological structures could be analyzed. Single chain molecular stress-strain curves for axial tension and compression were calculated, and the strain dependence of the molecular modulus and vibrational frequencies were compared to measurements of molecular deformation, such as IR and Raman spectroscopy. However, of special interest is the distinctly different response of alpha-helical biopolymer chains to strain. Indeed, in this study we compare on a theoretical basis the 'spring-like' microscopic mechanical response of alpha-helical biopolymers having a reinforcing *intra*-molecular hydrogen bonding network to analogous synthetic extended chain polymers, especially poly(*para*-phenylene terephthalamide) (PPTA) [KEVLAR™]. The theoretical verification of the absence of compressive buckling in alpha-helical biopolymer chains rationalizes the molecular elasticity and resistance to 'kinking' of those strands, manifested by the prevalence in Nature for *coiled coils*. The understanding of the structure-to-function relationship in biopolymers explaining the role of the alpha-helix in these systems as a requirement for superior compressive mechanical properties, may enable new guidance for the synthesis of motifs consistent with molecular frameworks optimized by Nature.

INTRODUCTION

The emerging importance of the design of new polymeric materials is well established [1]. For example, the advent of the so-called high-performance 'rigid-rod' polymer fibers [2] has led to a series of studies on their properties [3], showing tensile properties high enough to make them candidates for incorporation into aerospace structures. However, these materials show low compressive strength, and their failure mode has been demonstrated and studied in detail for improvement [4]. In pursuing the objective of developing new materials that may overcome some of these disadvantages, at least at the molecular level, as well as for the design of new synthetic materials with specific properties, for instance, as a flexible backbone for the derivation of nonlinear optical chromophore-bound polypeptides [5], we are investigating the possible use of various polymers, particularly biopolymer systems.

Computational chemistry has become a valuable tool for analyzing the dynamics, structure and elasticity of polymer systems, while the theoretical prediction of the ultimate mechanical properties is of special continuing interest [6]. However, previous calculations focus mainly on the use of empirical potential energy functions [7,8,9]. A theoretical evaluation of chain moduli and electronic properties of polymers by a molecular orbital approach constitutes a continuing effort of our laboratory. Analysis of molecular structures of rigid-rod polymers (PBI, PBZT, PBO) [10,11,12], PE [13], and of highly conjugated structures (PPP [14] and C_{60} [15]) on the application of axial strain offers insight into deformation processes at the molecular level and their strain-dependent stiffness behavior. The predicted stiffness, namely the second derivative of the potential energy, compared well, for example, with macroscopic stress-strain curves for rigid-rod fibers, since the elastic behavior of materials is better described by a cubic than by a harmonic potential, being asymmetric and stiffer on compression. The theoretical moduli were however shown to be higher than those determined experimentally, which may be rationalized on the basis of the observation that real solid material properties are limited by imperfections and morphology (e.g., multiple phases and micro fibril orientation distribution), while these calculations are performed on models of idealized single polymer chains. Also, the semi-empirical method systematically overpredicts bond stiffness by about 10%, confirmed by a comparison with *ab initio* calculations carried out for polyethylene [7]. The theoretical approach is most advantageous for comparisons of properties for a series of related polymers, and for properties prediction of polymers not yet synthesized.

It is the purpose of the present study to compare the application of a semi-empirical quantum mechanical approach for the study of biopolymers to similar synthetic molecular structures. This offers new insight into the mechanical properties of flexible *coiled coil* arrangements of alpha-helical motifs found in Nature, while also holding promise for the design of new materials. The importance of such biopolymers and their mechanical function is profound, for example, alpha-helical structures are found in keratin in hair, myosin and tropomyosin in muscle, epidermin in skin, and fibrin in blood clots. In the case of the myosin tail, the *coiled coil* superstructure leads to a hierarchy of reinforcing interactions within the alpha-helices, hence culminating in the highly ordered array of a thick filament that provides the means for its mechanical function in muscle contraction [16]. Similarly, membrane skeletons that consist of spectrin networks which enable erythrocytes to resist strong shearing forces in blood flow, are comprised of flexible triple-stranded alpha-helical *coiled coils* providing the underlying mechanical stability and resilience of the erythrocyte membrane [17]. Other similar membrane skeletons in erythrocytes are also important in altering and stabilizing the shapes of various types of cells [18] and structural elements. Likewise, it is supposed that alpha-helical strands are acting as a rubbery reinforcement matrix to provide elasticity to spider silk [19], validated to some extent by our experimental study of these fibers in compression [20] that indicate no 'kinking' [21] failure. Indeed, the development of new biopolymer fibers is of special interest since spider silk designs were found to be governed by the same principles that apply to synthetic materials. This study presents a theoretical verification of the absence of 'kinking' in biopolymer chains of an alpha-helical structure, thus explaining their extraordinary mechanical functions in these examples, especially in supercoiling architectures.

RESULTS AND DISCUSSION

In our analysis we employ a rigorous method that we recently developed and applied [10-15]. Within this approach [22] we apply the so-called cluster method [23] that characterizes a polymer by a translation vector Tv [24]. The modulus and strain-dependent frequency calculations for a polymer cluster model follow a two-stage protocol: after an equilibrium geometry of the cluster is calculated, Tv is incrementally increased or decreased, representing molecular tensile or compressive strain, and the geometry under this constraint optimized. The dependence of the heat of formation on molecular strain can thus be established. The stiffness of the polymer chain is given by the second derivative of the heat of formation *vs.* strain relationship, used to evaluate the single chain polymer chain modulus as described briefly below. For each of these strained geometries a normal mode analysis may also be carried out in order to determine the strain-dependence of the system's characteristic frequencies.

The elastic modulus of a polymer is given by the ratio of the stress σ (force/unit area), and strain ε (fractional change in cluster length $\Delta L/L_{eq}$): $E=\sigma/\varepsilon=(F/A_{eq})/(\Delta L/L_{eq})=KL_{eq}/A_{eq}$; K is the force constant (K=F/ΔL, N/m) and L_{eq} the equilibrium length derived from the semi-empirical calculation. K is determined by fitting the potential to a third-order polynomial [11]: $\Delta H_{ff}=a(\Delta L)^3+K/2(\Delta L)^2+b(\Delta L)+c$; ΔH_{ff} is the change in heat of formation as a function of strain, and a, b and c the coefficients of the polynomial fit. The cross-sectional area of the polymer A_{eq} (Å^2) is derived from X-ray diffraction data or estimated from the polymer density d (g/cm^3) by: $A_{eq}=M_w/dN_AL_{eq}$; M_w is the molecular weight of the cluster (g/mol), and N_A Avogadro's number.

The ΔH_{ff} *vs.* ΔL dependence (Fig. 1) for PPTA [25] results in a modulus of 330 GPa, where d=1.5 g/cm^3 [26], L_{eq}=13.1 Å, M_w=238.25 g/mol, A_{eq}=20.1Å^2, and K=50.6 N/m., overestimating the experimental range of 120-200 GPa [27]. However, the overestimation can be partially corrected by biasing the Hessian with experimental vibrational frequencies [28], yielding a value of approximately 290 GPa, which is comparable to atomistic simulations of PPTA recently reported [7, 29].
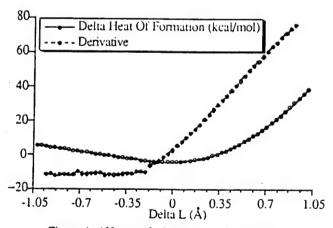
Figure 1: ΔH_{ff} *vs.* ΔL dependence for PPTA

The dashed line is the force curve (10^{-10} N) obtained by taking a numerical derivative of the energy, and is given as an example of the additional data that can be derived, namely that 'kinking' occurs at approximately 2.5% compressive strain (the force curve is the molecular equivalent of a strain-stress curve). The overall response is similar to that of other rigid-rod polymers [10]. The equilibrium geometry and heat of formation for a two-repeat unit was also determined, resulting in a difference in (ΔH_{ff}/repeat unit) of approximately 5 kcal/mol.

Molecular deformations on tension and compression, as compared to the equilibrium geometry of PPTA, are depicted in Figs. 2a-2c. Note that a molecular buckling phenomenon is observed in PPTA about the center of the amide bond (NH-CO) that is especially important to the understanding of the possible mode of compressive failure in fibers. Figure 2b shows that at elongation the bond between the phenyl and carbonyl groups breaks. The calculated result supports in part the supposition of a conformational change in PPTA upon compression [30].

(a)

(b)

(c)
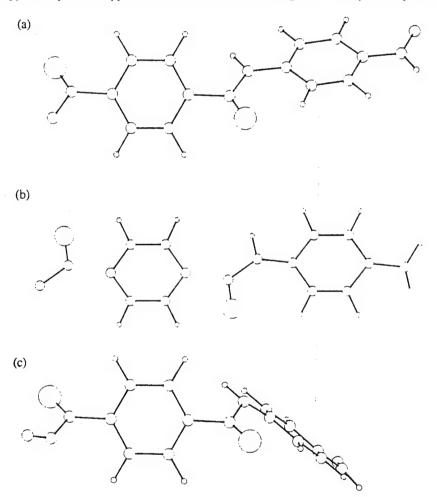
Figure 2: Equlibrium structure of PPTA(a), in tension (b), and in compression (c)

66

A preliminary study of the strain dependency of the PPTA normal mode frequencies, using a single repeat unit as the unit cell, shows that few of the PPTA modes (not unlike those of PDA) exhibit frequencies with a linear dependence on strain. This is demonstrated for example, in Fig. 3 for the 1711 cm^{-1} frequency, and a similar behavior was also found for the 3454 cm^{-1} frequency, with slopes of -16.3 cm^{-1}/%strain and 4.1 cm^{-1}/%strain, respectively. The former mode represents a torsional vibration between the phenyl groups and the latter a C-H motion at the joints linking the phenyl groups. A negative slope for some strain-induced frequency changes in PPTA single fibers has been observed [31].
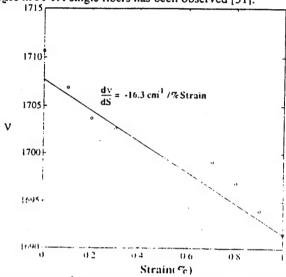
Figure 3: Change in 1711 cm^{-1} mode frequency of PPTA as a function of the percentage strain applied; the solid line denotes a liner fit

Next, we examine extended biopolymer strands based on naturally occurring amino acids, namely poly(L-Ala) and poly(L-Glu). The polypeptides are helix 'makers' and are used as model compounds, and were used in the calculations to assume either an extended or an alpha-helical conformation. The cluster length requisite for this calculation is determined by the electron delocalization length within the polymer [32]. We have used six repeat units for poly(L-Ala) and five repeat units for poly(L-Glu) in the unit cell. Our use of the maximal possible cluster length ensures that there are no non-zero off-diagonal elements in the density matrix. We compared the geometries calculated by using the amide bond correction to the Hamiltonian to those optimized with a classical force-field [33], confirming that the alpha-helical configuration is conserved within our approach since we use a large number of repeat units within the unit cell. Fig. 4 outlines the calculated response of the extended poly(L-Ala) and poly(L-Glu) to the application of strain. It is interesting to point out that a computation of the modulus from the equilibrium structure of poly(L-Ala) by a novel method we recently derived [15] is in good agreement with the calculated result obtained by straining the molecule. Within this approach an applied force F

$$H\delta R = F$$

and $H_{ij}=\partial^2 E/\partial R_i \partial R_j$, is left multiplied by the inverse of H to yield the displacements

67

$$\delta R = H^{-1} F$$

The modulus is then calculated by using the cluster's geometry. An application of the method to the extended chain of poly(L-Ala) by using a force of 2 mD along the translation vector, results in a modulus of 179 GPa. Obviously, high tensile strengths are predicted for the extended biopolymers, while only a small change in energy is observed in compression since the molecular structure of these biopolymers enables more conformational variation resulting from the additional rotatable bond. These data suggest new design possibilities for the 'molecular engineering' of polymers with enhanced compressional strength.
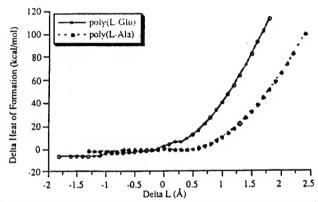
Figure 4: ΔH_{ff} vs. ΔL dependence for the extended biopolymer chains: poly(L-Ala)-modulus of 160 GPa; A_{eq}~20 $\mathring{A}^2$, L_{eq}=21.7 $\mathring{A}$, and K=145 N/m and poly(L-Glu)-modulus of 230 GPa; A_{eq}~20 $\mathring{A}^2$, L_{eq}=14.3 $\mathring{A}$, and K=320 N/m.

A distinctly different response of an alpha-helical chain to the application of strain is shown in Fig. 5, which does not show buckling. On the other hand, small energy variations are calculated in tension, with a similar response revealed for poly(L-Glu). Even at *ca.* 40% tensile strain there was incomplete extension of the chain with breaking of the hydrogen bonds, and at higher extensions a structure approaching more β-sheet type may result.

Although overestimated, the predicted tensile modulus for poly(L-Glu) is in qualitative agreement with experiment [34], where the ΔH_{ff} vs. ΔL dependence for the alpha-helical model of poly(L-Glu) results in a modulus of 60 GPa; A_{eq} ~ 20 $\mathring{A}^2$, L_{eq}=5.2 $\mathring{A}$, and K=240 N/m. These results reveal a 'spring-like' behavior of alpha-helical biopolymer chains, in contrast to the extended systems. Interestingly, it has been shown experimentally that all synthetic high performance polymers [2] fail by 'kinking', whereas spider silk fibers that contain alpha-helical structures on the surface do not 'kink' [19] consistent with our calculations. Our analysis helps explain the molecular elasticity and resistance to 'kinking' of biopolymers that consist of alpha-helical strands and hence the apparent prevalence in Nature for coiled coils.
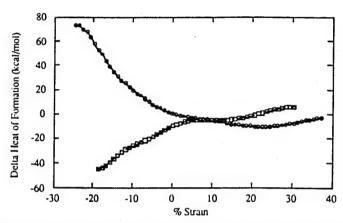
Figure 5: ΔH_{ff} vs. ΔL dependence for the alpha-helical model of poly(L-Ala)-modulus of 60 GPa, where $A_{eq} \sim 20\ \text{Å}^2$, $L_{eq}=10.2\ \text{Å}$, and $K=107$ N/m. The force (10^{-10} N) curve (squares) shows that in distinct contrast to PPTA (Fig. 1), there is no evidence for 'kinking'.

In conclusion, this study reveals the potential of molecular simulations to predict from first principles the macroscopic mechanical response of alpha-helical biopolymers with a reinforcing hydrogen bonding network, *viz.*, a 'spring-like' behavior. This calculation explains the pivotal role of such motifs in biological systems requiring superior compressive mechanical properties. Our foreknowledge of the absence of 'kinking' and the understanding of the structure-to-function relationships in biopolymers is significant in that it may enable the synthesis of structural motifs consistent with molecular frameworks optimized by Nature, *e.g.*, damage resistant composites. Moreover, direct comparisons (*cf.* Table I) of our predictive capability with experimental studies of the mechanical properties of polymers and biomolecules, as have been recently initiated, for example, for DNA strands [35], will further enhance the ability to design new materials.

Table I: Comparison of Experimental and Theoretical Moduli

Polymer	E_{macro}	E_{X-ray}	$E_{empirical}$	$E_{semi-empirical}$
PPTA	186 GPa [36]	207 GPa [37]	203 GPa [38] 271 GPa [39]	290-330 GPa
Extended poly-Glu	-	-	-	230 GPa
Extended poly-Ala	-	-	-	160 GPa
Helical poly-Glu	30 GPa [34]	-	-	60 GPa
Helical poly-Ala	-	-	-	60 GPa

REFERENCES

[1] H.R. Allcock, *Science*, **255**, 1106 (1992).

[2] *Cis*- and *trans*- PBI [poly(*para*-phenylene benzobisimidazole)] rigid rods were first synthesized in 1975 and reported by R.F. Kovar and F.E. Arnold, *J. Poly. Sci., Poly. Chem. Ed.*, **14**, 2807 (1976), while *cis*- and *trans*- PBO rigid rods by T.E. Helminiak, F.E. Arnold, and C.L. Benner, *Polymer Preprints, ACS Poly. Div.* **16**, 659 (1975). *Cis*- PBO [poly(*para*-phenylene benzobisoxazole)] is under study at present by Dow Chemical and others for use as a high performance fiber or film, while *trans*- PBO is difficult to synthesize in high molecular weights due to quinone formation in the *para*-OH monomer. *Cis*- and *trans*- PBZT [poly(para-phenylene benzobisthiazole)] rigid rods, which were first synthesized in 1978 (J.F. Wolfe, B H. Loo, and F.E. Arnold, *Polymer Preprints, ACS Poly. Div.*, **19**, 1 (1978)), are the sulfur analogs to *cis*- and *trans*- PBO. Both materials have been studied structurally, and are also of interest in the area of nonlinear optics. Model compounds were examined by X-ray crystallography (M.W. Wellman, W.W. Adams, R.A. Wolff, D.S. Dudis, D.R. Wiff, and A.V. Fratini, *Macromolecules*, **14**, 935 (1981)), revealing that *cis*- PBZT appears as a bowed, less extended structure than *trans*- PBZT.

[3] Reviews of ordered polymers have recently appeared by S. Kumar, *International Encyclopedia of Composites* , **4**, 51-74 (1991) and by J.F. Wolfe, *Encyclopedia of Polymer Science and Engineering* , **11**, 601 (1988). Also, a symposium was directed to that subject at a Materials Research Society Meeting, edited by W.W. Adams, R.K. Eby, and D.E. McLemore, *The Materials Science and Engineering of Rigid rod Polymers, Materials Research Society Symposium Proceedings*, **134**(1989).

[4] F.J. McGarry and J.E. Moalli, *Polymer*, **32**, 1816 (1991); T.D. Dang, L.S. Tan, K.H. Wei, H.H. Chuah, and F.E. Arnold, *Proc. Polym. Mat. Sci. Eng. (ACS)* **60**, 424 (1989); M. Dotrong and R.C. Evers, *ibid.*, 507 (1989); H.H. Chuah, T.T. Tsai, C. Wang, and F.E. Arnold, *ibid.*, 517 (1989); D.L. Vezie, Ph.D. Dissertation, Massachusetts Institute of Technology, 1993..

[5] R. Pachter, T.M. Cooper, L.V. Natarajan, K.A. Obermeier, R.L. Crane, and W.W. Adams, *Biopolymers* **32**, 1129 (1992)

[6] P.E. Klunzinger, R.K. Eby, *Polymer*, **34**, 2431 (1993).

[7] G.C. Rutledge, U.W. Suter, *Polymer*, **32**, 179 (1991).

[8. R.A. Sorensen, W.B. Liau, R.H. Boyd, *Macromolecules*, **21**, 194 (1988).

[9] K. Tashiro, M. Kobayashi, and H. Tadokoro, *Macromolecules*, **11**, 908 (1978).

[10] S.G. Wierschke, J.R. Shoemaker, R. Pachter, P.D. Haaland, and W.W. Adams, *Polymer*, **33**, 357 (1992).

[11] J.R. Shoemaker, T.R. Horn, P.D. Haaland, R. Pachter, W.W. Adams, *Polymer*, **33**, 351 (1992).

[12] J. R. Shoemaker, M.Sc. Thesis, Air Force Institute of Technology, 1991.

[13] T.R. Horn, P.D. Haaland, R. Pachter, W.W. Adams, *Polymer*, in press

[14.] P.D. Haaland, R. Pachter, and W.W. Adams, Polymer, *Polymer*, in press

[15] P. D. Haaland, R. Pachter, M. Pachter, W.W. Adams, *Chemical Phys. Lett.*, **199**, 379 (1992).

[16] H.M. Warrick and J.A. Spudich, *Ann. Rev. Cell Biol.* **3**, 379 (1987).

[17] T.J. Byers and D. Branton, *Proc. Nat. Acad. Sci.* **82**, 6153 (1985).

[18] V.T. Marchesi, *Ann. Rev. Cell Biol.* **1**, 531 (1985).

[19] D.L. Kaplan, S.J. Lombardi, W.S. Muller, and S.A. Fossey, "Silks: Chemistry, Properties, and Genetics-Biomaterials: Novel Materials from Biological Sources", Macmillan Press (1991); F. Vollrath, *Scientific American*, **70**, March (1992); F. Vollrath and D.T. Edmonds, *Nature*, **340**, 305 (1989).

[20] D. Mahoney, D.L. Vezie, R.K. Eby, and W.W. Adams, manuscript in preparation.

[21] F.J. McGarry and J.E. Moalli, *Polymer*, **32**, 1816 (1991); S.J. LeTeresa, R.S. Porter, and R.J. Farris, *J. Mater. Sci.*, **23** 1886 (1988).

[22] J.J.P. Stewart in MOPAC (Version 5.0), *Quantum Chemistry Program Exchange* #455.

[23] Similar to the Hückel treatment of cyclic bonding in simple cases developed by J.J.P. Stewart, *New Polym. Materials*, **1**, 53 (1987).

[24] H.E. Klei, J.J.P. Stewart, *Int. J. Quant. Chem., Quant. Chem. Symp.*, **20**, 529 (1986).

[25] The invention by duPont of the spinning of liquid crystalline acid solutions of the stiff-chain of PPTA opened the field of extremely high performance organic fibers (S. Kwolek, U. S. Patent No. 3 600 356 1971).

[26] W.W. Adams and R.K. Eby, *MRS Bulletin*, **23** (1987).

[27] S. R. Allen, *Polymer* **29**, 1091 (1988); K. Tashiro, M. Kobayashi, and H. Tadokoro, *Macromolecules*, **10**, 413 (1977); R. J. Gaymans, J. Tijssen, S. Harkema, and A. Bantjes, *Polymer*, **17**, 517 (1976).

[28] N. Karasawa, S. Dasgupta, and W. A. Goddard, *J. Phys. Chem.*, **95**, 2260 (1991).

[29] G.C. Rutledge, U.W. Suter, C.D. Papaspyrides, *Macromolecules*, **24**, 1934 (1991).

[30] D. Tanner, J.A. Fitzgerald, B.R. Phillips, *Adv. Mater.*, No. 5, 151 (1989).

[31] C. Chang, S.L. Hsu, *Macromolecules*, **23**, 1484 (1990), and by R.J. Young, private communication.

[32] P.G. Perkins, J.J.P. Stewart, *J. Chem. Soc. Faraday Trans. II*, **76**, 520 (1980).

[33] CHARMm (Chemistry at HARvard Macromolecular mechanics) developed by B.R. Brooks, R.E. Bruccoleri, B.D. Olafson, D.J. States, S. Swaminathan, M. Karplus, *J. Comp. Chem.* **4**, 187 (1983), coded in Quanta: Release 3.0, Polygen Corporation, 1990.

[34] G. Wegner, private communication, estimates the modulus as *ca.* 30 GPa.

[35] C. Bustamante, J. Vesenka, *Polymer Preprints, ACS Poly. Div.* **33**, 743 (1992).

[36] E.E. Magat, *Philos. Trans. R. Soc.*, (London), A, **294**, 463 (1980).

[37] P.G. Lenhert and W.W. Adams, Air Force Wright Laboratory Technical Report WRDC-TR-90-4070, 1990.

[38] G.S. Fielding-Russell, *Textile Research Journal*, **41**, 861 (1971).

[39] K. Tashiro, M. Kobayashi, and H. Tadokoro, *Macromolecules*, **10**, 143 (1977).

ANISOTROPIC STRESS AND MOLECULAR MODULI OF C$_{60}$
Dr. Peter Haaland

Anisotropic stress and molecular moduli of C_{60}

Peter Haaland [a], Ruth Pachter [b], Meir Pachter [a] and Wade Adams [b]

[a] *Air Force Institute of Technology, Wright-Patterson AFB, OH 45433, USA*
[b] *Wright Laboratory, Wright-Patterson AFB, OH 45433, USA*

An exploration of mechanical properties at the molecular level based on inversion of the Hessian matrix is described. The molecular response of buckminsterfullerene (C_{60}) to isotropic and anisotropic stresses has been examined using semiempirical molecular orbital methods. Although C_{60} is very stiff when compressed isotropically, its modulus is decreased by over an order of magnitude when the stresses are anisotropic.

1. Introduction

As an architect Buckminster Fuller was doubtless intrigued by the mechanical strength of truncated icosohedra which, in the microscopic guise of C_{60} clusters, now bear his name. Early suggestions [1] that C_{60} is stiffer than diamond were followed by molecular mechanics calculations [2], and experiments at pressures which probe the intermolecular interactions in solid C_{60} [3–5]. Under non-hydrostatic conditions C_{60} is converted to diamond, leading to speculation that it cannot resist being squeezed anisotropically [6]. Variation of the critical temperature with pressure in superconducting alkalimetal doped buckminsterfullerene has also been reported [7–9], illustrating that the molecular response to pressure is coupled to the solid's electronic structure. We report here analysis and prediction of the response of C_{60} molecules to isotropic and anisotropic stresses using semiempirical electronic structure methods. The bulk modulus of C_{60} molecules for isotropic stress is calculated to be $\approx 10^{12}$ Pa, substantially larger than any other known compound. However, its response to anisotropic stress is less dramatic. Uniaxial moduli perpendicular to the hexagonal and pentagonal faces (parallel to S_6 and S_{10} axes) are 261 and 234 GPa, respectively. The

Correspondence to: P. Haaland, Air Force Institute of Technology, Wright-Patterson AFB, OH 45433, USA.

modulus along an axis connecting two atoms and the center of the icosohedron is smaller still, 174 GPa.

2. Methods

The geometry of C_{60} was optimized without symmetry or constraints using the Austin Model 1 Hamiltonian in the MOPAC suite of semiempirical electronic structure codes [10]. The diameter of the molecule was computed to be 7.09 Å, with carbon–carbon bond lengths of 1.38 and 1.46 Å, in plausible agreement with extant structural data. Its enthalpy of formation was 16 kcal/mol per carbon atom. The second derivative or Hessian matrix $\mathcal{H}_{ij} = \partial^2 E / \partial R_i \partial R_j$ was computed as a prelude to analysis of its mechanical properties.

There are two ways of calculating the mechanical moduli from the Hessian. The first introduces a force vector F whose 180 elements specify the Cartesian components of the forces applied to each atom in the molecule,

$$\mathcal{H} \delta R = F.$$

F is then left multiplied by the inverse of the Hessian to yield the virtual displacements of each atom in the cluster [11]:

$$\delta R = \mathcal{H}^{-1} F.$$

The ratio of the force to the displacements is con-

379
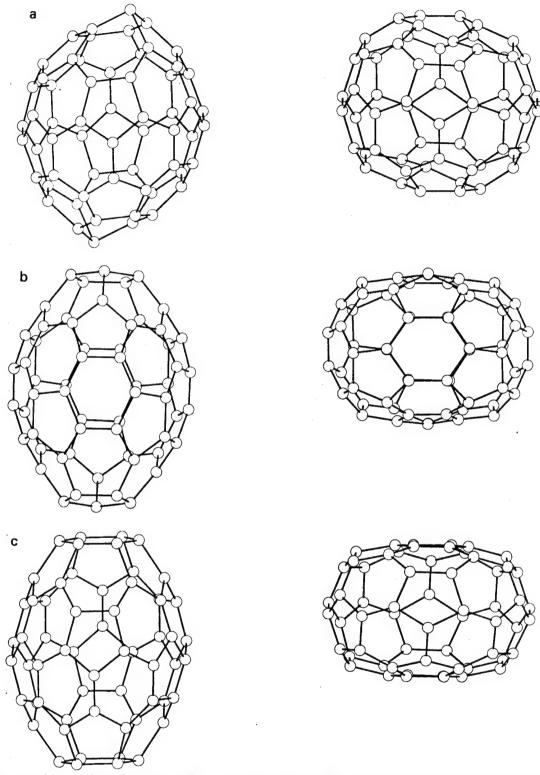
Fig. 1. Response of C_{60} to anisotropic stresses applied to two opposing atoms which are colinear with the center (a), parallel to an S_{10} symmetry axis (b), and parallel to an S_6 axis (c). The virtual displacements in tension and compression are shown side by side with a vertical stress axis. The amplitude of the distortions has been adjusted separately for each stress axis.

380

verted to a modulus with reference to the geometry. For an isotropic stress of 1 mdyn on each carbon the corresponding displacement is 0.6476 Å. The molecular modulus is then:

$$\epsilon = \frac{60 \text{ mdyn}}{0.6746 \text{ Å}} \frac{1}{4\pi r} = 2.00 \text{ TPa} ,$$

where $r = 3.543$ Å is the radius of the cluster. Alternatively, one can compute the virtual energy change associated with a displacement vector R:

$$V = \tfrac{1}{2} R \mathcal{H} R^{\dagger} .$$

For a 2 Å symmetric stretch $V = 46.52$ mdyn Å and $\epsilon = 2.09$ TPa, suggesting numerical error from inversion of the Hessian of about 5%.

3. Results and discussion

Isotropic stress on C_{60} results in very small distortion and an enormous modulus of 2 TPa, as computed with the AM1 Hamiltonian. The predicted response of buckminsterfullerene to anisotropic stresses, which are more likely to be realized in experiments, is more intriguing. Deformation of C_{60} by uniaxial stress along three directions is illustrated in fig. 1. Stress on two atoms which are colinear and intersect the center of the icosohedron deforms the cage structure more easily. Using the cross-sectional area of the cluster and the projection of this distortion on the strain axis we find a uniaxial modulus of 174 GPa, less than one tenth that of the isotropic modulus. The two atoms stressed directly by a 1 mdyn force have virtual displacements of 1.02 Å. The atoms connected to the stressed centers shift 0.4 Å, while all others are displaced by less than 0.1 Å.

Stress normal to the ten atoms that form opposing pentagonal faces (parallel to an S_{10} axis) have a different distortion and larger modulus – $\epsilon = 234$ GPa. Forces applied to opposing hexagonal faces (parallel to an S_6 axis) yield a modulus of 260 GPa. Compressive distortions are similar in these modes, showing an increase in the cross-sectional area at the midplane as the molecular framework is squashed.

The rapid rotational relaxation of C_{60} in the solid state [12] precludes shear stress in crystalline buckminsterfullerene. However the anisotropy of the mechanical modulus may constrain crystal packing and rotational relaxation under non-hydrostatic conditions.

Hessians computed with single determinant wavefunctions systematically overestimate vibrational frequencies due to a neglect of electron correlation [13]. It is possible to compensate for this error either by performing ab initio electronic structure calculations which include correlation, or by biasing the Hessian with experimental vibrational frequencies [14]. The latter approach uses the calculated normal modes U but substitutes experimental frequencies λ_{exp} for their calculated counterparts:

$$\mathcal{H}_b = U \lambda_{exp}^2 U^{\dagger} .$$

The drawback of this method is that experimental data are not available for all 47 normal modes of C_{60}. Based on published spectroscopic data [15–18] and earlier calculations [19,20] we have constructed a partially biased Hessian for C_{60}. A modulus of 1.3 TPa for isotropic stress is computed from the biased Hessian, substantially less than that derived from the unbiased AM1 Hessian but still implying a very stiff material. The uniaxial moduli inferred from the partially biased Hessian are also smaller; 147 GPa (2-point), 209 (S_{10}), and 237 GPa (S_6), but support the conclusion that the molecule is more susceptible to anisotropic than isotropic stresses.

4. Conclusions

We have illustrated a novel approach for inferring mechanical properties of a molecule directly from the computed Hessian using a semiempirical Hamiltonian and the familiar C_{60} cluster. We find that the fullerene is stiff when stressed isotropically but is more easily deformed under the experimentally realizable conditions of anisotropic stresses. The approach can be extended by using more sophisticated computational chemistry paradigms for calculation of the Hessian. As chemists probe larger molecular systems the techniques of finite element analysis which have gained widespread acceptance in mechanical engineering offer insight into the coupling between mechanical and electronic properties in new materials.

381

References

[1] R. Ruoff and A. Ruoff, Nature 350 (1991) 663.

[2] R. Ruoff and A. Ruoff, Appl. Phys. Letters 59 (1991) 1553.

[3] J. Fischer, P. Heiney, A. McGhie, W. Romanow, A. Denenstein, J. McCauley and A. Smith, Science 252 (1991) 1288.

[4] S. Duclos, K. Brister, R. Haddon, A. Kortan and F. Thiel, Nature 351 (1991) 380.

[5] M. Regueiro, P. Monceau, A. Rassat, P. Bernier and A. Zahab, Nature 354 (1991) 289.

[6] M. Regueiro, P. Monceauy and J. Hodeau, Nature 355 (1992) 237.

[7] O. Zhou, G. Vaughan, Q. Zhu, J. Fischer, P. Heiney, N. Coustel, J. McCauley and A. Smith, Science 255 (1992) 833.

[8] M. Schluter, M. Lannoo, M. Needels, G. Baraff and D. Tomanek, Phys. Rev. Letters 68 (1992) 526.

[9] R. Fleming, A. Ramirez, M. Rosseinsky, D. Murphy, R. Haddon, S. Zahurak and A. Makhiga, Nature 352 (1991) 787.

[10] M.J.S. Dewar, E.G. Zoebisch, E.F. Healy and J.J.P. Stewart, J. Am. Chem. Soc. 107 (1985) 3902.

[11] L. Meirovitch, Analytical methods in vibrations, (Macmillan, New York, 1967).

[12] R. Johnson, C. Yannoni, H. Dorn, J. Salem and D. Bethune, Science 255 (1992) 1235.

[13] V.I. Pupyshev, Y.N. Panchenko, C.W. Bock and G. Pongor, J. Chem. Phys. 94 (1991) 1247.

[14] S. Dasgupta and W. Goddard, J. Chem. Phys. 90 (1989) 7207.

[15] D. Bethune, G. Meijer, W. Tang and H. Rosen, Chem. Phys. Letters 174 (1990) 219.

[16] D. Bethune, G. Meijer, W. Tang, H. Rosen, W. Golden, H. Seki, C. Brown and M. de Vries, Chem. Phys. Letters 179 (1991) 181.

[17] R. Cappelletti, J. Copley, W. Kamitakahara, F. Li, J. Lannin and D. Ramage, Phys. Rev. Letters 66 (1991) 3261.

[18] G. Gensterblum, J. Pireaux, P. Thiry, R. Caudano, J. Vigneron, Ph. Lambin, A. Lucas and W. Krätschmer, Phys. Rev. Letters 67 (1991) 2171.

[19] F. Negri, G. Orlandi and F. Zerbetto, Chem. Phys. Letters 190 (1992) 174.

[20] R. Stanton and M. Newton, J. Phys. Chem. 92 (1988) 2141.

382

ELECTRONIC STRUCTURES OF STRAINED POLYMERS 3: SCALED HESSIANS FOR POLYETHYLENE
Dr. Thomas Horn

Electronic Structure of Strained Polymers 3: Scaled Hessians for Polyethylene

Thomas Horn, W. Wade Adams
Ruth Pachter, and Peter Haaland
Materials Directorate
Wright Laboratory, Wright-Patterson AFB, OH 45433

August 5, 1992

Abstract

Earlier estimates for the Young's modulus of polyethylene based on the AM1 semiempirical molecular orbital method were 15% larger than the largest experimental value. Neglect of electron correlation in the single determinant wavefunction for polyethylene leads to a Hessian matrix which is too stiff. Here we apply the biased Hessian approach of Dasgupta and Goddard [1] to the polyethylene chain at equilibrium and under tensile and compressive strain. The chain modulus is 340 GPa with the biased Hessian, in agreement with extant experimental results. Although the variation of the vibrational spectrum with strain is reduced with biasing, the *stress*-dependence of vibrational frequencies are unchanged.

The first papers of this series described the mechanical response of polyethylene [2] and rigid-rod polymers [3] when strained along the chain axis. The approach used the Austin Model 1 (AM1) Hamiltonian and periodic boundary conditions. [4, 5] The calculated chain moduli were found to exceed published experimental values by $\approx$ 15%, although the source of this discrepancy was unclear. One might reason that moduli calculated for a single

chain do not include intermolecular forces or bulk defects which would render real materials less stiff than an idealized single chain. Alternatively, single determinant wavefunctions are known to overestimate vibrational frequencies since they neglect electron correlation [6] so that the calculated stiffness may have a systematic error.

The overestimation of vibrational frequencies by *ab initio* methods is well-documented. The physical basis for this systematic error has been discussed recently by Pupyshev *et al.* [7] in terms of electron correlation. Techniques pioneered by Pulay [8] and Goddard [1] incorporate experimental vibrational frequencies into the analysis. In the absence of a complete vibrational spectrum for the (3N-6) modes of an N-particle system, non-linear least-squares techniques and transfer of scaling factors among analagous bonds are vital to quantitative agreement between computed and observed molecular spectra.

Here we apply the biased Hessian approach of Dasgupta and Goddard [1] to the stiffness and variation of vibrational frequencies with strain in polyethylene. As in reference [2] we use the semi-empirical Austin Model 1 (AM1) Hamiltonian and periodic boundary conditions on the chain axis of a C_6H_{12} unit cell.

1   Method

We have used the cluster model with an AM1 Hamiltonian in the Mopac suite of semiempirical electronic structure codes.[9] Finite chains of n C_2H_4 units are subjected to translationally periodic boundary conditions. The computed energy thus represents an average of n uniformly spaced points

along the chain axis in the first Brillouin zone. [10] The enthalpy per repeat unit converges rapidly for polyethylene, which proves that dispersion in its electronic band structure makes no contribution to the intramolecular enthalpy. [11] The geometry is optimized without constraints, at which point analysis of the second derivative or Hessian matrix:

$$\mathcal{H}_{ij} = \frac{\partial^2 H}{\partial x_i \partial x_j}$$

is performed. Eigenvalues of the mass-scaled Hessian:

$$\mathcal{H}_{ij}^{ms} = \frac{\mathcal{H}_{ij}}{\sqrt{m_i m_j}}$$

are the vibrational frequencies (squared) and its eigenvectors are the normal modes of the system. The geometry is then reoptimized subject to a single constraint on the length of the repeat unit along the crystallographic c-axis, followed by Hessian and frequency analyses.

The Young's modulus is computed directly from the variation of enthalpy with tension or distension:

$$\epsilon = \frac{d^2 H}{dx^2} \frac{l}{\sigma}$$

where x is the unit cell distension, l is the chain length and σ is the cross-sectional area. It is also possible to compute the modulus directly from the Hessian. The virtual displacements $\vec{R}$ corresponding to an arbitrary force $\vec{F}$ are computed from the inverse of the Hessian matrix:

$$\vec{R} = \mathcal{H}^{-1}\vec{F}.$$

The Young's modulus ϵ is proportional to the norm of the force divided by the projection of the virtual displacements onto the strain axis:

$$\epsilon = \frac{|\vec{F}|}{\vec{R} \cdot \vec{j}} \frac{l}{\sigma}$$

where $\vec{j}$ is a a unit vector in the direction of the applied force, l is the chain length and σ is the cross-sectional area.

Vibrational spectra were computed at eleven evenly spaced points from 1% compression to 1% tension. A linear least-squares routine was used to estimate $\frac{d\nu}{d\Delta}$ for each mode. There are 51 non-trivial modes for the infinite C_6H_{12} chain as discussed in reference [2]. The near degeneracy of modes in unstrained polyethylene may be lifted by strain, so that correlations among strained modes were verified by examining the inner product of the eigenvector matrices for different strain values.

A complete vibrational spectrum for polyethylene is available from the experimentally based force-field of Schneider.[12] These vibrational frequencies were used to generate a biased Hessian [1]:

$$\mathcal{H}_b = U \Lambda U^\dagger$$

where U is the AM1 eigenvector matrix and Λ is a diagonal matrix of the squared experimental frequencies. We then define a non-unitary scaling transformation:

$$S\mathcal{H} = \mathcal{H}_b$$

which provides a convenient way to bias the Hessians away from equilibrium. While not rigorous, this approach appeals to the transferability of scaling

factors described by Pupyshev [7], and is expected to be valid for cases where the vibrational eigenvectors are weakly perturbed by stress. The scarcity of experimental information on strained polymers obviates the more direct biasing approach.

2   Results and Discussion

The uniaxial modulus computed by the constrained optimizations or the inverse Hessian approach is 400 GPa This substantially exceeds the experimental values, which are between 210 and 340 GPa as summarized in reference [2]. Inverting the biased Hessian yields a modulus of 340 GPa, in excellent agreement with recently reported force field of Karasawa *et al.* [11], and within the range of reported experimental results. Physically this means that the form of the normal modes computed with the AM1 Hamiltonian is reasonable, but the computed stiffness is too large, a result which is plausible given the overestimation of vibrational frequencies by the AM1 approach. (Figure 1)

Figure 2 illustrates the strain dependence of each vibrational mode with the unbiased Hessians. As outlined in reference [2], the calculations are in qualitative agreement with extant experimental data on the variation of IR and Raman spectra with stress. Most of these data are reported as spectral shifts versus stress $\frac{d\nu}{ds}$, so the computed values, which are shifts versus strain, must be divided by the calculated modulus:

$$\frac{1}{\epsilon}\frac{d\nu}{d\Delta} = \frac{d\nu}{ds}$$

if they are to be compared with experiment. Values of $\frac{d\nu}{d\Delta}$ found with the scaled Hessians are less than their unbiased counterparts as shown in figure 3. The change in the magnitudes of $\frac{d\nu}{d\Delta}$ and ϵ after scaling are nearly equal (85%); when they are divided we see that biasing the Hessian has no net effect on the *stress*-dependence of vibrational frequencies.

The vibrational modes at 1059, 1127, and 1385 cm^{-1} were found to have large variations with strain. Figure 4 compares these variations using the biased and unbiased Hessians. Scaling the strained Hessians causes a 15% drop in computed values of $\frac{d\nu}{d\Delta}$ in these modes. In figure 5 the connection between the equilibrium frequency error, ν_{obs}/ν_{calc}, and the shift in $d\nu/d\Delta$ with biasing is reiterated. These results are entirely consistent with the heuristic description of biasing as a shift in the distance scale of a frequency calculation. [7]

Scaling the Hessian is not compatible with distortions that cause a radical reorganization of the normal modes. The implicit assumption is that the calculated eigenvectors are similar to the natural normal modes. Although straining the system perturbs the vibrational eigenvectors the additional corruption caused by scaling is modest. As one measure for changes of the equilibrium eigenvectors consider the inner products:

$$mx_i(s) = max(|ev(s) * u_i|)$$

where $ev(s)$ is the matrix of eigenvectors at strain s and u_i is the unstrained eigenvector for the ith mode. The value of $mx_i = 1$ for all i when $s = 0$, by definition. The extent to which it decreases with s for each mode describes the anharmonic mixing caused by strain. Contour plots of mx_i using unbiased

and biased hessians are shown in figure 6. Although differing in detail the loss of the equilibrium modes' integrity with stress is qualitatively retained after biasing the Hessian.

We believe that the large moduli computed with the semi-empirical molecular orbital methods are a consequence of neglecting electron correlation in the single determinant wavefunctions. The most efficient way to remedy this systematic effect is to bias the equilibrium Hessian with experimental data. In cases where experimental frequencies are unavailable it should be possible to carry out correlated *ab initio* calculations on fragments and oligomers to estimate the scaling coefficients.

Proper scaling of the semi-empirical Hessian reduces the chain modulus by about 15%. We expect this result to be general, so that discussions of *ultimate* modulus based on single chain stiffness become less divisive. Briefly, the discussions concern predictions for the maximum attainable modulus in a fiber. Theoreticians armed only with unscaled AM1 results would unjustly accuse their synthetic counterparts of making material with morphological defects that cause it to perform more poorly than implied by calculations, which set the target or *ultimate* modulus. Reducing the AM1 chain moduli by 10 − 15% still leaves room for discussion on the interplay of intermolecular and intramolecular forces in determining mechanical stiffness while narrowing the gap between theory and experiment.

3 Conclusions

An estimate of 340 GPa for the Young's modulus of polyethylene chains has been obtained directly from an experimentally biased AM1 Hessian matrix. The modulus is in good agreement with extant experimental data as well as recently reported force fields. Scaling the Hessians of strained chains also reduces the magnitude of vibrational frequency shifts with strain $\frac{d\nu}{d\Delta}$. No change is found for the stress-dependence of the vibrational frequencies, since this is equal to the strain dependence divided by the modulus, both of which are reduced by the same amount (15%). The heuristic description of biasing as an empirical estimate of electron correlation suggests that unscaled estimates of stiffness from single determinant wavefunctions will be systematically too high by $10 - 15\%$.

References

[1] S. Dasgupta and W. Goddard, *J. Chem. Phys.*, **90**, 7207 [1989].

[2] Shoemaker, J., Horn, T., Haaland, P., Pachter, R., and Adams, W.W., *Polymer* in press.

[3] Wierschke, S., Shoemaker, J., Haaland, P., Pachter, R., and Adams, W.W., *Polymer*, in press.

[4] Dewar, M.J.S., Zoebisch, E.G., Healy, E.F., and Stewart, J.J.P., *J. Am. Chem. Soc.*, **1985**, *107*, 3902.

[5] P.G. Perkins and J.J.P. Stewart, *J. Chem. Soc. Faraday II*,**76**, 520 [1980].

[6] S. Wilson, **Electron Correlation in Molecules**, (Oxford:Clarendon Press), 1984 pp. 57-9.

[7] V. Pupyshev, Y. Panchenko, C. Bock and G. Pongor, *J. Chem. Phys.*, **94** 1247 [1991].

[8] P. Pulay, G. Fogarasi, G. Pongor, J. Boggs, and A. Vargha, *J. Am. Chem. Soc.*, **103** 7037 [1983].

[9] J.J.P. Stewart, Mopac version 5.0, 1989.

[10] J. Chandrasekhar and P. Das, *J. Phys. Chem.*, **96**, 679 [1992].

[11] N. Karasawa, S. Dasgupta, ans W. Goddard, *J. Phys. Chem.*, **95**, 2260 [1991].

[12] R.G. Snyder and J.H. Schachtschneider, *Spectrochimica Acta*, 19,85 and 117, (1963).

Figure 1: AM1 vibrational frequencies of polyethylene chains (ν_{calc}) versus frequencies from the experimentally-based force-field from reference [12].

Figure 2: Linear least-squares estimates of $\frac{d\nu}{d\Delta}$ for polyethylene based on a C_6H_12 repeat unit. Linear least-square errors indicate the fidelity of the assumed linear strain dependence.

Figure 3: Linear least-squares estimates of $\frac{d\nu}{d\Delta}$ for polyethylene based on a biased Hessian.

Figure 4: Comparison of vibrational frequency versus strain in three modes for which experimental data are available using the unbiased and biased AM1 Hessians.

Figure 5: Correlation between the ratio of computed and experimental frequencies to the ratio of unbiased and biased strain dependencies.

Figure 6: Contour plot of the function $mx_i(s)$ for the biased and unbiased hessians. Contour intervals are 5%. with the unstrained case having mx = 1. Modes are numbered in order of increasing equilibrium frequency, and strain is varied from -1% (compressive) to +1% (tensile) distortion of the unit cell.

Fig. 1

Modal Strain Derivatives

Unbiased Results

Fig. 2

Modal Strain Derivatives

Biased Results

Fig. 3

Fig. 4

$\nu_0=1059$ cm^{-1}

$\nu_0=1127$ cm^{-1}

$\nu_0=1385$ cm^{-1}

ν(cm^{-1})

Strain(%)

16

26

39

94
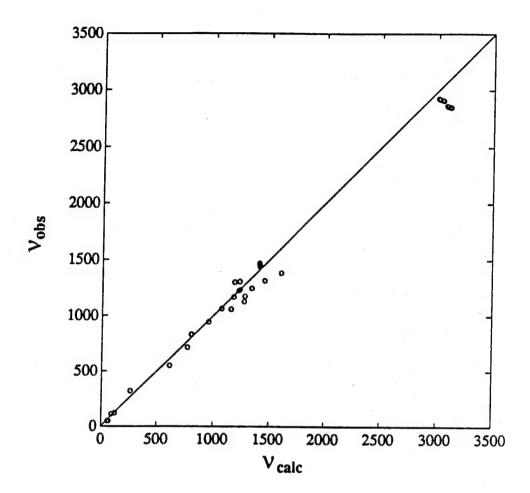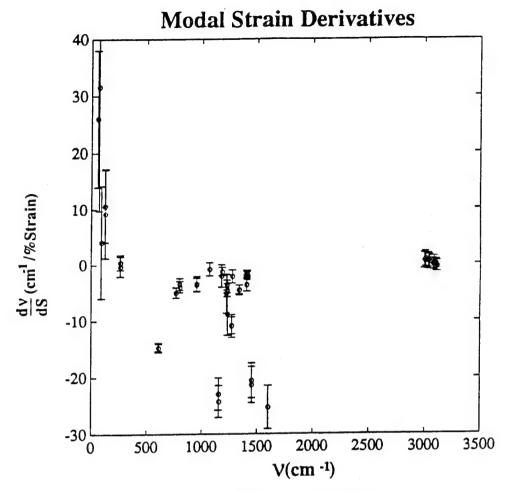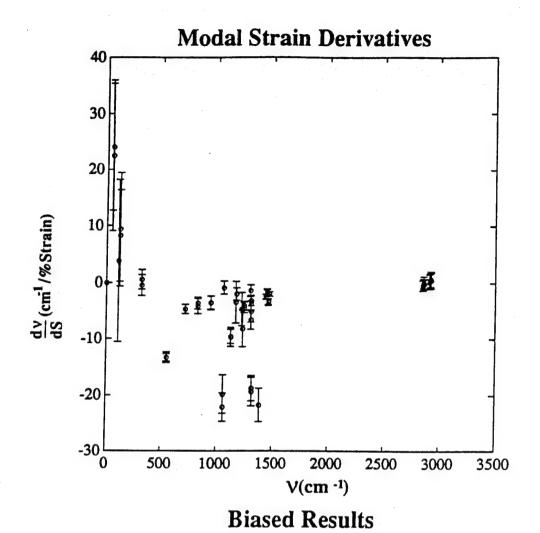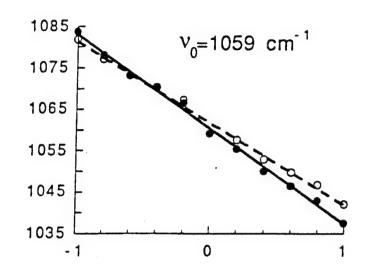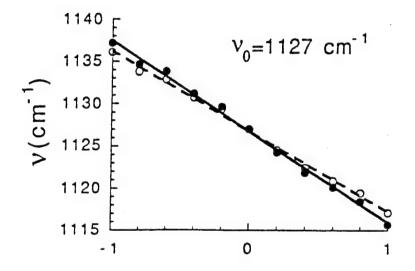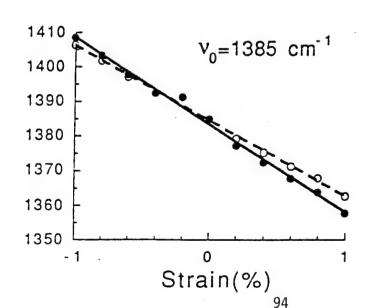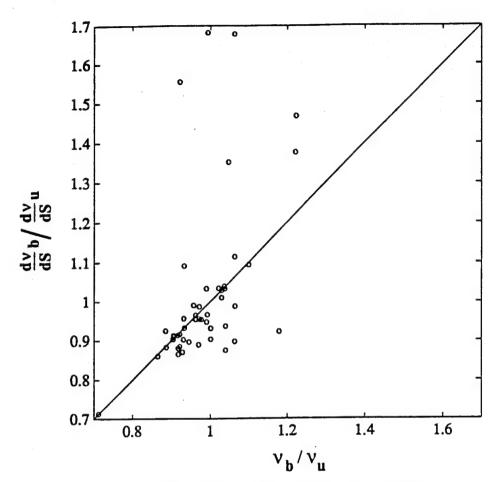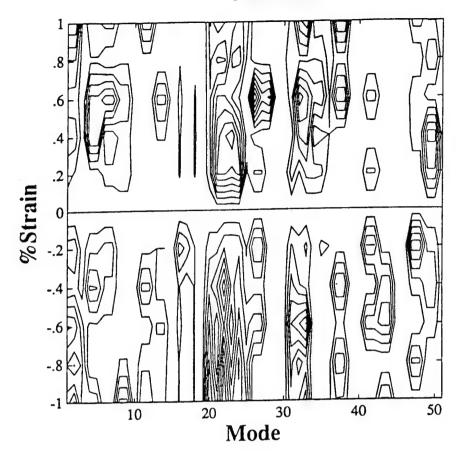
Slope vs. Frequency Ratios

Fig. 5

Unbiased

Biased
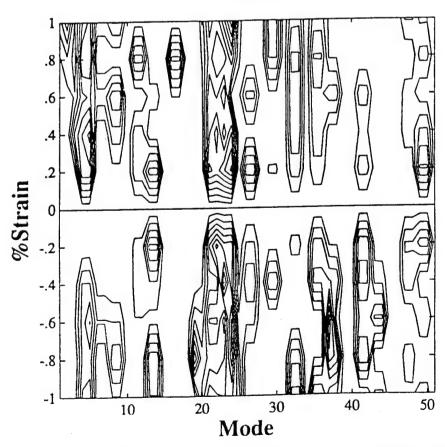
Fig 6

Strain-Induced Eigenvector Distortion

NATURAL SPRINGS:
MECHANICAL PROPERTIES OF BIOPOLYMER CHAINS
Dr. Ruth Pachter

Natural Springs:
Mechanical Properties of Biopolymer Chains

Ruth Pachter, Peter Haaland, Robert Crane, and Wade Adams

Purpose

Demonstrate that a simulation with a semi-empirical approach of biopolymers versus a similar synthetic molecular structure offers new insight into the mechanical properties of flexible coiled coils arrangements of α-helical motifs in Nature, while also holding promise for the design of new materials

Mechanical Properties of Alpha-Helical Strands in Nature

Importance of such biopolymers and their function is profound

- keratin in hair, myosin and tropomyosin in muscle; epidermin in skin; and fibrin in blood clots, play vital mechanical roles

  myosin tail: the *coiled coil* super structure leads to a hierarchy of reinforcing interactions within the alpha-helices, culminating in a highly ordered array of a thick filament that provides the means for its mechanical function in muscle contraction

- membrane skeletons that consist which enable erythrocytes to resist strong shearing forces in blood flow

  spectrin networks: flexible triple-stranded alpha-helical *coiled coils* that provide the underlying mechanical stability and resilience of the membrane

- Supposition: alpha-helical strands act as a rubbery reinforcement matrix to provide the elasticity to spider silk, which in compression indicate no 'kinking'

Prediction of Mechanical Properties

- Prediction of mechanical properties of polymers based on calculations employing empirical potential energy functions is limited

  - it applies a classical force-field dependent on a particular parametrization scheme

  - not all the possible deformation modes can be taken into account

- A theoretical study of single chain moduli at the semi-empirical is performed

Method

Polymer Structure Calculations

- Semi-empirical Neglect of Differential Overlap approximation at the modified level AM1(Austin Model 1) for energy calculation

Cluster method

- Defines a fragment of a polymer chain by one or more repeat units

- The position of the atoms of the cluster in a repeat unit are determined by internal coordinates

- Periodic boundary conditions are used to describe the pseudo-bond between the end atoms of different repeat units -- characterized by the translation vector (Tv)

Advantage in cluster method is that 'end effects' present in oligomer approximations of polymers are eliminated

Modulus Calculation

- Equilibrium geometry of the cluster is calculated by energy minimization using the AM1 Hamiltonian

- Translation vector is incrementally increased or decreased by an amount ΔL, representing molecular tensile or compressive strain. The geometry of the cluster is re-optimized under this constraint, and the heat of formation ΔH_f calculated

- The dependence of the heat of formation on molecular tension and compression is established

- Modulus calculation performed

Polymers Studied

Extended biopolymer strands

- poly(L–Ala) and for comparison poly(L–Glu) vs. synthetic PPTA containing an amide bond

Alpha-helical structure

- poly(L–Ala) and poly(L–Glu)--helix 'makers' and used as model compounds
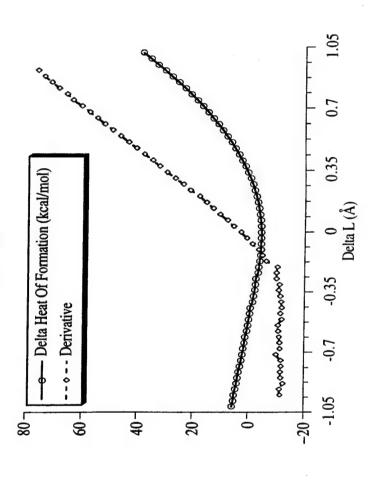
  -Geometries calculated by using the amide bond correction to the Hamiltonian were compared to those optimized with a classical force-field (CHARMm): the alpha-helical configuration is conserved within the semi-empirical approach since a large number of repeat units within the unit cell was used

PPTA

ΔH_{ff} vs. ΔL dependence for PPTA: modulus of ca. 330 GPa

density (d=1.5 g/cm^3); Leq=13.1 Å, Mw=238.25 g/mol; Aeq= 20.1Å^2, and K=50.6 N/m

Force curve (10^{-10} N) obtained by taking a numerical derivative of the energy, indicates 'kinking' at ~ 2.5% compressive strain

PPTA

PPTA Result

- **Molecular Deformation Analysis Indicates**

  in tension - similar behavior to other rigid rods(PBI, PBO, PBZT, and PPP)

  in compression - 'kinking'

- **Vibrational Frequencies Strain Dependence**

  in qualitative agreement with an experimental result of R. Young (personal communication) of $d\upsilon/ds \sim -5.5 \ cm^{-1}/\%$ strain

poly(L-Ala) & poly(L-Glu)

Extended Polypeptide Chains

Delta Heat of Formation (kcal/mol)

Delta L (Å)

Legend:
- poly(L-Glu)
- poly(L-Ala)

poly(L-Ala)

Modulus of ca. 160 GPa

$A_{eq} \sim 20 \ \text{Å}^2$,

$L_{eq} = 21.7 \ \text{Å}$,

K=145 N/m
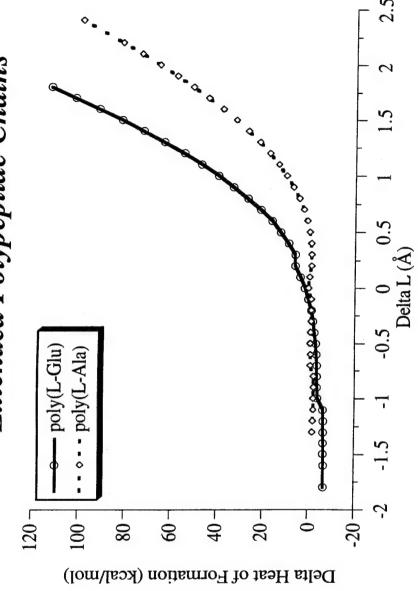
poly(L-Glu)

Modulus of ca. 230 GPa

$A_{eq} \sim 20 \ \text{Å}^2$,

$L_{eq} = 14.3 \ \text{Å}$,

K=320 N/m

The molecular structure of the extended biopolymers enables more configurational variation since there is an additional rotatable bond⇒only a small change in energy in compression

Modulus Calculation from Equilibrium Geometry of poly(L-Ala)

Method
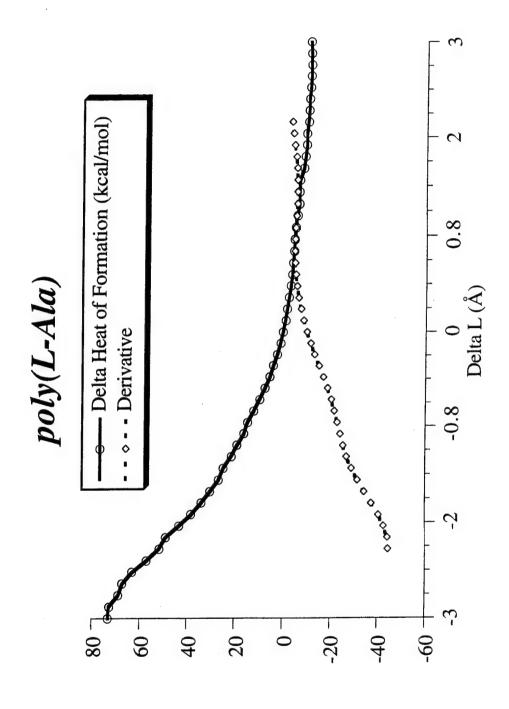
- Hessian derived by performing a normal mode analysis of the cluster

- An applied force $\mathbf{F}$ ($H\delta R=\mathbf{F}$, where $H_{ij}=\partial^2 E/\partial R_i\partial R_j$) is left multiplied by the inverse of H to yield the virtual displacements of all atoms: $\delta R=H^{-1}\mathbf{F}$

- Modulus then calculated by using the cluster's geometry

Result

An application of this procedure to the extended chain of poly(L-Ala) by using a force of 2 mD along the translation vecto results in a computed displacement projected onto the translation vector of 23.1 Å and a modulus of 179 GPa

Apha-Helical Strands

Distinctly different response of an alpha-helical chain to the application of strain

poly(L-Ala)

Legend:
- Delta Heat of Formation (kcal/mol)
- Derivative

Axes: Delta L (Å); x-axis from -3 to 3; y-axis from -60 to 80

Biopolymer Chains Result

- **poly(L-Ala)**

  - $-\Delta H_{ff}$ vs. ΔL dependence for the alpha-helical model of poly(L-Ala) results in a modulus of ca. 60 GPa, where Aeq~ 20 Å^2, Leq=10.2 Å, K=107 N/m

  - The force curve shows that in distinct contrast to PPTA there is no evidence for 'kinking'

  - This observation is supported by the fact that no buckling is found in the α-helical biopolymer conformations in compression

- **Similar observation for poly(L-Glu)**

  - $-\Delta H_{ff}$ vs. ΔL dependence for the alpha-helical model of poly(L-Glu) results in a modulus of ca. 60 GPa, where the Aeq~20 Å^2, Leq=5.2 Å, K=240 N/m

  - G. Wegner, private communication, estimates the modulus as ca. 30 GPa

Conclusion

- This study

  - predicts the mechanical response of alpha-helical biopolymers with a reinforcing hydrogen bonding network - a **'spring-like' behavior**

  - presents a theoretical verification on the **absence of 'kinking'** in biopolymer chains of an alpha-helical structure

  - explains the pivotal role of such motifs in biological systems requiring **superior compressive mechanical properties**⟹ their extraordinary mechanical functions in *super coiling* architectures

- A foreknowledge on the absence of 'kinking' and the understanding of the structure-to-function relationships in biopolymers may enable the **synthesis of structural motifs consistent with molecular frameworks optimized by Nature**

  - direct comparisons of a predictive capability with experimental studies, for example, for DNA strands, **will further enhance the ability to design new materials**

COMPUTATIONS OF MODULI IN EXTENDED CHAIN POLYMERS USING MOPAC

P. E. Klunzinger and R. K. Eby

Computations Of Moduli

In Extended Chain Polymers

Using Mopac

P. E. Klunzinger and R. K. Eby

  The University of Akron

  Department and Institute of Polymer Science

  Akron OH, 44325-3909, USA

W. W. Adams

  Wright Research and Development Center

  Dayton OH 45433-6533, USA

INTRODUCTION

A useful macro-molecular modeling tool is Mopac[1], a semi-empirical molecular orbital modeling package developed.   A primary advantage is that it models the electrons in the molecular bond as opposed to modeling the bond as a simpler, (but easier to calculate), spring as is done with force fields. We have used Mopac to study: modulus[2], thermal expansion of crystals[3] (using normal mode analysis), charge distribution calculations, force field parameter fitting, conformational analysis, and calculation of index of refraction.

This note describes some experience with Mopac with an emphasis on methods of data analysis and calling attention to differences which have been observed between results obtained with Mopac 5 and Mopac 6. As an example a study of the modulus

of poly (p-phenylene benzobisthiazole) (PBZT) will be discussed.

BACKGROUND

A characteristic often observed in rigid rod polymers is nonlinear elasticity (a reversible change of Young's modulus with increasing stress or strain), with the modulus increasing as tensile stress is applied[4,5]. Much of the nonlinear elasticity can be attributed to the reversible realignment of crystals within the fiber as stress is applied. This realignment can be observed by examining the change in the χ width of the crystal x-ray reflections. The crystal orientation distribution gained from this experiment can be used in conjunction with the elastic constants of the crystal and some assumptions of how the crystals are connected within the fiber to calculate the Young's modulus of the fiber. The extent of the increase in modulus predicted from these calculations is smaller than that observed experimentally[6].

The hypothesis we seek to test is, "Can this discrepancy be explained at an atomistic level using available computational tools?". Because of the novel chemistry of PBZT and the harmonic form of most force fields we felt that current force field calculations were inadequate. If the source of the NLE is due to the novel bonding in PBZT a model is needed which does not constrain the bonds to be Hookian. Mopac, due to its modeling of electrons, removes such constraints and was the primary argument for using a semi-empirical molecular orbital modeling method.

116

The modulus of polymers has been modeled by a number of researchers. The polymer is treated as a one dimensional crystal using the cluster calculation of Mopac[7]. Initial results were obtained with Mopac 5 using the AM1 Hamiltonian. The cluster calculation technique attempts to simulate the long chain of the polymer by applying periodic boundary conditions at the ends of the cluster. The operation defining the direction of the chain axis and the repeat distance is called the translation vector.

Young's modulus (E) can be calculated from the second derivative of the energy (U) with respect to the translation vector (L):

$$E = (L_o/A) \frac{\partial^2 U}{\partial L^2}_T \qquad (1)$$

where (A) is the basal area of a single chain and (L_o) the equilibrium length of the translation vector.

By constraining the length of translation vector to a specified distance and minimizing the remaining degrees of freedom the energy (U) as a function of (L) and hence the modulus can be obtained. The procedure for calculating this curve is as follows: 1) start with a fully minimized structure, (no constraints), 2) calculate the energy, 3) increase (L) by 0.02 Å, 4) minimize given this new constraint, 5) calculate the new energy, and 6) repeat from step 3 until enough data have

117

been obtained.   The same approach was used to compress the module.

The choice of 0.02 Å as a step size in changing the length of the translation vector was a compromise.   Too small a step would cause the minimizer to abort too early because the change in energy was not large enough.   Too large a step would cause the minimizer to locate another (higher energy) minimum than that found in the initial case.

USING MOPAC 5

The procedure above will give good results with curves reasonably smooth enough so that two derivatives can be taken. To test reproducability and increase the number of data points the above procedure was repeated but with the initial configuration stretched by multiplies of 0.001 Å.   Thus giving us 50 points per Angstrom as opposed to 50 points for the entire curve.   The result of combining this series of runs, (shown in Figure 1), was not smooth enough to take derivatives at the accuracy needed for this study.

The apparent reason for this 'noise' (it is not gaussian) is that on different cycles the geometry minimizer would locate false minima.   Since the lower energy minimum is the correct one, the higher energy values must be discarded.   To remove these non-global minima values, an algorithm was developed to reduce subjective bias.   The method is as follows: 1) fit a polynomial to the data points, 2) remove any data points that were above the fitted line by about one standard deviation

(keeping all below the fitted line), and 3) repeat steps 1 and two until removing points does not statistically improve the fit. The fitting to the polynomial and determination of statistical significance is important and will be discussed next.

The polynomial fitted was of the form:

$$E(L) = E_o + \frac{k}{2}(L - L_o)^2 + \sum_{i=3}^{N} A_i (L - L_o)^i.$$

L_o was determined independently in each iteration by fitting a 2nd order polynomial. The number of terms (of order greater than) two to keep in the final fitting was determined by testing the improvement of the fit by incorporating the extra terms. The test of improvement was the standard F-test at a 95% confidence interval[3].

This analysis of the data demonstrated a nonlinear modulus, (indicated by a fitted polynomial of order higher than 2). The sign and magnitude of the calculated non-linearity matched that which was unexplained in the previous work[4]. These results have been reported previously[2,6]. Figure 2 shows the final results with the retained data points, the fitted curve, and the modulus.

USING MOPAC 6

After the work above was completed, Mopac 6 became available. This version was of interest, initially, because of improved parameters for sulfur. Version 6 was also faster

because of new minimization algorithms and optimizations to use the hierarchial memory and multiple CPU's available. To test this version of Mopac and check the previous work, the calculations were redone using Mopac 6.

Preliminary results showed much less 'noise'. However, the sign of the non-linearity has changed as shown in the first two rows of Table 1. The reason for the difference is not clear. There are two obvious changes in the new Mopac which may be the cause: the new sulfur parameters or the new algorithms. Both versions of Mopac were compiled using both the new and the old parameters for sulfur, the results are shown in Table 1. The energy versus length curves are also plotted in Figure 3. Here the minimum energy of each curve is subtracted from all the data for that curve so that all curves fit to the same minimum.

Table I
Comparison of Methods Used.

| Version | | Minimum Energy (kcal/mol) | Modulus (GPa) | ΔModulus per 1% Strain (GPa) | Smooth Curves |
Mopac	AM1				
5	old	137.243	590.5	+1.0	no
6	new	119.285	607.0	-10.0	yes
6	old	137.201	608.0	-10.0	yes
5	new	119.286	592.5	0.0	no

The new parameters can be seen to produce a lower energy. The new minimization algorithms in Mopac 6 initially appear to produce better results because of their consistency as shown graphically by the smooth curves. However, the modulus appears to be dependent on the algorithm, not the parameters. Also, examining the nonlinearity in the modulus given in the table as Δmodulus per 1% strain shows that the algorithms of Mopac 6

120

produce a nonlinearity that on average is about an order of magnitude greater than that obtained with Mopac 5. Also there is a reversal of sign.

SUMMARY

Which of the four curves in Figure 3 is correct? To obtain others' answers, this note was presented WP-AFB Symposium in Computational Modeling. The consensus there, based on others' experience using Mopac 6, was that Mopac 6 might generate some errors when putting systems in tension[10]. However, the exact cause of the differences is not completely clear and hence the question is not completely answered.

REFERENCES

1.   J.J.P. Stewart MOPAC, QCPE program #455

2.   P.E. Klunzinger, K.A. Green, R.K. Eby, B.L. Farmer, W.W. Adams, G. Czornyj, in Tech. Papers XXXVII (Society of Plastics Engineers, Brookfield, CT1991) pp. 1532-1536.

3.   P.E. Klunzinger, K.S. Macturk, R.K. Eby and W.W. Adams, Polymer Preprints, **32**, No. 2, 187 (1991).   See also P.E. Klunzinger, R.K. Eby, W.W. Adams and John M. Liu, Proceeding and Program of Carbon 1991, edited by P.A. Thrower, (american Carbon Society 1991) p. 546.

4.   H. Jiang, P. Arsenovic, R.K. Eby, J.M. Liu, W.W. Adams, Polymer Preprints, Japan (English Edition) **36** (5-10), E10-13 (1987).

5.   H. Jiang, R.K. Eby, W.W. Adams, Galen Lenhert, "Nonlinear Elasticity of Poly(p-phenylene benzobisthiazole) Fibers", in The Materials and Science and Engineering of Rigid-Rod Polymers, edited bye W.W. Adams, R.K. Eby, D.E. Mclemore, (Mater. Res. Soc. Proc. **134**, Pittsburgh, PA 1989).   pp. 341-350.

6.   P.E. Klunzinger, R.K. Eby, W.W. Adams, Hierarchy in Extended Chain Polymers, (Mat. Res. Soc. Symp. Proc. **255**, Pittsburgh, PA 1992). pp. 119-128.

7.   H.E. Klei, J.J.P. Stewart, Int. J. Quant. Chem. **20**, 529-540 (1986).

8.   J.J.S. Dewar, W.J. Theil, J. Am. Chem. Soc., **99**, 4899 (1977).

9.   William H. Beyer, <u>CRC Standard Mathematical Tables, 28th Edition</u>; CRC Press Inc., (1987) CRC Press Inc., pp 573-578.

10. Thanks especially to Dr. R. Pachter, for her comments and help.

5) FIGURE NOTES

FIGURE 1: Mopac 5- old AM1 (all data)
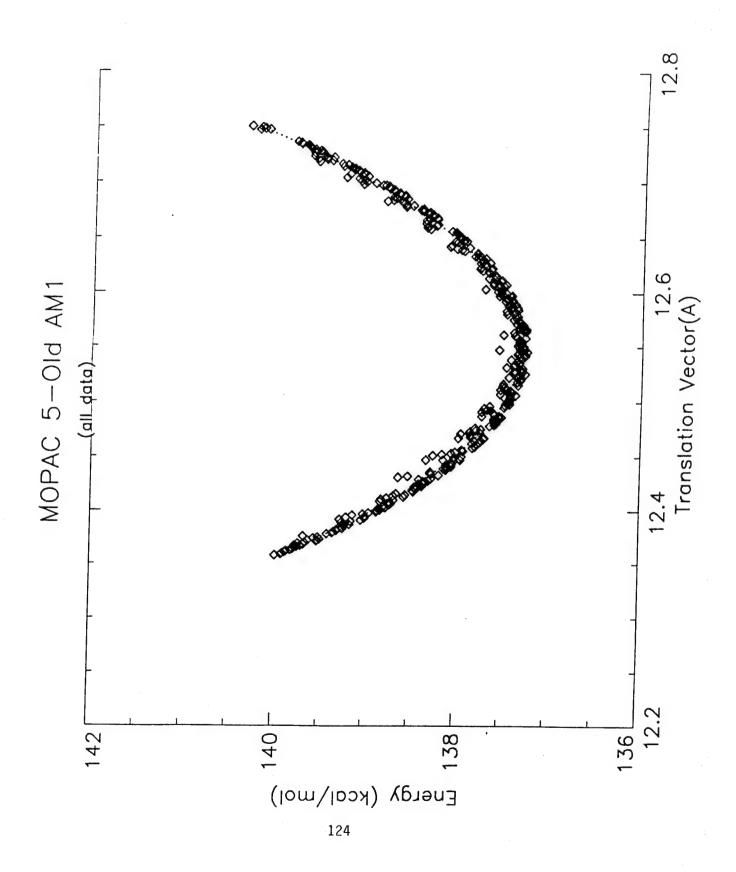
Caption: Energy as a function of translation vector (length) showing all the data generated using Mopac 5, (old AM1 parameters).
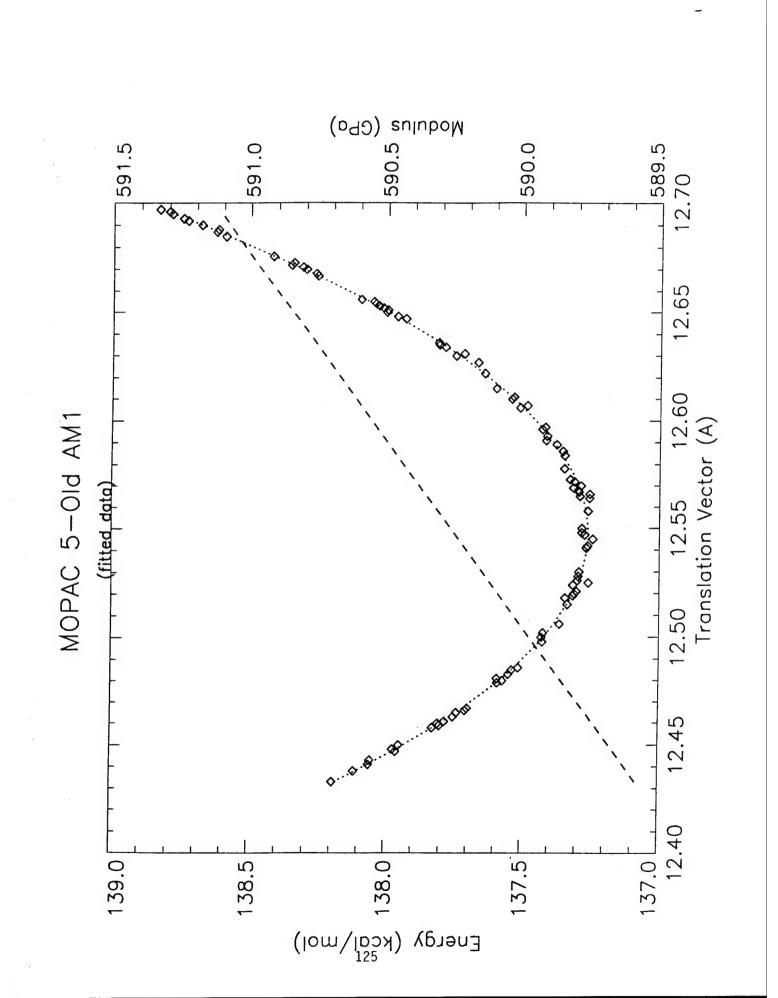
FIGURE 2: Mopac 5- old AM1 (fitted data)
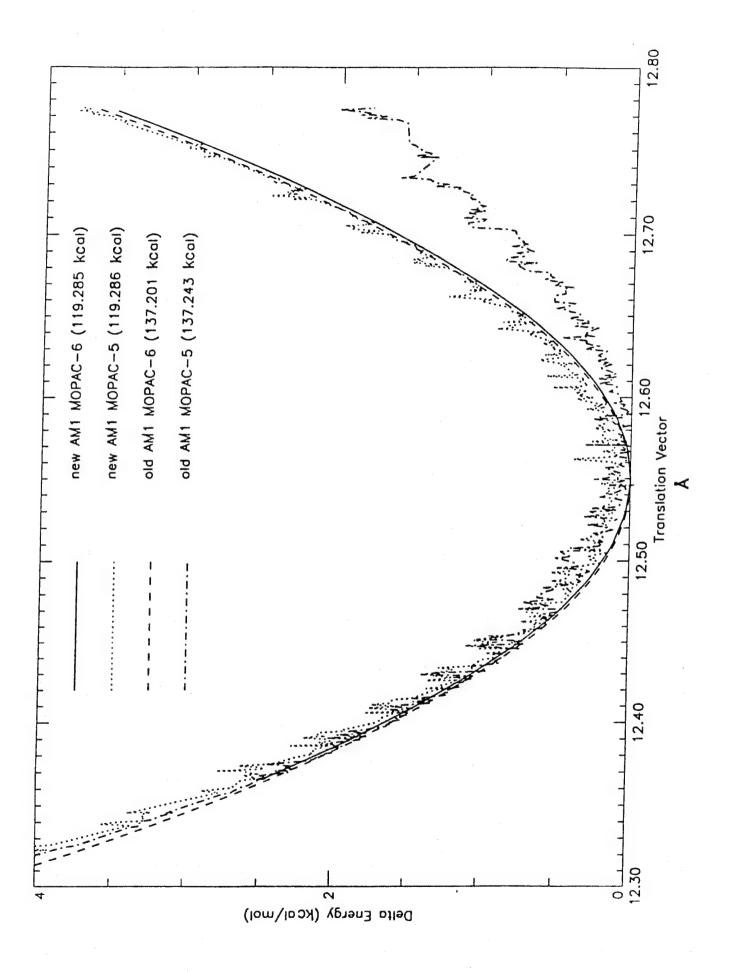
Caption: Energy as a function of translation vector and the modulus calculated from the fitted curve. The data have been selected using the algorithm described in the text.

FIGURE 3:

Caption: Comparison of the energy vs translation vector curves using the four methods discussed in the text. Lines connect all data points.

MOPAC 5–Old AM1

(all data)

Energy (kcal/mol)

Translation Vector(A)

142

140

138

136

12.2   12.4   12.6   12.8

124

MOPAC 5—Old AM1

(fitted data)

X-axis: Translation Vector (Å) — 12.30, 12.40, 12.50, 12.60, 12.70, 12.80

Y-axis: Delta Energy (kcal/mol) — 0, 2, 4

Legend:
- new AM1 MOPAC-6 (119.285 kcal)
- new AM1 MOPAC-5 (119.286 kcal)
- old AM1 MOPAC-6 (137.201 kcal)
- old AM1 MOPAC-5 (137.243 kcal)

MOLECULAR MODELING OF SUBSTITUTED SILOXANES
Dr. B. L. Farmer

Molecular Modeling of Substituted Siloxanes

B. L. Farmer

Department of Materials Science and Engineering
University of Virginia
Charlottesville, Virginia 22903-2442

and

W. W. Adams

Wright Laboratory
Materials Directorate
WL/MLPJ
Wright Patterson Air Force Base, Ohio 45433

Abstract

A molecular dynamics study of substituted siloxane molecules has been undertaken. Siloxane stars having four biphenyl mesogens (4B), four cholesteryl mesogens (4C), or two of each (2B2C), have demonstrated the remarkable flexibility of the allyloxybenzoate leader group connecting the siloxane core and the biphenyl or cholesteryl moieties. In each case, three mesogens aggregated fairly rapidly in the *in vacuo* simulations, with the fourth mesogen eventually joining the aggregate as well. Cholesteryl mesogens in the {2B2C} star seemed to form an especially long-lived association, showing little tendency to dissociate once formed. Linear dimer and trimer siloxanes having {2B} and {BC} substituents have also be examined. They likewise have substantial flexibility. Somewhat surprisingly, preliminary results suggest that the dimer might more readily adopt conformations that bring its substituents into proximity than does the trimer. The times required to do so are short, nonetheless, and comparable to those observed for the siloxane stars.

The influence of intermolecular interactions on the biphenyl torsion angle were examined for the star containing four such mesogens. Oscillations over the barrier at 90 deg, which are prevalent when the mesogens are far apart, diminish when the mesogens are close together. The biphenyl rings then reside in energy minima near 45 deg. Occasional transitions through coplanar conformations are observed, but there is no indication of a tendency to remain at such torsion angles.

Molecular Modeling of Substituted Siloxanes

INTRODUCTION

Molecular dynamics (MD) techniques have been used previously (1-3) to investigate the structure and properties of a commercially available liquid crystalline material based on a cyclic penta(methyl siloxane) whose structure is shown in figure 1a. The hydrogens attached to the silicon atoms can each be replaced by a suitable mesogen to yield the liquid crystalline material. Especially of interest (4) has been the material having pendant biphenyl-4'-allyloxybenzoate {B} (figure 1b) and cholesteryl-4'-allyloxybenzoate {C} (figure 1c) mesogens. The material, even though it is not polymeric, can be drawn into fibers showing high degrees of orientation (4). Depending on the specific composition (i.e., the relative numbers of {B} and {C} mesogens), variations in the observed x-ray spacings can be interpreted as changing degrees of interdigitation between mesogens belonging to different molecules (1,3,4). The MD simulations (1-3) offered insight into the amount of interdigitation that might occur between pendant groups within and between lamellae.

Molecular modeling on these systems to date has been confined to the cyclic penta(methyl siloxane) having two cholesteryl and three biphenyl mesogens. These studies presumed different general topologies of the mesogens with respect to the siloxane ring [(cone, disk, or cylinder models (1-4)], as well as different configurations for the locations of the methyl and mesogenic groups. Further, for the cylinder model, relative placements of the {B} and {C} mesogens were also assumed at the outset. Simulation times long enough to eliminate any dependence of the results on the starting geometry would be quite computationally intensive and were not attempted. Instead, the problem of dealing with the limitations of the initial geometry has been approached by exploring other siloxane geometries to identify the important effects of that geometry as well the effects of interactions between mesogens.

The role of the geometry of the siloxane core has now been explored by studying linear di- and tri-siloxane oligomers and star geometries. The structures of the unsubstituted siloxane moieties are shown schematically in figures 1d-1f. Stars having mesogen compositions consisting of all biphenyl, {4B}, all cholesteryl, {4C}, and two of each, {2B2C}, have been considered. Stars substituted with mesogens having a vinyl group in the leader (rather than an allyl group - i.e., with one less $-CH_2-$ at the connection to the siloxane core) have also been examineded. Linear siloxanes with {2B} and {BC} substituents were also considered.

METHOD

The MD simulations were carried out using the Sybyl molecular modeling program (5) using the Tripos force field (6) modified as described below. The starting geometries were minimum energy structures as determined using the same force field. Simulations were carried out for 100 ps, using a time step of 1 fs, and a simulated temperature of 300 K. All atoms were considered explicitly. Electrostatic interactions were not considered (see below). Trajectories were saved every 50 fs for subsequent analysis.

As part of the Polymer module, the Tripos force field has the parameters necessary to describe the non-bonded interactions of silicon atoms, but it does not have parameters for the bonded silicon interactions - bond stretching, angle bending

and torsions. Initial parameters for these potentials were taken from the CHARMm force field (7), appropriately converted to the Sybyl potential form and units.

Two views of starting models of the star siloxane, one depicting the {2B2C} and one the {4B} molecule, are shown in Figure 2. Among the four mesogens, there are six inter-mesogen distances which were determined as a function of time. For the biphenyl mesogens, the carbon most remote from the center of the star was used in this distance determination. For the cholesteryl mesogens, the dimethyl substituted carbon atom in the hydrocarbon tail was used for measurement purposes. This measurement shows the relative change in distance between mesogens fairly well. A measure of the minimum distance between any pair of atoms of the mesogens, or the value of the total interaction energy between all the atoms of a pair of mesogens might better portray the persistence and relative stability of aggregations that occur.

RESULTS

Unsubstituted Star Siloxane

The star molecules are somewhat smaller than the cyclic systems and the MD simulations are somewhat less computationallly intensive. More importantly, by the nature of the tetrahedral geometry of the star molecules, the starting geometry need not predispose particular pairs of mesogens to interact, since they are all roughly equidistant from each other at the start of the MD simulation (as shown in figure 2). Those dominant interactions which rightfully should dictate the course of the simulation have an opportunity to do so without requiring long simulation times that would be necessary to allow major conformational transitions in the cyclic siloxanes. The star and linear oligomers also offer the possibility of investigating the dependence of material behavior on the geometry of the siloxane moiety and on the length of the leader joining the cholesteryl and biphenyl groups to the siloxane core.

The geometry resulting from the molecular mechanics minimization of the unsubstituted siloxane star using the supplemented Tripos force field was not in suitable agreement with the results from a semiempirical molecular orbital minimization using the AM1 Hamiltonian in MOPAC (8). In particular, the Si-O-Si bond angle was 158 deg from the MM calculations and 169 deg from MOPAC. Suitable agreement was obtained by changing the Si-O-Si minimum energy bond angle to 170 deg. The full set of modifications and supplements to the Tripos force field are given in Table 1.

Molecular orbital calculations (MOPAC AM1) were used to calculate the partial charges on the atoms. This brought to light a difficulty with the modeling of silicon atoms in siloxanes. Modeling programs typically use a predefined van der Waals radius for the purpose of generating space-filling or ball-and-stick representations of the molecules. The radius of a silicon atom is about 1.18 Å and that of a neutral oxygen atom is about 0.60 Å. Using these values, space-filling renderings of the star result in missing atoms, where apparently some atoms are enveloped in the volume occupied by others (2). The minimum energy distances between these atoms are not consistent with these standard fixed radii, and consequently the graphical representations of the atoms are not realistic.

In the siloxanes, especially the star siloxanes where the silicon atom at the core of the star is bonded to four oxygen atoms, there is sufficient difference in electronegativities that the atoms are far from neutral. By MOPAC calculations, the central silicon atom, has a charge of +1.97, the attached oxygens have charges of -0.96, and the silicons attached to them have charges of +1.45. The volumes associated with such ions would be considerably different from those of neutral atoms. For example, in silicate structures, silicon atoms (ions) are assumed to carry a +4

charge and have a radius of 0.42 Å. The oxygens are considered to have a charge of -2 and a radius of 1.40 Å. As a result, the silicon ion fits interstitially at the center of a tetrahedron formed by four oxygen ions. In the star siloxanes, the central silicon atom, whose bonding environment is like that in the silicates, might be expected to have a radius comparable to that of a magnesium ion with charge of +2, namely, about 0.66 Å and the oxygen radius might be comparable to that of a fluorine ion, 1.33 Å. Figure 3 shows ball and stick and space-filling renderings of the siloxane star showing the greater size of the silicon atoms based on the radii neutral atoms. In the space-filling renderings, oxygen atoms are either barely visible or are entirely subsumed in the oversized silicon atoms. To depict the molecules accurately, the atomic charges should be taken into account when determining the radius for the purposes of rendering.

The inaccurate depiction of atomic sizes might contribute to misconceptions of the relative role of the silicon atoms as strong X-ray scattering centers. Were they neutral, the silicon atoms would indeed have a scattering factor more than 2.5 (=14/6) times that of carbon atoms. In the silicate form, however, silicons have the same scattering power as the oxygen ions. In the star siloxanes, their scattering would be only 1/3 more than that of the oxygens. They are by no means comparable to heavy atoms in their influence on the diffraction from a material. The volume associated with siloxane units, whether star, cyclic or linear, would not appear to differ significantly from the corresponding carbon-based materials. It is not clear that the electron density associated with a siloxane chain, cycle, or star would be appreciably different from that associated with the attached mesogens. Applying concepts such as microphase separation may result in misconceptions of the structures of the material.

The MD calculations reported here did not include electrostatic interactions. An initial minimization of the siloxane star *was* carried out with electrostatic interactions included. Charges calculated in MOPAC were assigned to each atom, and a dielectric constant of 1.0 was used. The geometry resulting from this minimization was totally unrealistic. Because the electrostatic interactions so vastly dominated the minimization, bond lengths and angles took on absurd values (e.g. Si-Si bonds 0.37 Å and Si-O-Si angles of 12 deg) as the ionic interactions almost implode the molecule. The geometry resulting from a minimization which did not include electrostatic interactions, on the other hand, was in quite reasonable agreement with the MOPAC results. Thus electrostatic interactions were not included in subsequent MD calculations.

Substituted Star Siloxanes

With a reasonable starting geometry in hand for the star, mesogens were substituted for the hydrogen atoms on the four silicon atoms. The mesogen geometries (including allyloxybenzoate leader groups) were first minimized, then attached, and then the full star model was minimized. Stars having four biphenyl mesogens {4B}, four cholesteryl mesogens {4C}, or two biphenyl and two cholesteryl mesogens {2B2C} were assembled for subsequent MD simulations.

It was initially anticipated that the mesogens of the {2B2C} star would form pairwise interactions dictated by the relative energies/stabilities of those interactions. What was observed instead, for {2B2C}, (and {4B}, and {4C} stars as well) was that fairly rapidly three of the mesogens would come into close proximity, and the fourth would eventually join the cluster as well. Figure 4 shows the six distances as a function of time for {2B2C}. For reference the cholesteryl mesogens can be identified as C_1 and C_2 and the biphenyl mesogens as B_1 and B_2. The distances between C_1-C_2, B_2-C_2, and B_2-C_1 are less than 10 Å after 25 ps, while B_1 remains farther away until about 90 ps. Figure 5 shows the star near the mid-point

of the simulation. Once the two cholesteryl mesogens come together, they remain together for the duration of the simulation. Although their relative orientation changes with time, they remain close together once they have come in contact. The biphenyl mesogens associate with the opposite faces of the cholesteryl mesogens, but do not appear to hold any particular position for prolonged times.

The star having four cholesteryl mesogens was also examined. As shown in Figure 6, the behavior is similar to that seen in the {2B2C} star. The distances between the closest 3 mesogens are about 10-15 Å after about 50 ps, while the third remains 40 Å away. Once again, after about 80 ps, all four mesogens come into close proximity. It appears again that C_1-C_2, C_1-C_4, and C_2-C_4 remain at close distances once they come together. Longer simulations are necessary to determine if the same could be said of C_3 once it finds the group. It should also be pointed out that the mesogens which are closest together at the start of the simulation are not the ones which first come together. This suggests that the starting model does not predetermine (at least in an obvious way) the resulting cluster of mesogens that forms.

Two simulations of the {4B} star were carried out. One used the same force field as the {2B2C} and {4C} described above. The second used a force field further modified to make the energy *versus* torsion within the biphenyl group similar to that calculated by MOPAC AM1 calculations. Though a little different in detail, the distance results are in general about the same for the two force fields. Both show the fourth mesogen belatedly joining the initial cluster formed by the three others. The distance *versus* time data calculated with the unadjusted force field are shown in Figure 7. Figure 8 shows the three shortest distances between mesogens (B1-B2, B1-B3, and B2-B3) from the simulation using the adjusted force field.

Simulations of a {2B2C} star having a vinyloxybenzoate leader group - that is, having one less carbon atom in the leader - were also carried out. The results, shown in figure 9, are not dramatically different than those obtained with the longer leader group (compare figures 4a and 9). Certainly the cholesteryl mesogens are still able to associate quite closely, and show a tendency to remain so. However, at 75 ps, the distance between cholesteryl mesogens increases for a short time to about 15 Å. Such a separation fluctuation was not observed with allyl leaders, and thus may indicate increased strain energy resident in the leader when the mesogens are in close proximity. Obviously, longer simulations are required and other leader groups need to be examined before the role of leader flexibility on mesogen associations can be fully understood.

Biphenyl Torsions

Using the unadjusted biphenyl force field parameters, the minimum energy torsion angle for biphenyl is 90 deg, and there is a barrier of 7.1 kcal/mol at 0 deg and a relative energy of 0.15 kcal/mol at 40 deg. (Torsion angles of 0 and 180 deg make the rings coplanar.) AM1 results, on the other hand, place the minimum at 40-45 deg, with barriers of 2.1 and 1.0 kcal/mol at 0 and 90 deg, respectively.

Figure 10 shows the biphenyl torsion angle in the B_1 mesogen as a function of time from the simulation using the original force field. (Distance data were given in Figure 7. Note also that the time axis in figure 10 extends from 0 to 100 ps.) When the mesogens are well separated at the start of the simulation, the biphenyl torsion oscillates between values of about -40 and -150 deg. After about 30 ps, when the distances among B_1, B_2 and B_3 are in the range of 5 to 15 Å, the oscillations settle down somewhat into wells centered at either -60 or -120 deg. Similar behavior was seen in the other three mesogens, though the settling is most apparent in the B_1 mesogen. Transitions through the coplanar torsion values did not occur at any time for any of the mesogens.

Figure 11 shows the biphenyl torsion angles for two mesogens from simulations using force field parameters adjusted to better agree with the AM1 rotational barrier in biphenyl. Figure 11a shows the torsion angle for the most confined mesogen, B2 (distances were shown in figure 8) while 11b shows the torsions in B4 which remains at a distance of 12-17 Å from the other three through most of the simulation. In all four mesogens, transitions through coplanar conformations are observed, no doubt because of the more realistic energy barrier at the 0 and 180 deg torsion angles. The oscillations between minima at 45 and 135, with frequent excursions over the low energy barrier at 90 deg are likewise evident in all four mesogens. The three closest mesogens, B_1, B_2 and B_3, appear to settle preferentially into one of these minima soon after the mesogens come into proximity. As seen in Figure 8, the distances are short after about 35 ps, and mesogens B_2 and B_3 especially seem to decrease the number of excursions through 90 deg at about the same time. Mesogen B_2, which (observation shows) resides between B_1 and B_3, is the more settled of the three mesogens. Mesogen B_4, in contrast, continues its oscillations through 90 deg for most of the simulation. The times when there is a hint of settling into a particular minimum correspond to the times when its distances from B_2 and B_4 are reasonably short. Further localization of the torsion angles, for example at coplanar values, was not observed.

Regardless of the mesogens present, the same tendency is observed - namely for three to aggregate rather quickly, to be joined somewhat later by the fourth. This behavior is not surprising, since the MD simulations are carried out for single molecules *in vacuo*. Rather than dangle in space with no contact to other atoms, the arms of the star gather to minimize their distances from one another. What is somewhat less expected is that aggregates of three closely interacting mesogens and one remote mesogen interaction is apparently preferred to two pairs of closely interacting mesogens. Given the tetrahedral geometry of the star, it is relatively easy for three of the mesogens to come together, essentially collapsing one face of the tetrahedron of the starting model. The fourth mesogen has more difficulty, bending essentially all the way around the core of the star. That it is able to do so in this system speaks to the great flexibility of the allyloxybenzoate leader group, and perhaps to a slightly lesser degree, the vinlyoxybenzoate leader as well.

Linear Siloxanes

Linear dimer and trimer siloxanes having {2B} and {BC} substituents were also examined. Figure 12 shows the starting conformations of the {2B} molecule. The distances between mesogens from the MD simulations are shown in Figure 13. Comparing the dimer (solid lines) and trimer (broken lines) behavior, it can be seen that the dimer more rapidly brings its substituents into close proximity, both for {2B} and {BC}. The extra -Si-O- unit in the backbone of the trimer apparently makes it somewhat more difficult for the mesogens to aggregate, perhaps by introducing a kink that must gradually be worked out of the backbone. Close associations between the phenyl rings of the ester groups were also noted, and tended to remain at close distances, even more so than the biphenyl and cholesteryl groups. This may be attributable to the shorter tether that connects them to the siloxane and makes it more difficult for them to move apart. In any event, the substituents on these linear oligomers are indeed able to come together in a short time, comparable to the times observed for the siloxane stars. Further analysis and simulations of the {2C} linear siloxanes are currently underway.
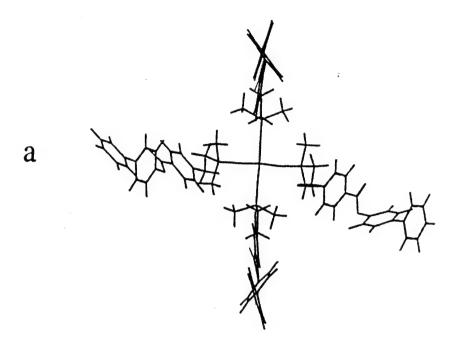
References

1. E. P. Socci, B. L. Farmer, T. J. Bunning, R. Pachter and W. W. Adams, *Liquid Crystals*, 13, 811 (1993)
2. R. Pachter, T. J. Bunning and W. W. Adams, *J. Comput. Polymer Science*, 1, 179 (1991)
3. R. Pachter, E. P. Socci, B. L. Farmer, T. J. Bunning, R. L. Crane and W. W. Adams, *Die Makromoleculare Chemie, Theory and Simulations*, (in press)
4. T. J. Bunning, H. E. Klei, E. T. Samulski, R. L. Crane and R. J. Linville, *Liquid Crystals*, 10, 445 (1991)
5. SYBYL Version 5.4, Tripos Associates, St. Louis, MO., 1991
6. M. Clark, R. D. Cramer, III, M. van Opdenbosch, *J. Comp. Chem.*, 10, 982 (1989)
7. Quanta/CHARMm, Parameters Release 3.0, Polygen Corp., 1990
8. MOPAC Version 5.0, J. J. P. Stewart, QCPE Program Number 455, Indiana University

Table I. Force Field Modifications

Stretches

Si-H	1.460	463.0
Si-Si	2.351	266.0
Si-C	1.806	465.0
Si-O	1.692	912.0

Bends

Si-O-Si	170.0	0.0038
C-Si-O	109.5	0.0564
O-Si-O	109.5	0.0590
H-Si-C	111.2	0.0487
H-Si-O	109.9	0.0192

Torsions

-C-O-	0.5626
-C-Si-	0.1626
-Si-O-	0.2857
-Si-Si-	0.1352

Figure 1. Siloxane and mesogen structures (schematic). (a) Five-membered siloxa:
ring. (b) Biphenyl mesogen with leader group. (c) Cholesteryl mesogen wi
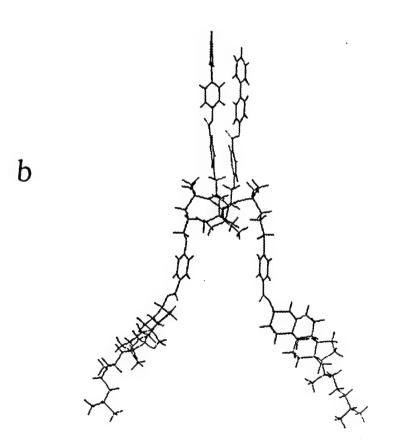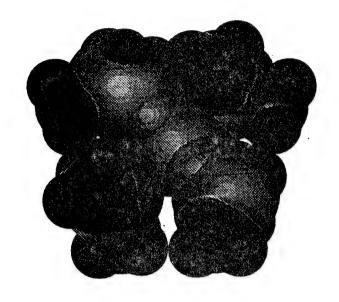leader group. (d) Star siloxane. (e) Linear dimer. (f) Linear trimer.

Figure 2. Starting geometries of the star siloxane (a) substituted with four biphenyl mesogens: (4B); and (b) substituted with two biphenyl and two chloesteryl mesogens: (2B2C).
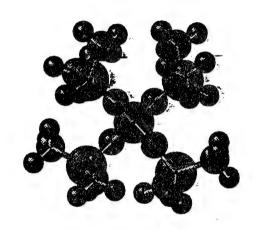
Figure 3. Space-filling and ball-and-stick renderings of the unsubstituted star siloxane, showing (improperly) the relative sizes of the atoms.
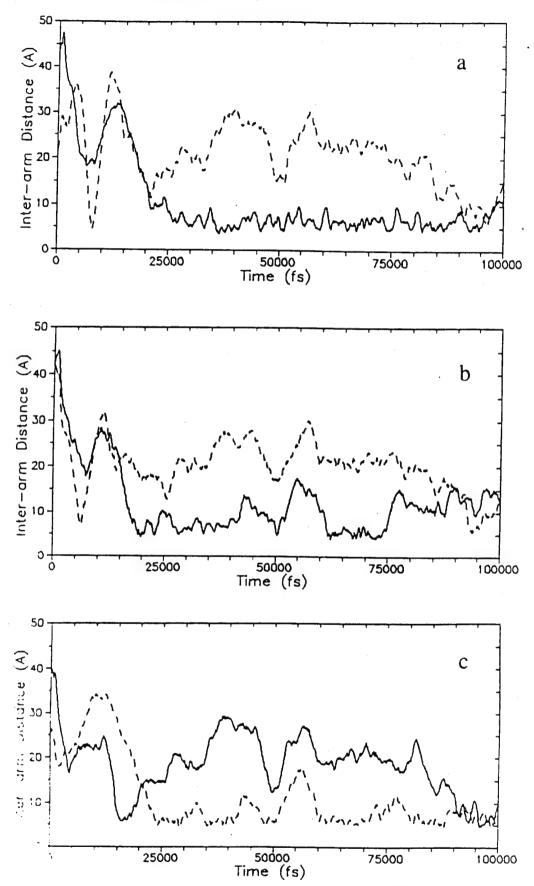
Figure 4. The distances between mesogens for the (2B2C) star as a function of time during the simulation: (a) Distances between the two cholesteryl mesogens (solid line) and the two biphenyl mesogens (broken line); (b) Distances between B1 and the two cholesteryl mesogens; (c) Distances between B2 and the two cholesteryl mesogens.
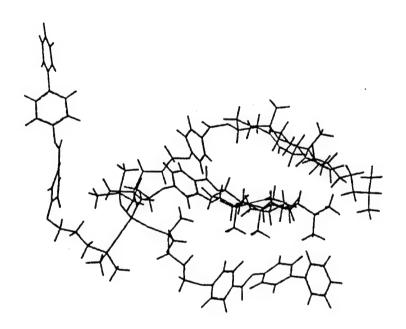
139

Figure 5.   View of the {2B2C} star at time of 56450 fs during the simulation.
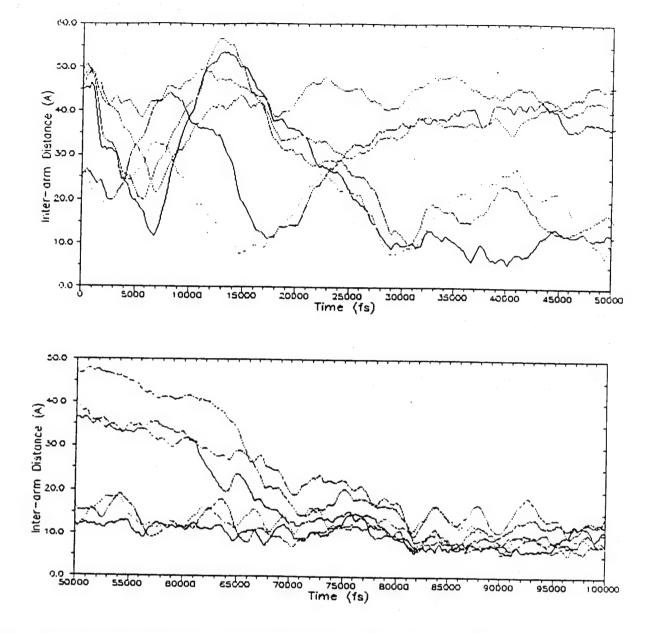
Figure 6. The distances between mesogens for the {4C} star as a function of time during the simulation: (top) from 0 to 50 ps and (bottom) from 50 to 100 ps.
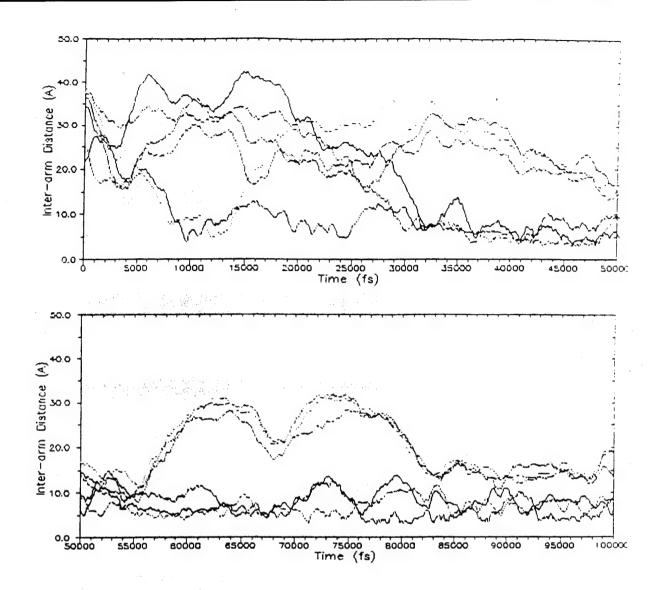
Figure 7. The distances between mesogens for the **(4B)** star as a function of time during the simulation, using the original force field: (top) from 0 to 50 ps and (bottom) from 50 to 100 ps.
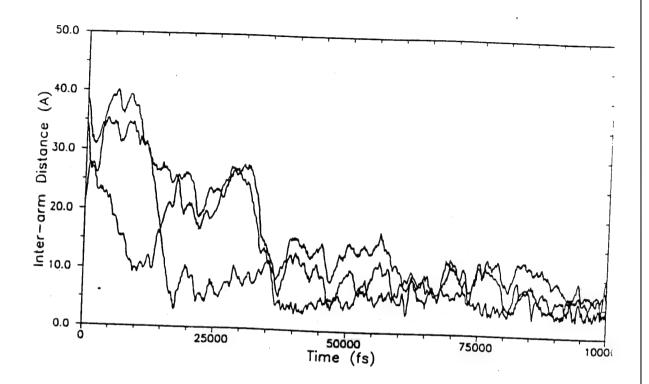
Figure 8. The three closest inter-arm distances between for the {4B} star as a function of time during the simulation, using a force field adjusted for the biphenyl torsion.
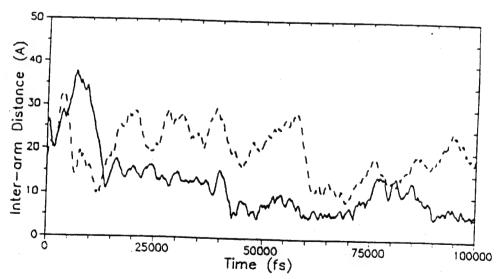

Figure 9. The distances between the two cholesteryl mesogens (solid line) and the two biphenyl mesogens (broken line) for a (2B2C) star with vinly leader groups.
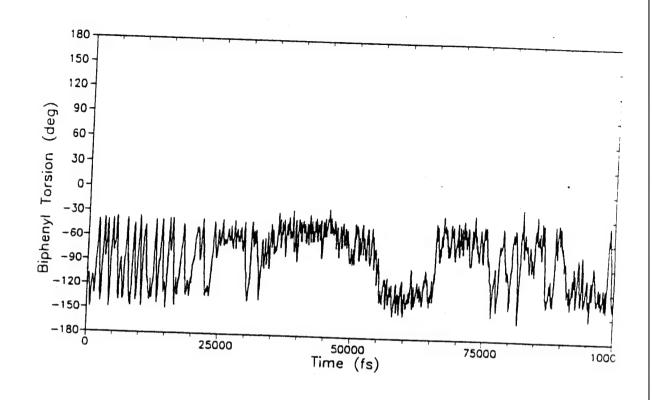
143

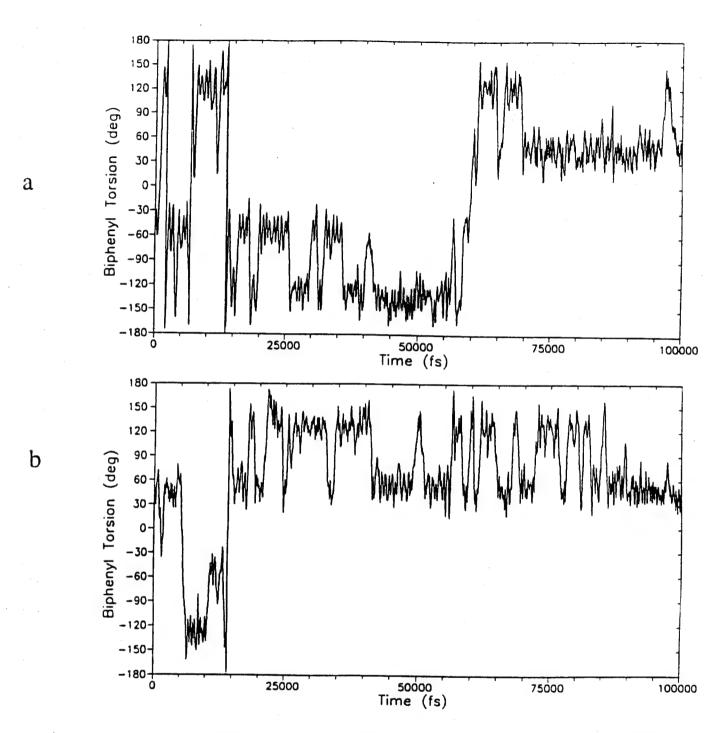Figure 10. The biphenyl torsion angle as a function of time for the (4B) star, using the original force field.

Figure 11.   The biphenyl torsion angles as a function of time for the {4B}, using the adjusted force field for (a) mesogens B_2 and (b) mesogen B_4.

145
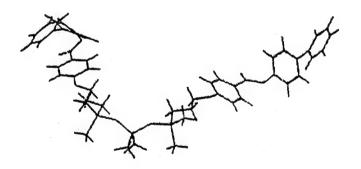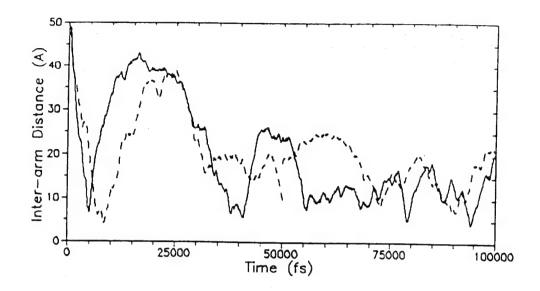
Figure 12. The starting structures of the linear siloxane dimer (top) and trimer (bottom) containing two biphenyl mesogens.
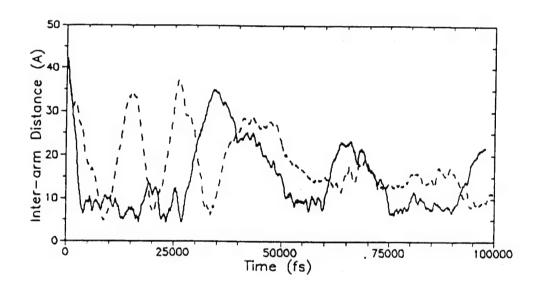
Figure 13.   The distances between mesogens for the linear dimer (solid lines) and
            trimer (broken lines) containing two biphenyl mesogens (top) and one
            cholesteryl and one biphenyl mesogen (bottom).

147

MOLECULAR DYNAMICS OF CYCLIC SILOXANES BASED LIQUID CRYSTALS

Dr. Soumya Patnaik

Molecular Dynamics of Cyclic Siloxane Based Liquid Crystals

By
Soumya S. Patnaik

University of Virginia
Department of Materials Science and Engineering
Charlottesville, VA 22903

Table of Contents

Introduction

The structure of siloxane based liquid crystals has been studied with a view to develop highly ordered structures which act as suitable medium for low molecular weight organic non-linear materials. By substituting NLO moities in liquid crystalline molecules interesting new materials can be developed for application in imaging technology, optical storage media and integrated optical devices. The liquid crystalline nature of these materials gives rise to easy processibility. In order to be able to tailor the optical properties of these materials, their structure has to be known and the interactions between the various mesogens has to be understood. Molecular mechanics and dynamics and X-ray diffraction have been used to study the structural aspects and the molecular packing of these molecules. The result of this study is expected to lead to a better understanding of this class of materials and ultimately to developing materials with improved properties.

Molecular Mechanics and Dynamics

Molecular mechanics (MM) is based on the premise that a molecule can be simulated by empirical energy functions. The molecule is considered as a collection of atoms held together by elastic or van der Waals forces, which are described by potential energy functions of bond length, bond angles, non-bonded interactions, etc. The strain energy E of a molecule is the difference in the energy between the molecule and a hypothetical molecule where all the bond lengths, bond angles, etc have ideal values. This strain energy is given by equation 1,

$$E = \sum_{i=1}^{N_{nb}} E_{nb} \sum_{i=1}^{N_{bonds}} E_{stretch} \sum_{i=1}^{N_{angles}} E_{bend} \sum_{i=1}^{N_{tor}} E_{twist} \sum_{i=1}^{N_{nb}} E_{elec} \qquad (1)$$

where E_{nb} is the non bonded energy, $E_{stretch}$ is the bond stretching energy, E_{bend} is the bond angle bending energy, E_{twist} is the torsional energy due to twisting about bonds and E_{elec} is the electrostatic energy. E is minimized so that it is as small as possible and stable conformations are found as minima in the total energy function. The parameters which describe the force field are derived from analysis of vibrational spectra and from structures determined by X-ray diffraction.

Molecular dynamics (MD) is an extension of molecular mechanics as it takes into account the effect of temperature and time. It is a more realistic description of a molecule than MM and can yield time averaged properties and dynamic properties of molecular systems. It is also more likely to get out of local energy minima than MM. At temperature greater than 0 °K the atoms in a molecule are in constant motion. MD incorporates the time and temperature effects by using classical equation of motion to describe the motion of an atom under the influence of the forces exerted on it by all the other atoms. This force is calculated from the gradient of the potential energy expression as used by MM. From this the atomic velocities can be calculated and subsequently the temperature can also be calculated using Equation 2,

$$3KBT = m.v_i^2 \Big/ N \qquad (2)$$

where m_i and v_i are the mass and velocity of atom i and N is the number of atoms.

Molecular Systems

(1) X-ray diffraction measurements on a family of cyclic siloxanes where a cyclic(Penta methyl siloxane) core is attached to biphenyl-4 allyloxybenzoate (B) and cholesteryl-4-allyloxybenzoate (C) mesogens show very complex patterns [2]. The diffraction patterns show strong dependence on the mesogen composition, i.e. the molar

ratio of B and C. We have studied molecules with all B mesogens attached to the cyclic Penta methyl siloxane core (ABCS).

ABCS

X-ray diffraction patterns of ABCS show unusually well defined order. It shows many sharp reflections at room temperature and is nematic above 60 °C. It is a simpler molecule to study than the molecules with mixed B and C mesogens and is expected to help our understanding of this whole family of liquid crystals.

(2) The effect of incorporating a chromophore of the spiropyran family in ABCS molecule was also studied. Recently there has been a lot of interest in photosensitive liquid crystals [5]. The combination of photochromic and liquid crystalline properties of the same molecule makes it a potential useful material for many applications, the most important one being in imaging technology. Spiropyran is a photochromic dye which transforms to a merocyanine molecule on irradiation with UV light.

Spiropyran   Merocyanine

155

Spiropyran substituted ABCS

ABCS with 10% spiropyran has been found to be nematic. This low molecular weight siloxane can be drawn into fibers and the fibers are birefringent and photochromic. Upon irradiation with UV light a thin film of the sample turns blue. This is contributed to the ring opening reaction of the spiropyran molecule. The blue color disappears when the film is allowed to stand in the dark for about 24 hours. This process can be accelerated by heating the film in which case it regains color in few minutes. We have used MM and X-ray diffraction analysis to get a better understanding of the liquid crystalline order of these molecules and the effect of the spiropyran chromophore on the structure.

Modelling Packages Used

We have two commercial packages available to us to carry out MM and MD simulations, Quanta and Polygraf. Quanta uses the CHARMm force field [1] whereas the default force field for Polygraf is Dreiding II [4]. These two force fields were compared to find out the most

suitable force field for our molecular systems. Dreiding II is a generic force field based on simple hybridization considerations rather than individual force constants. This is generally good for atoms about which very little experimental data is available. CHARMm force field on the other hand is atom specific and has been parametrized using experimental data. It has also been found very successful for biological molecules. Therefore, Quanta was used for all of our molecular simulations. The simulation package CERIUS was used to calculate the cylindrically averaged X-ray scattering for the various models.

Results and Discussions

(1)ABCS: Previous works on this family of cyclic siloxanes have indicated that a cylindrical model is most likely the best representation of the molecule [6]. There can be two variation in this cylindrical model. Model A - The plane of the siloxane ring almost normal to the long axis of the molecule (Figure 1(a)). Model B - The plane of the siloxane ring parallel to the plane of the mesogens (Figure 1(b)). In order to distinguish between these two models, MM minimization using 100 cycles of steepest descent and 2000 cycles of Adopted basis newton raphson algorithm were carried out. The energy was found to be comparable for both the models. However, model B was found to be difficult to interdigitate. This is contrary to what has been found experimentally (the molecules show high degree of interdigitation). Molecular dynamics calculations were undertaken to determine the flexibility of the siloxane ring and the rigidity of the mesogens.

In the molecular dynamics simulations all the atoms were considered explicitly and the Verlet algorithm was used. In order to be able to use longer time steps the Shake algorithm was applied, i.e. the C-H stretch were constrained. The molecule was first gradually heated to 300 °K by periodically increasing the atomic velocities and then equilibrated at 300 °K by periodically scaling the atomic velocities to maintain a constant temperature. A 5 picosecond heating cycle was used and a 25 ps equilibration was found sufficient. The

final simulation was done for 50 ps with an integration time step of 1 femtosecond. In liquid crystals the intermolecular interactions are very important. therefore a good model should incorporate both inter- and intra- molecular interactions. This can be achieved by modelling larger molecular systems which require extensive computer resources. One way of getting around this is to use periodic boundary conditions. Periodic boundary conditions help simulating infinite molecular systems and minimize the boundary effects. Only the coordinates of the primary structure are stored and the images of the primary structure are generated by using transformation matrices. The primary structure and its images are then treated as a single molecular system. We decided to determine the X-ray unit cell and use its dimension in the periodic boundary matrix.

The X-ray diffraction pattern taken by Bunning [3] were analyzed. The room temperature wide angle diffraction pattern showed many sharp reflections indicating that the sample had long range order. Fiber diffraction patterns (Figure 2) however showed most of the reflection localized on the meridian. All the reflections except one could be analyzed as higher order reflection of a repeat distance of 23.2 A°. This corresponds to the long axis of the mesogens. A strong diffuse reflection corresponding to the mesogen-mesogen spacing in the liquid crystalline phase was also observed. Except for a four point pattern no distinct off-meridional sharp reflections could be observed. Therefore it was not possible to determine the lateral spacing of the molecules. The four point pattern was also observed in the diffraction pattern of magnetically and electrically aligned nematic samples. This has been attributed to a cybotactic nematic phase where smectic like ordering exits. In this phase the molecules are arranged in layers and the long axis of the molecule is tilted with respect to the layer (Figure 3) The azimuthal angle between the spilt reflections was measured to be 33 deg [3]. From this and the width of the layers the repeat distance of the nematic was found to be 27 A°. The mesogen length was earlier calculated to be 23.2 A°, therefore the remaining must be due to the rings.

The lateral packing distance was determined by getting two molecules maximally close to each other by monitoring the non-bonded and the electrostatic interactions and a distance of 16.5 A^o was found. Dynamics simulations were carried out using a rectangular periodic matrix with a=b=16.5 and c=27 A^o. 26 images of the original molecule were created and in effect molecular dynamics was carried out on 27 molecules. The final structure after 50 ps dynamics simulation of model A is shown in Figure 4. It was found that using the periodic boundary conditions minimized the boundary effects. Figure 5 and Figure 6 show the average and the lowest energy structures. It was found that on average the mesogens align parallel to each other. The rings are very flexible and the dominant interactions is between the mesogens. The rings are not rigid to have a particular shape , therefore the molecular shape is most likely an intermediate structure (of model A and model B).

(2) Spiropyran Substituted ABCS: Spiropyran and merocyanine molecules were substituted on ABCS and the conformational energy was calculated and compared. Assuming that our model of ABCS is correct, there are three positions where a substitution can take place. For each case the energy was minimized using 100 cycles of steepest descent and 1000 cycles of conjugate gradient. In the case of 20% substitution (one chromophore per molecule), all the six cases (three with merocyanine molecules substituted at different positions and three with spiropyran substitution) were found to have comparable energies (Table 1) This implies that the substitution at the three different sites are equally probable and both the chromophores are equally acceptable.

Table 1

| | Energy in kcal/mol | |
	Spiropyran Substitution	Merocyanine Substitution
Case I	184.0	192.0
Case II	188.0	185.0
Case III	188.0	184.0
Average Energy	186.5	187.0

Four molecules were packed together by monitoring the intermolecular interactions using the {12-6} Lennard-Jones and the electrostatic energy potentials (Figure 7 and 8). Meridional scattering along the long axis of the molecule was calculated using CERIUS Diffraction II module. After minimization the merocyanine molecules could align parallel to the B mesogens It is also less bulky than the spiropyran molecule and thereby allows better packing. This effect was more pronounced for 40% substituted ABCS as shown in Figure 9 and 10. The merocyanine substituted ABCS shows more number of reflections.

Summary and Future Work

The feasibility of using boundary conditions has been established and an initial periodic boundary matrix has been determined. The structure after dynamics simulation has to be thoroughly analyzed. The effect of using different boundary conditions on the molecular conformation is being currently studied by varying both the shape and the size of the matrix. After a through analysis of the mesogen conformation and packing has been done the molecules will be packed in cybotactic groups and their X-ray scattering will be calculated and compared with the experimental data.

Merocyanine was found to less disrupt the liquids crystalline packing than spiropyran. Molecular dynamics calculations with periodic boundary conditions have to be carried out on the substituted molecules to get a more realistic picture. The effects of different spacer groups on the spiropyran unit will also to be studied.

References

(1) Brooks B.R., Bruccoleri R.E., Olafson B.D., States D.J., Swaminathan S. and Karplus M., *J. Comp. Chem.*, 1983, vol. 4, no. 2, p. 187.

(2) Bunning T.J., Klei H.E., Samulski E.T., Crane R.L. and Linville R.J., *Liquid Crystals*, 1991, vol. 10, no. 4, p. 445.

(3) Bunning T.J., *Ph.D Dissertation*, 1992, Univ. of Connecticut.

(4) Mayo S.L., Olafson B.D. and Goddard III W.A., *J. Phys. Chem.*, 1990, vol. 94, no. 26, p. 8891.

(5) Natarajan L.V., Bunning T.J., Klei H.E., Crane R.L. and Adams W.W., *Macromolecules*, 1991, vol. 24, no. 24, p.6554.

(6) Pachter R., Bunning T.J. and Adams W.W., *Comp. Poly. Sci.*, 1991, vol. 1, no. 3, p.179.
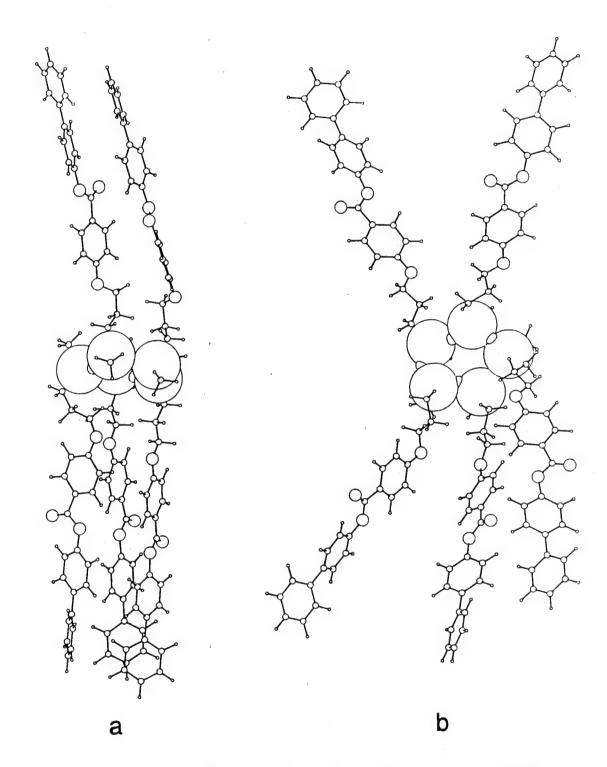
Figure 1: Ball and Stick Figure of Cylindrical Models. (a) - Model A, (b) - Model B.
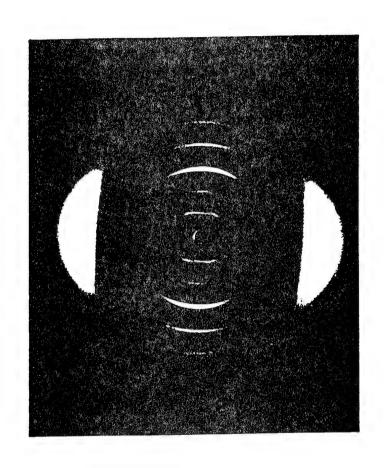
Figure 2: Wide Angle Fiber Diffraction Pattern [3].
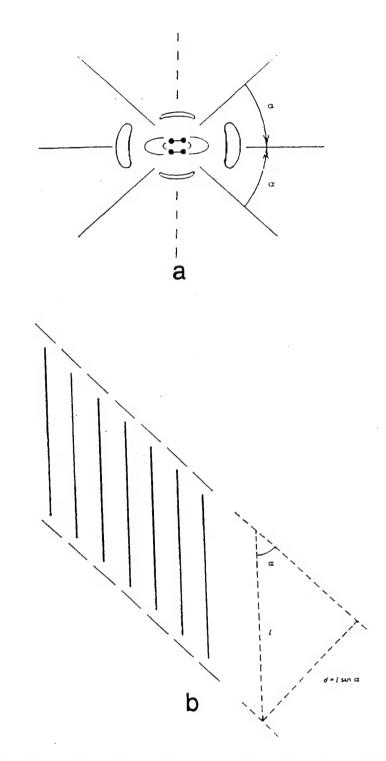
Figure 3: (a) Schematic Diagram of X-ray Pattern of Cybotactic Nematic Phase. (b) Schematic Diagram of a Cybotactic Group.

a   b
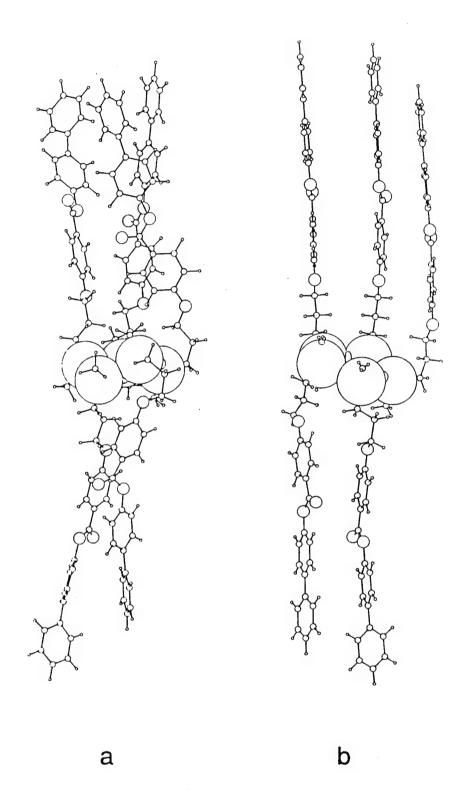
Figure 4: Molecular Structure After 50 picosecond Dynamics Simulation. (a) Without Boundary Condition; (b) With Boundary condition.
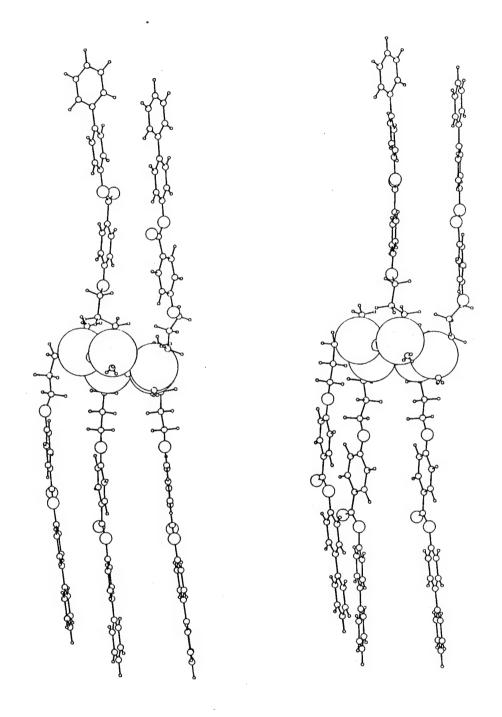
Figure 5: Two Different Projection of the Average Molecular Structure After 50 picosecond Dynamics Simulation.

a   b
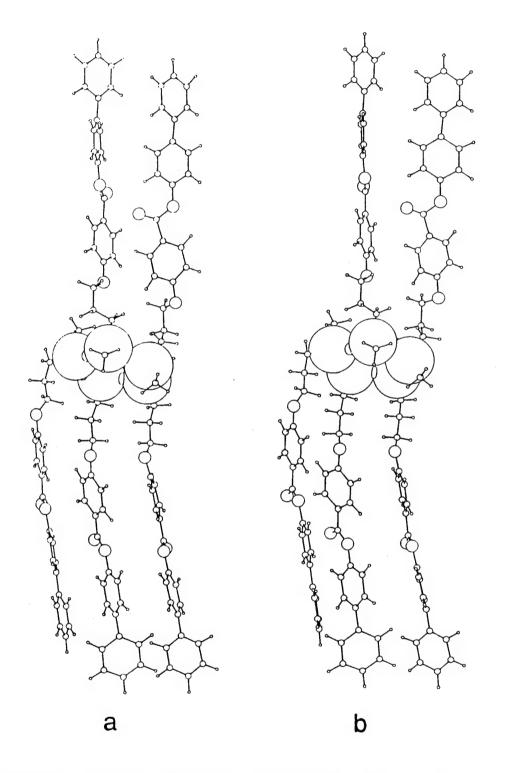
Figure 6: Two Different Projection of the Lowest Energy   Molecular
Structure After 50 picosecond Dynamics Simulation.
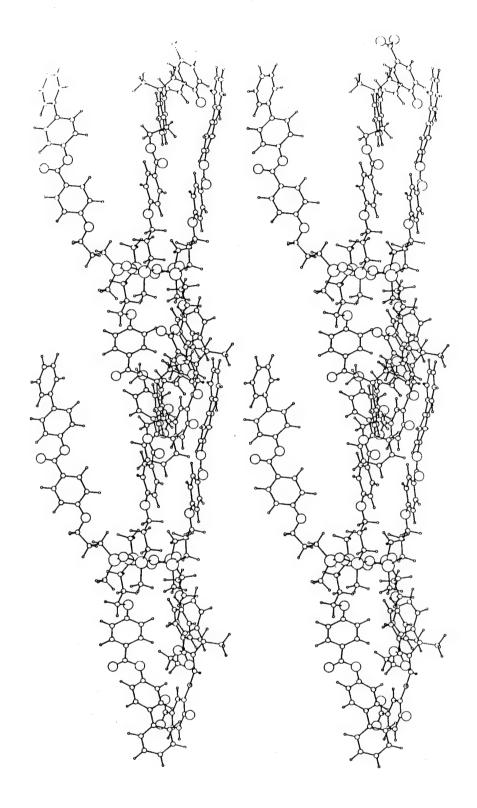
Figure 7: Four Merocyanine Substituted ABCS Molecules.
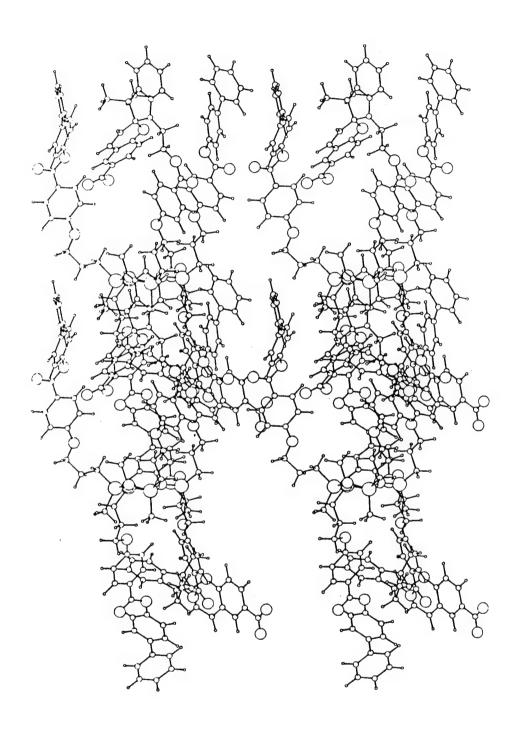
Figure 8: Four Spiropyran Substituted ABCS Molecules.
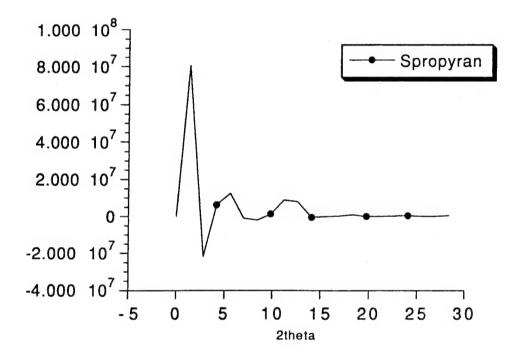
Figure 9: Meridional X-ray Scattering of Spiropyran
Substituted ABCS .
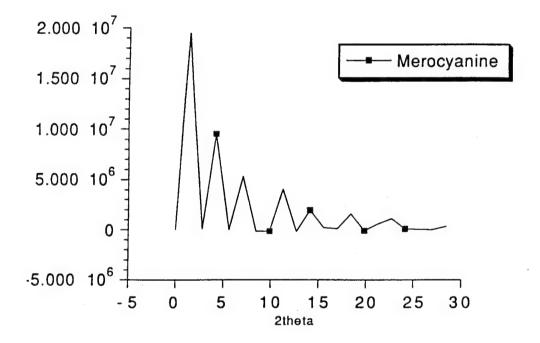
Figure 10: Meridional X-ray Scattering of Merocyanine
Substituted ABCS.
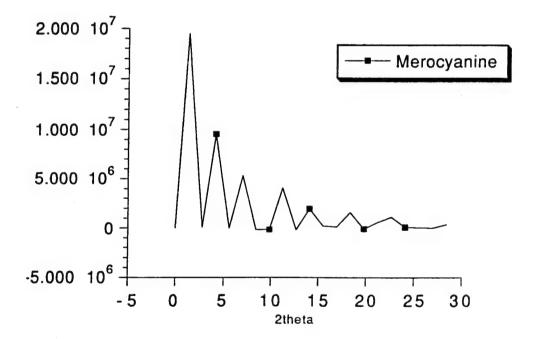
Figure 10: Meridional X-ray Scattering of Merocyanine
Substituted ABCS.
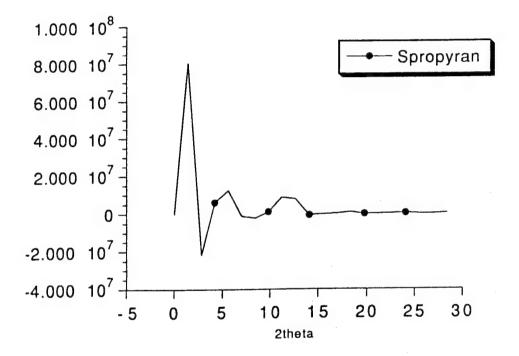
Figure 9: Meridional X-ray Scattering of Spiropyran Substituted ABCS .

EFFECTS OF INTERMOLECULAR INTERACTIONS IN A CYCLIC SILOXANE BASED LIQUID CRYSTAL
Edward Peter Socci

175

EFFECTS OF INTERMOLECULAR INTERACTIONS
IN A
CYCLIC SILOXANE BASED LIQUID CRYSTAL

Edward Peter Socci

Department of Materials Science and Engineering
University of Virginia
Charlottesville, VA 22903-2442

October 1992

Effects of Intermolecular Interactions
in a
Cyclic Siloxane Based Liquid Crystal

Edward Peter Socci
Department of Materials Science and Engineering
University of Virginia

Abstract

A substituted cyclic penta(methylsiloxane) liquid crystal containing combinations of pendant biphenyl-4'-allyloxybenzoate {B} and cholesterol-4'-allyloxybenzoate {C} mesogens was examined using computer molecular modeling. These compounds are of interest for possible use in the fabrication of laser resistant optical devices. Molecular mechanics (MM) and dynamics (MD) calculations were undertaken to assess the conformation and mesophase structure of this material.

The Gibbs free energy of likely interactions of {B} and {C} mesogens was calculated. Dissociation temperatures for pairs of {B} and {C} mesogens were also calculated. Results suggest possible models for the structural ordering of the mesophase based upon strong interactions between mesogens in certain preferred orientations. These interactions could lead to the formation of a supramolecular, pseudo main chain polymer from this low molecular weight liquid crystal, which would account for the unusually good fiber forming characteristics of this material.

Section 1

CYCLIC SILOXANE-BASED LIQUID CRYSTALS

The focus of this work is the cyclic penta(methylsiloxane) based liquid crystal (LC) with combinations of cholesteryl-4'-allyloxybenzoate and biphenyl-4'-allyloxybenzoate mesogens pendant on the siloxane ring (Figure 1.1). These low molecular weight liquid crystals can be drawn into fibers tens of meters in length, but their fiber drawing characteristics are highly dependent upon the mole fraction of cholesterol mesogen ($X_{cholesterol}=P/(P+Q)$) present in the material [1]. In this chapter the results of a computer molecular modeling study of this LC are presented in which we attempt to understand the intermolecular packing order of these LC molecules in the mesophase.

Figure 1.1:   General Chemical Structure of the cyclic siloxane-based liquid crystal

The work of Bunning and co-workers [1] involving characterization of cyclic siloxane-based LC's by X-ray diffraction has suggested a variety of possible conformations and packing arrangements for the mesogens pendant on the siloxane ring.   Each of these packing schemes is dependent upon the conformation of the LC and the mole fraction of individual mesogens present in

179

the system. One possible conformer as suggested by X-ray diffraction is cylindrically shaped (herein named the cylinder model) and is illustrated in Figure 1.2. Molecules in this conformation could form strong intermolecular interactions with mesogens of neighboring molecules causing the formation of an interdigitated structure (i.e. like the meshing of fingers on two hands).

When drawn into fibers, the mesogens pendant on the siloxane ring are oriented parallel to the draw direction (orienting the lamellae at $90°$ to the draw direction) and form what amounts to a S_A mesophase. It has been shown experimentally [1] that materials with a low mole fraction of cholesterol mesogen can be drawn into fibers over 10 meters long. However, fibers cannot be drawn in material with a high mole fraction of cholesterol mesogen. It is apparent that the cholesterol mesogen {C} and the biphenyl mesogen {B} each play important roles in 1) determining the structure of the mesophase, and 2) determining the macroscopic properties of the material. Specifically, the addition of {C} mesogen has a drastic effect on the fiber forming properties of the system.

The first topic in this study addresses the possible orientations that {B} and {C} mesogens may adopt in an effort to find their lowest energy packing relationships. Results of this calculation are useful in predicting possible structural ordering in the mesophase. The method used is molecular mechanics which calculates (in this case) non-bonded interactions between rigid molecules at different orientations in space.

The second topic is the dynamics of mesogen interactions. An analysis of the interactions between mesogen pairs at temperatures between 0 K (minimum energy structures) and the calculated dissociation temperature is made. The ordering of the dissociation temperatures for each mesogen pair is a good indication of the relative stability of each interaction.
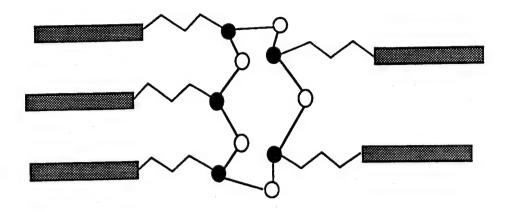
Figure 1.2: Cylindrical conformer of cyclic siloxane based liquid crystal

METHODS

1.1.1. Molecular Mechanics Calculations

MM techniques were used to study the packing behavior of the {B} and {C} mesogens <u>independent</u> of the siloxane ring, i.e. calculations were made only on the mesogens, (the allyloxybenzoate leader group and the {B} or {C} moiety: see Figure 1.1). Mesogens were constructed and optimized (energy minimized) using the SYBYL molecular modeling package [2].

By quantifying the number and magnitude of favorable mesogen interactions, insight into the structure of the mesophase may be made. MM is used to study six possible interactions likely to occur in a mesophase of cylindrical conformers. These six interactions are illustrated in Figure 1.3. Shown in Figure 1.3(a) are the two orientations for a biphenyl mesogen pair, {B}-{B}. In the parallel orientation, the leader groups of each mesogen are side by side, while in the anti-parallel orientation, the leaders are located next to the biphenyl group. Each of these orientations is possible in postulated models for the structure of the mesophase. The two starting orientations considered for the mixed mesogen pair {B}-{C} are shown in Figure 1.3(b). Likewise, the starting orientations for the cholesterol mesogen pair {C}-{C} are shown in Figure 1.3(c).
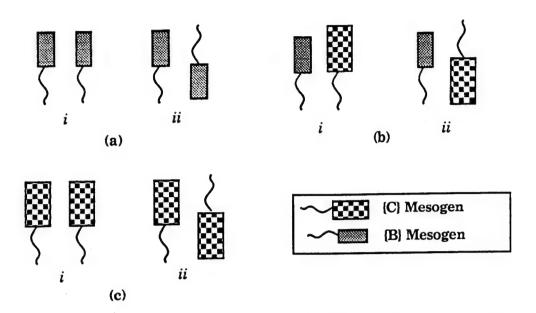
Figure 1.3: Six interactions likely to occur between mesogens in a mesophase of cylindrical siloxane conformers: {B}-{B} parallel (*i*) and anti-parallel(*ii*) (a), {B}-{C} parallel (*i*) and anti-parallel (*ii*) (b), and{C}-{C} parallel (*i*) and anti-parallel (*ii*) (c)

The initial orientation of the mesogens was optimized by allowing a z-translation (along the molecular axis) for each mesogen in the pair. Once an optimal translation was found (minimum energy translation), it was used throughout the calculations. Orientations between mesogens in each pair were then systematically surveyed to locate most favorable relationships by calculation of the intermolecular energy between mesogens. In each case, the angular orientations θ_1 and θ_2 were varied in 40 degree intervals for a given inter-chain distance, **d** (see Figure 1.4 for an explanation of these variables). This process was repeated for inter-chain distances between 3 Å and 10 Å in 0.5 Å increments. The contour maps resulting from these calculations on {B}-{B}, {B}-{C} or {C}-{C} pairs indicate the most favorable orientations for the molecules as a function of θ_1, θ_2 and **d**, i.e. each data point on the contour map corresponds to the value of **d** which gave the lowest intermolecular energy for the two mesogens at that particular set of orientation angles θ_1 and θ_2. Only those orientations with

intermolecular energies within 50% of the minimum energy orientation are shown.

θ1   θ2

d
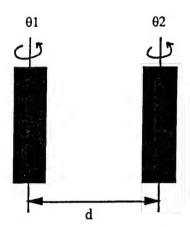
Figure 1.4: Illustration of orientation angles θ_1 and θ_2 and separation distance d

MD simulations (for calculation of mesogen dissociation temperatures) were initiated by slowly heating the molecules to a starting temperature (between 100 K and 125 K) at a rate of 25 K/500 fs. The time step used in all calculations was 1 fs, non-bonded interaction lists were updated every 25 fs and molecular trajectories were saved every 100 fs. The non-bonded cut-off distance was 12 Å. The mesogens were equilibrated at the starting temperature for a period of 10^4 fs. From this point, the temperature of the system was increased in either 5 K or 10 K increments over a period of 500 fs (heating step) and then simulated at this new temperature for 10^4 fs. Upon completion of the simulation at a specific temperature, the trajectories were analyzed for dissociation. The variations in intermolecular energy and distance between mesogens were calculated as a function of simulation time. If the mesogens remained close (i.e. the intermolecular energy between mesogens was non-zero) the simulation was continued at the next highest temperature. This procedure was repeated until the calculated dissociation temperature.

Section 1.2

RESULTS

1.2.1. Molecular Mechanics Calculations

1.2.1.1. Biphenyl Mesogen Pair

The contour maps for the {B}-{B} mesogen pair (Figure 1.5) illustrate the low energy packing relationships available to these mesogens. The number of favorable orientations (those within 50% of the energy minimum) is approximately equal for the parallel and the anti-parallel orientations. Although the number of favorable orientations is comparable, the magnitudes of the interaction energies are different. The calculated intermolecular energies between mesogens are generally more negative (for most values of θ_1 and θ_2) when the {B} mesogens are in the anti-parallel orientation. Table 1.1 gives a quantitative comparison of the magnitudes of the calculated intermolecular energies between mesogens for several of the low energy orientations in both the parallel and the anti-parallel positions.

Table 1.1.

Calculated Intermolecular Energies for {B} mesogen pairs in favorable orientations

Parallel				Anti-parallel			
θ_1 (deg)	θ_2 (deg)	d (Å)	Inter E (kcal/mol)	θ_1 (deg)	θ_2 (deg)	d (Å)	Inter E (kcal/mol)
160	200	4.0	-13.8	200	200	4.0	-15.0
320	0	4.0	-13.1	40	40	4.5	-14.2
320	160	4.5	-12.4	0	0	4.0	-13.8
0	240	4.5	-12.2	40	200	4.5	-12.6

1.2.1.2. Biphenyl-Cholesterol Mesogen Pair

Contour maps of the interaction search for {B}-{C} mesogen pairs (in the parallel and anti-parallel orientations) as a function of θ_1, θ_2 and **d** are shown in Figure 1.6. In each map, only those *inter*molecular energies within 50% of the lowest energy are shown. By visual inspection of the contour maps, their are more favorable packing arrangements for <u>anti-parallel</u> {B}-{C} pairs. The intermolecular energies, itemized in Table 1.2, are more negative in the <u>parallel</u> orientation.

Table 1.2

Calculated Intermolecular Energies for {B}-{C} mesogen pairs in favorable orientations

Parallel				Anti-parallel			
θ_1 (deg)	θ_2 (deg)	d (Å)	Inter E (kcal/mol)	θ_1 (deg)	θ_2 (deg)	d (Å)	Inter E (kcal/mol)
0	200	4.5	-15.8	200	200	4.5	-14.4
320	200	4.5	-13.4	320	40	5.0	-12.5
0	40	5.0	-13.2	240	200	5.0	-12.1
240	40	5.0	-12.9	200	40	5.0	-12.0

1.2.1.3. Cholesterol Mesogen Pair

The intermolecular energies calculated for the {C}-{C} mesogens (in both the parallel and anti-parallel orientations) as a function of θ_1, θ_2 and **d** are shown in contour maps in Figure 1.7. The populations of these two maps (in terms of orientations with 50% of the minimum energy orientation) reveal a dramatic difference in the packing behavior of {C} mesogens. There are substantially fewer favorable orientations available to mesogens in the <u>anti-parallel</u> orientation than there are available to mesogens in the <u>parallel</u> orientation. This indicates that {C} mesogens cannot pack as efficiently in the anti-parallel position, possibly because

of steric effects (axial methyl groups in the {C} moeity), for many values of θ_1, θ_2 and **d**.

Although the favorable interactions between {C} mesogens are fewer in the anti-parallel orientation, the calculated intermolecular energies are generally more negative in this orientation. The intermolecular energies for several of the most favorable orientations of {C} mesogens in both the parallel and the anti-parallel positions are given in Table 1.3.
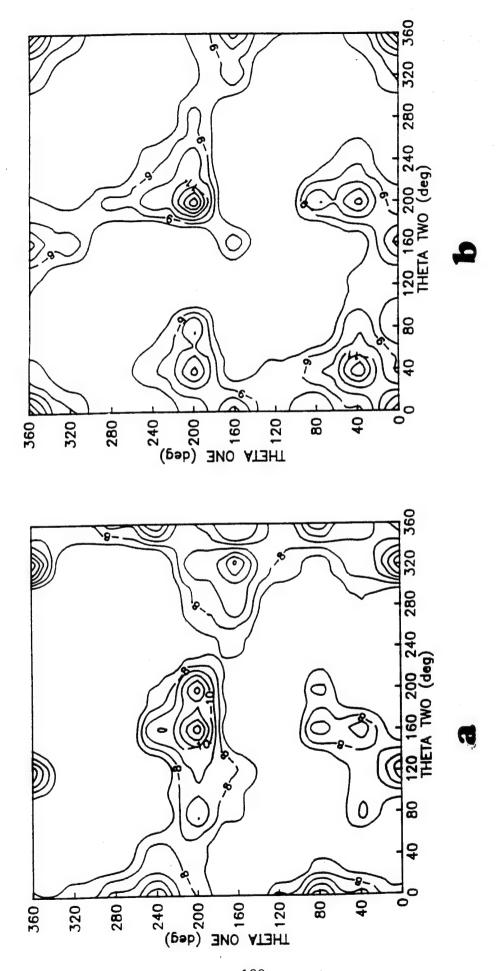
Table 1.3.

Calculated Intermolecular Energies for {C} mesogen pairs in favorable orientations.
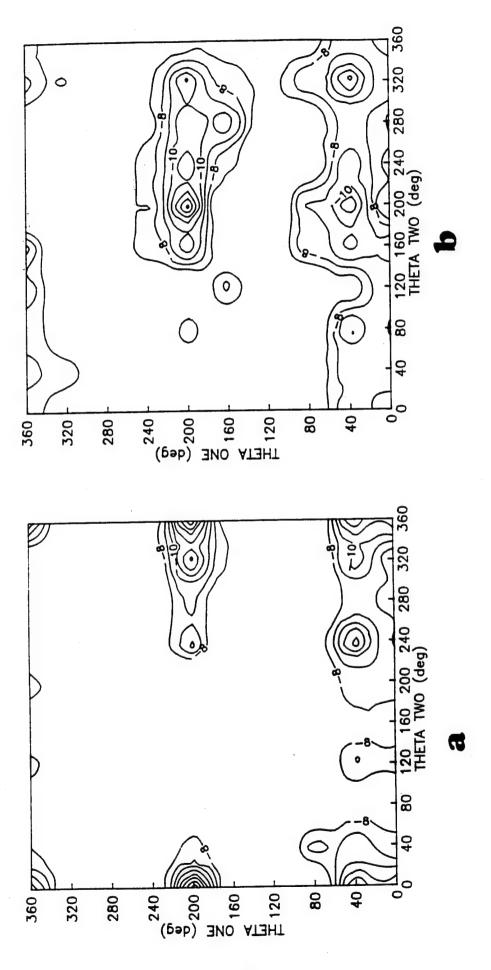
Parallel				Anti-parallel			
θ_1 (deg)	θ_2 (deg)	d (Å)	Inter E (kcal/mol)	θ_1 (deg)	θ_2 (deg)	d (Å)	Inter E (kcal/mol)
240	0	5.5	-13.9	0	0	5.5	-17.4
80	320	6.0	-13.1	320	320	5.0	-14.1
200	200	5.5	-12.8	320	0	5.5	-13.1
200	80	6.5	-12.7				

1.2.2. Molecular Dynamics Simulations
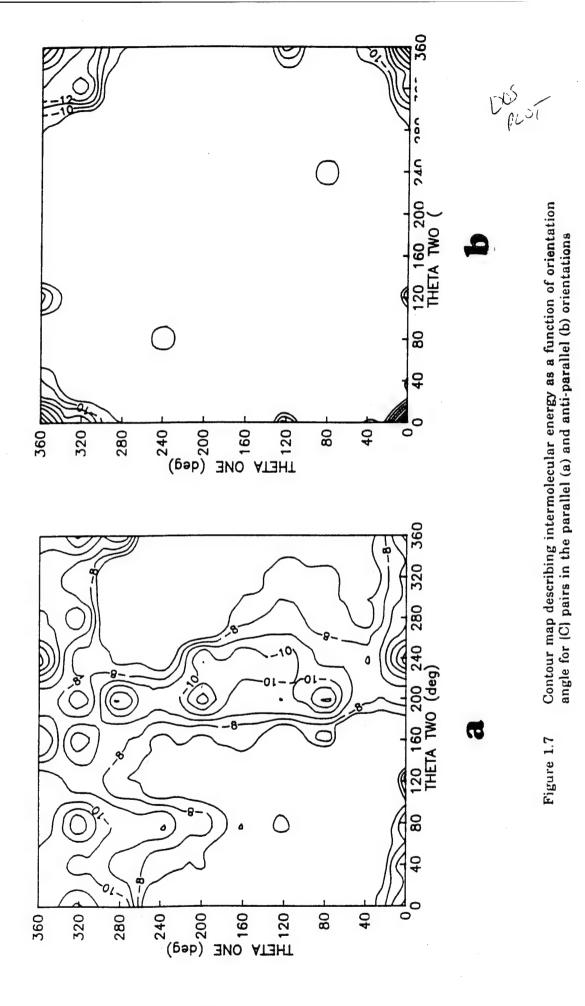
MD simulations were completed in order to evaluate the behavior of {B} and {C} mesogens at elevated temperatures. Emphasis was placed on determining a "dissociation temperature" for the {B}-{B}, {B}-{C} and {C}-{C} mesogen pairs in order to quantify the relative stability of each interaction.

Figure 1.5   Contour map describing intermolecular energy as a function of orientation
angle for (B) pairs in the parallel (a) and anti-parallel (b) orientations

188

Figure 1.6   Contour map describing intermolecular energy as a function of orientation angle for (B)-(C) pairs in the parallel (a) and anti-parallel (b) orientations

Figure 1.7   Contour map describing intermolecular energy as a function of orientation angle for (C) pairs in the parallel (a) and anti-parallel (b) orientations

The dissociation temperature was defined as the temperature where the intermolecular energy between mesogens equalled zero. At this temperature, the attractive force between mesogens is overcome by thermal (kinetic) energy input into the system. As a result, the molecules become separated by a distance greater than 12 Å (the non-bonded cut-off distance) and no longer interact.

The graphs in Figure 1.8 indicate the variation of temperature and intermolecular distance for the {B} mesogen pair during the MD simulation (behavior of the {B}-{C} and {C}-{C} mesogen pair was similar). Intermolecular distances were measured between neighboring carbon atoms in each of the mesogens. The observed dissociation temperatures are: $T_{d(B)-(B)}$ = 245 K, $T_{d(B)-(C)}$ = 370 K and $T_{d(C)-(C)}$ = 445 K.
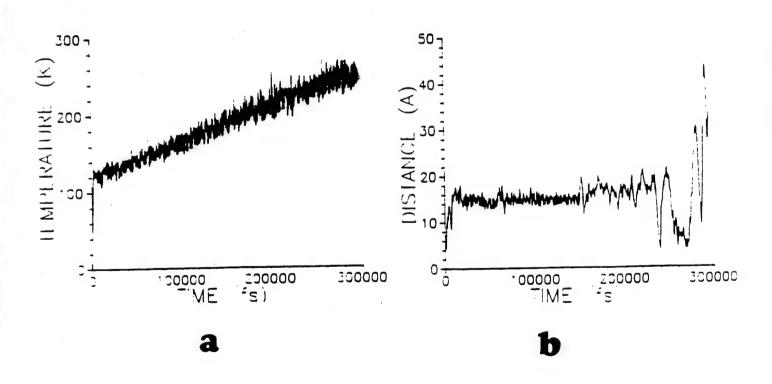
Figure 1.8   Plot of temperature (a) and intermolecular distance (b) versus simulation time for (B) pairs during MD simulation.

Section 1.3

DISCUSSION

As previously indicated, the structure and macroscopic properties of this cyclic siloxane-based LC are affected by the mole fraction of {C} mesogen present in the system. The effect on mesophase structure is revealed by X-ray diffraction measurements. Shown in Figure 1.9 are the measured primary and low angle d-spacings for this LC as a function of mole fraction {C} mesogen [1]. For low mole fraction {C} mesogen ($X_C < 0.30$), there are no measured low angle reflections. The measured primary d-spacings are approximately 25 Å and are consistent with intermolecular ordering of mesogens based upon interdigitation. The 22 Å primary d-spacing ($X_C = 0$) is consistent with a packing pattern based upon complete interdigitation of {B} mesogens. A primary d-spacing of 28 Å ($X_c = 1.0$) is consistent with complete interdigitation of {C} mesogens.

At higher mole fraction {C} mesogen ($X_C > 0.30$) a low angle reflection is consistently observed. This low angle reflection, corresponding to a d-spacing of approximately 50 Å, may describe regions of partially interdigitated {C} mesogens (i.e. {C} mesogens which cannot completely interdigitate because of steric hindrances) which form a secondary packing structure in the mesophase. It is clear from this graph that two or more distinct packing morphologies exist: one dominant at low {C} mesogen concentration and the other at high {C} mesogen concentration.
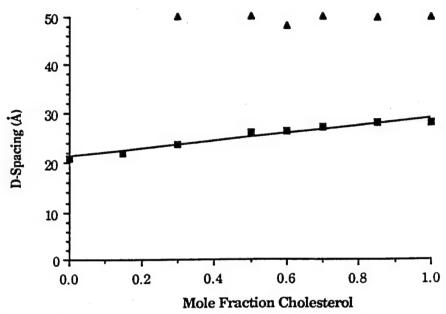
Figure 1.9: Measured primary (-o-) and low angle (-Δ-) d-spacings as a function of mole fraction cholesterol mesogen

1.3.1. Analysis of Molecular Mechanics Results

MM calculations on {B}-{B}, {B}-{C} and {C}-{C} mesogen pairs illustrate the effect each can have on the degree of interdigitation in the mesophase. The calculated favorable packing orientations (i.e. parallel or anti-parallel) for each mesogen pair aid in interpreting the structure of the mesophase. A visual inspection of the contour maps in Figures 1.5, 1.6 and 1.7 indicates the different degrees of conformational freedom available to pairs of {B} and {C} mesogens. To quantify this visual impression, the conformational entropy for each pair was computed. The overall partition function and the probability, P_i for a given pair-wise interaction, were computed at 298 K. The energies from which the contour maps were based upon were used to calculate the conformational entropy for each interaction. An entropy of mixing contribution to the total entropy was included for the {B}-{C} mesogen pairs. The conformational entropy is given by:

$$S = -R\Sigma_i P_i \ln P_i \qquad\qquad (1)$$

where R is the ideal gas constant and:

$$P_i = E_i / \Sigma_i \exp(-E_i/RT) \qquad\qquad (2)$$

The computed conformational entropies for each mesogen pair interaction are listed in Table 1.4.

Table 1.4.
Conformational entropies of mesogen interactions (at 298 K)

Interaction Type	Conformational Entropy (kcal/mol·K)
{B}-{B} parallel	3.5
{B}-{B} anti-parallel	3.0
{B}-{C} parallel	3.0
{B}-{C} anti-parallel	2.3
{C}-{C} parallel	3.6
{C}-{C} anti-parallel	2.8

Consistent with the similarity of the contour maps in Figure 1.5, the conformational entropies for {B} mesogen pairs in the parallel and anti-parallel orientation are comparable. However, the conformational entropy is slightly higher for the case of {B}-{B} parallel packing. This result indicates that the parallel orientation for {B} mesogens is slightly less restrictive (i.e. strong interactions can form easier) than the anti-parallel orientation. For the case of {C} mesogen pairs, the conformational entropy of the parallel orientation is significantly higher than for the anti-parallel orientation, indicating that the parallel orientation would be favored. Similarly, the mixed pair of {B} and {C}

mesogens have greater conformational freedom (higher conformational entropy) in the parallel orientation .

The Gibbs free energy of each mesogen pair interaction can also be computed. The thermal average energy, <E>, for each mesogen interaction ({B}-{B}, {B}-{C}, {C}-{C}) was calculated from the intermolecular energies of the contour maps in Figures 1.5, 1.6 and 1.7 using the relation:

$$<E> = \sum E_i \exp(-E_i/RT)/\sum_i \exp(-E_i/RT) \qquad (3)$$

The Gibbs free energy for the interaction (ignoring the $p\Delta V$ term in the enthalpy) is then given by:

$$G = <E> - TS \qquad (4)$$

The computed values for the Gibbs free energy at 298 K are listed in Table 1.5 and are presented graphically in a "phase diagram" in Figure 1.10. Results from the thermodynamic calculations indicate that the {B}-{B} and {C}-{C} pairs have the lowest free energy in the anti-parallel orientation, while the {B}-{C} mixed pairs are most favorably oriented in the parallel orientation.
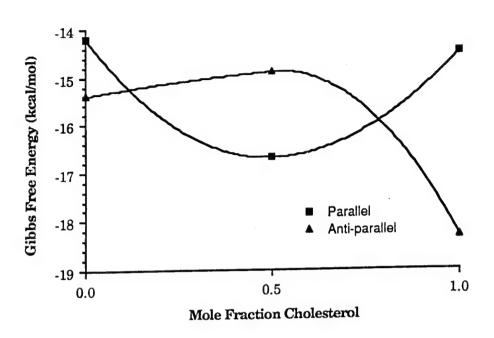
Figure 1.10: Free energy of mesogen interactions as a function of mole fraction cholesterol

Table 1.5.

Gibbs free energy of mesogen interactions (at 298 K)

Interaction Type	Free Energy (kcal/mol)
{B}-{B} parallel	-14.2
{B}-{B} anti-parallel	-15.4
{B}-{C} parallel	-16.7
{B}-{C} anti-parallel	-14.9
{C}-{C} parallel	-14.5
{C}-{C} anti-parallel	-18.3

In the context of actual molecular interactions of siloxane conformers, parallel packing relationships correspond to *intra*molecular interactions and anti-parallel packing relationships correspond to *inter*molecular interactions (see Figure 1.11: note that mesogen attachment to the ring is via the leader group).

(a)

(b)
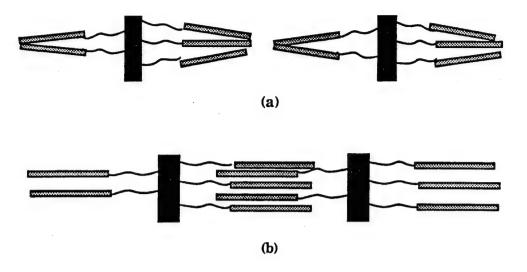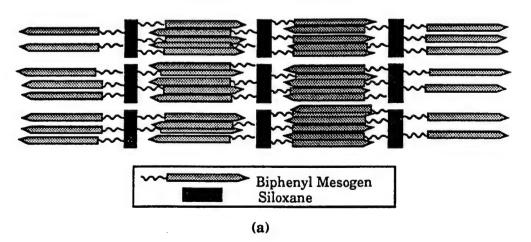
Figure 1.11: Relationship between parallel packing and intramolecular interactions (a) and anti-parallel packing and intermolecular interactions (b)

Illustrated in Figure 1.12 are two possible packing schemes supported by the MM results. In Figure 1.12(a) the pendant mesogens on the siloxane ring are all of type {B} ($X_C=0$). The predicted structure, based upon calculated free energies is one in which the mesogens are fully interdigitated (i.e. *inter*molecular, anti-parallel interactions between {B} mesogens are favored). This structure of fully interdigitated {B} mesogens corresponds to the experimentally observed d-spacings.

Biphenyl Mesogen
Siloxane

(a)
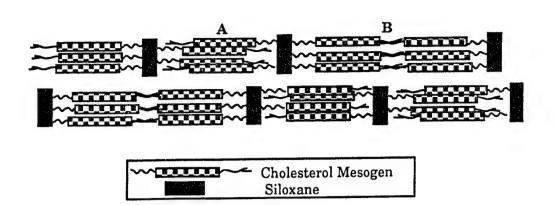
Figure 1.12: Schematic of packing in: {B} mesogen substituted siloxane molecules (a) and {C} mesogen substituted siloxane molecules (b)

The influence of {C} mesogen content is illustrated in Figure 1.12(b) which depicts a structure based upon an LC with all {C} mesogens pendant on the siloxane ring (X_C=1.0). The packing shown in the figure accounts for both the primary and low angle d-spacings present in the X-ray pattern. Region A of Figure 1.12(b) corresponds to the structural order predicted by the free energy calculations. The four {C} mesogens in region A are fully interdigitated (i.e. *inter*molecular, anti-parallel packing is dominant). In region B, the packing of {C} mesogens is not that predicted by the free energy calculations. The packing in this region is of the parallel (*intra*molecular) type. It is postulated here that in these regions of the lamellae (where six {C} mesogens must pack together), the bulky {C} mesogens cannot achieve the favorable low energy intermolecular interactions of the anti-parallel orientation. Interdigitation is disallowed in these regions due to steric hindrances and excluded volume effects.

In the case of {B}-{C} interactions, one must compare several possible packing arrangements of mesogens (illustrated in Figure 1.13). In Figure 1.13(a), the {B}-{B} and {C}-{C} *intra*molecular (parallel) interactions must "compete" with {B}-{C} *inter*molecular interactions (anti-parallel orientation) . The average free energies for each of these packing patterns are: -28.72 kcal/mol for the

interdigitated (I) structure and -29.72 kcal/mol for the non-interdigitated (NI) structure. These results indicate that interdigitation would be favored in this environment. A second packing scenario is illustrated in Figure 1.13(b), in which {B}-{B} and {B}-{C} *intra*molecular interactions compete with {B}-{B} and {B}-{C} *inter*molecular interactions. Based upon the calculated free energies for these interactions (I=-30.25 kcal/mol, NI=-30.9 kcal/mol), a non-interdigitated structure is expected. The third {B}-{C} mesogen ordering pattern is illustrated in Figure 1.13(c). In this packing pattern, {B}-{C} and {C}-{C} *intra*molecular interactions compete with {B}-{C} and {C}-{C} *inter*molecular interactions. Free energy calculations predict an interdigitated structure (I=-33.12 kcal/mol, NI=-31.16 kcal/mol) in this environment of mesogens. Illustrated in Figure 1.13(d) is a fourth environment for {B} and {C} mesogens. In this packing pattern, {B}-{C} *intra*molecular interactions compete with {B}-{B} and {C}-{C} *inter*molecular interactions. The lower free energy is associated with an interdigitated structure (I=-33.65 kcal/mol, NI=-33.34 kcal/mol).
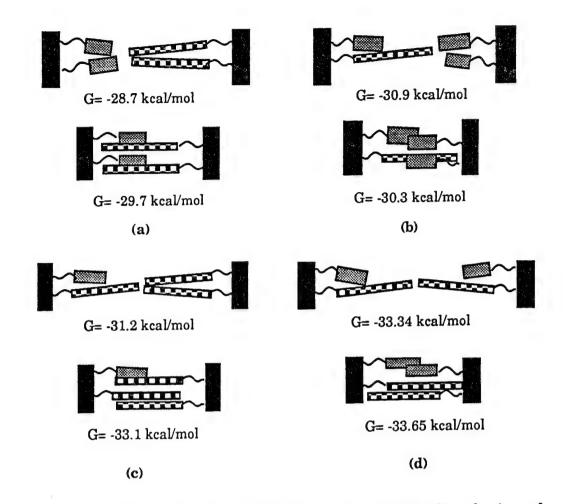
Figure 1.13: Schematic diagrams of packing in a {B}-{C} substituted siloxane. The free energy for parallel (non-interdigitated) and anti-parallel (interdigitated) structures is given.

The results of these calculations indicate that a mesophase of a {B}-{C} substituted LC should contain two general packing patterns. The first is based upon interdigitation of mesogens, in which *inter*molecular interactions are dominant. The second packing pattern is based upon non-interdigitation, in which *intra*molecular interactions are dominant. Indeed, the experimentally observed d-spacings (both low and high angle reflections) indicate two distinct types of structural ordering in a {B}-{C} mesophase.

1.3.2. Analysis of Molecular Dynamics Simulations

Molecular dynamics calculations of the dissociation temperature of the {B}-{B}, {B}-{C}, and {C}-{C} pairs are also useful in describing the stability of this siloxane based LC. The ordering of the calculated dissociation temperatures for each of the mesogen pairs indicates the relative stability of each interaction. Results from the MD simulations indicate that {C}-{C} mesogen interactions are the most stable, followed by {B}-{C} and {B}-{B} mesogen interactions, respectively. These results are in agreement with the free energies calculated for the individual interactions ($|G_{BB}| < |G_{BC}| < |G_{CC}|$. This suggests that {C}-{C} interactions, once formed, will be difficult to overcome.

The relative positions of mesogens during the MD simulation is also of interest. Each mesogen pair underwent some intermolecular reorganization during the initial heating stage of the simulation. Each of the mesogen pairs changed their relative orientations during the first 10^4 fs of the simulations (See Figure 1.9(b) as an example). These positional fluctuations were accompanied by a significant increase (and a subsequent decrease) in the intermolecular energy between mesogens, caused by the introduction of kinetic energy to the system.

From the graph in Figure 1.9(b), the positional behavior of {B} mesogens during the dynamics simulation can be assessed. At the onset of the MD simulations, the mesogens were <u>anti-parallel</u>. A re-orientation of the mesogens occurred (as a result of heating) after 20000 fs to the parallel position. This parallel orientation was maintained through 240000 fs of the simulation, at which time the mesogens returned to anti-parallel. These results suggest that both the parallel and the anti-parallel orientations can be populated by {B} mesogens. Favorable relationships are found in both orientations of mesogens, as each are within k_bT of one another.

Section 1.4

RECOMMENDATIONS FOR FUTURE WORK
AND
CONCLUSIONS

1.4.1. Recommendations for Future Work

Further study on the interactions between mesogens should be undertaken. Calculations on the packing of three {B} and three {C} mesogens may help describe the structural ordering of the mesophase. Identification of low energy packing relationships between three mesogens and the types of packing which would result (parallel or anti-parallel) could yield information on the d-spacings and relative intensities of their corresponding reflections that would result from such a structure.

Additional MM calculations should be undertaken to examine the lowest energy conformation of a substituted cyclic penta(methylsiloxane) liquid crystal with various combinations of {B} and {C} mesogens. A systematic study of the conformation of this molecule as a function of mole fraction {C} mesogen should be undertaken to determine the lowest energy conformation for each possible substitution ratio of {B} and {C} mesogens.

1.4.2. Conclusion

The use of computer molecular modeling has been useful in interpreting X-ray diffraction data of a cyclic siloxane-based LC. MM calculations support structural differences in the mesophase as the mole fraction of {C} mesogen is varied. Intermolecular ordering of mesogens ranging from partial to complete interdigitation is predicted. Calculated dissociation temperatures for {B} and {C} mesogen pairs indicate the stability of the various interactions. Results of this

computational study lend support to proposed structural models for the mesophase ordering in this LC.

References

(1)   Bunning, T. J., Klei, H. E., Samulski, E. T., Crane, R. L., Linville, R. J., Liquid Crystals, 1991, **10**, 445.

(2)   SYBYL program and manual, release 5.4, Tripos Associates, 1991.

COMPUTATIONAL CHEMISTRY IN LIQUID LUBRICANT RESEARCH
Dr. Harvey Paige

COMPUTATIONAL CHEMISTRY IN LIQUID LUBRICANT RESEARCH

Harvey L. Paige
15 July, 1992

The Nonstructural Materials Branch is relatively new to computational chemistry. Our in-house efforts began in 1987 with a search for structure-property relationships using molecular graph theory. The present emphasis started in 1989 with the initiation of a project using computational chemistry to understand the physical and chemical properties of perfluoropolyalkylether (PFPAE) liquid lubricant base stocks and additives.

Two important properties of any lubricant are the thermal and thermo-oxidative stability in the presence of metals and the temperature coefficient of viscosity (viscosity index).

Two commercial materials, Krytox and Fomblin Z, possess the minimum acceptable stability and viscosity index, respectively. It is thought that the stability of Krytox might be due to the presence of a pendant trifluoromethyl group and the favorable viscosity behavior of Fomblin Z to a difluoroacetal linkage. Explanations of these observations are being sought via experimental and computational studies.

Thermodynamic data is being derived from *ab initio* calculations in a cooperative program with David Dixon of DuPont. This data is expected to provide insights into the relative stabilities of several fluoroether structural types. It is also planned to study the relative ease of fluoride ion abstraction with these data. An in-house computational study of small fluorocarbon ethers is directed towards understanding the conformational mobility of molecules. Vibrational frequencies and relative energies of conformers are being compared to experimental results. Calculated force constants and torsional potentials will be used in molecular dynamics simulations which, in turn, will be used to predict the relative viscosities of various structure types. These studies will provide insights which will help determine the best structures to synthesize for future experimental studies.

COMPUTATIONAL CHEMISTRY IN LIQUID LUBRICANT RESEARCH
Harvey L. Paige
15 July, 1992.

The Nonstructural Materials Branch is relatively new to computational chemistry. Our in-house efforts began in 1987 with a search for structure-property relationships using molecular graph theory. The present emphasis started in 1989 with the initiation of a project using computational chemistry to understand the physical and chemical properties of perfluoropolyalkylether (PFPAE) liquid lubricant base stocks and additives.

Two important properties of any lubricant are the temperature coefficient of viscosity (viscosity index) and the thermal and thermo-oxidative stabilities in the presence of metals. Two commercially available materials, Krytox and Fomblin Z, possess the minimum acceptable stability and viscosity index, respectively. It is thought that the stability of Krytox might be due to the presence of a pendant trifluoromethyl group and the favorable viscosity behavior of Fomblin Z could be attributed to the difluoroacetal linkage. Explanations of these observations are being sought via experimental and computational studies.

Thermodynamic data is being derived from *ab initio* calculations in a cooperative program with David Dixon of DuPont. This data is expected to provide insights into the relative stabilities of several fluoroether structural types. It is also planned to study the relative ease of fluoride ion abstraction with these data. An in-house computational study of small fluorocarbon ethers is directed towards understanding the conformational mobility of molecules. Vibrational frequencies and relative energies of conformers are being compared to experimental results. Calculated force constants and torsional potentials will be used in molecular dynamics simulations which, in turn, will be used to predict the relative viscosities and temperature coefficients of viscosity of the various structure types. These studies will provide insights which will help determine the best structures to synthesize for future experimental studies.

COMPUTATIONAL METHODS FOR MODELING
SEMICONDUCTOR THIN-FILM EPITAXY
Donald L. Dorsey

COMPUTATIONAL METHODS FOR MODELING

SEMICONDUCTOR THIN-FILM EPITAXY

Donald L. Dorsey, Wright Laboratory, Materials Directorate (WL/MLPO), 3005 P ST STE 6, Wright Patterson AFB, OH 45433-7707

ABSTRACT

The semiconductor materials thin-film epitaxy modeling program of the Electronic and Optical Materials Branch of Wright Laboratory (WL/MLPO) is reviewed. Specifically, we are interested in gaining an understanding of the physics of thin-film growth by the molecular beam epitaxy (MBE) process. The research is progressing in three complementary directions. The kinetic Monte Carlo (MC) method is used to study the evolution of the surface morphology at the atomic level by simulating the essentially random processes which occur during the deposition and growth of a film. In the MC method, various physical processes (atomic motions) are attempted at probabilities based on rates calculated using a standard Arrhenius form. The activation energies associated with these rates in general cannot be measured. For this reason, we are developing quantum chemical (QC) methods to predict the activation energies and frequency factors for the important surface processes during epitaxy. These methods are also useful for verifying surface atomic structures and for determining the preferred adsorption sites of incoming atoms. The third approach that we utilize is the stochastic model, where epitaxy is described by a series of balance equations for each atomic layer. The random distribution approximation is used to determine the coverage dependent effective rates of the important surface processes. This method is computationally more efficient than the MC method, but yields less information since it only calculates the time evolution of the concentration of each specie within the film (and not their actual atomic configurations). This method is particularly useful for studying the problem of dopant segregation, where the small concentrations (typically ppm level) preclude the use of the MC method.

II. BACKGROUND

There are many potential (and existing) Air Force applications for semiconductor thin-films, including high-speed and high-temperature electronics, linear/nonlinear optics, lasers and detectors. We are particularly interested in the development of improved infrared detectors that operate at higher temperatures and at longer wavelengths than current state-of-the-art devices. Mailhiot and Smith [1] have proposed a promising structure, a strained-layer superlattice (SLS) grown in the [111] crystallographic orientation and consisting of alternating layers of gallium indium antimonide (GaInSb) and indium arsenide (InAs). Structures of this type will be grown as part of our in-house program. The concepts of a SLS and of quantum effect devices in general are described below.

A quantum effect device is a structure in which an electrical carrier (an electron or hole), is confined to a region which is of approximately the same dimension as the wavelength of the carrier (on the order of 50-100Å or 25-50 atomic layers). The simplest example is a quantum well (figure 1a), in which carriers are confined to a thin plane sandwiched between two barrier layers. Quantum wells can be "stacked" by growing any number of alternating layers of well and barrier material. Structures consisting of stacked quantum wells are classified into two categories, depending on whether the individual wells "communicate" with each other. The wave function of an electron or hole in a well extends into the barrier material due to quantum tunneling effects. If the barrier layer is thick enough such that the wave functions of adjacent wells do not interact, the structure is known as a multiple quantum well. If the wave functions interact, the structure is known as a superlattice. These structures are illustrated in figures 1b and 1c. The system of interest, GaInSb/InAs, is a strained-layer superlattice because of the mismatch in lattice constant between the GaInSb and InAs layers. Strain effects can alter the electronic band structure of a layer in a beneficial manner, particularly for [111] oriented films. A strained layer is more difficult to grow defect free, however. As the film grows thicker, the strain increases until a critical level is reached, at which point dislocations form to relax the strain. Superlattices with more than 100 periods have been grown.

A commonly used method for growing these layered structures is molecular beam epitaxy (MBE), which is depicted in figure 2. Semiconductor thin films are grown in an ultra-high vacuum (UHV) environment by impinging molecular beams of the constituent elements onto a heated substrate (a semiconductor wafer) which has the desired crystallographic orientation. The molecular beams are formed by heating solid or liquid material in effusion cells and exposing the cells to the UHV

chamber. Group III beams are monatomic, while group V sublimation typically yields tetramers. These are often cracked to produce dimers. Shutters across the cells are used to turn the species flux on and off.

An important calibration and in-situ monitoring tool is reflection high-energy electron diffraction (RHEED). The RHEED method involves shooting a beam of high-energy electrons (around 10 keV) at a glancing (< 5°) angle to the surface of the growing film. The angle is selected to put the system in the off-Bragg condition, meaning that the reflections from adjacent layers destructively interfere. This technique is very sensitive to the surface structure. It is used to determine when the surface oxide has been driven off, and whether the surface is under the appropriate reconstruction for growth. If the growth is proceeding in the desired "layer-by-layer" mode, the specular spot of the RHEED pattern will have a minimum intensity when a layer is half grown, and a maximum intensity when the layer is fully grown (when the surface is atomically flat). This results in an oscillating intensity with each oscillation corresponding to the deposition of an atomic layer. This data can be used to calculate the growth rate of the film and to exactly determine the number of atomic layers that have been deposited.

In general, explicit knowledge of how well a specific thin-film material system will grow is obtained only through rules of thumb and past experience. An MBE grower attempting to develop a new thin-film material faces a difficult (typically trial and error) task of optimizing growth parameters to avoid problems such as rough interfaces, alloy segregation, twinning and dislocation formation. In support of developing the above structures, a more complete understanding of the physics of MBE is required. Particular emphasis has been placed on modeling the epitaxy of material systems of current interest, such as [111] oriented GaAs and other III-V compounds. Silicon and germanium have also been studied, since they represent simpler monatomic systems with the same basic crystal structure. Our modeling objectives are to develop a greater understanding of the physics of MBE growth and to use this to reduce the amount of time and effort required to developed new thin-film material systems, to improve the quality of these films, and to enable the growth of previously unattainable films.

THE MONTE CARLO MODEL

At the atomic level, growth by MBE is the result of random deposition of atomic or molecular species followed by a series of random

atomic rearrangements. Order and smooth growth can arise due to the configuration-dependent energetics of the growing surface. The most common approach to modeling this process is the kinetic Monte Carlo method. Here we will describe the method in terms of homoepitaxy of a single component film on a simple cubic lattice. This lattice has actually been successfully used to model growth of GaAs in the [100] direction [2]. An excellent review of MC simulations for growth on GaAs (100) substrates using a zincblende lattice is available [3].

The processes which must be simulated are the random deposition of atoms, the adsorption of these atoms onto some site in the lattice and the diffusion of adatoms across the surface. A substrate of size M x N is specified for the start of the simulation. For computational efficiency, the values of M and N should be as small as possible without introducing finite size effects. Periodic boundary conditions are invoked, meaning that if an atom diffuses off the north edge of the lattice, another atom appears at the south edge. The solid-on-solid (SOS) approximation is employed, disallowing any vacancies or overhangs. Atoms are typically constrained to exist only on bulk lattice sites. This precludes studying the effects that the surface reconstruction have on growth. Some recent simulations, however, have found methodologies to introduce this effect for some systems [4].

The random deposition and adsorption steps of the algorithm are handled simultaneously. A site is randomly selected, and then a search is made over some region (generally either the four adjacent columns or in some n_a x n_a region) for the most energetically favorable site (i.e. the site which will yield the most neighbors). The atom is then adsorbed at this site. The value of n_a depends on the system and the growth conditions but a typical value is on the order of 2 or 3.

Surface diffusion of adatoms is conducted in terms of a series of atomic hops from a site to an adjacent site. The configuration-dependent hopping rate is evaluated using the following form:

$$R_h = R_0 \exp[-E_a/kT] \tag{1a}$$

$$R_0 = 2kT/h \tag{1b}$$

where T is the substrate temperature and the attempt frequency R_0 is determined using the equipartition theorem, assuming that the adatoms behave as 2D harmonic oscillators. The activation energy for an atomic hop, E_a, is given by

$$E_a = E_s + nE_n \qquad\qquad (1c)$$

where E_s is the hopping activation energy for an isolated adatom, n is the number of in-plane nearest neighbors (n = 0,...,4) and E_n is the additional binding energy associated with each in-plane neighbor. When it has been determined that a hop will take place, a random direction is selected and the hop is executed. Note that various rules may be used such as disallowing all "uphill" hops. Also, additional energy barriers may be introduced for atoms hopping up or down a level. Anisotropy in the attempt frequency or in the activation energy are further refinements. All of these approaches have been used in the past in order to account for the growth behavior of various systems.

The simulation results can be compared to experimental results in two ways. First, the predicted surface morphology can be compared to STM images of a grown film to verify that the appropriate shape, size and density of islands and steps are predicted. No one has done this in practice. To do it correctly, an STM must be attached to the same UHV system as the MBE chamber, so that the sample does not have to brought up to air. Bringing the sample up to air causes the formation of a surface oxide. This can be removed by heating the sample within the STM, but the resultant changes in the surface morphology of the film will invalidate any comparisons to the model predictions. We currently have a STM and a MBE chamber connected to the same UHV system, and plan in the near future to perform model validation studies.

The second approach is to compare the predicted surface step density evolution to the RHEED specular spot intensity variation measured during growth. The surface step density is calculated by counting the number of surface atoms at step edges (those with fewer than 4 in-plane neighbors) and normalizing this by the total number of sites in one layer of the substrate. It is thought that the steps act as diffuse scatterers so that the step density should be inversely proportional to the RHEED intensity [2]. To make this comparison, the surface step density is plotted using an inverted ordinate, and then scaled in an attempt to match all the features of the RHEED response. We have done this for the case of GaAs [111]B growth. These results are available elsewhere [5].

The surface step density evolution and the resultant surface morphologies for both high and low temperature growth of a simple cubic thin film are shown in figure 3. The roughness of the low temperature growth is characterized by the fast damping of the surface step density oscillations and the high average value of the surface step density relative to the high temperature case.

QUANTUM CHEMISTRY CALCULATIONS

For systems more complicated than silicon or gallium arsenide (e.g. ternaries), the number of unknown kinetic parameters required by both the MC and stochastic models is too large to credibly (or easily) fit to experimental data. We are therefore interested in using quantum chemical methods to estimate the values of some or all of these parameters. Furthermore, these methods can be used to validate proposed atomic structures of reconstructed surfaces, to determine favorable adsorption sites and to study the mechanisms of group V molecular dissociation. Dynamical quantum chemical methods are not directly applicable to thin-film epitaxy simulation because of the disparity in time scales. The QC code must use a time step which is on the order of a characteristic vibration time ($\sim 10^{-13}$s), while it takes on the order of a second to deposit an atomic layer by MBE.

Our preliminary efforts in this area involved applying the semi-empirical, self consistent molecular orbital program (MOPAC) and its solid state version (MOSOL) to the determination of the binding energies of Si atoms on the Si (111) surface and of Ga and As atoms on the GaAs (111)B surface [6]. Both the AM1 and PM3 parameterizations were used for silicon, and these results are compared to those of Krishnamurthy et al [7] in Table I. The diffuse limit corresponds to an isolated adatom and the concentrated limit to the case of all neighboring sites filled. The values we predict are higher because we have allowed the surface atoms to relax to the lower energy reconstructed positions rather than constraining them to remain in bulk lattice positions.

Table I Binding energies for Si surface atoms on the Si (111) surface.

Lattice Site	Diffuse AM1	PM3	Conc. AM1	PM3	Ref. [7] Diffuse	Conc.
3-fold	5.92	3.40	6.25	7.80	4.2	6.4
1-fold	1.71	3.10	3.35	6.40	2.5	4.6

We have moved away from MOPAC and MOSOL for several reasons, mainly because they are designed for clusters and not for crystal lattices. In order to perform the calculations for GaAs, the clusters had to be artificially terminated with cap bonds, whose parameters were adjusted to maintain the appropriate dipole moment. Unfortunately, the number of

electrons per atom cannot be made to match the actual case using this approach. Furthermore, very large cluster sizes are required in order to include the large $\sqrt{19}x\sqrt{19}R$ 23.4° surface reconstruction of GaAs (111)B and to avoid finite size effects. Since there are currently no commercially available codes that are adequate for our needs, we are in the process of developing our own quantum chemical code for calculating surface atom energetics.

THE STOCHASTIC MODEL

A disadvantage of the MC method is that it is computationally very intensive. It is therefore desirable to have other methods available which are less costly, even if they yield less information. A further consideration is that the MC method is totally unsuitable for doping studies. Since doping concentrations are typically on the order of ppm, the MC lattice size required to include a statistically significant number of dopant atoms is well beyond that which is computationally feasible. For these reasons we have developed the stochastic approach as part of our modeling effort.

The stochastic method involves using a master equation with the SOS and QCA (quasi-chemical) assumptions. A master equation is simply a balance equation for each specie in each layer. In the QCA assumption, the activation energy barrier for each process is considered to vary linearly with the concentration of the constituents of the layer. Also, the atoms are considered to be randomly distributed throughout the layer. The concentration of each specie in a layer is determine by solving a system of first-order, non-linear coupled ODEs. This system of ODEs is solved for each layer of growth simulated, with the results of higher layers dependent on those of the layers beneath them. In general, numerical solutions are required.

We have used this method to study a number of different phenomena which occur during MBE growth. The transition temperature from smooth to rough growth for germanium (100) was accurately predicted as is shown in figure 4 [8]. The average RHEED intensity is a measure of how smooth the growth is. It can be seen that the transition region for both the predicted and measured data is the same (500-620°C). Note that a low roughness corresponds to a high RHEED intensity.

Stochastic simulations have also been used to explain the amorphous-crystalline transition in Si (111) [9], to study the surface ordering which occurs during MBE of AlGaAs [10], and to model dopant segregation for the case of indium doping of silicon [11]. Our future plans

for the stochastic model are to concentrate on doping studies, particularly Si doping of GaAs (111)B.

V. CONCLUSIONS

The MBE process modeling effort within the Electronic and Optical Materials Branch of the Materials Directorate, Wright Laboratory, has been reviewed. A three prong approach using Monte Carlo, quantum chemical and stochastic models in a complementary manner is required to meet the simulation needs of the in-house III-V thin-film epitaxy program.

VI. ACKNOWLEDGEMENTS

VII. REFERENCES

1. C. Mailhiot and D.L. Smith, Phys. Rev. B **35**, 1242 (1987)
2. T. Shitara, D.D. Vvedensky, M.R. Wilby, J. Zhang, J.H. Neave and B.A. Joyce, Appl. Phys. Lett. **60**, 1504 (1992)
3. A. Madhukar and S.V. Ghaisis, CRC Crit. Rev. in Solid State and Mat. Sci., **14**, 1 (1988)
4. J.M. McCoy and P.A. Maksym, Semicond. Sci. Technol. **6**, 141 (1991)
5. D. L. Dorsey, R. Venkatasubramanian, M.Y. Yen and T.W. Haas, to appear in Compound Semiconductor Epitaxy, edited by C.W. Tu, L.A. Kolodziejski and V.R, McCrary, MRS Symposium Proceedings Series, Vol. 340, (1994)
6. S.G. Das and D.L. Dorsey, to appear in Int. J. Comp. Methods
7. S. Krishnamurthy, J. Appl. Phys. **68**, 4020 (1990)
8. R. Venkatasubramanian and D. L. Dorsey, J. Vacuum Sci. Technol. B, Vol. 11 p. 253-258 (1993)

9. R. Venkatasubramanian, D. L. Dorsey and S. G. Das, in <u>Evolution of Surface and Thin Film Microstructure</u>, edited by H.A. Atwater, E. Chason, M. Grabow and M. Lagally, MRS Symposium Proceedings Series, Vol. 280, 179 (1993)

10. R. Trivedi, R. Venkatasubramanian, D. L. Dorsey and S. Krishnamurthy, in <u>Common Themes and Mechanisms of Epitaxial Growth</u>, edited by P. Fuoss, D.W. Kisker, J. Tsao, A. Zangwill and T.F. Kuech, MRS Symposium Proceedings Series, Vol. 312, 71 (1993)

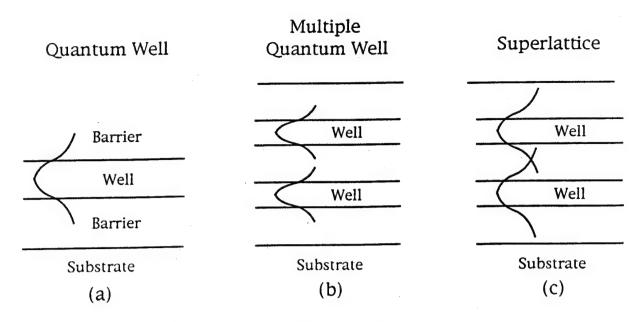11. S. Bendi, R. Venkatasubramanian and D.L. Dorsey, submitted to J. Appl. Phys.

Figure 1. Quantum effect devices. The wave functions of the confined carrier must overlap for a superlattice.
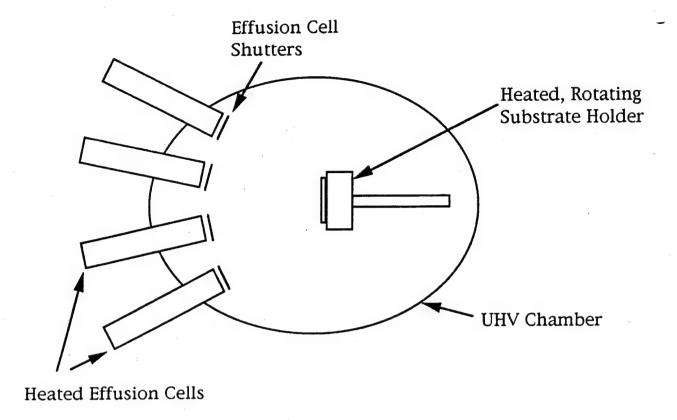
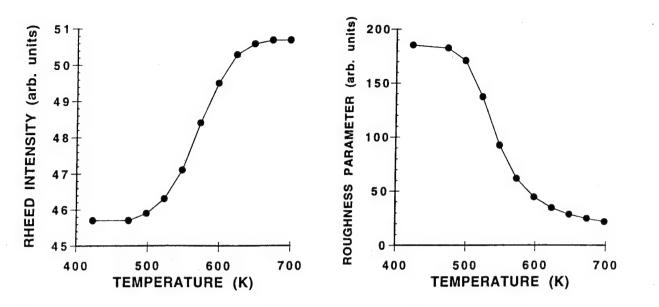**Figure 2.** Diagram of the molecular beam epitaxy process.

Figure 4. Comparison of the average RHEED intensity to the surface roughness predicted by the stochastic model for Ge (100) growth.

Figure 3. Comparison of low and high temperature growth of a simple cubic crystal.

223

MOLECULAR DYNAMICS SIMULATION OF POLY(SPIROPYRAN-L-GLUTAMATE): INFLUENCE OF CHROMOPHORE ISOMERIZATION
Dr. Ruth Pachter

Molecular Dynamics Simulation of Poly(Spiropyran-L-Glutamate): Influence of Chromophore Isomerization

RUTH PACHTER,[1,*,†] THOMAS M. COOPER,[1] L. V. NATARAJAN,[2] KEITH A. OBERMEIER,[1]
ROBERT L. CRANE,[1] and W. WADE ADAMS[1]

[1]Wright Laboratory, Materials Directorate, WL/MLPJ, Wright-Patterson Air Force Base, Ohio 45433; and
[2]Science Applications International Corporation, Dayton, Ohio 45432

SYNOPSIS

A study of the influence of the spiropyran to merocyanine ring opening on a model of poly(spiropyran-L-glutamate) as implied by the experimental data (T. M. Cooper, K. A. Obermeier, L. V. Natarajan, and R. L. Crane (1992) *Photochemistry and Photobiology*, 55, 1–7) is presented. The individual chromophore is studied by the AM1 semiempirical approach, while molecular mechanics and dynamics calculations are employed in the analysis of the poly(spiropyran-L-glutamate) model. It is shown that the α-helical secondary structure is less conserved in the polypeptide substituted with the merocyanine form of the chromophore. In particular, larger side-chain flexibility, increased backbone hydrogen-bond lengths, as well as a larger helix bending are calculated. Furthermore, a random conformational minimization calculation finds the intrinsic behavior of the spiropyran molecular system as being more of a helix "maker" than its merocyanine analogue. The interactions of the chromophore substituent with other side chains prove, in part, that an early event in the decay of the α-helical structure is the formation of hydrogen bonds between the carboxylic acid groups and the merocyanine oxygens. The results lend support to the experimental observation that the merocyanine group destabilizes the α-helical framework of the polypeptide, thus possibly allowing the entry of solvent molecules into the α-helical core, while spiropyran in its closed form shields it from the solvent. © 1992 John Wiley & Sons, Inc.

INTRODUCTION

The synthesis and characterization of new polymeric nonlinear optical materials are of increasing interest,[1] for example, photochromic polypeptides.[2] Thus, it is of importance to understand the underlying effects of the conformational changes in the chromophore on the resulting polypeptide response in such systems. In general, photochromic polypeptides (reviewed in Ref. 3) show complex light-induced conformational changes. For example, poly(L-lysine), derivatized with an azo dye, shows a light-induced β-sheet/coil equilibrium,[4] while a copolymer of β-benzyl-L-aspartate β-(m-phenylazo)benzyl L-aspartate undergoes a light-induced conformational change from a left-handed to a right-handed helix.[5] Azo-modified poly(L-glutamic acid) shows light modulated changes,[6] also with solubility.[7] Photoresponsive polypeptides, in which spiropyran units were incorporated in the side chains, include poly(L-tyrosine)[8] and poly(L-lysine),[9] while doped spiropyran was found to induce reversible changes in thin films of poly(γ-benzyl L-glutamate).[10] Photomodulation of the α-helix/coil equilibrium of spiropyran-containing poly(L-glutamate) has also been observed.[11,12] The light-adapted polymer exists in an α-helical conformation and the photochromic side chain in its spiropyran form, namely with the indoline and benzopyran parts linked by an oxygen-carbon bond.[11] On the other hand, during dark ad-

* This work was done while the author held a National Research Council Research Associateship.

† To whom correspondence should be addressed.

aptation a slow helix-to-coil dark reaction occurs, as the chromophores convert to the merocyanine form.[11] The reaction of this polymer dissolved in hexafluoroisopropanol exhibits complex kinetics consistent with a single intermediate series mechanism,[13] and the data obtained from ir spectroscopy suggest polypeptide aggregation sensitive to the degree of light adaptation of the polymer. Chromophore and polypeptide backbone CD data[13] indicates that the polypeptide environment induces optical activity only when merocyanine is covalently attached to the peptide. In order to gain a partial understanding of the disparity between the effect of the spiropyran moiety and that of the merocyanine species of the chromophore on the α-helical core of this system, a molecular dynamics simulation was carried out.

Methods for modeling protein conformation and dynamics in general and polypeptides of defined secondary structure in particular have been reviewed.[14] Also, random coil conformations of polypeptide chains were studied,[15-17] taking into account, however, only the local intraresidue interactions, and the motions of an α-helical polypeptide in general were examined by molecular and harmonic dynamics.[18] A number of theoretical calculations, recently reviewed,[19] have been reported on spiropyrans. Specifically, a model of 1',3',3'-trimethylspiro-[2H-1]-benzopyran-2,2'-indoline], viz., BIPS, in which hydrogen atoms were substituted for the methyl groups, was studied,[20] as well as the general interconversion of spiropyrans to merocyanines of model molecules,[21,22] and of a related chromophore, namely 2,2'-spirobi[2H-1]-benzopyran (SBP).[23]

It is the purpose of the present study to investigate the possible influence of a side-chain chromophore conformation on a model of poly(spiropyran-L-glutamate) implied by the experimental data,[11,13] as an initial step toward the design of new nonlinear optical photochromic biopolymers. The relative effects of the spiropyran to merocyanine ring opening on a model of the polypeptide I (Ac-E_{20}-amide) are studied. The interactions of the chromophore substituent with the peptide backbone and other amino acid side chains are examined by using semiempirical, and molecular mechanics and dynamics, calculations. In particular, a smaller side-chain flexibility is calculated in the α-helical model of the spiropyran-substituted poly(spiropyran-L-glutamate), namely II (Ac-E_9-$E_{spiropyran}$-E_{10}-amide), as compared to that of the merocyanine analog III (Ac-E_9-$E_{merocyanine}$-E_{10}-amide), where $E_{spiropyran}$ or $E_{merocyanine}$ denote a chromophore molecule (cf. Figure 1) covalently attached to the glutamate side chain by an

Figure 1. Reverse photochromism of poly(spiro-L-glutamate).

ester linkage. Moreover, it is shown that the α-helical conformation is more conserved in II, and a larger bending of the helix occurs in model III of the peptide, indicating the destabilization of the polypeptide model with the chromophore conformational change. Additionally, a random conformational minimization calculation, carried out to further search conformational space of such a molecular system when assuming a coil conformation, finds the intrinsic behavior of the spiropyran more of an α-helix former than its merocyanine analogue. These results offer an insight into some of the effects of chromophore substitution that influence the conformational changes of the peptide, in support of the experimental data.[11,13]

METHODS

The semiempirical molecular orbital method at the AM1 (Austin Model 1) level of approximation[24] was employed in this study for the geometry optimization of the spiropyran and the merocyanine-like species, to be subsequently merged with model I. On the other hand, for a molecular structure determination of complex molecules, molecular mechanics is in general a well-established approach,[25] and has proven useful even for an analysis of nmr chemical shifts data.[26] Such potentials have been developed specifically for biomolecules,[27] and a new generic force field has also been derived.[28] In this study the CHARMm[29] functional form of the force field and its parameters[30] was used, including the suggested partial atomic charges for the contribution to the nonbonded electrostatic potential. The use of these charges is justified since the CHARMm force field has been specifically developed to model peptide and protein conformations, although this may not be the case for general organic molecules.[31-33]

The polypeptide was modeled as an α-helical chain of 20 L-glutamic acid residues (I) by using the molecular modeling option of the Quanta/

CHARMm molecular design program.[34] The N- and C-termini were blocked by acetyl and amide groups, respectively, in order to avoid the helix-destabilizing interactions of these groups with the helix dipole.[35] Nonpolar hydrogen atoms on the peptide chain were implicitly included by adjusting the parameters of the heavy atoms to which they are bonded. In general, the chromophore-bound poly(spiropyran-L-glutamate) system is difficult to model, since although the experimental modification by spiropyran is known (33%),[11,13] its distribution along the polypeptide chain is unknown. In order to discern the influence of a chromophore substitution on the peptide backbone, the substitution of one such molecule was modeled (II and III). The coordinates of the initial spiropyran and merocyanine molecules were generated from the AM1-optimized geometries, and substituted on to the chain at residue {10}, rotating for best conformation (by distance) around the {O — BIPS} bond. The geometries of the complete molecular systems were then optimized without any constraints by employing molecular mechanics, using first 100 cycles of the steepest descent method, followed by the conjugate gradient technique for the CHARMm potential energy minimization.

An assessment of the conformational changes of the chromophore-bound peptides was obtained with molecular dynamics simulations, a well-documented[36] procedure, using the CHARMm force field and the Verlet algorithm[37] for the numerical integration. A gradual heating simulation of the minimized structure from 0 to 300 K is first performed, which is obtained by initially assigning and then periodically adjusting atomic velocities. An equilibration is then carried out at 300 K until no systematic changes in temperature are evident, and the energy is shown to be conserved. The actual dynamics simulation is carried out after full equilibration has been achieved, by continuing to integrate the equation of motion. This protocol was thus followed, with the energy and temperature examined after each of these stages in order to ensure the trajectory accuracy. An integration step of 0.5 fs was used for the unsubstituted model, and the peptides substituted with one spiropyran molecule (I–III). A comparison test found a time step of 1 fs to be sufficiently small in order to maintain energy conservation, and was subsequently used in simulations of the larger systems considered. In order to simulate solvation effects, a distance-dependent dielectric constant [$\epsilon(r) = r$] was applied in all cases.

A molecular dynamics calculation comparing the changes between the molecular systems II and III was carried out for 30 ps, after appropriate heating and full equilibration periods. The different stability trends in the systems considered are clearly observed in this simulation time period. The variations in II and III were qualitatively compared to analogous systems substituted with six spiropyran molecules: IV (Ac-$E_{spiropyran}$-E_3-$E_{spiropyran}$-E_3-$E_{spiropyran}$-E_3-$E_{spiropyran}$-E_3-$E_{spiropyran}$-E_2-$E_{spiropyran}$-amide), and the merocyanine analogue V (Ac-$E_{merocyanine}$-E_3-$E_{merocyanine}$-E_3-$E_{merocyanine}$-E_3-$E_{merocyanine}$-E_3-$E_{merocyanine}$-E_2-$E_{merocyanine}$-amide). The distribution of the chromophores in these systems was chosen to be homogeneous, although it is not known. Model building and geometry optimization of these multiply-substituted peptides was performed in accordance with the procedure outlined for the singly substituted models. The simulation was performed for 40 ps at 300 K, after applying the heating and full equilibration procedures.

RESULTS AND DISCUSSION

Chromophore Molecular System

The optimized geometry of the spiropyran molecular system is shown in Figure 2a, and Figures 2b–2e depict the geometry optimization results for four conformations of the merocyanine open form, with respect to the C1 — C2, C2 — C3, and C3 — C4 dihedral angles of the central carbon–carbon bonds (atom numbering is shown in Figure 2b). The four conformations considered are *trans* with regard to the central C2 — C3 bond, since the respective *cis* conformations are known to be unstable for BIPS,[38] and also for its 6-NO$_2$ derivative.[39] The following relative orientations around the C1 — C2 and C3 — C4 bonds were then considered: *cis-cis, cis-trans, trans-cis,* and *trans-trans,* in Figure 2b–e, respectively. An examination of the spiropyran geometry reveals the calculated C(spiro) — O bond length to be larger (1.454 Å) than a standard single C — O bond,[40] which may explain, in part, the relative ease of this bond cleavage. Furthermore, this result was observed also for the geometry of SBP.[23] The calculated bond lengths for spiropyran, and the *cis-cis, cis-trans, trans-cis,* and *trans-trans* merocyanine configurations, are summarized in Figure 3a. Wiberg's bond orders[41] for the definition of the character of a bond between atoms A and B, namely the sum of the squares of the elements of P_{kl} (P is the density matrix of the semiempirical MO calculation invoking the Neglect of Differential Overlap approximation for all orbitals k on atom A and l on atom B), are given in Figure 3b, while the partial

atomic charges derived from **P** relative to those in the closed form are shown in Figure 3c. The calculated bond lengths, bond orders, and partial atomic charges are shown to be independent of merocyanine conformation. The bond length–bond order relationship follows a recently proposed correlation,[42] and a linear correlation between the bond lengths calculated from the bond orders in spiropyran and an average of the merocyanine structures, with the corresponding optimized parameters, is obtained (correlation coefficient $r = 0.98$). A larger contribution of the *ortho*-quinoidal than that of the zwitterionic form to the resonance hybrid structure of the merocyanine intermediate species in the ground state is shown by these results, for example, as demonstrated in Figure 3b and c. The charge density evaluation and the amount of π-electron conjugation is known to be of importance for an understanding of electronic structure effects on hyperpolarizabilities.[43] Thus, an electronic structure analysis for these compounds may serve as the basis for an assessment of their potential for nonlinear optics applications in future studies.

It is interesting to point out that similar results were obtained for SBP, although the relative energies of the four conformations of merocyanine and SBP using the same level of multielectron configuration interaction show a slight difference.[23] The relative energy ordering of the four conformations in the 6-NO$_2$ BIPS derivative was found to be *trans–cis* > *trans–trans* > *cis–cis* > *cis–trans*. In particular, although the *trans–cis* configuration is calculated to be least stable in both cases, the merocyanine *cis–trans* and *cis–cis* configurations are of slightly lower energy (by 1.0 and 0.5 kcal/mol, respectively) than *trans–trans*, while this conformation was calculated to be more stable in the comparable intermediate species of SBP.[23] This may be due, in part, to electrostatic interactions between the indoline section and NO$_2$ group in our case. The general photochromic interconversion of these molecular systems and the geometries of the excited states are at present under study by INDO/S calculations.

Poly(Spiropyran-L-Glutamate) Model

The *cis–trans* merocyanine form of the spiropyran system was used as a starting point for the simu-

Figure 2. The semiempirical AM1-optimized geometries of (a) spiropyran and (b)–(e) merocyanine isomers: *cis–cis*, *cis–trans*, *trans–cis*, and *trans–trans* with respect to the C1—C2 and C3—C4 bonds, respectively. All conformations are *trans* with respect to the central C2—C3 bond.
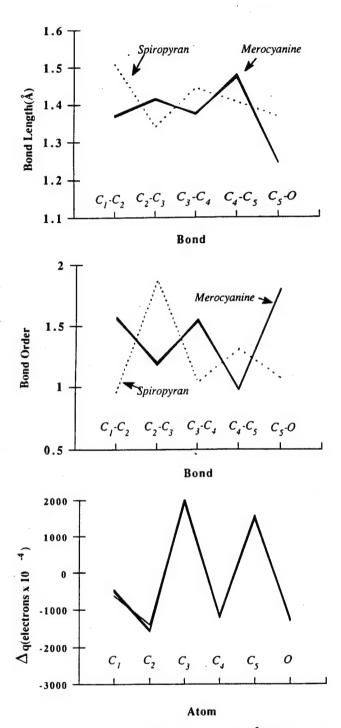
Figure 3. Calculated (a) bond lengths (Å), (b) bond orders, and (c) relative [$\Delta q = q(III) - q(II)$] partial atomic charges (in electrons $\cdot 10^{-4}$) for the merocyanine intermediate species considered in the ground state.

lation of the poly(spiropyran-L-glutamate) model. Calculations were also performed by starting with the *cis–cis* merocyanine conformation, providing, however, very similar results, which will not be further discussed. The optimized geometry of **III** indicates that the dihedral angles of the chromophore

with respect to the C1—C2 and C3—C4 bonds change from $-6°$ to $-19°$ and $177°$ to $173°$, respectively. The left-handed twist of the dihedral angle with respect to C3—C4 gives negative chirality to the merocyanine chromophore.[44] The dark-adapted polymer has a positive CD band at 392 nm (p-nitrobenzopyran charge transfer transition) and a negative band at 525 nm (merocyanine $\pi\pi^*$ transition), while the free merocyanine chromophore shows no optical activity.[13] The two bands were superimposed upon a weak, broad, negative background, which compares to a previously published[11] negative value on this system. This implies a molecular weight dependence (MW 74,000[13] vs. 250,000[11]) on dark-adapted conformation. This $\pm$ pattern of the side-chain CD spectrum of system **III**, observed experimentally,[13] is consistent with the negative chirality. Explicit calculations of the effect of twisting on the CD spectrum of merocyanine are currently being performed in order to shed light on this issue. A similar study on the linkage between biphenyl twist sense and polypeptide conformation was recently reported[45] on poly(p-biphenylmethyl L-glutamate).

The hydrogen bonds pattern of the α-helix, namely the $N(H)\cdots C(O)$ distances, is more conserved in system **II** than in **III**, as shown in Table I, which also lists, for comparison, the results for the unsubstituted polypeptide **I**. The spiropyran-substituted polypeptide model **II** shows deviations from an α-helical framework, which may be attributed to steric interactions with the backbone, although much less than that of the polypeptide model substituted with the open merocyanine form (**III**). This additional α-helical deformation may be a consequence of hydrogen-bond formation between the unmodified -COOH and the merocyanine chromophore. In addition, an examination of the differences between the backbone dihedral angles of the mean molecular dynamics conformation and those of the initial minimized α-helical structure were examined. Specifically, histogram plots of each of the backbone dihedral angles distribution during the simulation were analyzed for the unsubstituted model, and for its spiropyran and merocyanine analogues. Thus, the mode for the $\{\phi, \psi\}$ angle set could be determined, which approximates the mean in this case since a normal distribution is in general observed for these changes. The backbone dihedral angle variations indicate that the largest fluctuations are calculated for **III** (as shown in Figure 4), particularly in the $\{4-16\}$ region of residues in which end effects are eliminated. This is also shown by the average angles, given relative to the values in the initial

Table I   Mean Hydrogen-Bond Lengths and Dihedral Angles for the I, II, and III Molecular Systems

System[a]	$\langle R_h \rangle$[b]	$\langle \Delta\phi \rangle$[c]	$\langle \phi \rangle$[d]	$\langle \psi \rangle$[e]
I	2.28 (0.08)[f]	2.0 (1.4)	−63.9 (1.4)	−38.0 (1.7)
II	2.74 (0.20)	2.4 (1.9)	−63.6 (3.1)	−40.5 (3.0)
III	3.18 (0.26)	9.8 (6.8)	−65.2 (12.8)	−41.2 (3.0)

[a] I (Ac-E_{20}-amide); II (Ac-E_9-$E_{spiropyran}$-E_{10}-amide); III (Ac-E_9-$E_{merocyanine}$-E_{10}-amide).

[b] R_h is the N(H)$\cdots$C(O) hydrogen bond in angstroms.

[c] Mean deviation of backbone dihedral angle from the angle of the energy-minimized structure (°).

[d] Mean backbone torsion angle ($C_{i-1}N_iC_{\alpha i}C_i'$) (°).

[e] Mean backbone torsion angle ($N_iC_{\alpha i}C_i'N_{i+1}$) (°).

[f] Quantity in parentheses is standard deviation.

minimized structure, for example of $\langle \Delta\phi \rangle$ (Table I). Unsubstituted α-helical polyalanine[46] and polyglycine[47] were similarly studied by examining the correlation of the backbone angle variation for a particular residue with those of the full range of residues.

The importance of chromophore substitution on the amount of helix bending is further demonstrated
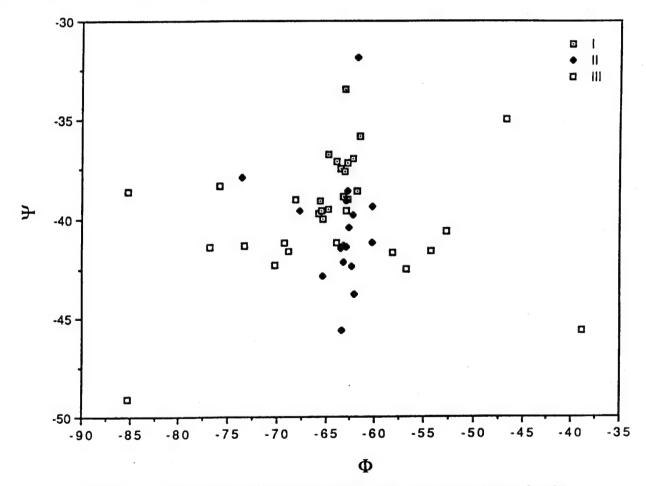

Figure 4. Backbone dihedral angles in the unsubstituted model **I**, and substituted models **II** and **III**. The dihedral angle values are those of the mode, which is the angle for which the largest number of conformations were found during the dynamics simulation, as explained in the text.

by an observation of the **I, II,** and **III** structures during the dynamics simulation, for example after 20 ps, in Figure 5a–5c, respectively. Indeed, the helical structure of **II** is shown to bend away from the substitution site (Figure 5a vs b), with a larger response observed in **III** (Figure 5c). The scatter observed in the mean $\{\phi, \psi\}$ angles for **III** in Figure 3 lends partial support to this assumption. Thus, the larger bending of **III** on ring opening of the spiropyran may allow the possible entry of solvent molecules into the α-helical core, while spiropyran in its closed form will shield it more from the solvent.[13] Interestingly, the mean $\{\phi, \psi\}$ magnitudes ($\{-65°, -41°\}$ for system **III** in Table I) are similar to the mean angles of an α-helix in a "hydrophilic environment" $\{-66°, -41°\}$,[48] assuming hydrogen bonding to a side chain or solvent molecule. Furthermore, model **III** is calculated to deviate by an average rms value of 2.1 Å from the initial minimized structure, for example, during the first 10 ps of molecular dynamics simulation, while the polypeptide substituted with the spiropyran in its closed form shows 1.0 Å rms deviations to the initial structure.

Overall side-chain conformational fluctuations in the molecular systems **II** and **III** were monitored by examining the $\{Glu(H)_i \cdots Glu(H)_{i+4}\}$ (δ_i) distances. This distance equals 7.5 Å in an ideal α-helical poly(L-glutamic acid) model, and may serve as a useful criterion for the purpose of elucidation of the general effect of photochromic substitution on side-chain flexibility. Evidence of conformational perturbations statistically different from 7.5 Å were observed in δ_2, δ_6, and δ_{12} for **II**, and δ_2, δ_{5-8}, and δ_{12} for **III**, and for δ_8 and δ_{12} when comparing **III** and **II** (cf. Figure 6). The magnitude of δ_6 was shown to be significantly lower than 7.5 Å for both systems, implying the formation of a hydrogen bond between the carboxylate hydrogen at residue $\{6\}$ and the chromophore. Model **III** shows a larger number of significant deviations, especially the large positive deviation δ_8, which contrasts with the negative value of δ_{12}. This result suggests that the α-helix is bending in response to the chromophore substitution. A comparison of the δ_i distribution histograms for model **II** (Figure 7a) vs model **III** (Figure 7b) reveals the distribution for **III** to be broader than that for **II**. The δ distribution of **III** is possibly bimodal with maxima centered at $\delta = 7-8$ Å and at $\delta = 9-10$ Å, which may reflect breaking of the backbone hydrogen bonds or extreme bending of the α-helix. Another criterion that also takes into account the existence of oscillations around a perturbed distance ($\neq 7.5$ Å) during the simulation can be defined as

$$\delta_{i(\text{eff})} = \frac{\delta_i}{1 - \frac{|\langle \delta_i \rangle - 7.5|}{7.5}}$$

where a value of 7.5 Å for $\langle \delta_i \rangle$ implies that $\delta_{i(\text{eff})} = \delta_i$. The average magnitude of $\delta_{i(\text{eff})}$ for model **III** is larger by 10%, respectively, than the comparable values for **II**. These distance variations are especially different near the substitution site. For example, the time variation in δ_7, shown in Figure 7a and b during a 10-ps sample of the simulation, shows significant differences. In particular, δ_7 fluctuates around 7.5 Å during the entire sampling time for model **II** (Figure 8a). In contrast, in **III** (Figure 8b), this distance fluctuates around 7.5 Å during the first 5 ps of the sample, and then increases to 14 Å during the last 5 ps. This change further suggests the break of a backbone hydrogen bond and subsequent bending of the helix. Indeed, the chromophore in the merocyanine form is shown in general to have a larger effect on δ than spiropyran. This is also shown by a comparison of Figure 5a and b vs Figure 5c.

The relative conformational changes observed in the singly substituted polypeptides **II** and **III** are more pronounced in analogous systems substituted with six spiropyran molecules (**IV** and **V**). However, no systematic study of multiple chromophore substitution was performed at this stage. Larger variations in the average of δ_i were observed for the merocyanine derivative **V** than for **IV**, and the hydrogen bonds pattern of the α-helix is more conserved on average for model **IV**. The last structure of **V** after the dynamics simulation differs by 4.9 Å rms deviations from the initial model, while **IV** shows a 3.5 Å deviation from the initial structure. Moreover, numerous hydrogen bonds are formed between the unmodified -COOH and the merocyanine oxygens in **V** during the 40 ps of molecular dynamics simulation. Only one such hydrogen bond is formed during this simulation period for **IV**. An event in the decay of the α-helical structure is the formation of hydrogen bonds between the carboxylic acid groups and the merocyanine oxygens. The side chain's role suggests that a variation of the unmodified residues may affect the polypeptide backbone, recently confirmed by a study on poly(methyl-L-glutamate) partially transesterified with BIPS (E. T. Samulski, personal communication). Particularly, the methylation of poly(spiropyran-L-glutamate) stiffened the polypeptide backbone and made it less susceptible to light (E. T. Samulski, personal communication).

233

(a)

(b)
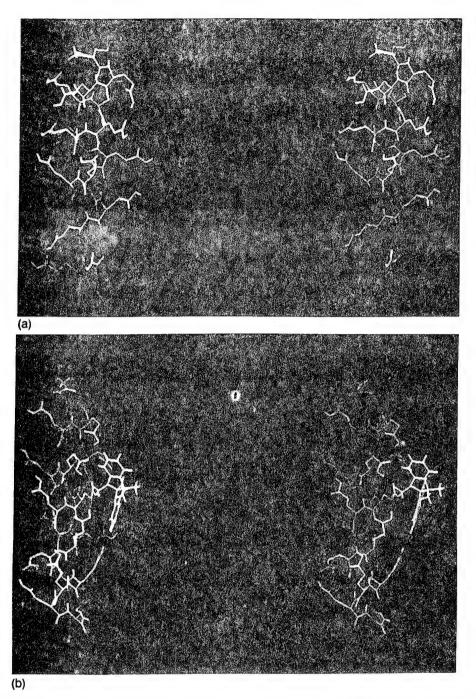
Figure 5. A stereoview of the models (a) **I**, (b) **II**, and (c) **III** during the dynamics simulation, e.g., after 20 ps.

A further partial prediction of the relative conformation of an initial random coil of such a polypeptide model with either spiropyran or merocyanine substitution can be obtained by a random minimization technique for exploring conformational space, followed by a molecular dynamics simulation. Due to computational restrictions, a molecular system consisting of only five glutamic acid residues was used, substituted by one spiropyran, or alternatively, by the merocyanine species. An initially minimized extended coil conformation of the model peptide consisting of planar *trans* peptide groups was considered.[15] A random minimization procedure was then employed,[49] in which the backbone dihedral angles are treated as variables for conformational perturbations, to be used, in turn, as the starting point for an energy minimization procedure. Conformational space was explored with respect to the $\{\phi, \psi\}$ dihedral angle set of the peptide (varied within a range of 30°) by using a technique[50]

(c)
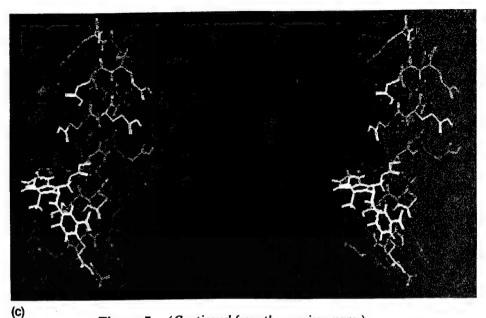
Figure 5. (*Continued from the previous page.*)

that employ the Metropolis algorithm. If the new conformation thus generated was of lower energy, it was selected for further exploration, although upward jumps in energy were also possible, with a probability proportional to the Boltzmann factor. This procedure was continued until the rms deviation in the $\{\phi, \psi\}$ angles of the current and initial conformations was larger than a defined threshold (0.5°). The thermal perturbation sequence was then terminated, and a full energy minimization performed. The algorithm was carried out for 3000 conformations, shown to explore a large region of the $\{\phi, \psi\}$ torsional space of L-amino acids, including that for α-helix and β-sheet conformations, so that

MODEL II

MODEL III
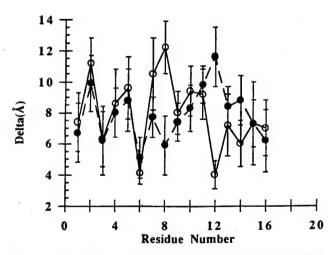
Figure 6. The δ_i variations (as explained in the text) of side-chain–side-chain distances (Å) during the dynamics simulation for the molecular systems **II**—full circle and **III**—open circle.
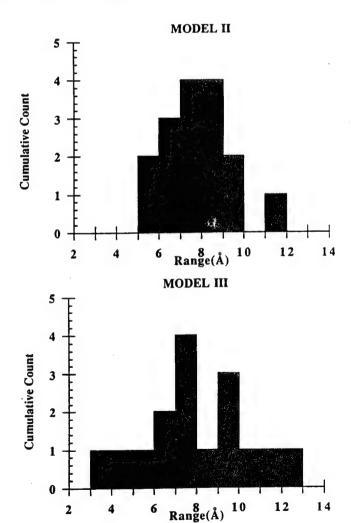
Figure 7. Cumulative count of δ_i (as explained in the text; Å) during the dynamics simulation for the molecular systems **II** and **III**.

235
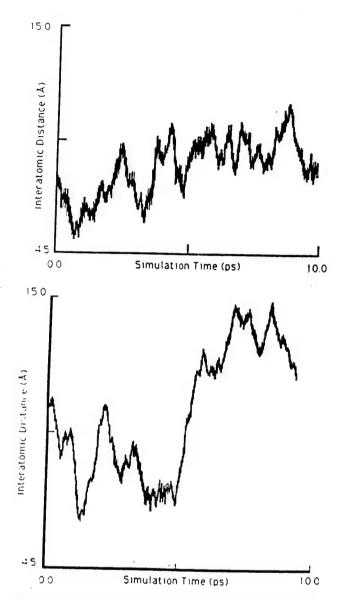
Figure 8. Distance (Å) fluctuations during the simulation between the side chains of residues {7} and {11}, for the (a) II- and (b) III-substituted analogues.

the conformation of lowest energy (by 31 kcal/mol lower than the starting conformation) was selected. The backbone atoms of this conformation are shown to deviate by 1.6 Å from a similar minimized α-helical structure of the polypeptide model. Following the heating and equilibration protocol outlined above, a 20-ps molecular dynamics simulation was carried out for further refinement. The last structure of this dynamics simulation shows rms deviations of 1.3, and 0.7 Å, for the backbone and C_α atoms, respectively, from a corresponding minimized α-helical model. A similar calculation of the alternative merocyanine-substituted model results in rms respective deviations of 1.8 and 2.2 Å. Clearly, the α-helical structure of poly(spiropyran-L-glutamate) is

not a local minimum when searching conformational space.

An examination of chromophore side-chain influence on a polypeptide may enable the derivation of a general modeling strategy to be used in future molecular design studies of new nonlinear optical photochromic biopolymer derivatives of defined secondary structure. The multiple-minima problem of the conformational energy that has to be resolved can be partially overcome by calculations with constraints. These may be based for example, on the σ and s parameters of the Zimm–Bragg theory[51] of the helix-to-coil transition,[52] considering sequence-specific interactions,[53] statistical information from x-ray data[54,55] or by the so-called build-up procedure.[56] The investigation reported in this study offers an initial step toward this objective for chromophore-bound peptides. Specifically, the elucidation of some of the general effects of chromophore side chains on the polypeptide backbone and the intrinsic behavior of particular chromophores, may validate the derivation of computational "constraints" for such systems, for example, when comparing spiropyran vs merocyanine substitution in various polypeptides. These can then be used, for example, with the recently introduced[57] double-iterated Kalman filter method, also validated and applied,[58,59] in order to derive an initial mean position for further conformational energy calculations of a newly designed polypeptide. The double-iterated Kalman filter result is unique in that it reflects the initial variance associated with any constraint introduced, so that relative effects of chromophoric side chains toward α-helicity in this case can be taken into account, and the method appropriate.

In summary, the molecular dynamics simulation of a poly(spiropyran-L-glutamate) model provides insight into some of the effects of the ring opening in spiropyran on an α-helical model of the polypeptide. The experimental observation[11,13] demonstrates the relationship between light adaptation and polypeptide conformation, revealing the light-adapted polymer to have an α-helical conformation. Similarly, the molecular dynamics simulations indicate that the spiropyran to merocyanine ring opening destabilized the polymer. In particular, larger side-chain flexibility, increased backbone hydrogen-bond lengths, as well as larger helix bending are calculated in the merocyanine substituted model III as compared to that of the α-helical model of II. Additionally, a random conformational minimization calculation finds the intrinsic behavior of the spiropyran molecular system as being more of a helix "maker" than its merocyanine analogue. However,

the experiment was performed in hexafluoroisopropanol as the solvent,[8] which is a strong hydrogen-bond acid. The simulation performed in this study includes solvent effects only by the use of a distance-dependent dielectric constant, so that explicit inclusion of solvation in the simulations would allow the modeling of hydrogen-bond formation between hexafluoroisopropanol and amide and carboxylic groups, increasing the destabilization of the polypeptide. Also, the experimentally determined kinetics of the helix-to-coil dark reaction were on the order of hours, while the simulation models processes occurring on a picosecond time scale. Thus, this calculation simulates correctly the observed stability trends of **II** and **IV** vs **III** and **V**, and offers a qualitative understanding of the interactions involved, but no quantitative measure. The computational study shows that there is some degree of coupling between the spiropyran to merocyanine ring opening reaction, and the backbone conformational changes, thus supporting the classical nucleation-propagation folding model.[60]

REFERENCES

1. Yitzchaik, S., Berkovic, G. & Krongauz, V. (1990) *Macromolecules* **23**, 3539–3541.
2. Ishii, T., Wada, T., Garito, A. F., Sasabe, H. & Yamada, A. (1990) *Mat. Res. Soc. Symp. Proc.* **175**, 129–134.
3. Pieroni, O., Fissi, A. & Ciardelli, F. (1986) *Photochem. Photobiol.* **44**, 785–791.
4. Yamamoto, H., Miyagi, Y., Nishida, A., Takagishi, T. & Shima, S. (1987) *J. Photochem.* **39**, 343–350.
5. Ueno, A., Takahashi, K., Anzai, J. & Osa, T. (1981) *J. Am. Chem. Soc.* **103**, 6410–6415.
6. Ciardelli, F., Pieroni, O., Fissi, A. & Houben, J. L. (1984) *Biopolymers* **23**, 1423–1437.
7. Fissi, A. & Pieroni, O. (1989) *Macromolecules* **22**, 1115–1120.
8. Vandewyer, P. H. & Smets, G. (1970) *J. Polym. Sci. A.* **8**, 2361–2374.
9. Smets, G. (1972) *Pure Appl. Chem.* **30**, 1–24.
10. Suzuki, Y., Ozawa, K., Hosoki, A. & Ichimura, K. (1987) *Polym. Bull.* **17**, 285–291.
11. Ciardelli, F., Fabbri, D., Pieroni, O. & Fissi, A. (1989) *J. Am. Chem. Soc.* **111**, 3470–3472.
12. Ciardelli, F., Fabbri, D., Pieroni, O. & Fissi, A. (1990) *Chim. Indust. (Milan)* **72**, 115–116.
13. Cooper, T. M., Obermeier, K. A., Natarajan, L. V. & Crane, R. L. (1992) *Photochem. Photobiol.* **55**, 1–7.
14. Scheraga, H. A. (1989) *Chem. Script.* **29A**, 3–13.
15. Oka, M., Hayashi, T. & Nakajima, A. (1984) *Polym. J.* **16**, 693–709.
16. Oka, M., Hayashi, T. & Nakajima, A. (1985) *Polym. J.* **17**, 621–631.
17. Paterson, Y. & Leach, S. J. (1978) *Macromolecules* **11**, 418–424.
18. Perahia, D., Levy, R. M. & Karplus, M. (1990) *Biopolymers* **29**, 645–677.
19. Guglielmetti, R. (1990) in *Photochromism: Molecules and Systems*, Durr, H. & Bouas-Laurent, Ed., Elsevier, New York, p. 314.
20. Tinland, B., Guglielmetti, R. & Chalvet, O. (1973) *Tetrahedron* **29**, 665–667.
21. Zerbetto, F., Monti, S. & Orlandi, G. (1984) *J. Chem. Soc. Faraday Trans. II* **80**, 1513–1527.
22. Le Beuze, A., Botrel, A., Appriou, P. & Guglielmetti, R. (1979) *Tetrahedron* **35**, 31–42.
23. Hashimoto, S., Shimojima, A., Yuzawa, T., Hiura, H., Abe, J. & Takahashi, H. (1990) *J. Mol. Struct.* **242**, 1–14.
24. Stewart, J. J. P. (1988) *Quantum Chemistry Program Exchange*, no. 455.
25. Burkert, O. & Allinger, A. L. (1982) *Am. Chem. Soc. Monograph* 177.
26. Pachter, R. & Wessels, P. L. (1989) *Magn. Reson. Chem.* **27**, 277–282, and references therein.
27. Kollman, P. A. & Merz, K. M., Jr. (1990) *Acc. Chem. Res.* **23**, 246–252.
28. Mayo, S. L., Olafson, B. D. & Goddard, W. A., III (1990) *J. Phys. Chem.* **94**, 8897–8909.
29. Brooks, B. R., Bruccoleri, R. E., Olafson, B. D., States, D. J., Swaminathan, S. & Karplus, M. (1983) *J. Comp. Chem.* **4**, 187–217.
30. Polygen Corporation (1990) Quanta Parameters: Release 3.0.
31. Pachter, R., Bunning, T. J. & Adams, W. W. (1991) *Comput. Polym. Sci.* **1**, 179–187.
32. Pachter, R. & Wessels, P. L. (1988) *J. Mol. Struct. (Theochem.)* **164**, 189–194.
33. Pachter, R. & Wessels, P. L. (1988) *J. Mol. Struct. (Theochem.)* **178**, 323–333.
34. Polygen Corporation (1990) Quanta/CHARMm (Chemistry at HARvard Macromolecular mechanics): Release 3.0.
35. Vasquez, M., Pincus, M. R. & Scheraga, H. A. (1987) *Biopolymers* **26**, 351–371.
36. McCammon, J. A. & Harvey, S. C. (1987) *Dynamics of Proteins and Nucleic Acids*, Cambridge University Press, New York.
37. Verlet, L. (1967) *Phys. Rev.* **159**, 98–105.
38. Takahashi, H., Yoda, K., Isaka, H., Ohzeki, T. & Sakaino, Y. (1987) *Chem. Phys. Lett.* **140**, 90–94.
39. Takahashi, H., Murakawa, H., Sakaino, Y., Ohzeki, T., Abe, J. & Yamada, O. (1988) *J. Photochem. Photobiol.* **45**, 233–241.
40. Harmony, M. D., Laurie, V. W., Kuczkowski, R. L., Schwendeman, R. H., Ramsey, D. A., Lovan, F. J.,

Lafferty, W. J. & Maki, A. G. (1979) *J. Phys. Chem. Ref. Data* **8,** 619–625.

41. Wiberg, K. G. (1968) *Tetrahedron* **24,** 1083–1096.

42. Paolini, J. P. (1990) *J. Comp. Chem.* **11,** 1160–1163.

43. Goldfarb, I. J., Reale, H., Wierschke, S. & Medrano, J. (1989) *Mat. Res. Soc. Symp. Proc.* **134,** 609–619.

44. Harada, N. & Nakanishi, K. (1983) *Circular Dichroic Spectroscopy: Exciton Coupling in Organic Stereochemistry,* Mill Valley, University Science Books.

45. Reidy, M. P. & Green, M. M. (1990) *Macromolecules* **23,** 4225–4234.

46. Cooper, T. M., manuscript in preparation.

47. Go, M. & Go, N. (1976) *Biopolymers* **15,** 1119–1127.

48. Blundell, T., Barlow, D., Borkakoti, N. & Thornton, J. (1983) *Nature* **306,** 281–283.

49. Go, N. & Scheraga, H. A. (1970) *Macromolecules* **3,** 178–187.

50. Kirpatrick, S., Geilat, C. D., Jr. & Vecchi, M. P. (1983) *Science* **220,** 671–680.

51. Zimm, B. H. & Bragg, J. K. (1959) *J. Chem. Phys.* **31,** 526–535.

52. Sueki, M., Lee, S., Powers, S. P., Denton, J. B., Konishi, Y. & Scheraga, H. A. (1984) *Macromolecules* **17,** 148–155.

53. Vasquez, M. & Scheraga, H. A. (1988) *Biopolymers* **27,** 41–58.

54. Kabsch, W. & Sander, C. (1983) *Biopolymers* **22,** 2577–2637.

55. Gibrat, J.-F., Garnier, J. & Robson, B. (1989) *J. Mol. Biol.* **198,** 425–443.

56. Gibson, K. D. & Scheraga, H. A. (1987) *J. Comp. Chem.* **8,** 826–834.

57. Altman, R. B. & Jardetzky, O. (1989) *Methods Enzymol.* **177,** 218–227. [Coded in Altman, R. B., Pachter, R., Carrara, E. A. & Jardetzky, O. (1990) *Quantum Chemistry Program Exchange* **10,** 596.]

58. Pachter, R., Altman, R. B. & Jardetzky, O. (1990) *J. Magn. Reson.* **89,** 578–584.

59. Pachter, R., Altman, R. B., Czaplicki, J. & Jardetzky, O. (1991) *J. Magn. Reson.* **92,** 468–479.

60. Zimm, B., Doty, P. & Iso, K. (1959) *Proc. Natl. Acad. Sci.* **45,** 160A.

238

NONLINEAR OPTICAL PROPERTIES OF POLYPEPTIDE-BOUND CHROMOPHORES
Marc C. Martin

Nonlinear Optical Properties of Polypeptide-Bound Chromophores

Marc C. Martin, Ruth Pachter, Robert L. Crane and W. Wade Adams

Wright Laboratory, Materials Directorate, WPAFB

- The prediction of nonlinear optical properties is an important step towards the design of biomaterials with controlled nonlinear optical properties

- In the present study the effect of a polypeptide backbone on the nonlinear optical properties of a series of poly(L-Glutamic acid)-bound chromophores is reported

- Hyperpolarizability calculations were performed by the finite-field approach using a semi-empirical Hamiltonian

- Calculations were carried out for each of the individual chromophores, and for oligomers attached to a glutamic acid group, and to a backbone of three glutamic acid molecules

- Interestingly, hyperpolarizability values are shown to increase with the polypeptide backbone substitution in some cases, holding promise for our continuing effort towards the design of biomaterials with controlled nonlinear optical properties

X-RAY MODULI OF SILK FIBERS
D. V. Mahoney and Dr. R. K. Eby

X-ray Moduli of Silk Fibers

M. A. Becker, D. V. Mahoney, P. G. Lenhert[1], R. K. Eby,
D. L. Kaplan[2], W. W. Adams[3]

Department and Morton Institute of Polymer Science,
The University of Akron, Akron, OH 44325-3909
[1]Department of Physics, Vanderbilt University, Nashville, TN 37235
[2]Biotechnology Division, US Army Natick RD&E Center, Natick MA 01769-5020
[3]Wright Laboratory, Materials Directorate, WPAFB, OH 45433

X-ray moduli were determined for silk fibers from the golden orb-weaver spider *Nephila clavipes* and the domesticated silkworm *Bombyx mori* to provide insight into their physical properties. Differences between the respective moduli, 17 and 29 GPa, are discussed in terms of the lack of scaling with the basal area per molecule, the effect of the amorphous content and the stress history dependence. Both annealed and irradiated *B. mori* fibers yielded decreased X-ray moduli. All these results as well as the considerable difference between the experimental and computer modeled moduli raise questions regarding the applicability of the uniform stress assumption for the X-ray modulus calculation at room temperature conditions.

Many biological materials exhibit extraordinary physical properties considering that they are assembled *in vivo* from abundant natural resources. The silk dragline fibers (major ampullate gland) produced by *Nephila clavipes* provide structural support for orb-shaped webs and dissipate large quantities of energy when prey fly into the snare (*1, 2*). It is the combination of high strength, modulus and extensibility that yields the latter property and makes spider silk unique among the extracellular fibrous proteins. Their properties and the idea of obtaining silk fibers directly from a live creature, as opposed to the tedious task of unwinding cocoons, even lead to attempts at product development over a period of time going back at least to the beginning of the 18th century (*3-5*). Some unusual products, such as smothering caps of felted *Nephila* silk employed in the suffocation of people, dooming bags, fishing nets, optical cross hairs, strings for musical instruments, etc., have been reported (*5, 6*). Knowledge of the physical and chemical structures/properties is required to understand the unusual characteristics of silk produced by the spider.

Silk's physical properties are a consequence of both the composition and molecular architecture of a fibrous protein, fibroin. Amino acid compositions comprising a large percentage of glycine and alanine are characteristic of fibroins, and in general, of all extracellular matrix proteins. For the extruded fibroins, the conformation of the

polypeptide is influenced by the amino acid sequence as well as by the shear stresses imposed on the fibroin molecules during the extrusion process. It is the shear stresses which effectively orient and extend the polypeptide chains (7, 8). The high percentage of small side chain amino acids allows for close packing of the extended molecules and facilitates crystal formation.

The composition of *Bombyx mori* silk, the most extensively studied fibroin, has been investigated since the middle of the 19th century (9), however, the exact amino acid sequence of this highly repetitive molecule has been difficult to obtain. The sequence of the crystalline precipitate remaining after digestion of fibroin with chymotrypsin, the C_p fraction, is (10, 11)

Gly-Ala-Gly-Ala-Gly-Ser-Gly-Ala-Ala-Gly-[Ser-Gly-(Ala-Gly)$_n$]$_8$-Tyr

More recently, *B. mori* fibroin has been found to consist of a light (L-) and a heavy (H-) chain linked by a disulfide bond (12). The amino acid sequence of the L-chain (25 kd) has been determined by cDNA, while only the initial region of the repetitious H-chain (350 kd) has been reported (13-15).

The amino acid composition of *N. clavipes* silk has the characteristically high glycine and alanine content consistent with other fibroins (16, 17). The repeats -(Gly-Gly-Xaa)$_n$- and -(Tyr-Gly-Gly-Leu-Gly-Ser-Gln-Gly-Ala-Gly-Arg-Gly-Gly)-, however, have been proposed as part of *N. clavipes'* major ampullate gland silk sequence, replacing the classic repeat -(Gly-Ala-Gly-Xaa)$_n$- arrangement found in *B. mori* fibroin (18, 19).

The first scattering of X-rays by *B. mori* fibers was reported in 1913, but it wasn't until much later that a pseudo-unit cell was determined to be orthorhombic with monoclinic symmetry (20, 21). In 1960, Warwicker published a comparative study of the X-ray patterns from seventy different silks produced by species in the classes Insecta and Arachnida (22). This led to the silks being classified into five groups based on their X-ray patterns, specifically the two principle equatorial reflections (22). Some of the five groups were subdivided into "a", those which exhibited equivalent intensities of the principle equatorial reflections and "b", those with different intensities. A common c dimension of 6.95 ± 0.05 Å along the fiber axis was determined for all the fibroins (22). A b dimension of 9.44 Å, the direction of the hydrogen bonding within the anti-parallel β-pleated sheets, was also the same for all five X-ray groups (22). The variation in the a dimension, intersheet spacing, from 9.3 Å to 15.7 Å, was attributed to the different amino acid compositions and sequences of the fibroins (22). While the five X-ray groups are not identical to the taxonomical classification of the species, they do indicate a similarity in the basic structure and provide a basis for further comparative studies.

The distribution and size of the crystalline and amorphous regions of the extruded proteinaceous fibers influence the physical properties. One means of investigating the crystalline regions utilizes X-ray diffraction measurements to determine the lattice strain in the direction of the applied macroscopic stress (23, 24). The ratio of the applied stress to lattice strain is commonly referred to as the "X-ray modulus", "crystal modulus", or "lattice modulus" and, subject to certain assumptions, is the ultimate specimen modulus.

The lattice strain is determined by expressing the change in the position of a diffraction peak compared to the initial position as a fractional change in d-spacing with tension (23, 24). The calculation of the X-ray modulus assumes a uniform stress

distribution throughout the material (23, 24). Previous workers have argued for this assumption on the basis that the X-ray moduli of PVA and PE fibers are a function of only the lattice spacing and independent of overall crystal orientation and crystallinity (25). The fact that the same moduli were also determined for both dry and wet conditions of hygroscopic PVA fibers was also cited as indicating that the uniform stress assumption is valid (26).

Three conditions have been proposed as requirements for a high X-ray modulus in fibers (27). First, the molecular axis should be parallel to the applied stress. Second, the molecular conformation and configuration should allow a close-packing arrangement of the molecules. Third, the force constant for deformation of the molecule should be large. Deformation by bond stretching rather than bond angle bending or torsion generally carries a higher force constant. Helical polymers, for example, usually deform by changes in torsion and therefore have lower moduli than fully extended chain polymers.

The dimensions of the pseudo-unit cell proposed for *B. mori* are $a = 9.29$ Å, $b = 9.44$ Å and the fiber axis $c = 6.95 \pm 0.05$ Å corresponding to Group 1 in Warwicker's classification (22). The similarity in the X-ray diffraction by the fiber and the C_p fraction is interpreted to mean the sequence is representative of the crystalline regions of the fiber (28). The -(Gly-Ala-Gly-Xaa)- repeat in the crystalline regions allows for the closest packing of all the fibroins reported to date (22, 28). Therefore, Group 1 fibroins would be expected to have the highest X-ray moduli of all the β-pleated sheet proteins.

The similarity of the amino acid composition of *N. clavipes* to that of *Nephila madagascariensis* suggests that similar unit cell dimensions might be anticipated (16, 29). The pseudo-unit cell of *N. madagascariensis* is classified as Group 3b and has dimensions of $a = 10.6$ Å, $b = 9.44$ Å, and $c = 6.95 \pm 0.05$ Å (22). These dimensions are comparable to those of Tussah silk (*Antheraea pernyi*), also Group 3b, which is described as having an -(L-Ala)$_n$- sequence in the crystals (28). The amino acid residues in the unit cells of *N. clavipes*, *N. madagascariensis* and *A. pernyi* have not been determined explicitly. Nevertheless, the similarity of their pseudo-unit cell dimensions and β-pleated sheet conformation provides a basis for a comparison of their X-ray moduli.

In this paper, measurements and computations of the X-ray moduli for the silks of *B. mori* and *N. clavipes* are presented. The results are discussed in the context of the validity of the assumption of uniform stress.

Materials and Methods

The female *N. clavipes* spiders were obtained from Panama. Dragline fibers were collected in a manner similar to a recently published method as well as to one described as early as the 18th century (30, 31). The silk was collected at a rate of approximately 1.1 cm/s. A bundle of fibers (approximately 5100) was prepared, mounted in a sample holder and secured with room-temperature curing epoxy. The density was taken as 1.35 (± 0.005) g/cm^3 (32). An effective cross-sectional area of a fiber bundle was determined from the mass of a specific length and the density. This yielded a sample cross-sectional area of 9.5×10^{-8} m^2.

Commercially degummed *B. mori* yarns were bundled in groups of 40 or 100 yarns, mounted in sample holders and secured using room-temperature curing epoxy (33).

The silk yarns had approximately 8 twists/cm which is calculated to cause a very small error in the X-ray modulus (see Appendix). The density was taken as 1.353 g/cm^3 (34). This yielded an effective cross-sectional area of 9.8 x 10^{-8} m^2. Two additional B. mori samples were prepared from artificially-aged fibers. The first was exposed to 500 kJ/m^2 (0.75 W/m^2) of simulated sunlight-through-glass in an Atlas Ci-65 Weather-ometer. The irradiated fibers were then mounted in sample holders as described above. The second sample consisted of fibers mounted in the sample holders, secured with epoxy and then annealed at 200 °C for one hour at a fixed length. Both samples exhibited a discoloration after the aging.

A Rigaku Denki RU-200 rotating anode was the source of nickel-filtered Cu radiation used for all experiments. X-ray data for the N. clavipes sample was collected using a Siemens General Area Detector with stress applied by a dead weight. Data for B. mori samples were collected for both increasing and decreasing tension as well as various orientations of the tensioning device according to a published procedure (33). The stress relaxation of the B mori sample after the initial application of strain was compensated for by a further increase in applied strain before X-ray measurements were made. (There is a related creep effect in the method used for the N. clavipes sample.) The 002 diffraction peak was used for calculation of the X-ray moduli. For comparative purposes, the 006 diffraction peak of B. mori was also used. The relatively small effects of changes in relative humidity and temperature on density during the experiments were not investigated (34-36).

Molecular modeling was done on a Silicon Graphics system using the Sybyl 5.5 software from Tripos Associates, Inc. Arrays of nineteen peptides, each ten alanine residues in length and terminated with blocking groups, were constructed in the antiparallel β conformation to represent Group 3b. Various packing geometries and deformation protocols were applied to these arrays in order to obtain the energy of the central molecule as a function of strain. The second derivative of this energy with respect to strain was used together with a correction for end effects, the initial length and the basal area per molecule to obtain the modulus (37).

Results and Discussion

The 002 diffraction peak from the N. clavipes fiber bundle gave a d-spacing of 3.47 Å or a pseudo-unit cell c dimension of 6.94 Å. This agrees with the pseudo-unit cell c dimension, 6.95 ± 0.05 Å, for all fibroins in the β-pleated sheet conformation (22). The pseudo-unit cell dimensions perpendicular to the chain axis conformed with the published values for Group 3b, for which a = 10.6 Å and b = 9.44 Å (22). Presumably the increased spacing in the a direction is the result of bulkier side groups incorporated into the crystals (22). The X-ray modulus of the dragline silk was 16.7 ± 0.6 GPa (002) at 27 °C and approximately 15% relative humidity (Fig. 1).

The 002 diffraction peak from the B. mori sample gave a d-spacing of 3.50 Å or a pseudo-unit cell c dimension of 7.00 Å. This also corresponds with the characteristic c dimension of all fibroins in the β-pleated sheet conformation (22). Scans of the layer lines 0 to 6 showed only minor differences, after background corrections, between the peak positions and the cell corresponding to Group 1, a = 9.29 Å and b = 9.44 Å (22).

The X-ray modulus determined as a function of increasing strain for the crystals in *B. mori* silk fibers was 28.7 ± 0.2 GPa (002) at 20 °C and a relative humidity ranging between 40% and 60%. The modulus determined as a function of decreasing strain was a higher value, 30.5 ± 0.5 GPa (002). The difference in the data (Fig. 2) is related to the stress relaxation observed immediately after the strain was altered and to a hysteresis reported earlier (*1, 38*). Note also that the value of the modulus obtained depends somewhat upon the time elapsed between the application of the strain and the taking of the X-ray data. Effects relating to relaxation phenomena in silk have been known for a long time (*39*). The values of the modulus obtained for increasing and decreasing strains can be averaged to yield 29.6 GPa (002).

For *B. mori* fibers, the 002 reflection gave a lower X-ray modulus than the 006 reflection. The latter gave a value of 35.3 ± 0.2 GPa for increasing strain and 36.4 ± 0.8 GPa for decreasing strain with an average of 35.8 GPa (006). One possible cause of the difference between the (002) and the (006) modulus values is that the overlap of the amorphous halo and the 002 peak interferes with the baseline subtraction. If this overlap changes with the stress, it would introduce error to the change in the d-spacing. The 006 peak does not overlap the amorphous halo as much as the 002 peak and thus could yield a more accurate X-ray modulus. Another possibility, known to occur in some other polymers, is a change in the Laue lattice factor $|G|^2$ as crystallite size increases in the chain direction with applied tensile stress (*40-42*). However, the change in crystallite size with applied stress is negligible for *B. mori* fibers (*43*). Thus, the source of the discrepancy is probably in the overlap with amorphous scattering.

The artificially-aged *B. mori* fiber bundles had substantially reduced X-ray moduli. Those of silk irradiated with simulated sunlight-through-glass were 20.5 ± 0.4 GPa (002) and 24.8 ± 0.5 GPa (006). Those of the annealed silk were 22.3 ± 0.2 GPa (002) and 25.5 ± 0.3 GPa (006). A comparable X-ray modulus of 23 GPa has been reported for *B. mori* silk fibers which also had been annealed at 200 °C for one hour at constant length (*43*). Biochemical analyses have shown that the amorphous regions are affected initially by degradative photochemical mechanisms (*44*). Similarly, it might be anticipated that the oxidative degradation of the annealed fibers would primarily affect the amorphous regions which would be more accessible to oxygen. This has been concluded on the basis of other work (*45*). Changes in optical, mechanical and physical properties were interpreted in terms of changes in the amorphous regions upon heat treatment to about 260 °C (*45*). The present X-ray results agree with those in that work (*45*). That is, qualitative comparison of the diffraction patterns obtained before and after annealing to 200 °C indicates a small increase in crystallinity with the crystal structure remaining unchanged. Thus, the decreased X-ray modulus for the artificially-aged silk could be the result of changes in the amorphous regions. This suggests that the connectivity of the crystalline and amorphous regions affects the X-ray modulus measurements and might not correspond to the proposed uniform stress model (*43*). The measured X-ray moduli of pitch-based carbon and poly(paraphenylene benzobisthiazole) fibers are known to vary with changes in structure and morphology (*46, 47*).

The difference between the moduli of *N. clavipes* and *B. mori* could be the result of increased spacing in the a direction due to bulkier side groups in the crystals of *N. clavipes*. The difference between the moduli of *B. mori* and *A. pernyi* silk have been accounted for by such a change (*48*). When the modulus of *N. clavipes* is normalized to

the pseudo-unit cell dimension of *B. mori* in the a direction, the value is increased only slightly to 19 GPa, compared to the 29 GPa given above for *B. mori*. Thus, the change in cross-sectional area of the crystals does not fully account for the differing measured moduli of these two fibers. Since *N. clavipes* is more amorphous than *B. mori* silk (*1*), this difference in the moduli might result from the effects of overlap of the amorphous halo and the 002 peak as well as from differences in amorphous content per se. Further, there might be differences arising from the fact that *N. clavipes* was measured under fixed load and *B. mori* under fixed strain. These results raise the issue of the validity of the uniform stress assumption and the influence of the connectivity as well as stress relaxation on that assumption. It should be noted that the assumption of uniform stress yields the lower limit of the modulus, while the assumption of uniform strain yields the higher limit (*46, 47, 49*). The X-ray modulus can also be calculated using the assumption of uniform strain by making use of elastic constants and crystal orientation (*46, 47*). However, the elastic constants are unknown for β-pleated fibroin crystals.

Molecular modeling yielded a modulus of about 150 GPa for the arrays of molecules of -(L-Ala)$_{10}$-. This computational modulus for agrees fairly well with the value of 155 GPa calculated by Treloar's method for the pseudo-unit cell *B. mori* crystals (*50*). It has been argued that the latter result is in error because it neglects the low stiffness for torsion about the backbone bonds (*43*). However, intersheet restrictions on the torsion due to side chain interactions as well as intramolecular restrictions are known (*28, 51, 52*). It is our observation that there are also intrasheet restrictions due to the methyl branch interactions. All would add significantly to the effective torsional stiffness.

While poly-(L-alanine) may not explicitly correspond to the crystalline regions of *N. clavipes*, it is considered a model for the pseudo-unit cell of *A. pernyi* and both species are classified in Warwicker's Group 3b (*22*). In this sense, the computed modulus of 150 GPa for poly-(L-alanine) can be compared to the X-ray moduli of *N. clavipes*, 17 GPa, and *A. pernyi*, 20 GPa (*48*). Furthermore, computational moduli for single chain homopolymers of alanine, glycine and serine suggest that the molecular stiffness changes relatively little among homopolymers containing of the smaller side chain amino acids. This implies that the computed modulus can also be compared to the X-ray modulus of 29.6 GPa for *B. mori*. In contrast to these results, test calculations for polyethylene using similar modeling approaches, however, yielded a computational modulus much closer to that experimentally observed. Thus, the computational results for fibroins suggest that the measured values of X-ray moduli based on the proposed use of the assumption of uniform stress are too small (*43*).

The large disparity between the computational and the experimental X-ray moduli of the fibroins cannot simply be accounted for by various arrays and protocols of the modeling program. A discrepancy between the theoretical and experimental modulus values of nylon has been noted by others (*40, 53*). However, simple explanations, such as amide chain shortening for the case of nylon-6, do not correct for the discrepancy in moduli values for fibroins. While the assumption of a uniform stress distribution has been verified by others (*26, 43, 48, 54*), X-ray diffraction is known to yield lower experimental moduli than spectroscopic techniques such as Raman and coherent inelastic neutron scattering (*55*). The approximate 110 GPa difference between the computed modulus of poly-(L-alanine) and the X-ray moduli of *N. clavipes*, *A. pernyi*, and *B. mori*

silk cannot be accounted for. It does raise questions regarding the validity of the uniform stress assumption for fibroins at room temperature conditions.

Conclusions

The X-ray moduli (002) are 17 GPa for *N. clavipes* and 29 GPa for *B. mori*. These values do not scale according to the difference between the basal area per molecule in the two crystals. Further, they are much less than the values calculated by computational modeling for poly-(L-alanine) and by Treloar's method for the fibroin pseudo-unit cell (*48*). The modulus value for *B. mori* is altered by an observed stress relaxation phenomena and lowered by degradation effects in the amorphous components of the fiber.

All the discrepancies among the various X-ray and computational moduli determined for *N. clavipes* and *B. mori* raise questions regarding the effect of relaxation phenomena and crystalline-amorphous connectivity on X-ray modulus measurements for these silks. These observations, in turn, question the validity of the assumption of uniform stress used in the analysis of the experimental data.

Acknowledgements

Literature Cited
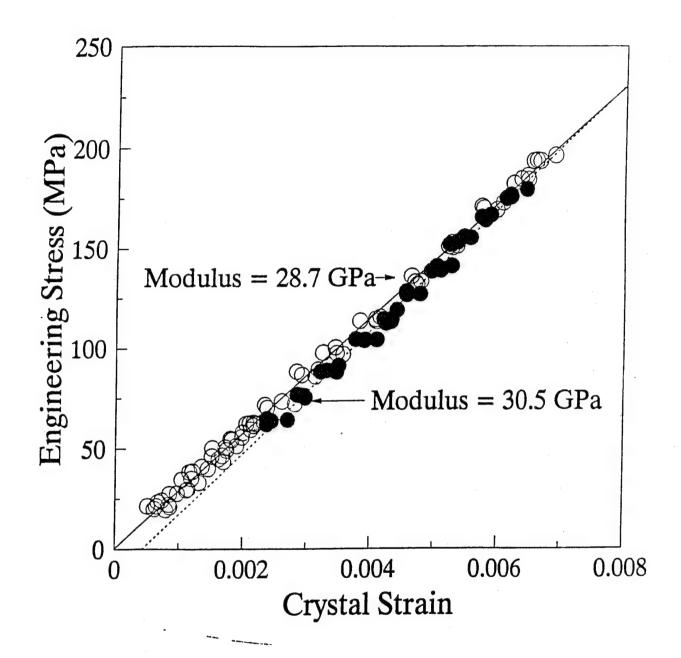
1. Gosline, J.M.; DeMont, M.E.; Denny, M.W. *Endeavor* **1986**, *10*, pp 37-43. See also Gosline, J.M.; Denny, M.W.; DeMont, M.E. *Nature*, **1984**, *309*, pp 551-552.
2. Vollrath, F. *Scientific American* **1992**, *3*, pp 70-76.
3. Wilder, B.G. *The Atlantic Monthly* **1866**, *18 (106)*, pp 129-145.
4. Dusuzeau, J. *Laboratorie d'etudes de la Soie Industrie,"Rapport presente a la Chambre de Lyons por Commerce d'Industrie"*, **1892**, pp 163-171 plus plates, refers to the work of Bon in 1708.
5. Mariox, M.J. *Laboratorie d'etudes de la Soie Industrie, "Rapport presente a la Chambre de commerce de Lyons por commerce et d'Industrie"*; **1899**, pp 23-34. See also Ref. 31.
6. McKeown, K.C. *Spider Wonders of Australia*; Angus & Robertson Ltd.: Sydney, 1936; pp 233-234.
7. Komatsu, K. *J. A. R. Q.* **1979**, *13(1)*, pp .64-72.
8. Magoshi, J.; Magoshi, Y.; Nakamure, S. In *Proc. of the 7th International Wool Textile Research Conference,* Tokyo, 1985, Vol.1. pp 329-336.
9. Cramer E. *Journal fur Praktische Chemie*, **1865**, *96*, pp 76-98; See also Roard, *Ann. de Chim.* **1807**, *65*, p 44.
10. Lucas, F.; Shaw, J.T.B.; Smith, S.G. *Biochem. J.* **1957**, *66*, pp 468-479.
11. Strydom, D.J.; Haylett, T.; Stead, R.H. *Biochem. Biophys. Res. Comm.* **1977**, *79(3)*, pp 932-938.

12. Sasaki, T,; Noda, H. *Biochim. Biophys. Acta* **1973**, *310*, pp 91-103.
13. Yamaguchi, K.; Kikuchi, Y.; Tagaki, T.; Kikuchi, A.; Oyama, F.; Shimura, K.; Mizuno, S. *J. Mol. Biol.* **1989**, *210*, pp 127-139.
14. Tsujimoto, Y.; Suzuki, Y. *Cell*, **1979**, *16*, pp 425-436.
15. Tsujimoto, Y.; Suzuki, Y. *Cell*, **1979**, *18*, pp 591-600.
16. Work, R.W.; Young, C.T. *J. Arachnol.* **1987**, *15*, pp 65-80.
17. Lombardi, S.J.; Kaplan, D.L. *J. Arachnol.* **1990**, *18*, pp 297-306.
18. Mello, C.; Senecal, K.; Young, B.; Vouros, P.; Kaplan, D.L. this monograph.
19. Lewis, R.V. *Acc. Chem. Res.* **1992**, *25*, pp 392-398.
20. Nishikawa, S.; Ono, S. *Proc. Math. Phys. Soc. Tokyo* **1913**, *7*, pp 131-138, plates.
21. Marsh, R.E.; Corey, R.B.; Pauling, L. *Biochim. Biophys. Acta* **1955**, *16*, pp 1-34.
22. Warwicker, J.O. *J. Mol. Biol.* **1960**, *2*, pp 350-362.
23. Sakurada, I.; Nukushina, Y.; Ito, T. *J. Poly. Sci.* **1962**, *57*, pp 651-660.
24. Dulmage, W.J.; Contois, L.E. *J. Poly. Sci.* **1958**, *28*, pp 275-284; also see Refs. *33, 46, 47*.
25. Sakurada, I.; Kaji, K.; Nakamae, K.; Wadano, S. *Bulletin of the Institute for Chemical Research, Kyoto University*, **1966**, *44*, pp 168-182.
26. Sakurada, I.; Ito, T.; Nakamae, K. *Die Makromolekulare Chemie* **1964**, *75*, pp 1-10.
27. Nakamae, K.; Nishino, T. In *Integration of Fundamental Polymer Science and Technology-5*; Lemstra, P.; Kleintjens, L.; Eds., Elsevier: New York, 1991, pp 121-130.
28. Marsh, R.E.; Corey, R.B.; Pauling, L. *Acta Cryst.* **1955**, *8*, pp 710-715.
29. Lucas F.; Shaw, J.T.B.; Smith S.G. *J.Mol. Biol.* **1960**, *2*, pp 339-349.
30. Work, R.W.; Emerson, P.D. *J. Arachnol.* **1982**, *10*, pp 1-10.
31. Anonymous *Seta-Bollettino di Sericoltura* **1957**, *18*, pp 17-20, refers to de Termeyer, R.M. *Opuscoli scientifici di Entomologia di Fisica e d'Agricoltura*, Vol 1, Milan, 1807 which reports work from the previous 30 years.
32. Zemlin, J.C. Technical Report 69-29-CM, 1968, U.S. Army Natick Laboratories, Natick, MA.
33. Lenhert, P.G.; Adams, W.W. In *The Materials Science and Engineering of Rigid-Rod Polymers*; Adams, W.W.; Eby, R.K.; McLemore, D.E., Eds.; Materials Research Society Symposium Proceedings; Materials Research Society: Pittsburgh, PA, 1989, Vol. 134; pp 329-340. See also Lenhert, P.G.; Adams, W.W. *Tensile Modulus by X-ray Diffraction; Instrument and Method*; Wright Laboratory, Materials Directorate, WPAFB, OH 45433, July 1990; WRDC-TR-90-407.
34. Goodings, A.C.; Turl, L.H. *J. Textile Inst.* **1940**, *31*, pp T69-80.
35. McLaren, A.D.; Rowen, J.W. *J.Poly. Sci.* **1951**, *7(2/3)*, pp 289-324.
36. Wright, B.A. *Nature*, **1948**, *162*, p 23.
37. Klunzinger, P.E.; Eby, R.K.; Adams, W.W. In *Hierarchically Structured Materials;* Aksay, I.; Baer, E.; Sarikaya, M.; Tirrell, D., Eds.; Materials Research Society Symposium Proceedings; Materials Research Society: Pittsburgh, PA, Vol. 255, 1992, pp 119-128.
38. Lenhert, P.G.; Becker, M.A.; Eby, R.K Presented at the Fiber Society 50th Technical Conference, Princeton, NJ, August 19-23, 1990.
39. Weber, W.; *Poggendorf's Ann. der Physik Chemie*, **1835**, *34*, pp 247-257.
40. T. Kaji, K.; Sakurada, I. *Makromol. Chem.* **1978**, *179*, pp 209-217.
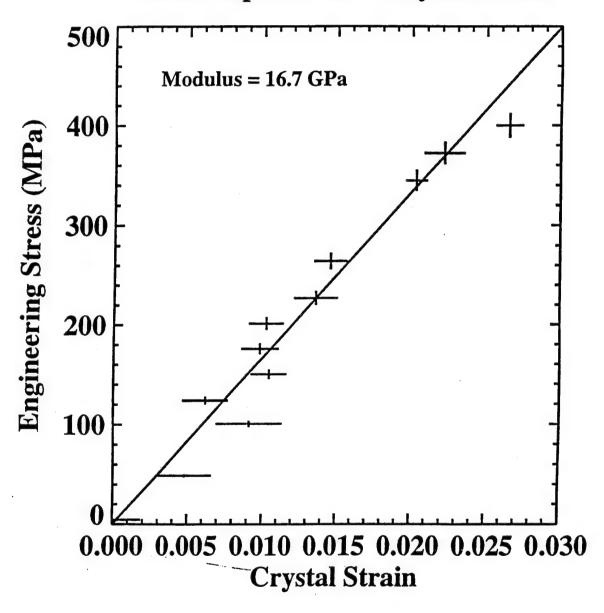
41. Kaji, K. *Makromol. Chem.* **1974**, *175*, pp 311-325.

42. Nishino, T.; Tada, K.; Nakamae, K. *Polymer*, **1992**, *33(4)*, pp 736-743.

43. Nakamae, K.; Nishino, T.; Ohkubo, H. *Polymer*, **1989**, *80*, pp 1243-1246.

44. Becker, M.A. Ph.D. Dissertation, The Johns Hopkins University, 1993.

45. Tsukada, M.; Freddi, G.; Nagura,M.; Ishikawa, H.; Kasai, N. *J. Appl. Poly. Sci.* **1992**, *46*, pp 1945-1953. See also Warwicker, J.O. *Biochim. Biophys. Acta*, **1961**, *52*, pp 319-328.

46. Arsenovic, P.; Jiang, H.; Eby, R.K.; Adams. W.W.; Liu, J.M. in *Carbon '88*; McEnaney, B; Mays, T.V., Eds.; IOP Publishing Ltd., Bristol, 1988; pp 485-487.

47. Jiang, H.; Eby, R.K.; Adams, W.W.; Lenhert, P.G. in *The Materials Science and Engineering of Rigid-Rod Polymers*; Adams, W.W.; Eby, R.K.; McLemore, D., Eds.; Materials Research Society Symposium Proceedings; Materials Research Society: Pittsburgh, PA, 1989, Vol. 134; pp 341-350. See also Jiang, H. Ph.D. Dissertation, The Johns Hopkins University, 1989.

48. Nishino,T.; Nakamae, K. *Polymer*, **1992**, *33*, pp 1328-1329.

49. Johnson, W. In *Strong Fibers, Vol 1*; Watt, W.; Perov, B.V. Eds.; Elsevier Science, New York, 1988; Chapter X.

50. Iizuka, E. *Biorheology*, **1965**, *3*, pp 1-8.

51. Lotz, B.; Colonna Cesari, F. *Biochimie*, **1979**, *61*, pp 205-214.

52. Oka, M.; Baba, Y.; Kagemoto, A.; Nakajima, A. *Polymer Journal*, **1990**, *22(5)*, pp 416-425.

53. Dumbleton, J.H.; Buchanan, D.R. *Polymer*, **1968**, *9*, pp 601-602.

54. Nakamae, K.; Nishino, T.; Ohkubo, H. *J. Macromol. Sci-Phys.*, **1991**, *B30(1&2)*, pp 1-23.

55. Fanconi, B.; Rabolt, J.F. *J. Polymer Sci.-Phys. Ed.*, **1985**, *23*, pp 1201-1215.

56. Mahoney, D.; Eby, R.K.; Kaplan, D.; Adams, W. *Bull. Am. Phys. Soc.* **1992**, *37(1)*, Abstract K'34 10.

57. Hearle, J.W.S. In *Structural Mechanics of Fibers, Yarns, and Fabrics*; Hearle, J.W.S.; Grosberg, P.; Backer,S. Eds.; Wiley-Interscience, New York, 1969; Chapter 4.

Appendix: Effect of Yarn Twist on Modulus Calculations

Consider the yarn to fiber modulus relationship using idealized helical geometry analogous to the single filament to X-ray modulus relationship. Based on the twist per unit length and the idealized helical yarn geometry, the fibers subtend an average angle θ of less than 5°, with respect to the yarn axis (57). The idealized helical geometry predicts the yarn modulus E_y is related to the fiber modulus E_f by a factor of $\cos^2 \theta$, $E_y = E_f \cos^2 \theta$. Assuming the analogous situation for the relationship between the measured crystal modulus of the yarn and the crystal or X-ray modulus of the fiber, the X-ray modulus would be altered less than 1%. This alteration is comparable to the experimental error of the X-ray modulus measurements.

Nephila clavipes
Macroscopic Stress vs Crystal Strain

Modulus = 16.7 GPa

Figure 1. The stress-strain curve based on x-ray diffraction by the (002) planes of crystals in *Nephila clavipes* fibroin for increasing strain. The line is a weighted fit to the data which are represented by crosses giving the uncertainty.

Figure 2. The stress-strain curve based on x-ray diffraction by the (002) planes of crystals in *Bombyx mori* fibroin for increasing (-O-) and decreasing strain (··●··). The lines are least-squares fits to the data which were obtained with one sample using four different sets of measurements, each using a different orientation of the tensioning device.

SECONDARY AND TERTIARY PROTEIN STRUCTURES PREDICTION WITH AN INTEGRATED COMPUTATIONAL APPROACH CONSISTING OF ARTIFICIAL INTELLIGENCE, NEURAL NETWORKS, AND MODELING TECHNIQUES
Steven B. Fairchild

SECONDARY AND TERTIARY PROTEIN STRUCTURE PREDICTION WITH AN INTEGRATED COMPUTATIONAL APPROACH CONSISTING OF ARTIFICIAL INTELLIGENCE, NEURAL NETWORKS, AND MODELING TECHNIQUES.

Steven B. Fairchild, Ronald Perrin, Ruth Pachter, Robert L. Crane, and W. Wade Adams, Wright Laboratory, Wright-Patterson AFB OH 45433.

An integrated computational approach consisting of artificial intelligence, neural networks, and modeling techniques for secondary and tertiary structure prediction is presented. An expert system is used to develop the training set consisting of specific protein structures obtained from the Brookhaven Protein Database, with the data files being preprocessed by a C-program that extracts the backbone atomic coordinates and calculates the appropriate torsion angles. The expert system determines the secondary structure by searching for sequential residues whose torsions fall within a user defined tolerance, classifying each residue in the file as an alpha-helix, appropriate beta-sheet, or coil region. Further, a neural network learns to predict secondary structural motifs and their folding for unsolved proteins. Specifically, a C-program is used to examine the training of the neural network by utilizing a sliding window technique for creating the input. A fully integrated application is then applied, developed using Hypercard on the Macintosh. Thus, the end user has an application that allows prediction of the secondary structure of a specific amino acid sequence.

Moreover, a distance matrix that detects spatial proximity of C_α carbon atoms is defined, with an associated uncertainty based on the homology considerations. Thereafter, the Double-Iterated Kalman filter method is employed in order to determine the initial fold of the protein. Indeed, this novel method is well suited for such an application, since it takes into account the structural uncertainty of the distance data, as well as being carried out at the C_α level of approximation. Further refinement is achieved by using molecular dynamics calculations at full atomic detail. Hence, tertiary protein structure prediction can be achieved, in part, by using this integrated approach.

INTERMOLECULAR TWIST DEFECTS IN EXTENDED-CHAIN POLYMERS

Dr. David C. Martin

Intermolecular Twist Defects in Extended-Chain Polymers

March 27, 1992

submitted to:

Macromolecules

David C. Martin

Materials Science and Engineering
The University of Michigan
2022 H. H. Dow Building
Ann Arbor, MI 48109-2136

ABSTRACT

We introduce here the geometry and general properties of a structural defect in extended-chain polymer fibers: intermolecular twist defects. These point defects are conceived as a local twisting of two polymer molecules about one another in the solid-state. The structure and impact on mechanical properties of intermolecular twist defects in extended-chain polymer solids were explored using molecular mechanics (PolyGraf and CERIUS software packages on a Silicon Graphics 4D25G Workstation). The intermolecular twist defects were topologically entrapped in the molecular simulation by first creating a two-chain unit cell under triply-periodic boundary conditions and then connecting the tail of chain one to the head of chain two and vice versa. The distance between defects (the reciprocal of which is the defect density) was systematically varied by increasing the length of the unit cell in the chain direction. The characteristics of these intermolecular twist defects were then examined for a particularly important extended-chain polymer system: poly(para-phenylene benzobisoxazole) (PBZO). Our results indicate that for PBZO the internal energy of these defects is approximately 100 kcal/mole, primarily due to an increase in the energy of bond torsions. We also obtain an estimate of the change in modulus of PBZO fibers as a function of the twist defect density: introducing one defect at every lattice site causes a reduction in the theoretical modulus by a factor of approximately two. Other salient features of these defects such as the distinction between left and right handedness, mechanisms for motion, and influence on slip behavior are also discussed. We finally interpret these results with a constitutive relationship derived from the elastic analysis of twisted wire rope.

INTRODUCTION

Certain polymer materials systems have a microstructure in which the chains exist in the solid-state in a fully extended conformation. These include the aromatic polyamides such as poly(paraphenylene terepthalamide) (PPTA); the rigid-rod polymers poly(paraphenylene benzobisthiazole) (PBZT) and poly(paraphenylene benzobisoxazole) (PBZO); gel-spun polyethylene (PE); and solid-state polymerized poly(diacetylenes). Fibers prepared from extended-chain polymers typically have high strength ($\sigma_t \sim 4$ GPa) and stiffness ($E_t \sim 400$ GPa), and have therefore found widespread interest for lightweight, high performance structural applications.

The microstructure of extended-chain polymers has been the subject of intense interest and has been reviewed elsewhere[1]. Studies of PBZO microstructure by High Resolution Electron Microscopy have revealed the evolution of local molecular structure as a function of processing condition[2]. While the details of microstructural organization of extended-chain polymers are now better understood, there is still a need to use this information to develop better constitutive models for characterizing macroscopic materials properties. This would make it possible to further optimize processing conditions to obtain ultimate properties and to design and synthesize new polymer materials for improved mechanical performance.

Theoretical studies of isolated, extended polymer chains have now been accomplished in some detail. Initially, information such as the theoretical tensile modulus and details about molecular-scale deformation were obtained[3]. More recently it has been possible to model the entire stress-

265

strain response[4]. Although the analysis of individual molecules is an important first step in understanding the behavior of polymer solids, there are legitimate concerns about how to relate these studies to systems in the condensed state that contain different sorts of structural defects. There is now a need to identify and isolate these defects to assess their impact on macroscopic properties.

Several single-chain defects in polymer crystals have been described by Reneker and Mazur[5]. Molecular mechanics simulations of chain defects in extended-chain polyethylene led van der Werff et al.[6] to conclude that the critical defects were taut tie molecules and entanglements in amorphous domains. Noid et al. simulated the dynamics of internal chain twists in poly(ethylene) crystals, but did not allow the chains to twist with each other[7].

It is reasonable to presume that the understanding of the microscopic origin of macroscopic extended-chain polymer properties would benefit from molecular simulations in which the defects involve more than one chain. Here, we introduce and analyze a multiple-chain defect we suspect should play an important role in extended chain polymers: intermolecular twist defects. These defects are conceived as a local twisting of two chains about one another. Apparently these twists represent local "physical entanglements" between the two chains.

The intent of this paper is to introduce the geometry of these defects, describe the procedures used to analyze the salient features of the defects, and then discuss the implications of these calculations. In particular, we describe physical situations in which these sorts of defects should play an important or

predominant role in determining macroscopic properties of extended-chain polymer fibers. We show how to calculate the energy required to form a twist defect (for PBZO, appx. 100 kcal/mole), and demonstrate how to determine the effect of twist defect density on the theoretical modulus. For PBZO, having one twist defect at every lattice site causes a reduction in the tensile modulus by a factor of approximately two. Future studies will be necessary to fully determine the validity and applicability of these theoretical assertions, and to address how the behavior of these twist defects changes from one polymer materials system to another.

PROCEDURE

The simulations presented in this work were generated using the PolyGraf and CERIUS software packages which are both commercially available from Polygen / Molecular Simulations Inc. These software packages have been used with reasonable success to simulate the structure and properties of extended-chain polymers[8]. A significant advantage that both of these simulation packages possess is the ability to analyze the energy of the molecules under triply-periodic boundary conditions. This analysis follows an Ewald sum approach where the energy of the crystal is calculated by taking a Fourier transform of the structure and summing over each reciprocal lattice site[9]. Most of the simulations reported here were performed in PolyGraf, using the Fletcher-Powell minimization scheme with a gradient convergence criterion of 0.1 kcal/mole. The Fletcher-Powell scheme seemed to give a faster, more reproducible means for obtaining a minimum than the conjugate gradient technique. Convergence of the model was usually

achieved in approximately 500 steps, which could amount to 12 hours of computer time or more on a Silicon Graphics 4D25G workstation.

The energies in PolyGraf were calculated using the Dreiding II parameters[10]. Specifically, the Dreiding II scheme uses the following potentials: for bond stretching, harmonic; bond angles, simple harmonic; bond torsions, cosine expansion; bond inversions, umbrella; van der Waals, Lennard-Jones 12-6; and hydrogen bonds, Lennard-Jones 12-10.

PBZO CRYSTAL STRUCTURE

Before proceeding with an analysis of defects in PBZO, it was first necessary to resolve some outstanding questions about the structure of crystalline PBZO itself. By Wide Angle X-ray Scattering (WAXS), Fratini and Adams have determined the structure of PBZO to be monoclinic, with unit cell parameters (a=1.120, b=0.3540, c=1.2050, α=90, β=90, γ=101.3 degrees)[11]. The microstructure of PBZO as a function of processing was studied by WAXS, Selected Area Electron Diffraction (SAED), Bright and Dark Field Transmission Electron Microscopy (BF and DF TEM), and High Resolution Electron Microscopy (HREM) by Martin and Thomas[2]. These authors demonstrated that it was necessary to consider a random +/- 1/4 c shift of laterally associated PBZO chains to obtain a structural model consistent with the available experimental data.

To construct the PBZO crystal two monomer units of PBZO (Figure 1) were created using the "draw" facility in PolyGraf. These two units were

terminated with hydrogen atoms, minimized in energy, oriented parallel to one another, and then placed in a periodic unit cell. Both monomers were "polymerized" by extending the system, removing the terminal hydrogen atoms, and connecting the head of each monomer unit to the image of its own tail in the neighboring unit cell. The polymer molecules so obtained were allowed to minimize their energy within this unit cell. At the start of the simulation there was no axial shift between the PBZO molecules. All the internal coordinates of the atoms as well as the unit cell parameters were allowed to be variable.

Figure 2 shows the minimum energy configuration of crystalline PBZO achieved by this approach. As predicted by experiment[2], the molecules adopt a local packing in which laterally associated neighboring molecules are displaced by + or - 1/4 c with respect to one another. From the view down the chain axis it is evident that the benzene ring and heterocyclic group are nearly coplanar, a result consistent with studies of isolated chains[3]. The unit cell parameters at the apparent minimum (a=1.0696, b=0.3684, c=1.2158 nms, α=90.001, β=90.672 γ=85.677 degrees) are in reasonable but not exact agreement with the experimental results of Fratini and Adams[11]. The angle between the direction normal to the PBZO benzene ring (and heterocyclic group) and the a axis is approximately 64 degrees. Figure 3 is a magnified view of the minimum energy configuration of the PBZO crystal viewed along the [010] direction. The benzene ring on a given PBZO chain fits into a space between the benzene ring and heterocyclic group on a neighboring chain.

Figure 4 shows the energy of the PBZO crystal as a function of the axial shift of the second PBZO molecule, calculated using the CERIUS software

package. There are predominant minima at relative positions of approximately +/- 1/4 c between molecules. The maximum energy (150 kcal/mole above the minimum) occurs when the PBZO molecules are both placed at the same position (i.e., with all the benzene rings and heterocycles arranged in planes strictly perpendicular to the chain axis). This energy barrier is significantly higher than that estimated from early studies of PBZO interactions (3 kcal/mole)[12]. However, these initial approaches only considered single-neighbor interactions between chains, not a triply-periodic unit cell.

The tensile modulus of PBZO was calculated by applying a stress in the chain direction and allowing the molecules to reequilibrate. By measuring the increase in the unit cell size caused by this deformation we obtained a value of 511 GPa for the theoretical tensile modulus of perfectly crystalline PBZO. This value compares reasonably well with previous theoretical results by Tashiro and Kobayashi (460 GPa)[13,14]. Weirshke[3] and Adams et. al.[4] obtained a value of 730 GPa using AM1 calculations on isolated molecules.

INTERMOLECULAR TWIST DEFECTS

A schematic diagram of an intermolecular twist defect is shown in Figure 5. To introduce the defects, a two chain unit cell was constructed using the energy minimized structure for the perfect crystal. The two chains were both cleaved at the single bond between the benzene ring and the heterocyclic group. The end of chain (1) was then attached to the head of chain (2) and vice versa. This procedure introduces a topologically trapped twist that

cannot escape because of the three-dimensional nature of the periodic boundary conditions. Both left and right handed examples of these twist defects are possible, although because of the symmetry of the PBZO molecule these do not differ significantly in this instance. However, with molecules that adopt helices with specific handedness this will become an important distinction. Also, it will be necessary to consider handedness in the analysis of defect-defect interactions.

The ability to change the length of the simulation in the chain direction makes it possible to systematically alter the effective density of the twist defects. As the length of the unit cell of the simulation increases, the twist defect density decreases. Since there is one twist defect in the simulation the reciprocal of the simulation length (defects per unit cell) is the defect density.

Figures 6 and 7 illustrate the structural changes introduced as a function of twist defect density. Figure 6 shows the minimized configuration with one twist defect per unit cell. The primary area of torsional deformation is the carbon-carbon single bond connecting the benzene ring to the heterocyclic group. Figure 7 shows the geometry of the twisted PBZO molecules after energy minimization with four unit cells in the chain direction. This corresponds to a twist defect density of 0.25 per lattice site. As the defect density decreases, the defects begin to adopt a configuration in which they are arranged in planes whose normals make a significant angle to the primary orientation axis. This is evidently because the twist defects introduce a local expansion of the crystal lattice and therefore have an unfavorable energy of interaction with one another.

It is possible to analyze the changes introduced into the PBZO molecules during twisting in detail. Figures 8 to 10 illustrate the variation of several important geometric parameters as a function of twist defect density. As the molecules become more twisted there is a systematic decrease in the length of the c-axis repeat distance (Figure 8). It is also possible to measure the local misorientation of the chain axis with respect to the primary axis of orientation (Figure 9). As expected, the misorientation systematically increases with twist defect density. The twisted simulations have a theoretical density on the order of 1.45 gms/cm^3 as compared to 1.63 gms/cm^3 for the perfect PBZO crystal (Figure 10). This density decrease occurs even for small twist defect densities. At the highest defect density the theoretical density begins to increase, perhaps due to local accomodations in chain packing from the shape of the PBZO molecule.

Figure 11 illustrates the change in the energy of the twisted simulations as a function of defect density. The primary source of the increase in energy during twisting comes from the energy of bond angle torsions. For PBZO, the increase in energy required to introduce one twist defect at every unit cell position is approximately 100 kcal/mole.

A central issue was to determine is the influence of these twist defects on mechanical properties. To accomplish this we examined the molecules under an applied stress in the chain direction. Figure 12 shows the change in the energetics of untwisted PBZO molecules as a function of tensile stress. The primary contribution to the tensile response arises from an increase in the energy of bond angle stretching and bending. In compression the increase

in energy is due to non-bonded van der Waals interactions. For comparison Figure 13 shows the energetic response as a function of stress for the simulation with one twist defect per lattice site. As before, the response in tension arises primarily from the energies of bond angle stretching and bending. However, the compressive response now has a significant contribution not just from van der Waals forces but also from an increase in the energy of bond torsions.

It is worth emphasizing that neither of these fully dense simulations (perfect PBZO crystals or perfect twisted PBZO crystals) show a compressive instability at ~0.4 GPa as seen in simulations of isolated chains and in experiment. This suggests that local fluctuations in density are particularly important for initiating compressive failure. This is an important issue which we address in more detail in the discussion.

Figure 14 shows the variation in the repeat distance along the chain axis as a function of applied stress and defect density. The slopes of these lines correspond to the tensile modulus. It is evident that as the chain axis repeat decreases (i.e., the twist density increases) the modulus systematically decreases. Figure 15 shows the tensile modulus as a function of twist defect density showing this decrease in modulus with increased twisting. The simulations predict that if there were one twist defect at every lattice site, the theoretical modulus of PBZO would decrease by a factor of approximately two.

DISCUSSION

Extended-chain polymers like PPTA and PBZO are processed from a nematic lyotropic liquid crystalline solutions in a dry-jet wet spinning process. The solutions usually employ a strong acid to dissolve the polymer. The fibers are formed by quenching the solution in a bath of non-solvent (typically water). This phase transition causes the formation of a continuous microfibrillar network[15] which is dried and heat treated under tension to optimize strength and stiffness[16]. It is reasonable to expect that intermolecular twist defects would be formed as the polymer passes through the phase transition from lyotropic liquid crystalline solution to solid polymer fiber. In practice, the defects would not strictly involve two unique chains twisting about one another, but instead would be randomly distributed from chain to chain. In this manner, one chain may be twisted with several of its neighbors.

The post-spinning heat treatment procedure causes local areas of crystallinity to develop, the dimensions of which (20 nm) which are well below the average dimensions of the polymer molecules themselves (100 nm). This means that as the lateral order between molecules increases during annealing, it is likely that intermolecular twist defects could be trapped into regions between two crystallites. Since the defects cause a local variation in density, regular modes of defect segregation into grain boundaries could result in crystallites with well defined shapes, and therefore these materials would exhibit characteristic and unique Small Angle X-ray Scattering (SAXS) patterns. This proposed segregation of twist defects forms the basis of Axial Chain Invariant (ACI) grain boundaries, using the

nomenclature suggested by Martin and Thomas[17]. Experimental evidence for ACI boundaries have been obtained in HREM images of PBZT[18] and PBZO[2,17]. Similar suggestions about twist defect segregation to grain boundaries have been presented by Reneker and Mazur[5].

With this mechanism of twist defect generation in mind, it is reasonable to expect to see twist defects in extended-chain polymers processed from solution or from the gel state (i.e., in PPTA, PBZT, PBZO, and PE). Our research group is currently involved in studies of solid-state polymerizable diacetylenes in order to isolate the impact of specific defects on local structural variations and macroscopic properties. Our goal is to systematically introduce grain boundary defects into ordered polymer systems in a well controlled and reproducible manner.

It is possible to reconsider information in the literature concerning the structure and properties of extended-chain polymers in terms of this twist defect model. For example, Prasad and Grubb have examined the (002) reflection in extended-chain polyethylene by synchrotron X-ray scattering and found that the peak shifts to lower angle and broadens under tension[19]. They interpeted these results in terms of a distribution in "stressed state" for the chains in an extended-chain sample. In other words, this result suggests that certain chains are more "twisted" than others.

A critical comparison of the results of these simulations with experiment reveals that twist defects alone do not provide a complete picture of the polymer solid state. In extended-chain polymer fibers the density is reasonably close to that of the perfect crystal, and the amount of

misorientation is small[1,2]. If we assume that the density of the fiber is 1.5 gms/cm^3 and the amount of misorientation 2.0 degrees, it is possible to estimate the effective number of twist defects by comparison with Figures 9 and 10. It is evident that the effective twist defect density in this case would be less than 1/20 twists/unit cell. Therefore, in order to fully account for the experimentally observed variations in modulus during post-spinning processing[16], it seems necessary to consider additional types of structural defects.

An inevitable source of defects in any polymer with finite molecular weight are chain ends. Martin and Thomas showed evidence for an edge dislocation which was rationalized as arising from the mutual segregation of a number of chain ends of like sign[2]. However the concentration of these should not change as a function of processing, although their relative position may change. Smith and Termonia examined chain ends using a kinetic model and predicted that both the strength and modulus decreased with increasing number of chain ends, although the strength was much more sensitive to the chain end density[20]. Further simulations on the effect of chain ends are certainly warranted, and we are proceeding in this direction in our laboratory at present. We believe that a similar scaling approach should enable us to examine the transfer of stress from chain to chain through non-bonded interactions.

As we discussed earlier, these systems do not exhibit the experimentally observed compressive instability associated with kinking, although compressive instabilities are seen in isolated chain simulations[3,4]. This observation suggests that it is important to consider the influence of

local density fluctuations. To address the impact of local heterogeneities in molecular packing it should be possible to use an analysis in which the unit cell dimensions are varied in both the **a** and **b** directions. Recent results on poly(diacetylene) crystals with significant void content have shown that kinking is sensitive to the local density[21]; regions where the poly(diacetylene) crystals are below some apparently critical density do not exhibit kinking at all, while the denser poly(diacetylene) crystals kink relatively often.

It is evident that intermolecular twist defects should disrupt the uniformity of strain during shear deformation. Because of the presence of the physical entanglement of the two chains, it will no longer be possible to develop a shear strain between them. Therefore, twist defects will disrupt the uniformity of shear deformation. The heterogeneity of deformation within sheared regions inside kink bands in extended-chain polymer fibers has been observed experimentally[22]. Since twists lead to lateral interactions between chains, they should also be important in creep and long term fatigue response.

It is possible to envision other types of defects constructed from assemblies of these and other defects. These might include chain-end dislocations, kinks, and other sorts of grain boundaries involving both tilt and twist. Reneker and Mazur have described the structure and energetic features of defects in crystalline poly(ethylene)[5], but it has not yet been possible to use this information to derive constitutive relationships to understand or predict materials properties. To do this task properly will require significantly more atoms per unit cell and a corresponding increase in the computational time required for each simulation.

Figure 15 indicates that the density of twist defects in PBZO must be relatively large before there is a significant reduction in tensile modulus. As discussed earlier, a more complete description of the microstructure of extended-chain polymers will require an analysis of additional defects; in particular chain ends and voids. Nevertheless, this result also suggests that efforts to manipulate microstructure by materials processing (i.e, changing the defect density) may only lead to a secondary effect on the ultimate mechanical properties of the polymer. It is reasonable to expect that much more significant changes in performance could occur by creatively altering the chemical structure of the molecules themselves. Current efforts in this direction include the synthesis of ladder polymers from soluable precursor polymers, and small, highly reactive crosslinkable groups which do not disrupt processing but can introduce lateral covalent bonds during a post-spinning thermal treatment[23].

Intermolecular twist defects are point defects which are apparently unique to macromolecular solids. Certain salient features which become evident after analyzing the geometry of the defects are worthy of further discussion. For example, consider first the highly anisotropic mobility of the twist defects. Because of the manner in which the two chains twist around one another, defect motion will be strictly limited to the direction of the chain axis if no covalent bonds are broken. Another topic worthy of further discussion and study are the mechanisms of defect annhilation. Annhiliation is possible when a left-handed twist runs into a right-handed twist on the same two chains. Also, the twist may annhilate when it encounters a chain end. Finally, one might speculate on the possibility of

twist defect sources. It is difficult to envision a means for introducing these twists defects after the molecules have been processed from the liquid crystalline mesophase. However, it might at least be feasible to design special processing routes which optimize the density of twist defects. It is not yet clear that twist defects are always to be removed or avoided, and perhaps some careful consideration about how to control them would provide a means for further optimizing the mechanical response of extended-chain polymers. For example, increasing the density of twist defects could lead to improved fiber toughness and creep resistance.

CONSTITUTIVE ANALYSIS

After considering the results of the simulations showing a decrease in the tensile modulus as a function of twisting, we examined the similarites of twisted, stiff molecules with the elasticity of twisted wire rope. The theory of wire rope has been the topic of a recent monograph by Costello[24]. Here, we demonstrate how this theory may be applied to intermolecular twist defects which are essentially two-wire ropes with no core wire. Using Costello's notation, for a wire rope constructed of an inner wire of radius R_1 surrounded by helical wires of radius R_2 twisted at a helix angle α, the amount of strain ε in the rope induced by an applied load is given by:

$$\varepsilon = \xi_1 = \xi_2 + \Delta\alpha/\tan\alpha$$

(1)

where ξ_1 is the strain in the inner wire, ξ_2 is the strain of an outer wire and $\Delta\alpha$ is the change in α after loading. It is assumed that $\Delta\alpha$ is a small quantity. The rotational strain β_2 in a outer wire is given by:

$$\beta_2 = \xi_2/\tan\alpha - \Delta\alpha + v\,(R_1\xi_1 + R_2\xi_2)/((R_1 + R_2)\tan\alpha)$$

(2)

where v is the Poisson's ratio of the wire strands. The modulus of a wire strand is:

$$Eo = S/\xi_2$$

(3)

where S is the applied stress. Likewise, the modulus of the wire rope is

$$E = S/\varepsilon$$

(4)

In our case, $R_1=0$, (there is no center wire). We also assume that since the two wires are equivalent, there is no net rotational strain (i.e., $\beta_2=0$). Using these boundary conditions and simplifying, we find:

$$\xi_2/\varepsilon = E/Eo = 1/(1 + (1+v)/\tan^2\alpha)$$

(5)

Here, E is the modulus of the twisted bundle, Eo is the untwisted reference state, α is the angle of twist, and v is Poisson's ratio. Figure 16 shows the comparison of this equation with the twisted PBZO simulations. The best fit to the simulation results requires a value of v equal to 2.0. This is remarkable, since values of v greater than 0.5 require the system to increase in density under stress. However, this is precisely the situation at hand. When

molecules twist about one another, pulling on the chains causes them to be forced closer together laterally. This is similar to the response of a twisted multi-stranded rope, or the familiar "finger torture" device that holds on more tightly as the victim attempts to escape.

Figure 17 shows the variation in density of the simulations as a function of stress and twist defect density. At the highest twist defect density examined (1.0 twists per cell), there is indeed an increase in density under stress. Although local increases in density might occur in real fibers due to this effect, it seems unlikely that a macroscopic Poission's ratio greater than 0.5 would ever be realized in practice due to the inevitable presence of heterogeneities of molecular packing over large length scales.

ACKNOWLEDGEMENTS

References

(1) Adams, W. W.; Eby, R. K.; McLemore, D.; eds;*The Materials Science and Engineering of Rigid Rod Polymers,*, Materials Research Society Symposia Proceedings, 134, 1989.

(2) Martin, D. C.; Thomas E. L. *Macromolecules* **1991**, 24(9), 2450-2460.

(3) Weirshke, S.; in *The Materials Science and Engineering of Rigid Rod Polymers*, Adams, W. W.; Eby, R. K.; McLemore, D.; eds; Materials Research Society Symposia Proceedings, 134, 1989.

(4) W. W. Adams, D. S. Dudis, S. G. Weirschke, P. D. Haaland, and J. R. Shoemaker, "Computational Predictions of Polymeric Single Chain Properties", in Deformation, Yield, and Fracture of Polymers, 8th International Conference, The Plastics and Rubber Institute, Churchill College, Cambridge, UK, 1991.

(5) Reneker, D.; and Mazur, J. *Polymer* **1988**, 29, 3.

(6) van der Werff, H.; van Duynen, P. T.; and Pennings, A. J. *Macromolecules* **1990**, 23, 2935-2940.

(7) Noid, D. W. ; Sumpter, B. G.; and Wunderlich, B. *Macromolecules* **1991**, 24, 4148-4151.

(8) Yang , X. ; and Hsu, S. L. *Macromolecules* **1991**, 24, 6680-6685.

(9) Karasawa, N.; and Goddard, W. A. *J. Phys. Chem.* **1989**, 93, 7320.

(10) Mayo, S. L. ; Olafson, B. D.; and Goddard W. A. *J. Phys. Chem.* **1990**, 94, 8897-8909.

(11) Fratini, A. V.; Lenhert, P. G.; Resch, T. J.; and Adams, W. W.; in*The Materials Science and Engineering of Rigid Rod Polymers,*, Adams, W. W.; Eby, R. K.; McLemore, D.; eds; Materials Research Society Symposia Proceedings, 134, 1989.

(12) Bhaumik, D.; Welsh, W. J.; Jaffe, H. H.; and Mark, J. E. *Macromolecules,* **1981**, 14, 951-953.

(13) Tashiro, K.; and Kobayashi, M.; *Sen-I Gakkaishi* **1986**, 62, 78-91.

(14) Tashiro, K.; and Kobayashi, M.; *Macromolecules* **1991**, 24, 3706-3708.

(15) Cohen, Y.; and Thomas, E. L. *Macromolecules* **1988**, 21, 43.

(16) Allen, S. R. ; Farris, R. J.; and Thomas, E. L. *J. Mat. Sci.* **1985**, 20, 2727-2734.

(17) Martin, D. C. and Thomas, E. L. *Phil. Mag.* **1991**, 64(4), 903-922.

(18) Boudet, A.; Martin, D. C.; and Thomas, E. L.; Proceedings of the European Symposium on Polymeric Materials, Lyon, France, 1987.

(19) Prasad, K.; and Grubb, D. T. *J. Poly. Sci.: B: Poly. Phys. Ed.,* **1990**, 28, 2199-2212.

(20) Smith, P.; and Termonia, Y. *Polymer Communications* **1989** 30, 66-68.

(21) Liao, J.; and Martin D. C., "Defects in [1,6-di(n-carbazolyl)-2,4-hexadiyne] Diacetylene Crystals", in*Electromagnetic and Optical Properties of the Organic Solid State*, Materials Research Society Symposia Proceedings, 1992.

(22) Martin, D. C.; and Thomas, E. L. *J. Mat. Sci.* **1991**, 26, 5171-5183.

(23) Walker, K.; Markoski, L.; Moore, J.; and Martin, D.; *Polymer Preprints,* 1992, in preparation.

(24) Costello, G. A. *Theory of Wire Rope,* Springer-Verlag, 1990.

Figures

Figure 1: Chemical structure of cis-PBZO.

Figure 2: Minimimum energy conformation of PBZO obtaining using a two-chain unit cell.

Figure 3: Close-up of minimum energy conformation. Lateral chains are displaced +/- 1/4 c with respect to one another.

Figure 4: Energy of the PBZO crystal as a function of axial shift in the c direction. Minima at positions of approximately +/- 1/4 c are indicated.

Figure 5: Schematic diagram of an intermolecular twist defect. The defects are created in the simulation by creating a two-chain unit cell and then breaking the chains. The chains are reconnected by joing the head of chain 1 to the tail of chain 2 and vice-versa.

Figure 6: Minimized configuration with one unit cell and one twist, corresponding to a twist density of one twist per unit cell. Most of the distortion of the molecule takes place in the single bond.

Figure 7: Minimized configuration with four unit cells and one twist, corresponding to a twist density of 1/4 twists per unit cell. As the defects move farther apart, they begin to line up into planes which are no longer perpendicular to the axis of orientation. This is apparently due to the fact that there is a unfavorable energy of interaction between the twist defects.

Figure 8: Length of the c-axis repeat distance as a function of twist defect density. As the amount of twisting increases, the c-axis repeat distance decreases.

Figure 9: Local misorientation of the PBZO chain as a function of defect density. As the amount of twisting increases, the misorientation increases.

Figure 10: Theoretical density as a function of twist defect density. The density drops from a value of 1.63 for the perfect PBZO crystal to a range of about 1.45 for the twist defects. At the highest degree of twist the density begins to increase again; the effect is probably due to the formation of local favorable packing contacts (Figure 6).

Figure 11: Relative energies of bond stretching, bond angle bending, bond inversions, bond torsions, and non-bonded interactions as a function of defect density. The primary contribution to the twist defect energy arises from the energy of bond torsions. The energetic penalty for introducing a twist defect at every lattice site in PBZO is 100 kcal/mole.

Figure 12: Relative energies of the untwisted PBZO molecule as a function of applied stress. In tension, the energetic contribution comes from bond stretching and bond angle bending. In compression, the energy of non-bonded van der Waals contacts increases.

Figure 13: Relative energies of the twisted PBZO molecule (1 twist/cell) as a function of applied stress. As before, the energetic contribution in tension comes from bond angle stretching and bond angle bending. However, in compression the response is due to both non-bonded interactions as well as the energy of bond torsions.

Figure 14: Change in c-axis repeat length as a function of applied stress and twist defect density. The slope of these lines corresponds to the theoretical tensile modulus. It can be seen that models with a higher twist defect density have a lower modulus. Also note that the models do not exhibit a compressive instability at stresses corresponding to the experimentallly observed compressive failure stress (~0.4 GPa).

Figure 15: Change in tensile modulus as a function of twist defect density. The theoretical modulus of the perfectly crystalline PBZO is similar in magnitude to that obtained by other studies. The twist defects cause a systematic decrease in the tensile modulus, with the tensile modulus of the sample with one twist per unit cell approximately half that of the perfect crystal.

Figure 16: From the results shown in Figures 8 and 15 it is possible to compare the results of the simulations with the elastic analysis of wire rope. The only adjustable parameter in this approach is the Poisson's ratio of the strand. In the figure several different choices for Poisson's ratio are shown. The best to the results of the simulation comes from a Poisson's ration equal to 2.0. Values of Poisson's ratio greater than 2.0 are peculiar, and indicate that the sample is capable of increasing its density during stress.

Figure 17: Density of twisted PBZO as a function of twist defect density and applied stress. The sample with the highest density of twist defects increases in density under stress, as predicted by the elastic analysis results. The phenomena is evidently related to the increased "packing" which is promoted by additional stress when there is a sufficient amount of twisting present.

PBZO

INTERMOLECULAR TWIST DEFECTS

IN EXTENDED-CHAIN POLYMER FIBERS

David C. Martin

Materials Science and Engineering

The University of Michigan

High-modulus–high-strength. poly-(p-phenylene benzobisthiazole) fibres

Part 1 *Heat treatment processing*

S. R. ALLEN,* R. J. FARRIS, E. L. THOMAS
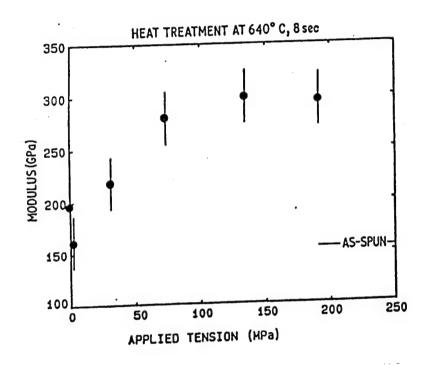*Polymer Science and Engineering Department, University of Massachusetts, Amherst, Massachusetts 01003, USA*
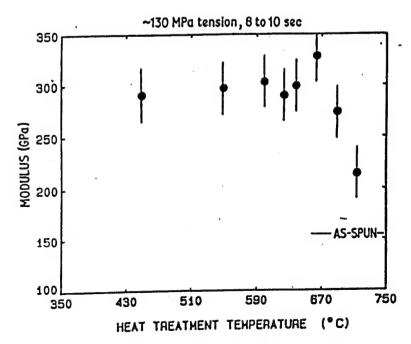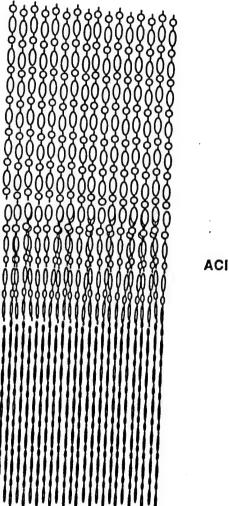
Figure 4 Modulus of 640° C, 8 sec tensioned heat-treated fibres.

Figure 5 Heat-treated fibre modulus for various heat treatment temperatures (8 to 10 sec residence time, ~ 130 MPa tension).

288

0.55 nm

0.35 nm

289

Fig. 12

ACl

Molecular interpretation of fig. 11 showing the two crystallites in axial registry with one crystallite oriented so the molecules are seen 'edge-to-edge' and the other 'face-to-face'. The axial width of the boundary is in the order of 5 nm, which is about ten times larger than is typical for most metallic and inorganic crystals. This is apparently due to the packing problems within the boundary imposed by the stiffness and chain connectivity of the long (100 nm) polymer molecules.

axial
5 nm
tion.

work on the twist boundaries in crystalline polyethylene. similar hydrocarbon parameters based on set IV of Ref. 10 were employed. In the current calculations the data from Kobayashi, Tashiro and Tadokoro[11] were employed for the intramolecular valence force constants. These constants are for interactions for bonded atoms and for atoms bonded to a common atom. For the torsional coordinates, a slightly higher value was used. which corresponds to a torsion barrier of 10.45 kJ mol⁻¹ and is the same value[6] used for polyethylene. In addition. the terminal atoms of a particular torsional coordinate are subject to non-bonded

TWIST BOUNDARY ENERGETICS

The oligomer selected for the computations is comprised of 21 carbon atoms, with a structure $CH_3(CF_2CH_2)_9CF_2CH_3$. The chain is packed in crystallographic register with lattice constants $a = 0.858$ nm. $b = 0.491$ nm. The planar zigzag segments are packed with their dipoles pointing along the b axis. The system includes a central chain. six neighbours which comprise the inner shell and 12 more distant neighbours. In order to minimize the packing energy of the entire
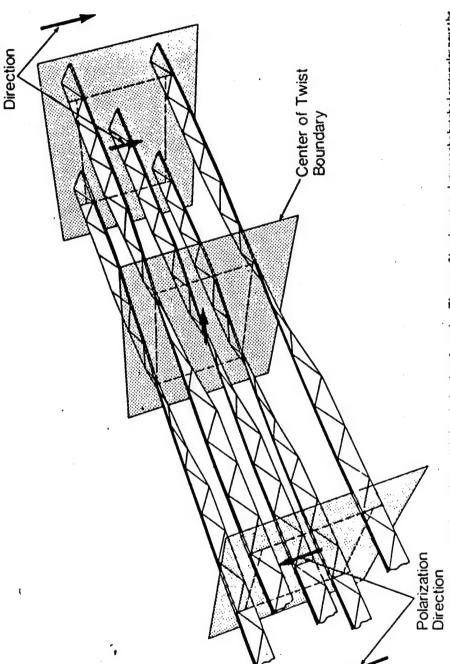
Figure 3 Twist boundaries in 5 chains are shown. with the calculated conformation. There are 21 carbon atoms between the hatched rectangles near the ends. The middle rectangle shows the location of the centre of the twist boundary. The polarization directions are shown by arrows. The direction of the dipole is reversed as the molecule passes through a twist boundary. When an external field is present. the total energy is lowered as the twist boundary moves in a direction that allows more of the dipoles attached to each molecule to align with the field

Polymer

PBZO

**poly(paraphenylene benzobisoxazole)   PBZO
rigid-rod**

**developed by WPAFB
under commercialization by Dow Chemical**

**solid-state structure studied in detail
(Martin and Thomas, 1991)**

Procedure

Molecular Mechanics:

PolyGraf by Molecular Simulations, Inc.

Dreiding II Force Field parameters

3-D Periodic boundary conditions

Fletcher-Powell minimization scheme

Silicon Graphics 4D25G, 16 MB memory

Dreiding II Parameters

Covalent Bonds	Harmonic
Bond Angles	Harmonic
Bond Torsions	Cosine Expansion
Inversions	Harmonic Umbrella
Van der Waals	Lennard-Jones 12-6
Hydrogen Bonds	Lennard-Jones 12-10
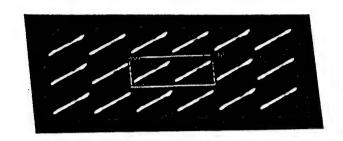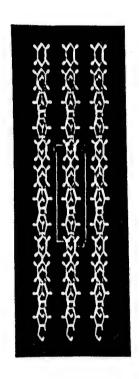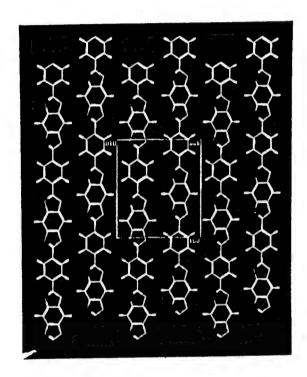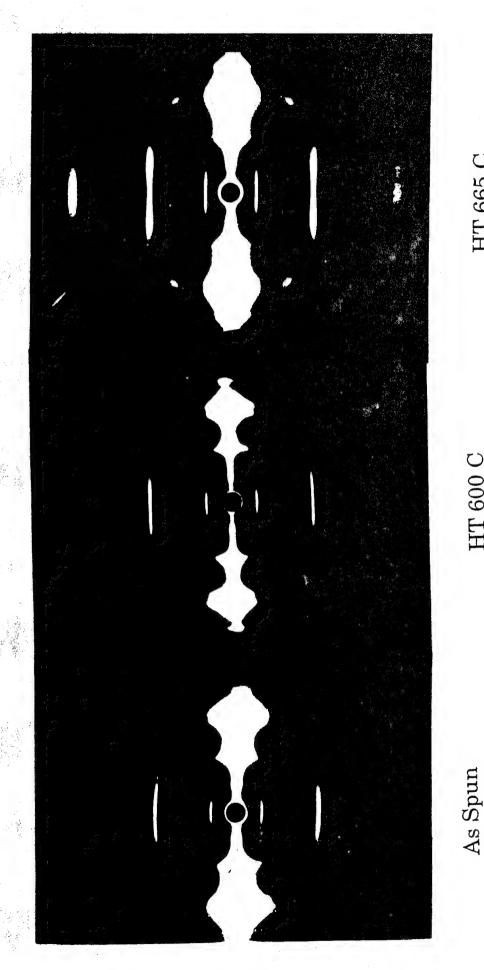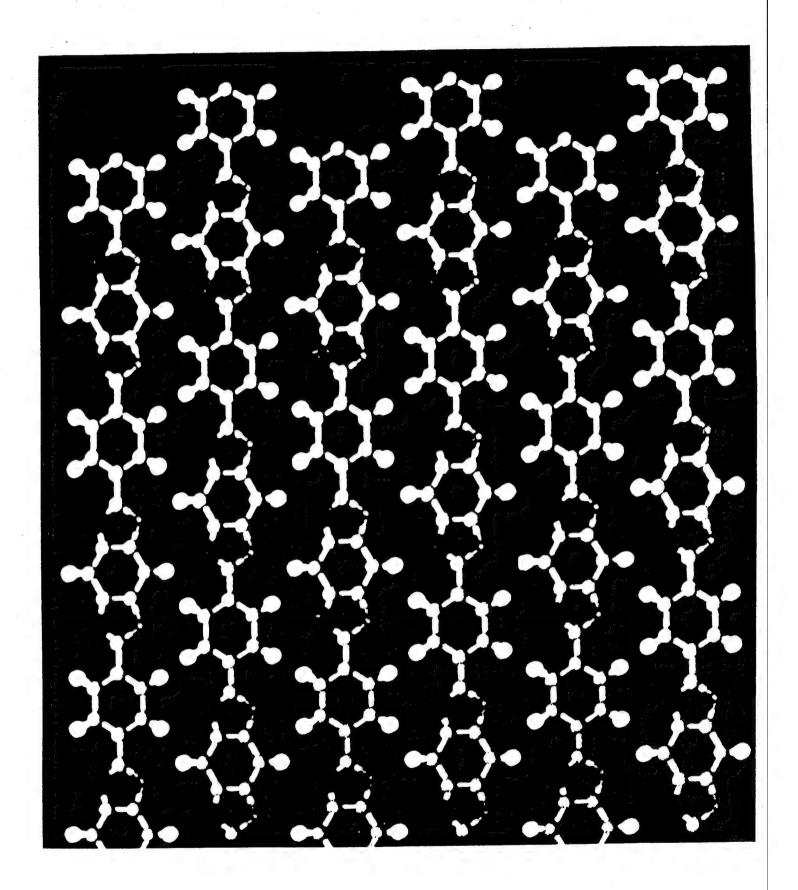
inifinite cells/twist

0 twists/cell

PBZO Wide Angle X-ray Scattering

As Spun　　　　　HT 600 C　　　　　HT 665 C

Energy of PBZO vs. axial shift

Energy (kcal/mole)
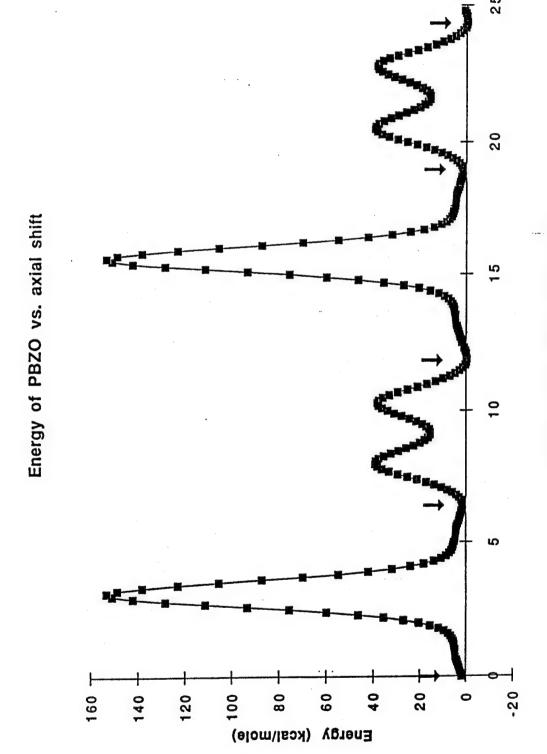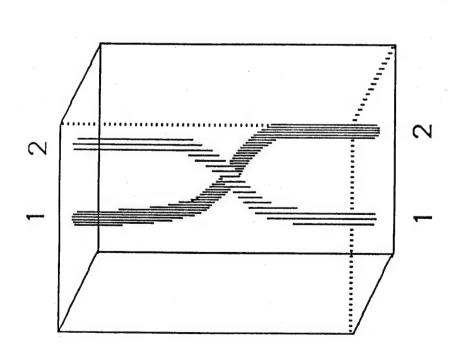
Relative Axial Shift (Angstroms)

Intermolecular Twist Defects

Use two chain unit cell

Connect tail of chain (1) to head of chain (2)

Introduces a topologically trapped defect
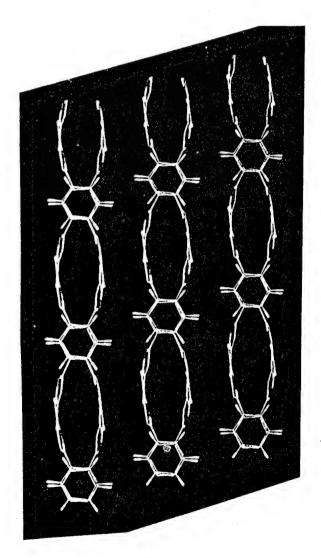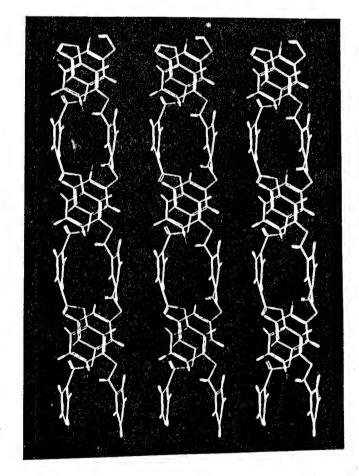
Both left and right handed examples exist

299

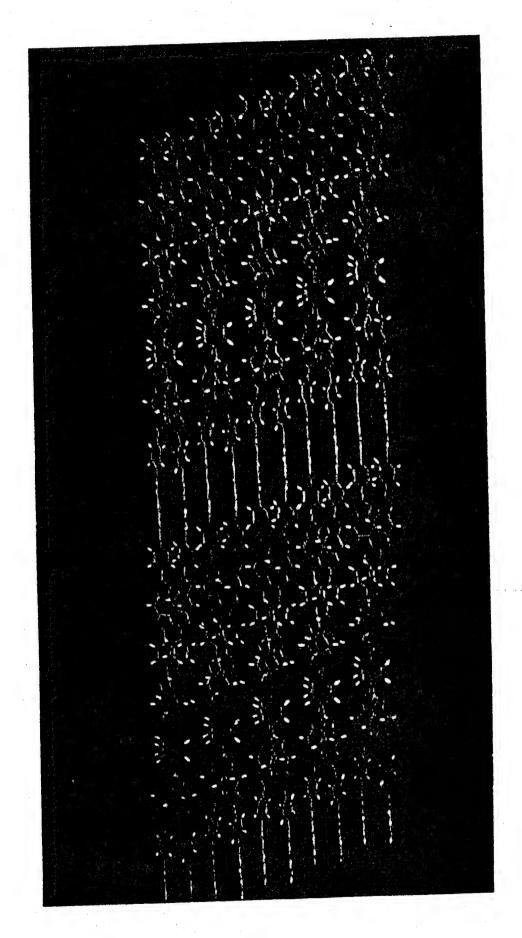| ∞ u.c. / twist | 4 u.c. / twist | 2 u.c. / twist | 1 u.c. / twist |
| 0 twist / u.c. | 1/4 twist / u.c. | 1/2 twist / u.c. | 1 twist / u.c. |
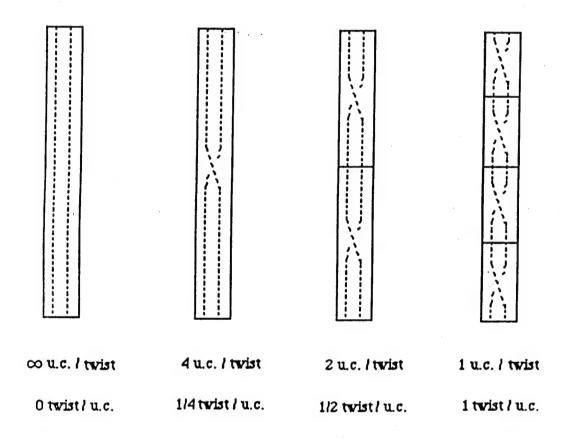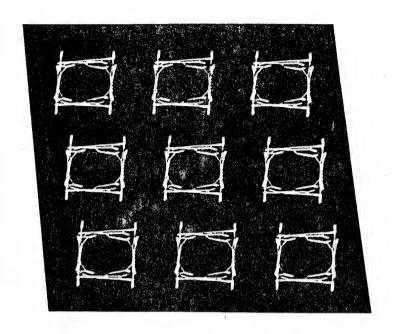
Figure 1: We have shown that it is possible to investigate intermolecular twist defects in extended polymer chains by creating a periodic two-chain simulation and connected the end of chain 1 to the head of chain 2 and vice versa. The defect density can be altered by increasing the length of simulation in the chain direction. As the number of unit cells per defect increases, the defect density decreases, eventually reaching the non-defective case as a limit.
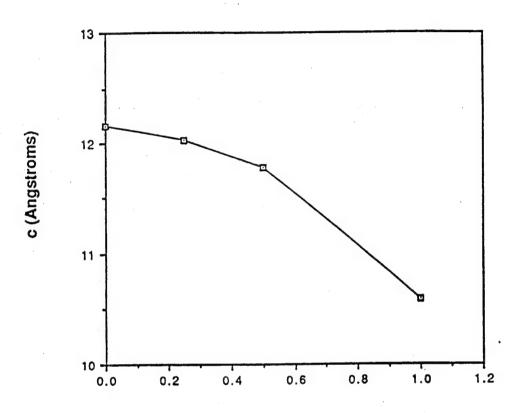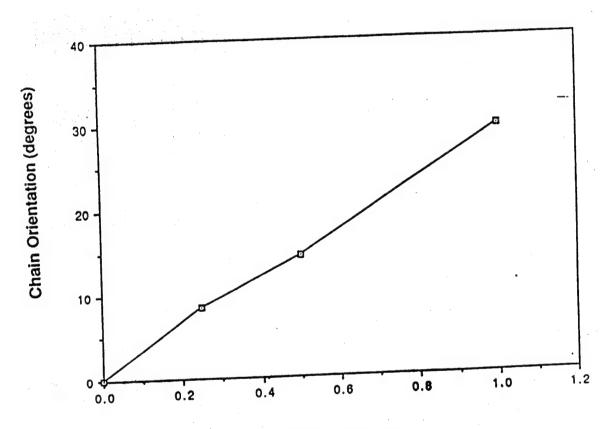
1 cells/twist

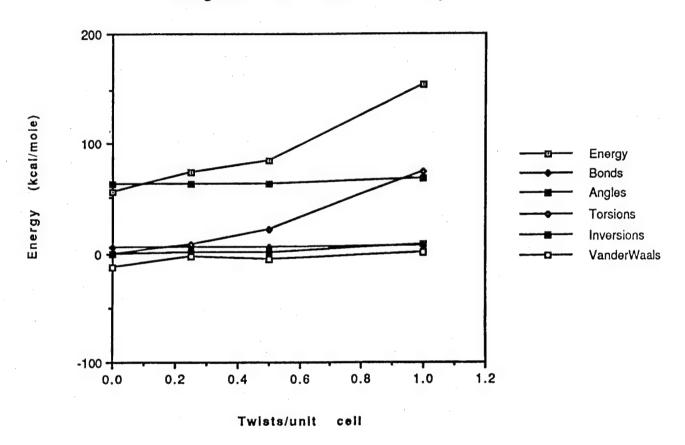1 twists/cell

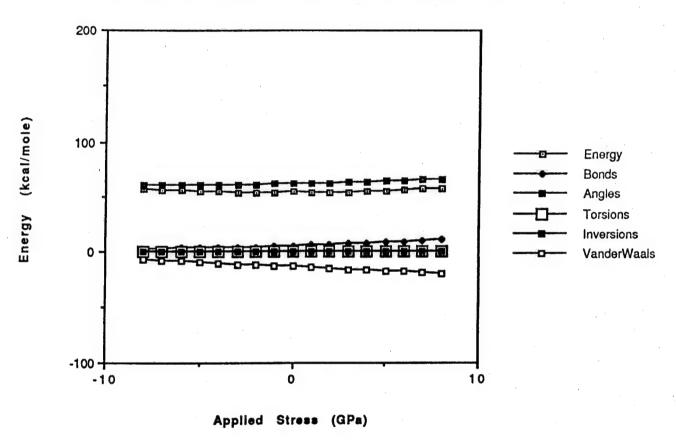# Axial Repeat Distance (c) vs. Twist Density

Chain Orientation vs. Twist Density

Energetics vs. Twist Density

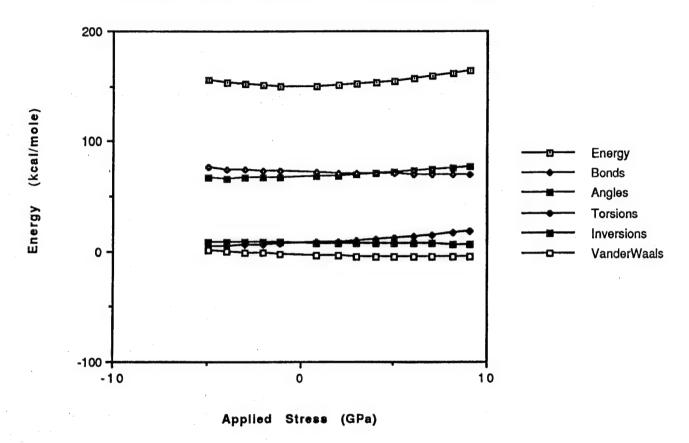

~100 kcal /mole; primarily from
bond torsions

Energy under stress: 0 twists/unit cell

Tension: bond angle stretching, bending
Compression: Van der Waals

306
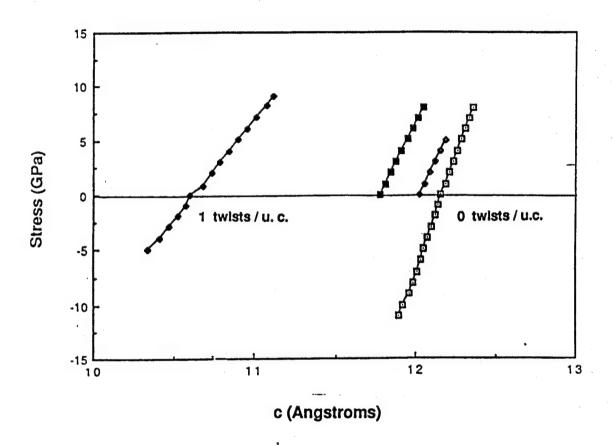
Energy under stress: 1 twists/unit cell
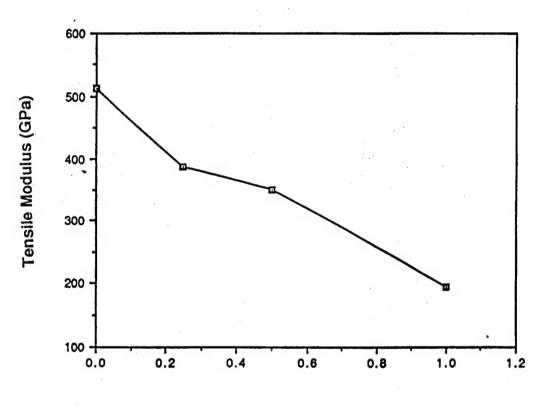
Tension: bond angle stretching, bending
Compression: Vander Waals, Torsions

Stress-Strain Response vs. Twist Density

Tensile Modulus vs. Twist Density

FIGURE 3.1. Loaded simple straight strand.
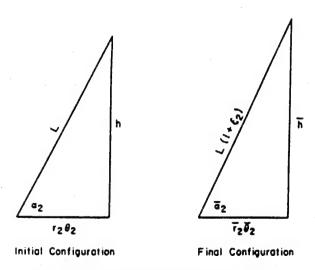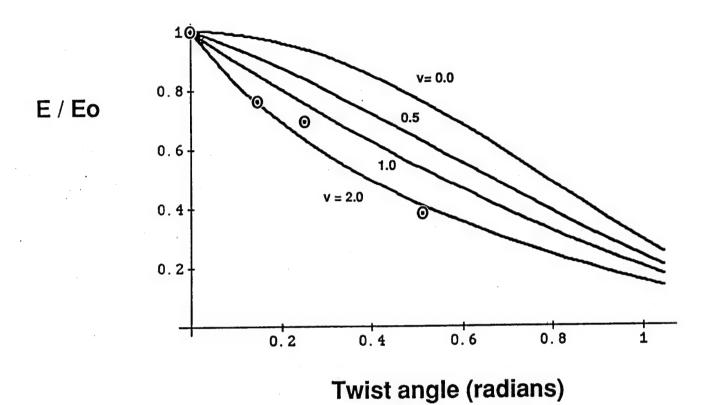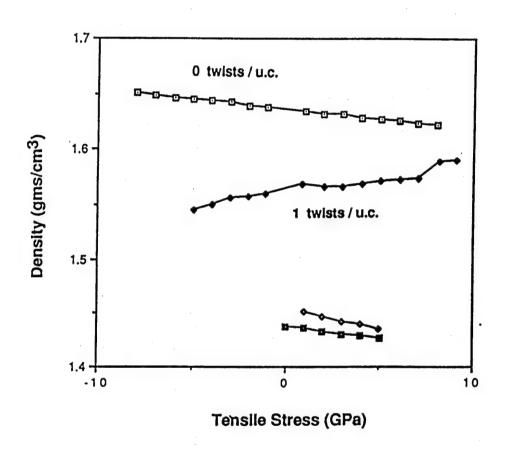
FIGURE 3.4. Developed view of outer wire centerline.

310

Twist angle (radians)

$$E/Eo = 1/(1+((1/Tan[alpha] + v)/Tan[alpha]))$$

George A. Costello, "Theory of Wire Rope", (1990).

Density vs. Tensile Stress

Summary

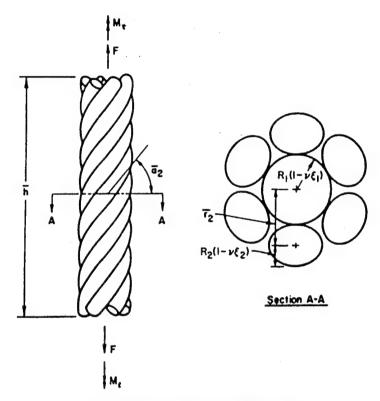- High molecular weight PPTA-co-XTA copolymers containing 0% to 100% XTA have been prepared.

- PPTA-co-XTA copolymers form lyotropic nematic solutions.

- PPTA-co-XTA copolymers are stable to the conditions currently used in dry-jet wet fiber spinning.

- PPTA-co-XTA copolymers can be thermally cross-linked in the temperature range 350-400°C. At low comonomer ratios of XTA, the cross-linked polymers swell reversibly in H_2SO_4.

- DSC data on model compounds suggests that reversible ring opening occurs in the temperature range 250-300°C. In the presence of a good dienophile, exothermic cross-linking also occurs in this temperature range. In the absence of a good dienophile, no cross-linking occurs until 350-425°C.

- Many new bis-substituted BCB monomers have been prepared. Their potential in high performance polymer networks is under investigation.

| ∞ u.c. / end | 4 u.c. / end | 2 u.c. / end | 1 u.c. / end |
| 0 end / u.c. | 1/4 end / u.c. | 1/2 end / u.c. | 1 end / u.c. |
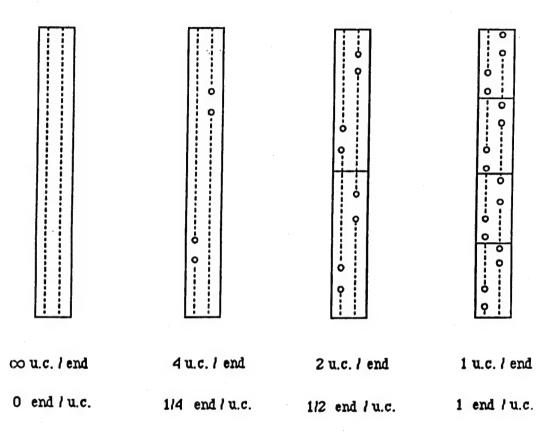
Figure 3: Proposed scheme for studying the influence of chain end defects. The route is similar to that used for investigating the twist defects. Here, it may be necessary to decrease the defect concentration enough to insure that it is possible for the molecules to interact with one another through frictional forces across their non-bonded lateral surfaces.
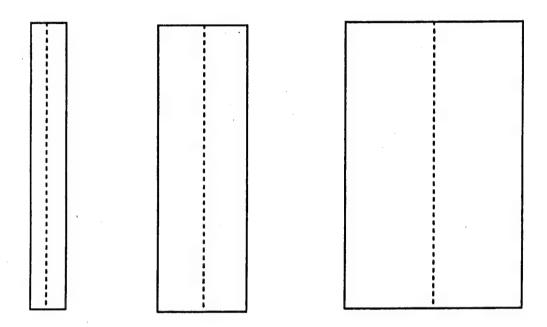
Figure 4: By increasing the distance between neighboring chains in either the a and b directions or both it will be possible to look at density fluctuations and the relative importance of face-to-face and side-to-side interactions. Also, it should be possible to reveal information about the onset of the compressive buckling instability thought to be involved in the initiation of kinking.

Extended Chain P _ mer   Physical Crosslinks   Chemical Crosslinks
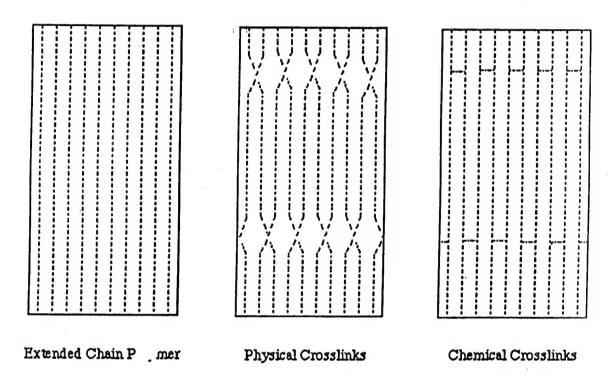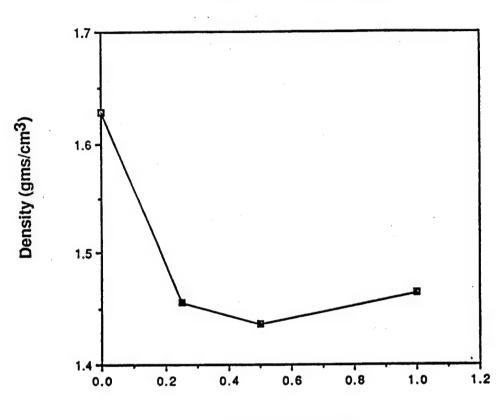
Figure 5: A current hy pothesis is that it should be possible to improve the compressive strength and creep properties of extended chain polymers by introducing lateral crosslinks. These crosslinks could be physical crosslinks (twists between chains) or chemical crosslinks due to reactive functionality on the chains. We intend to apply our methodology to both situations.

Density vs. Twist Density

Density (gms/cm³) vs. Twists / Unit Cell

XTA - A Versatile Comonomer for High Performance Polymer Networks

Kenneth A. Walker, Larry J. Markoski, Gary A. Deeter, Gary E. Spilman, David C. Martin, and Jeffrey S. Moore, The University of Michigan, Ann Arbor, MI 48109-1055

Terephthalic acid (TA) is widely used in a variety of high performance polymers (e.g. PET, PBO, PBZT, PPTA). We have recently developed a new comonomer, XTA, that is a cross-linkable substitute for TA. The cross-linking reaction is thermally triggered above 300°C and involves the highly reactive, o-quinodimethane intermediate. High molecular weight PPTA-co-XTA copolymers have been prepared and these polymers have been found to maintain the lyotropic ordering characteristics of PPTA in H_2SO_4. Thermally triggered network formation of these copolymers is currently under investigation. Model systems are also being studied to better understand the cross-linking chemistry. In addition to XTA, we have prepared several other cross-linkable monomers (e.g. **1-4**) that can be used in a wide range of high performance polymers (e.g. poly(arylketones), poly(carbonates), poly(urethanes)).
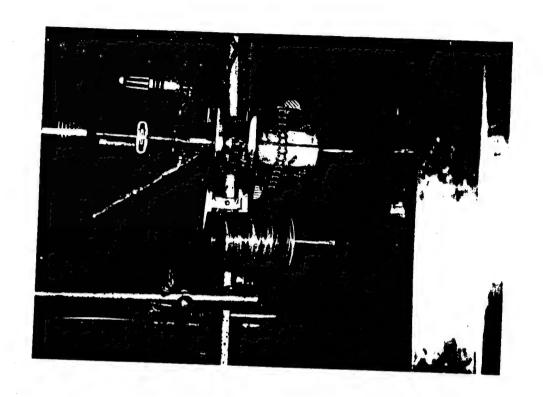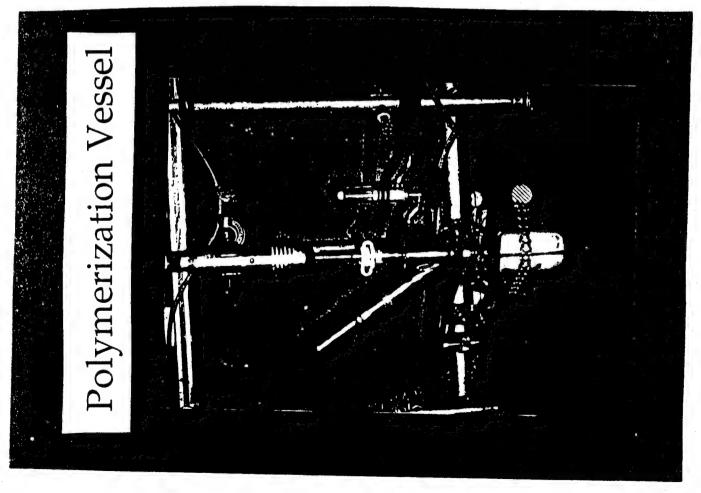
XTA

1

2

3

4

318
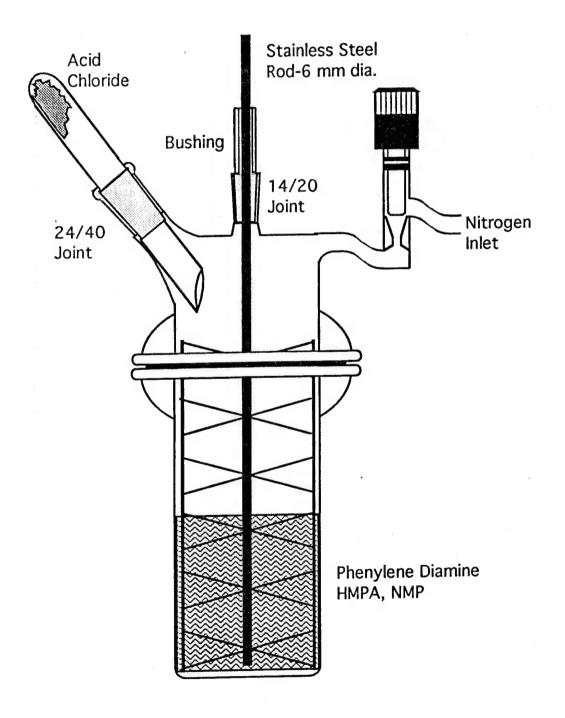
Crosslinkable monomers prepared from
3,6-Ditrimethylsilyl-1,2-Dihydrocyclobutabenzene

POTENTIAL POLYMERS FROM THESE MONOMERS
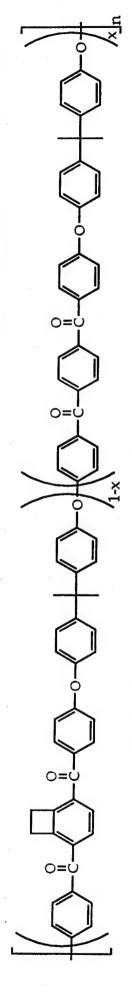
polycarbonates
polyamides
poly(aryl ketones)
polyesters
polyurethanes
polyimides
polybenzoxazoles
polybenzthiazoles
polybenzimidazoles...

Polymerization Vessel

Acid
Chloride

Stainless Steel
Rod-6 mm dia.

Bushing

14/20
Joint

24/40
Joint

Nitrogen
Inlet

Phenylene Diamine
HMPA, NMP
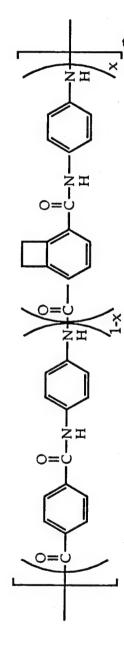
Polymers Prepared Incorporating Cyclobutabenzene Monomers

Polymer	x value	ΔH of Reaction (kcal/mol)	Average M.W. [a]
PEEKK	1	0	95,000
PEEKK	0.75	-6.98	85,000
PEEKK	0.5	-11.39	125,000
PEEKK	0	-23.93	90,000

[a] relative to polystyrene standards
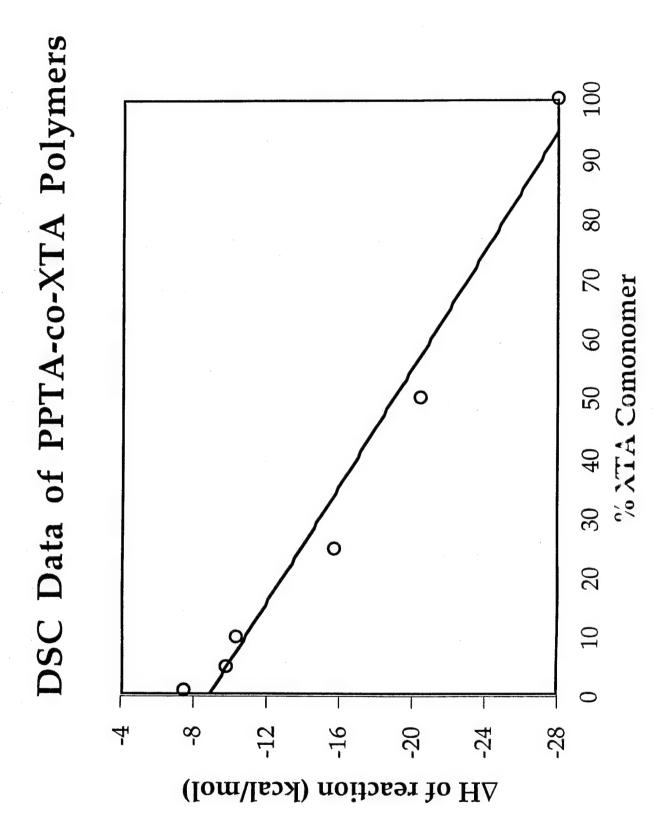
Polymer	x value	ΔH of Reaction (kcal/mol)	Intrinsic Viscosity [η]
PPTA	1	-27.90	5.7
PPTA	0.5	-20.31	6.6
PPTA	0.25	-15.68	4.9
PPTA	0.10	-10.29	5.3
PPTA	0.05	-9.68	5.2
PPTA	0.01	-7.45	5.3

Curve 1: DSC

File Info: ljmpolyD Wed Jun 24 01:05:27 1992

Sample Weight: 13.800   mg

XTA PolyD

XTA 100%

XTA 50%

XTA 25%

XTA 10%

XTA 5%

XTA 1%

Heat Flow (W/g)

Temperature (°C)

100.0   150.0   200.0   250.0   300.0   350.0   400.0   450.0

20.00   18.00   16.00   14.00   12.00   10.00   8.00   6.00   4.00   2.00
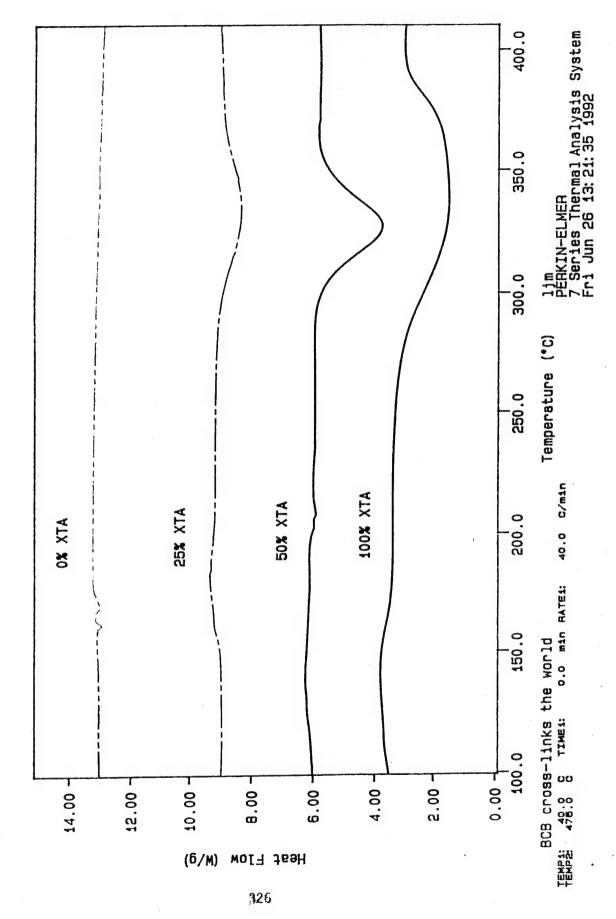
ljm
PERKIN-ELMER
7 Series Thermal Analysis System
Sat Jun 27 19:20:55 1992

TEMP1: 40.0 C   TIME1:   0.0 min RATE1:   40.0 C/min
TEMP2: 475.0 C

324

DSC Data of PPTA-co-XTA Polymers
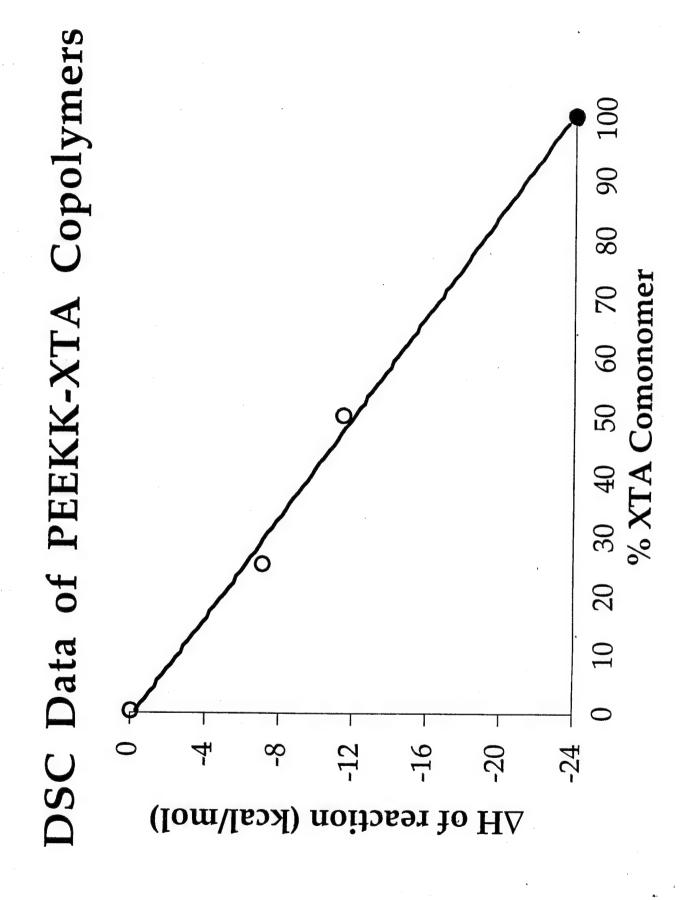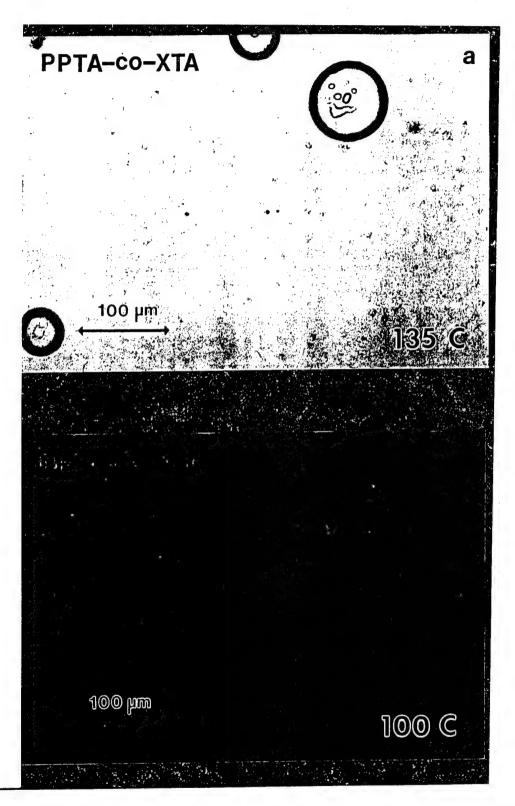
Curve 1: DSC
File info: ljmpeek100Fri Jun 26 12:53:57 1992
Sample Weight: 10.000   mg
XTA 100%

Heat Flow (W/g)

Temperature (°C)

0% XTA

25% XTA

50% XTA

100% XTA

BCB cross-links the world

TEMP1: 40.0 C   TIME1:   0.0 min RATE1:   40.0 C/min
TEMP2: 475.0 C

ljm
PERKIN-ELMER
7 Series Thermal Analysis System
Fri Jun 26 13:21:35 1992

DSC Data of PEEKK-XTA Copolymers

ΔH of reaction (kcal/mol)

% XTA Cononomer
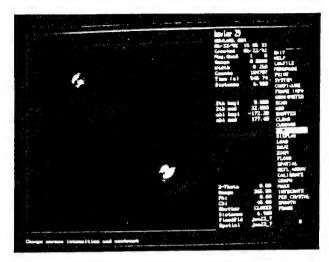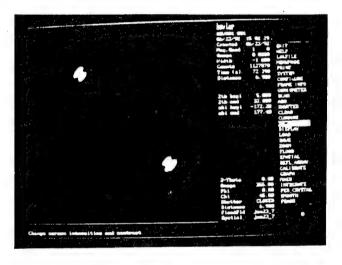
Hot Stage Optical Microscopy of PPTA-co-XTA copolymer (25% XTA) in H$_2$SO$_4$ solution (20 weight %). Above 135 C the sample is optically isotropic. Upon cooling the solution becomes birefringent. This texture is consistent with the nematic lyotropic liquid crystalline phase found in neat PPTA solutions. Micrograph taken on an Olympus BH-2 Optical Microscope under crossed polarizers with full wave red filter.
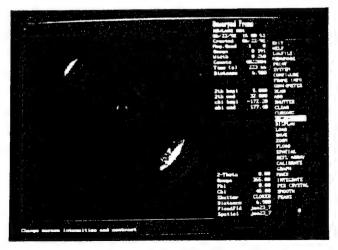
Kevlar® 29
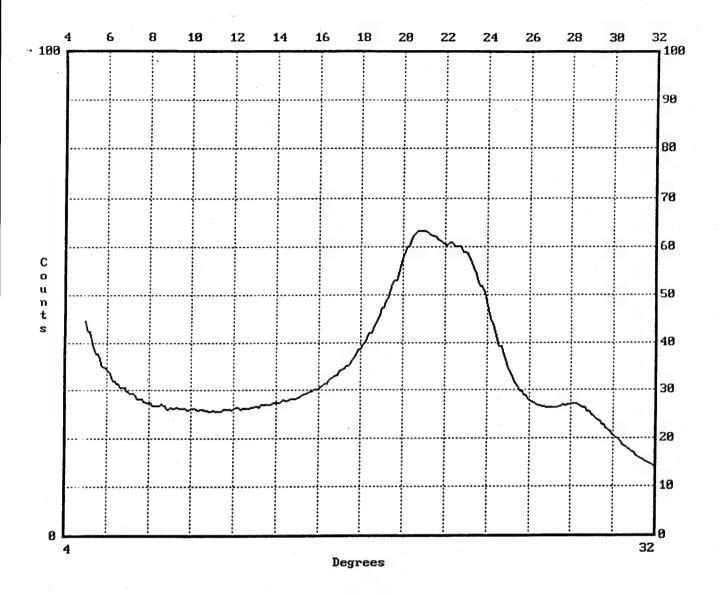
Kevlar® 149
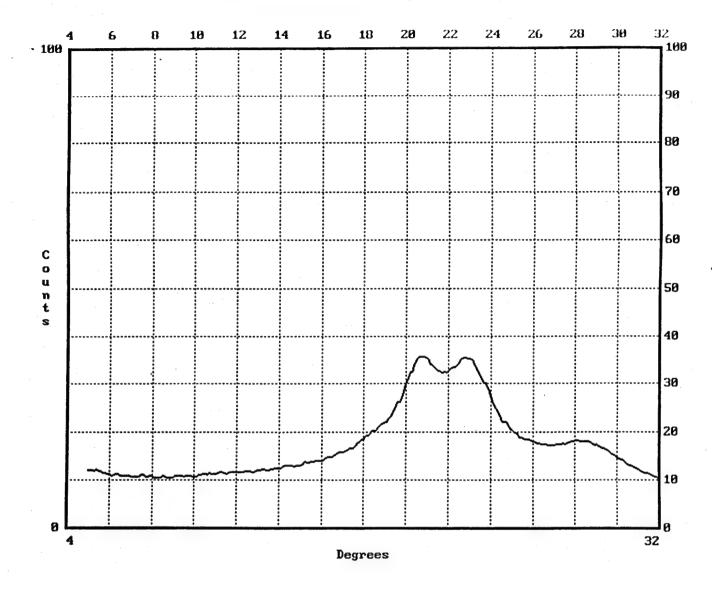
Kevlar® spun at Michigan

329

Kevlar, no heat treat

6/23/92
Siemens

330

Kevlar, heat treat @ 450C

6/23/92
Siemens

331

Curve 1: DSC

File info: gadpap-2   Wed Jun 24 15:53:35 1992

Sample Weight: 2.700   mg

gadpap-2

Heat Flow (mW)

Temperature (°C)

ph-pa2

TEMP1:	40.0	C	TIME1:	0.0	min	RATE1:	20.0	C/min

TEMP1:   40.0 C   TIME1:   0.0 min   RATE1:   20.0 C/min
TEMP2: 450.0 C   TIME2:   0.0 min   RATE2:   20.0 C/min
TEMP3: 450.0 C   TIME3:   0.0 min   RATE3:   20.0 C/min
TEMP4: 450.0 C   TIME4:   0.0 min   RATE4:   20.0 C/min
TEMP5: 450.0 C

BCB Model Compounds

1

2

3

4

5

6

7

8

333

Curve 1: DSC
File info: gad330-3   Thu Jun 18 06: 45: 26 1992
Sample Weight: 6.000   mg
gad3-30

Temperature (°C)

Heat Flow (mW)

bcb-pbo model

TEMP1:   40.0 C   TIME1:   0.0 min   RATE1:   20.0 C/min
TEMP2: 450.0 C

gad
PERKIN-ELMER
7 Series Thermal Analysis System
Wed Jun 24 09: 17: 48 1992

334

Curve 1: DSC

File info: gadc-3   Wed Jun 24 07:49:58 1992

Sample Weight: 5.300   mg

gadc-3

ket-pap mix

TEMP1:   40.0 C   TIME1:   0:0   min   RATE1:   20.0   C/min
TEMP2:   400.0 C   TIME2:   0:0   min   RATE2:   20.0   C/min
TEMP3:   400.0 C   TIME3:   0:0   min   RATE3:   20.0   C/min
TEMP4:   400.0 C   TIME4:   RATE4:   20.0   C/min
TEMP5:   400.0 C

gad
PERKIN-ELMER
7 Series Thermal Analysis System
Wed Jun 24 09:32:45 1992

Table 1: Differential scanning calorimetry data of BCB-model compound study.

Entry	Melt Temperature	Δ H kJ / mole	X-Link Temperature	Δ H kJ / mole
1	221.1 °C	28.7	391.9 °C	-71.0
2	293.0 °C	30.0	369.9 °C	-75.5
3	171.3 °C	38.0	395.0 °C	-56.0
4	313.3 °C	72.0	364.0 °C	-85.5
5	183.6 °C	35.7	393.2 °C	-97.3
6	68.2 °C	21.9	346.5 °C	-183.2
7	128.6 °C	29.1	263.8 °C	-207.9
8	161.0 °C	32.9	289.4 °C	-258.2
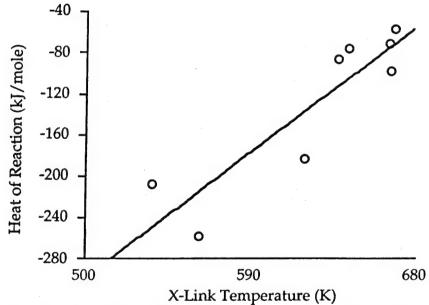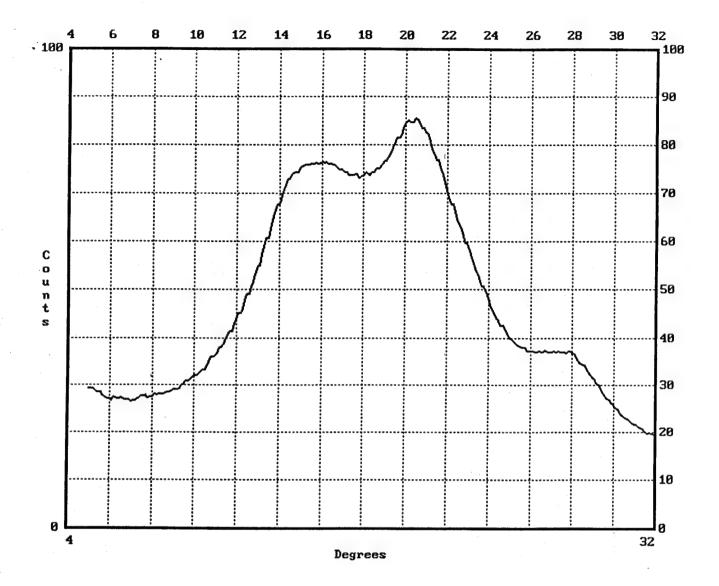
Figure 1: Plot of heat of reaction vs. maximum cross linking temperature for the BCB model compounds listed in Table 1.

ppxta 25%, no heat treat

6/23/92
Siemens

337

Table 2: Reaction exotherm maximum for BCB-model compound-dienophile mixtures.

	1	2	3	4	5	6
A	332.1 °C	313.8 °C	320.7 °C	315.4 °C	317.2 °C	298.6 °C
B	306.8 °C	290.6 °C	294.6 °C	300.5 °C	300.0 °C	280.5 °C
C	365.6 °C	354.5 °C	376.7 °C	348.4 °C	352.7 °C	336.2 °C

Dienophiles used in BCB Model Study

A

B

C

DEFECT STUDIES IN 1,6DI(N-CARBAZOLYL)-2,4 HEXADIYNE (DCHD) POLYDIACETYLENE DROPLETS
Patricia M. Wilson

Table of Contents

DEFECT STUDIES IN
1,6-DI(N-CARBAZOLYL)-2,4 HEXADIYNE
(DCHD) POLYDIACETYLENE DROPLETS

by

Patricia M. Wilson

Materials Science and Engineering
The University of Michigan
H.H. Dow Building
Ann Arbor, MI   48109-2136

Abstract

Droplets of 1,6-di(N-carbazolyl)-2,4 hexadiyne (DCHD) diacetylene were prepared by room temperature evaporation of dilute (0.01 wt %) solution of the monomer in chloroform onto amorphous carbon-coated mica substrates. HREM and SAED examination revealed small crystallographically textured droplets (~1 μm diameter) with cracks parallel to the [001] chain direction. The droplet geometry allowed us to investigate the structure of the polymer near edges both parallel and perpendicular to the chain axis. It was found that the curvature of the droplet edge caused a local bending of the polymer crystal lattice. The direct imaging of the molecular organization near the droplet surface allowed an investigation of the mechanisms of lattice bending via the formation of edge dislocations. An understanding of these defects is important in determining how they relate to the physical properties of poly(diacetylenes). Dislocations were etched in some droplets to gain information about the core structure of a defect in a polymer crystal.

Introduction

Poly(diacetylenes) are a relatively new class of polymers of general scientific and engineering interest. They first appeared in 1969 in a communication by Wegner [1] describing the solid state polymerization of crystals of diacetylene. Solid state polymerization is a topochemical process by which crystals of monomer are polymerized in the confines of the structure to yield nearly perfectly crystalline polymer crystals. Large polymer single crystals are extremely difficult to prepare in other systems, as evident by the large research efforts in rigid rod polymers for fiber applications, liquid crystalline systems, and research into lamellar crystals such as polyethylene. The interest in the orientation of macromolecules arises in the enhanced properties and uniform morphologies that can be created. In rigid rod and extended chain fibers such as poly(paraphenylene terepthalamide) (PPTA) (Kevlar™) and gel spun polyethylene (Spectra™) the orientation of the chain allows the load bearing capability to be transfered to the strong covalent carbon-carbon bonds which greatly increases the tensile strength of the materials. Orientation of chains that allows conjugation to become continuous makes it possible for polymers to be used for electromagnetic and optical applications that were formerly limited to semiconductors and metals. Polydiacetylenes possess the largest known nonresonant third-order susceptibility as well as a ultrafast response time [2]. The further attractiveness of the low specific gravity of polymeric materials for applications makes research into oriented macromolecules a lucrative area.

Polydiacetylenes have an extended chain orientation and high thermal stability. This also allows them to be used as model systems to study the chemistry and physics of polyconjugated systems, since other systems are not as homogeneous in structure.

Hirshfeld and Schmidt [3] were the first to formally introduce the concept of solid state reactions such as photodimerization. They postulated that the course of a solid state reaction could be

346

predicted on the basis of the configuration and nearest-neighbor geometry of the closest monomer molecules in the crystal lattice. Wegner [1] was the first to actually describe a topochemical reaction in diacetylenes. A topochemical reaction occurs as a diffusionless transformation where the centers of mass of the monomeric units retain their original crystallographic positions and the the symmetry of the monomeric units in the monomer and polymer single crystals remains the same.

The polymerization reaction of diacetylenes is a 1,4-trans-addition reaction. This is achieved from the rotation of the monomeric units on their center of mass. The polymerization is thus a very stereospecific reaction, giving a stereoregular polymer with a distinct orientation. Figure 1 shows schematically the general transition from monomer to polymer. The poly(diacetylene) structure can exist in two different mesomeric forms, enyene or butatriene, but in general the enyene form predominates [4].

The reaction is initiated via several different methods, thermal or gamma radiation, photoinduction, and by electron beam [5]. Thermal radiation initiates at defects in the monomer crystal and gamma radiation is seen to occur homogeneously [6]. The polymerization of diacetylenes is seen in several of the systems to be an autocatalytic process yielding a S-shaped curve of time vs. conversion. There is at least one diacetylene that goes through a phase transformation upon polymerization, DCHD. At nucleation, there is a solid solution of polymer in monomer and at a 10% conversion [7] a phase transformation occurs and a solid solution of monomer in polymer is left until complete polymerization.

The organization of polymers near defects is a general question of both scientific and technological interest. Defects in polymer systems have not been thoroughly studied because of the difficulties in imaging organic materials with high energy electron beams. Also, defects are difficult to isolate and study in detail because most polymer systems have small crystalline regions surrounded by regions of amorphous material. The optical and electromagnetic transport properties of these crystals should be

347

limited by the structure and density of defects which serve as sinks for photons and charge carriers.

To study a wide range of defects, droplets of 1,6-di(N-carbazolyl)-2,4 hexadiyne (DCHD) diacetylene were prepared and polymerized in order to perform High Resolution Electron Microscopy (HREM) to investigate local structure. Droplet experiments using TEM have been shown by Henkee [8] and Martin [9] to be useful in determining the organization of polymers as they approach a constraining surface. Martin discerned that poly(imide) molecules preferentially oriented parallel to droplet edges in small crystallites. As the thickness of the droplet increased, the orientation effect decreased. Droplets are useful in that near the edge the sample thickness decreases such that HREM imaging becomes feasible, minimizing artifacts produced by other methods of sample preparation.

The droplet sample geometry also allows us to produce a large number of defects for study, such as dislocations, cracks, and free surfaces. The reorganization of molecules near surfaces and defects in general is explored in this paper. DCHD was chosen for use in this study because it is relatively well studied and it exhibits electron radiation resistance which allows HREM to be performed [10]. The high degree of crystallinity also allowed the effect of other variables, such as amorphous regions or small crystallites, to be reduced. The unit cells are reported [11] for both monomer and polymer in Table 1.

Defects in highly crystalline diacetylenes (p(TS) and poly(DCHD)) have been previously studied by Young's group [10] [12] [13] [14] [15] using transmission electron microscopy. Young and Petermann [12] established the existence of dislocations with a line direction perpendicular to the chain axis using dark field imaging. They also established a dislocation density of approximately 10^{13} m^{-2} as a maximum observed in the crystals [12]. Later studies of Read and Young [10] showed that HREM of poly(DCHD) could be performed if imaging conditions were kept below the critical dose (J_e) for the reflections of interest. They determined that J_e for equatorial reflections in poly(DCHD) was 200,000 C/m^2. Yeung and Young [15]

also showed that using differing sample preparation techniques, they could look down the [001] zone axis of poly(DCHD) crystals.

This study is intended to understand the nature of defects in diacetyelenes and their resulting influence on properties.

TABLE I

Lattice Parameters of DCHD [11]

	Monomer Monoclinic P2$_1$/c	Polymer Monoclinic P2$_1$/c
a	17.75 Å	17.55 Å
b	13.70 Å	13.03 Å
c	4.57 Å	4.92 Å
γ	93.5°	108.7°

Experimental

A. DCHD monomer synthesis

The DCHD monomer was synthesized with the help of Prof. Jeffrey S. Moore of the Chemistry Department using oxidative coupling of substituted alkynes. Carbazole (75 grams) was first dissolved in 750 ml dry THF. A separate vessel was then charged with NaH as a dispersion and suspended in 150 ml of THF in a dry box. The NaH suspension was cooled to 0°C and carbazole solution was added dropwise over 10 minutes. Hydrogen evolution began immediately. At the end of the addition, it was warmed slowly to 50°C and a clear brown solution resulted after an hour. A third vessel was charged with 80 ml of propargyl bromide as a 80%

solution in toluene along with 200 ml of THF. The solution was cooled to 0°C and added to the solution of sodium cabazole dropwise. It was extracted in CH_2Cl_2 with water, dried with $MgSO_4$ and concentrated. FC (4:1 hexane:CH_2Cl_2) gave a pale yellow solid. 200 ml of Pyridine, 200 ml of MeOH and 100 gms of $Cu(OAc)_2$ were mixed together until nearly homogeneous. A solution of the acetylene was added and heated to reflux. A green color developed. After cooling for one hour, it was let to stand at room temperature for 18 hours. The mixture was poured into 10 liters of water in three 4000 ml Erlenmeyer flasks and a blue cloudy suspension resulted. The solution was filtered and the solids were washed with excess water, air dried, and then dried under vacuum.

Rf (1:1 CH_2Cl_2 : hexane) = 0.56. The crude product was allowed to dry overnight in the dark. The impurities were removed with acetone and then Et_2O. 5 grams of product was recrystallized from 600 ml of toluene. NMR characterization showed that there were less than 1% impurities in the final product.

B. Sample Preparation

A 0.01% by weight solution was prepared with white crystals of DCHD monomer and chloroform as received from Aldrich. This solution was used to prepare droplets by flooding amorphous carbon coated mica substrates with the solution and allowing the chloroform to evaporate at 21°C. The carbon film was floated onto the surface of water and collected with copper grids for examination using transmission electron microscopy (TEM). Some samples were shadowed with gold metal in a Denton vacuum evaporator at an angle of 12°. Larger droplets were produced by the above method but with evaporation occuring on a hot plate at approximately 100°C for less than five seconds. Samples were either polymerized in a vacuum oven at 150°C [7] for approximately 24 hours or in the electron beam [5]. Etched droplets were prepared by polymerizing the monomer as described thermally and then flooding the surface of the copper TEM grids with 100% chloroform The grids were supported by a wire mesh in a petri dish and kept in a

saturated chloroform atmosphere overnight until the chloroform evaporated.

C. TEM Operation

The DCHD droplets were examined in a JEOL 4000 EX transmission electron microscope operating at 400 kV using the minimum dose system (MDS) and a beam blanking device. A low dose procedure for taking micrographs was employed to reduce electron radiation damage of the samples as reported by Martin [16]. Focusing was aided by a Gatan TV monitor and was performed at 200 kX. The procedure used was to move to a fresh area of a grid, focus on the edge of a droplet at magnifications higher than 200 kX, move to a different area in search mode to look for droplets which had not been exposed to the beam and quickly take a micrograph in photo mode. This procedure greatly reduced the amount of radiation each droplet experienced by only focusing once on an area within the grid square. Since the area of interest was the edge of the droplet, the assumption was that the height of the area in a grid square was relatively constant and thus focusing only needed to be done once. Imaging was typically done at a screen current of 20 pA/cm^2 and an exposure time of one second giving, for a magnification of 100 kX, a total dose at the sample of 2,000 C/m^2. The electron damage sensitivity of the droplets was determined by monitoring the fading of reflections in diffraction mode and estimating the amount of time until these reflections faded. The time a sample was irradiated during searching and photo mode was kept below this limit. After the images were taken the integrity of the sample was checked by returning to diffraction mode to make sure the reflections of interest were still present.

Selected Area Electron Diffraction (SAED) patterns were calibrated using gold evaporated onto the surface of the grid. Lattice spacings were calibrated using a He/Ne laser optical bench setup. Negatives of turbostatic graphite with 0.34 nm lattice spacings were used to give accurate measurements of lattice spacings at the same magnification.

Scanning electron micrographs (SEM) and Scanning transmission electron micrographs (STEM) were taken using a JEOL 2000 EX at an operating voltage of 200 kV. The samples were prepared as above and gold coated with a very thin layer to increase scattering ability. The microscope was aligned using normal TEM procedures, but the scanning beam was used to generate both a SEM and STEM image simultaneously on the dual screens. Beam damage in the sample could be monitored by marks left on the surface, such as carbon deposits, as seen in the SEM image. SEM and STEM images were recorded of each area of interest in order to be able to correlate projection and surface information.

Results

Figure 2 shows a low magnification TEM image of DCHD droplets of approximately one micron in diameter on the amorphous carbon substrate dispersed in between many larger needle crystals. The DCHD system lends itself to many different crystal morphologies dependent on concentration and evaporation conditions. Several interesting single crystal textured morphologies such as "cross-hatched" and microfibrillar have been observed by Liao [5].

Figure 3 shows a single droplet, shadowed with gold at an angle of 12° to highlight topological features and determine the height of the droplet. The maximum height was measured to be on the order of 100 nm. All droplets were found to have the same crystallographic texture as shown in this droplet. The polymer chain was determined to be perpendicular to the beam from examination of the selected area electron diffraction (SAED) pattern shown in figure 4. Closer examination of the diffraction patterns in relation to the micrographs showed that the cracks present in the droplets are parallel to the [001] direction. Individual droplets are not aligned in relation to each other as can be seen in Figure 2.

Figure 4 shows a SAED of the droplet in Figure 3 in relation to the droplet. The diffraction pattern exhibits an extra plane of symmetry at the meridian that does not exist in the diffraction pattern for a single crystal of the polymer as reported by Apgar and

Yee [11]. The extra symmetry can be accounted for if the droplet was crystallographically textured like a fiber. The inset shows a simulation of a fiber textured diffraction pattern using CERIUS [17] and the unit cell proposed by Apgar and Yee [11]. The simulated SAED compares well to the observed diffraction pattern. HREM micrographs, such as figure 6, have shown regions of different orientations of the R groups about the chain axis next to each other, as would be expected for a fiber texture, a possible schematic explanation for this is shown in figure 5.

Lattice fringes were observed parallel to the cracks and edges of the droplets. Two different edges were found since the axis of the polymer chain was uniform over the entire droplet, one edge where the chain backbone is parallel to the edge and another where the chain backbone is perpendicular to the edge. Figures 6 and 7 illustrate examples of this. From shadowing and HREM images, the edges of droplets where the chains are parallel to the edge appear to have a Fresnel fringe which suggest a sharp drop in thickness whereas at edges with the chain perpendicular the droplets appear to change gradually in thickness.

Figure 6 shows a HREM image of a DCHD droplet showing the edge perpendicular to the chain axis. The micrograph illustrates that near the edge the packing of poly(DCHD) appears to remain regular up to the edge of the droplet. Quantitative measurements of the (010) spacings obtained with a video digitizer and Fast Fourier Transform routines from the image analysis software IMAGE showed that the spacings of the (010) planes remained constant (1.20 ± 0.05 nm) from the interior of the droplet to the edge. There are two different orientations of the polymer chains visible, one with a spacing of 1.2 nm (010) and one with a spacing of 0.8 nm (200). A region of fringes measuring 0.6 nm that stretch across the droplet in the middle of the image are believed to indicate a thickness of 100 nm.

Figure 7 shows bending of the lattice fringes (010) in the direction of the curvature of the droplet edge. The radius of curvature of the bending was determined to be 1.5 microns. Several edge dislocations are also apparent in this micrograph with a

Burgers vector of [010]. Figure 8 shows another droplet edge with lattice fringes corresponding to (010) planes bending near the edge. Drawing tangents to the fringes shows the bending to be actually a series of straight sections separated by a tilt where the chain is continuous across the tilt. The tilt was measured to be on the order of
5-8°.

In several regions of the droplets, lattice fringes of the (010) planes were obtained with high resolution. Figure 9 shows such a region with the corresponding simulated electron potential, simulated lattice image, and optical transform . The simulated image and electron potential were produced from the structure as reported by Apgar and Yee [11] with MacTempas using the multislice approach [18]. The operating parameters for the JEOL 4000 EX were C_s=1.0 mm, an aperture of 0.25 Å^{-1}, -1000 nm defocus, defocus spread of Δf=8 nm, and a sample thickness of 100 nm. Light contrast is seen to correspond to regions of low electron density, where as dark contrast corresponds to regions of high electron density (atoms). The optical transform of this region shows reflections up to 4th order, corresponding to a resolution of 0.3 nm. Micrographs with this resolution indicated that the dose used to image the droplets was under the critical end dose for the (010) planes found near the curved edge since radiation damage was held to a minimum.

Figure 10 shows a low angle ACR (axial chain rotation) [19] tilt boundary in a droplet. The angle of tilt varies from the left of the crystal from 6° to 4°. Eight edge dislocations of the type **b**=[010] can be located along the boundary, all having the same sense. There may be other dislocations with Burgers vector parallel to the chain axis also present but they were not imaged due to the damage sensitivity of the planes which would give rise to the fringes necessary to locate them. The regions around the dislocations where contrast is lost is measured to be between 6 nm x 5 nm and 36 nm x 30 nm depending on the number of dislocations in the core. The holes are elongated in the direction of the chain axis. The length between defects is 7.0 to 12.0 nm. This corresponds well to the

calculated distance, D, for this type of tilt boundary which is 11.5 nm. Figure 11 shows a schematic of a tilt boundary of this type. Figure 12 is an example of a different type of tilt boundary, it is shown schematically in figure 13. The Burgers vector is [010] which represents ends of chains being incorporated into the structure. The islands of dark contrast are gold drops used to shadow the droplets and calibrate spacings for SAED patterns.

Figure 14 shows an etched droplet with holes that are measured to be between 6 nm and 30 nm. Figure 15 also shows an etched droplet taken as a defocused (000) diffraction spot which shows holes in lines perpendicular to the chain direction radiating from the edges of the droplet. The holes appear to be polygonalized with distances between lines of holes to be approximately 125 nm. This is in the same order of magnitude as the distances between observed tilt boundaries in the bent regions of Figure 8.

Figure 16 is a SEM and STEM image taken of a poly(DCHD) droplet . A comparison of the light areas of contrast on the STEM picture to actual holes shown in the SEM of the same droplet show that there are both holes in the surface and holes in the bulk of the sample that do not continue to the surface. Regions of light contrast in the STEM image marked A are voids whereas the regions marked B are holes as seen in the SEM image. Many of the holes in the surface may be attributed to etched areas of unreacted monomer.

Discussion

Most of the droplets were found to to have a single orientation of the polymer chain axis. Only a few droplets were found which contained more than one orientation, as signified by two regions of the droplet containing cracks which were at an angle to each other. The texture of the regions were the same but were oriented at an angle to each other resulting in a high angle grain boundary.

The formation of the droplets is thought to be via the breaking off of the chloroform solution into large droplets during the evaporation process with the concentration of the solution rising as the solvent evaporates. As the critical solubility is approached

(approximately 0.25% of DCHD by weight), monomer is deposited onto the carbon substrate conforming to the shape of the liquid droplet, which is determined by surface tension. The monomer droplet is then in a swollen state where a slight reorganization of the monomer units may be possible to conform to defects such as surfaces. As the last residual solvent from the swollen matrix is evaporated, the cracks form due to drying. The cracks may form at the boundaries between two differing textures of the monomer crystal structure. It has been noted that the droplets are crystallographically textured with the long chain axis in the plane of the substrate and the R groups rotated in differing directions in domains of single crystal orientation. As the swollen droplet with these different domains shrinks due to solvent evaporation, the domain boundaries could be thought of as grain boundaries and would be concentrators of stress leading to cracking along them. Many droplets have only one predominant orientation of the polymer chain because of one nucleation event occuring during droplet formation. Some multiple nucleation event droplets have been observed. In these droplets, domains can be seen with cracks running in differing directions, indicating the chain direction in those regions.

Surface effects on the ordering of the monomer should ultimately determine the defects induced in the final polymer state. Since the polymerization is a topochemical reaction [1] from the monomer unit cell, any defects present in the monomer structure should be preserved in the polymer crystal. In Figures 7 and 8 bending of the lattice fringes corresponding to the (010) planes is seen near the curved edge of the droplet. The area in question can be thought of as a perfect crystal that is bent as shown in Figure 17. In order to incorporate the strain in a bent lattice, dislocations will form to lower the total energy of the region. The geometrically necessary dislocation density can be calculated by determining the strain gradient over the bent crystal and dividing it by the Burgers vector of the dislocation needed to relieve the strain (geometrically necessary dislocations = 1/r**b**) [20].

The dislocations needed to incorporate the bending can be envisioned as an extra monomer unit along the c direction or, after

357

polymerization, as an extra repeat unit along the chain in relation to the chain on the compressive side. The Burgers vector in the polymer would be the spacing along the chain axis of the R groups, 0.491 nm. For this geometry, it is calculated that there would be one dislocation needed every 735 nm² corresponding to a dislocation density of approximately 10^{15} m⁻².

In metals, it is frequently found that dislocations will tend to polygonalize in a bent crystal forming a low angle tilt boundary [21]. If Figure 7 is examined closely, the bending occurs between two regions which are tilted with respect to one another. The angle between the two areas is 5°. Using an analysis by Hirth and Lothe [22] the spacing of dislocations along a symmetrical tilt boundary, D, is approximately equal to b/θ, where b is the Burgers vector and θ is the tilt angle. For edge dislocations with a Burgers vector along the chain axis (b=0.49 nm), the spacing between dislocations would be 5.6 nm, which would correspond to a dislocation every 5 polymer chains in the [010] direction. Young and Petermann [12] showed that similar tilt boundaries in toluene sulphonate poly(diacetylene), p(TS), single crystals were formed when there was a large enough dislocation density with Burgers vector of [001].

Dislocations with Burgers vector along the c axis have not been imaged to this date, although edge dislocations with a Burgers vector along the [010] direction have been imaged. This corresponds to an extra polymer plane inserted perpendicular to the electron beam direction. Such edge dislocations can be seen in Figures 7, 10, and 12.

Since the polymerization of the monomer is dependent on the positions of the monomer units in its crystal structure, Baughman [23] proposed a scheme to predict if new diacetylene molecules would polymerize in the solid state. His study used the principles of least motion of the molecules as the requirement and the possibility for the units to pack unhindered by steric interactions. The principle of least motion states that the reaction pathway must be one in which the smallest mean square displacement of the atoms would take place. His study concluded that the optimum conditions for reaction were when the packing of the monomer unit allowed for

the angle between the diacetylene chain with the center of mass was 45° and the relative lattice contraction $(d_1 - d_2)/d_2$ during polymerization should not exceed 0.1. The value of d_2 for all polymerized diacetylene chains is approximately 0.491 nm, which is mainly dependent on the diacetylene backbone length. Figure 1 shows the relative parameters.

The benefit of the analysis lies in the possibility of the organic chemist using a molecular simulation program to design possible molecules and determining whether they may react in the solid state before attempting to synthesis them. The main factor in the selection of the side groups (R groups) is to select one that is not bulky enough to sterically interact with the packing such that the lattice contraction would be high, but one that is large enough to not allow the chains to pack so closely that favorable overlap of π orbitals cannot occur to have the reaction proceed.

This analysis fails to not predict the reactivity of DCHD, which actually undergoes an expansion along the chain axis during polymerization. Gersamov et al. [24] has found that the application of high hydrostatic pressure during polymerization retards polymerization of DCHD because of the unfavorable overlap, but increases polymerization in p(TS). Figure 18 shows the unfavorable overlap of the π orbitals of DCHD.

Defects in the monomer lattice may effect the polymerization by retarding the polymerization in the neighborhood of the defect in regions of heterogeneous hydrostatic pressure. Figure 19 shows the regions of compressive and tensile hydrostatic pressure around a edge dislocation [25].

The misalignment of the monomer units could prevent polymerization of those units which do not satisfy Baughmann's conditions. The area of monomer units which would remain unpolymerized could be related to the size of the dislocation core by the area over which the misfit of the dislocation extends. The calculation of the misfit induced by such a edge dislocation is made difficult due to the lack of elastic constants for this material and the inherent difficulty presented by the severe anisotropy present in polymers. Young and Petermann [12] have treated this question by

using the model by Frenkel and Kontorova which is applicable for isotropic solids and applying it in one direction in the polymer using averaged data available for the p(TS) system. Even with the crude approximation, they found that the misfit would extend over about 30 structural units for a dislocation with a Burgers vector along the chain axis. Given this, it could be expected that a reasonable amount of monomer would remain unreacted in the area of a edge dislocation with **b** along the b [010] direction.

Gersamov et al. [24] has shown that the polymerization of DCHD is retarded when the lattice is strained by an applied hydrostatic pressure. They found that pressure increases the deformation of the growing chain in the monomer crystal. The monomer crystal structure determines the reactivity of the growing chains and thus the reactivity is changed. Using Raman spectroscopy they measured shifts in the C=C and triple bonded carbons. They found a greater than 50% decrease in polymerization yield in DCHD crystals when thermal polymerized at 150°C at 4 kbar for 40 min. The DCHD polymerization is retarded under high hydrostatic pressure in both thermal and photoinduced polymerization. The applied pressure causes the monomer crystal to be compressed in the direction of the growing chain. The increase in deformation increases the bond angle deformations and not the bond lengths causing a twisted chain formation that hinders further chain growth, see Figure 18. A schematic of an edge dislocation in DCHD monomer and the resulting area after polymerization of the crystal is shown in Figure 20. There is a region around the defect where the monomer polymerization is retarded. These regions of unreacted monomer could be etched out using a solvent that does not affect the polymer.

There are precedents for doing etching experiments on organic systems [6]. Schermann [6] has reported etching dislocations emanating at the surface of crystals of p(TS) monomer. His observations were made via scanning electron microscopy and optical microscopy. The crystals were grown from solution of methanol-acetone (3:2) and p(TS) and etching was done using freshly distilled methanol followed by washing in distilled water on the monomer crystals. Via energetic reasoning they also concluded that

dislocations were nucleation sites for the hetrogeneous polymerization observed using thermal radiation but had no effect on the photoinduced polymerization which proceeded homogeneously though the crystals. Elliptical pits were reportedly formed on the (100) cleavage face of monomer crystals with the long axis parallel to [010]. They were not able to etch polymer crystals since there was not a solvent available for the polymer. Polymerization was observed under an optical microscope using transmitted polarized light at a temperature of 343 K. Polymerization was seen to grow from localized points that corresponded to the centers of elliptical etch pits. The size of pits observed were of the order of 2-5 μm.

Etching experiments in our laboratory have shown lines of holes perpendicular to cracks and the droplet edge (Figures 14 and 15) which would indicate that they were unreacted monomer around arrays of dislocations formed by the bending of the lattice. Further SEM/STEM experiments on etched droplets showed that many of the regions of light contrast found in TEM images corresponded to holes in the surface which would be consistent with the presence of etch pits. They also showed that there are many voids inside the crystals and illuminate the importance of determining which holes continue to the surface. Measurement of the holes yield sizes that are consistent with regions of low contrast in lattice images of grain boundaries shown in Figure 10. In both instances, the size of the disordered regions are approximately 6 nm square to 36 nm square. This range corresponds to regions produced by single dislocations up to dislocations that are actually three or more single dislocations of the same sense.

In trying to determine the origin of regions of 0.6 nm fringes in Figure 6 a Pendellosung plot was constructed for DCHD in the [100] projection using CERIUS [17]. A Pendellosung plot shows the amplitude of the exit wave from a multislice calculation [18] versus thickness of the sample (Figure 21). Plotted are the transmitted beam, (000) and the diffracted beam (010). At a thickness of 100 nm, the amplitude of the transmitted beam approaches zero. If there was no transmitted beam, the diffraction pattern would show an absent reflection for the (000) spot and only the remaining

reflections. The contrast of the 1.2 nm spacing would be weak, and only the interference of (010) with (0-10) would be seen, giving rise to 0.6 nm fringes.

Image simulations for samples at 100 nm were consistent with this conjecture. This effect was shown to be independent of focus by calculating a defocus series at 100 nm in thickness. In a range of defocus from -100 nm to 100 nm, the spacings did not deviate from 0.6 nm. Another series of images was calculated to determine how sensitive to thickness this effect was. It was seen to have a spread of approximately ± 4 nm, which correspond to a thickness change of only ± three unit cells. The image shows the (010) planes with spacings of 1.2 nm and a region with fringes of a spacing of 0.6 nm that may indicate a thickness of 100 nm.

Future Work

Future work will help illuminate further aspects of general questions raised by this investigation. One question is the nature of the texturing that is present in the droplets. Tilting of the droplet around the molecular axis while monitoring the SAED pattern will determine whether there is a texturing of a few predominant orientations, most likely being the preferred habit planes during bulk crystal growth. If there is true fiber symmetry, then the diffraction pattern will not change upon tilting. As evidenced by the cracks present and typical orientations observed using HREM, it seems likely that the cracks may be boundaries between different textures, being the obvious choice for cleavage.

Investigation of the droplet surface near the edge by Atomic Force Microscopy (AFM) would give additional information on the surface profile at each at a higher resolution of the two cases, where the polymer chain is perpendicular to or parallel to the edge of the droplet. It would confirm our observations that the slope of the droplet is different in either direction and give insight as to the nature of the observed ridges as the polymer chain exits the droplet.

Further joint studies using SEM/STEM and HREM will allow a better understanding of the nature of the surface pits that appear to form during etching. A similar study of unetched polymer droplets using SEM/STEM in concert will determine if there is a distinct difference in the surface structure and if in fact, removal of unreacted monomer is occuring. Care needs to be taken during the microscopy to determine whether damage is being induced in the sample that would alter the surface appearance. This could be quantified by a complete dose series being performed in the JEOL 4000 EX and determining the critical doses for all major reflections and using the operating parameters of the JEOL 2000 EX to determine the time required at each condition to destroy all crystallinity in the sample. Also a droplet could be imaged and damaged using the JEOL 4000 EX and then observed using SEM/STEM to determine the change in surface appearance.

Having two JEOL instruments with complimentary functions can be used to their fullest capabilities by using them to do a series of joint experiments. Since the sample preparation methods are the same for both and the operating systems are virtually the same, with care a single area can be imaged using HREM and SAED in the JEOL 4000 EX and then transported to the JEOL 2000 EX to be examined using SEM and STEM of the same area. This could be facilitated by using alpha-numeric grids that are currently available to keep track of imaged areas. Maps of grid squares could also be taken to use in determining sample positions. By carefully keeping doses to a minimum, estimation of the sample damage would also be possible. This multiple, complimentary data collection of local regions of a droplet holds great possibilities for gaining information of what occurs to a macromolecule near surfaces.

Modeling of defects in periodic systems would also be helpful for use in this work by allowing the theoretical HREM image to be simulated by multislice calculations. A better understanding of contrast mechanisms in HREM when using organic systems will follow.

Defect analysis will be greatly facilitated with the calculation of the compliance matrix of the monomer and polymer

crystals. This calculation will be done using a program that uses the existing POLYGRAF software to induce a stress on a unit cell and using a Dreiding force field [26], infer the changes in unit cell dimensions as strains and back calculate out the compliance matrix. This method is only a first approximation to the true elasticity values, but would be of great use in further modeling. Modeling of hydrostatic pressure around defects and arrays of defects, such as grain boundaries (Figure 22), will help in determining the effect of defects in such property measurements of carrier density that are ongoing in our lab. Quantifying the effect of specific defects in the carrier mobility of these materials is difficult because of the need to isolate single defects. Our research currently entails the building in of known specific grain boundaries into diacetylene monomer crystals by making bicrystals. The bicrystal is then polymerized and carrier mobility across the grain boundary, induced by a pulsed laser, can be measured.

This research on defects will allow the next phase of my research to proceed towards an understanding of specific mechanisms of deformation and other property effects in crystalline and semi-crystalline polymers.

Conclusions

Droplet experiments using diacetylenes which can be polymerized to yield macromolecule crystals with large regions of uniform crystallinity have been shown to be useful in determining local structure around individual defects. HREM examination of edges which are perpendicular to the chain axis have shown that there is uniformity, within the limits of resolution of the technique used (approximately 0.3 nm), of the packing of the chains as the approach the edge. There is no observed loss of orientation or splaying of the molecules.

At edges that are parallel to the chain axis, it has been demonstrated that the molecules exhibit a local curvature to conform to the curvature of the surface. The resulting curvature of the polymer chains are thought to be the result of the conforming of

365

the monomer precursor crystal structure to the surface and the freezing in of defects into the polymerized droplet. Dislocations with the Burgers vector parallel to the chain axis are needed to incorporate the the bending. Examples of polygonalization of the bending are the result of polygonalization of these defects. The effect of existing dislocations in the monomer structure may effect the ability of neighboring monomer units to polymerize in the growing chains and lead to regions of unreacted monomer in the polymer crystal that can be removed to gain information on the size of dislocation cores in anisotropic systems. Etching of droplets has given rise to etch pits that are approximately 6 nm square to 360 nm square with a slight anisotropy in the chain direction. The size variation is attributed to the congregation of defects such as in grain boundaries where three or more single dislocations may lie together.

HREM images of grain boundaries formed by the bending of planes of chains and the incorporation of planes of chain ends show that chain ends are important determining the amount of orientation that a macroscopic sample will have.

This study shows the importance of surface constraints on the perfection of the resulting polymer crystal. Fabrication of devices made of similar materials will need to be closely controled to eliminate the inclusion of a high density of defects which may adversely affect their performance.

Acknowledgements

References

1. G. Wegner, Z. Naturforsch., 24b, (1969), 824

2. M. Thakur and D.M. Krol, Appl. Phys. Lett., 56(13), (1990), 1213

3. F.L. Hirshfeld and G.M.J. Schmidt, J.Polymer Sci., A2, (1964), 2181

4. G. Wegner, in "Molecular Metals" (Ed., W.E. Hatfield), Plenum Press, New York, (1979)

5. J. Liao (private communication)

6. W. Schermann, G. Wegner, J. Williams, and J. Thomas, Journal of Polymer Science, 13, (1975), 753

7. K.C. Yee and R.R. Chance, J. Polym. Sci. Polym. Phys. Ed., 16, (1978), 431

8. C.S. Henkee, E.L. Thomas, and L.J. Fetters, J. Mat. Sci., 23, (1988), 1685

9. D.C. Martin, L.L. Berger, and K.H. Gardner, Macromolecules, 24, (1991), 3921

10. R.T. Read and R.J. Young, J. of Mat. Sci., 19, (1984), 327

11. P.A. Apgar and K.C. Yee, Acta Cryst., B34, (1978), 957

12. R.J. Young and J. Petermann, J. Polym. Sci. Polym. Phys. Ed., 20, (1982), 961

13. R.J. Young and J. Petermann, Makromol. Chem., 182, (1981), 621

14. R.J Young, R.T. Read, D. Bloor, and D.J. Ando, Discuss. Faraday Soc., 68, (1979), 509

15. P.H.J. Yeung and R.J. Young, Polymer, 27, (1986), 202

16. D.C. Martin, PhD Dissertation, University of Massachusetts, (1990)

17. Cambridge Molecular Design, a Molecular Simulations company (1990)

18. J.M. Cowley and A.F. Moodie, Acta. Cryst. 10, (1957), 609

19. Martin, D.C. and Thomas, E.L., Phil. Mag. A, 63, (1991), 903

20. T.H. Courtney, Mechanical Behavior of Materials, McGraw-Hill, New York, (1990)

21. F.R.N. Nabarro, Theory of Crystal Dislocations, Oxford University Press, (1967)

22. J.P. Hirth and J.Lothe, Theory of Dislocations, McGraw-Hill, New York, (1968)

23. R.H. Baughman, J. Polymer Sci., Polymer Phys. Ed., 12, (1974), 1511

24. G.N. Gerasimov, Mol. Cryst. Liq. Cryst., 187, (1990), 215

25. W.F. Smith, Principles of Materials Science and Engineering, McGraw-Hill, Inc., (1990)

26. S.L. Mayo, B.D. Oalfson, and W.A. Goddard III, J. Phys. Chem. 1, (1991)

27. D. Hull and D.J. Bacon, Introduction to Dislocations, 3rd Ed., Pergamon Press, (1984)
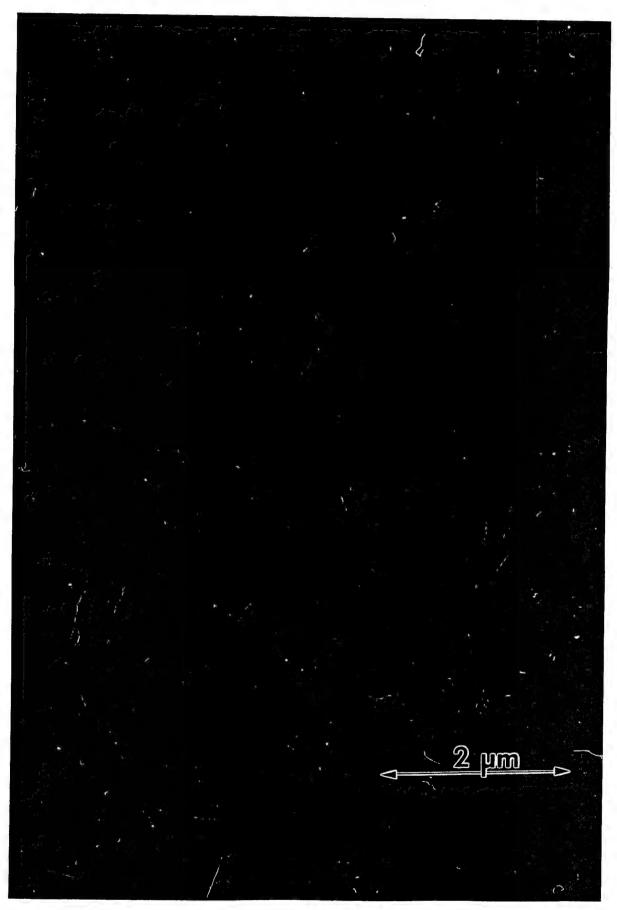
Figure 2: TEM micrograph of poly(DCHD) droplets showing how frequently they are formed and the lack of orientation of droplets with respect to each other as observed from the crack orientation.

Figure 3: TEM micrograph of a droplet of poly(DCHD) shadowed with gold from an incident angle of 12°. The chain axis is in the plane of the substrate and runs parallel to the observed cracks.
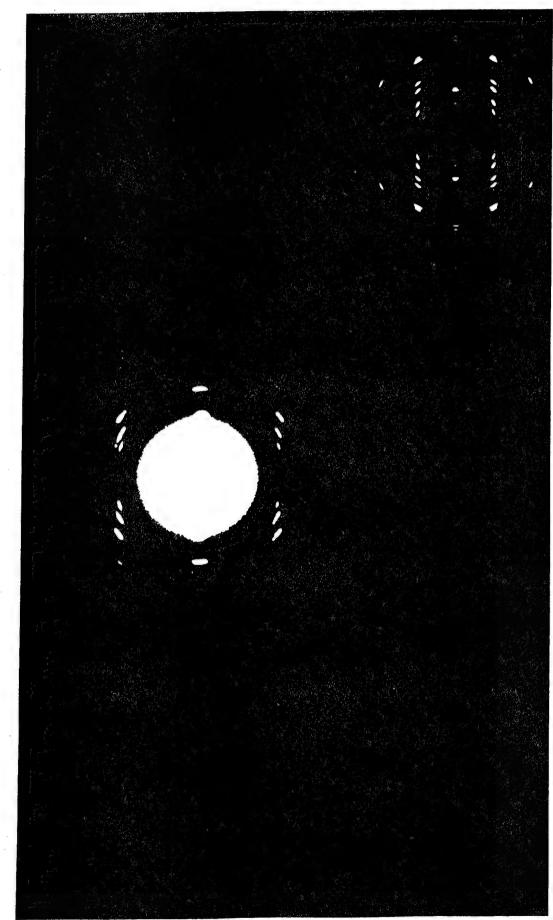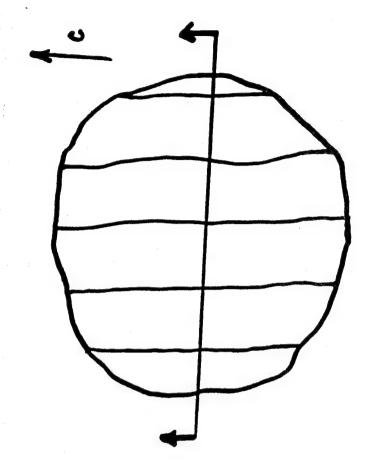
Figure 4: SAED of poly(DCHD) droplet. The mirror symmetry of the pattern suggests a fiber texture of the droplet. The inset shows a simulation of (CERIUS [17]) of the SAED pattern using a fiber texture geometry for the reported polymer crystal structure (Apgar and Yee [11]).
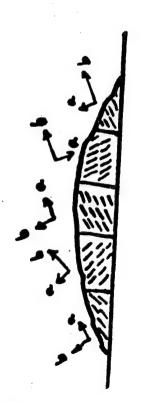
Figure 5: Schematic of droplet showing domains where the a and b axis are in differing orientations with respect to the substrate.
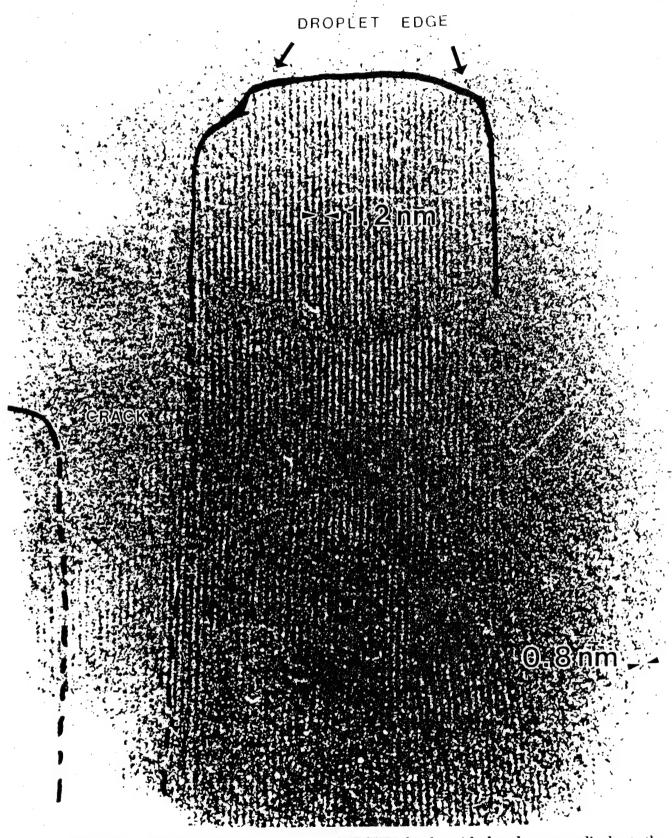
Figure 6: HREM image of the edge of a poly(DCHD) droplet with the edge perpendicular to the chain axis. There are two different orientations of the polymer chains visible, one with a spacing of 1.2 nm (010) and one with a spacing of 0.8 nm (200). A 0.6 nm fringe region stretching across the droplet in the middle of the image is believed to indicate a thickness of 100 nm.
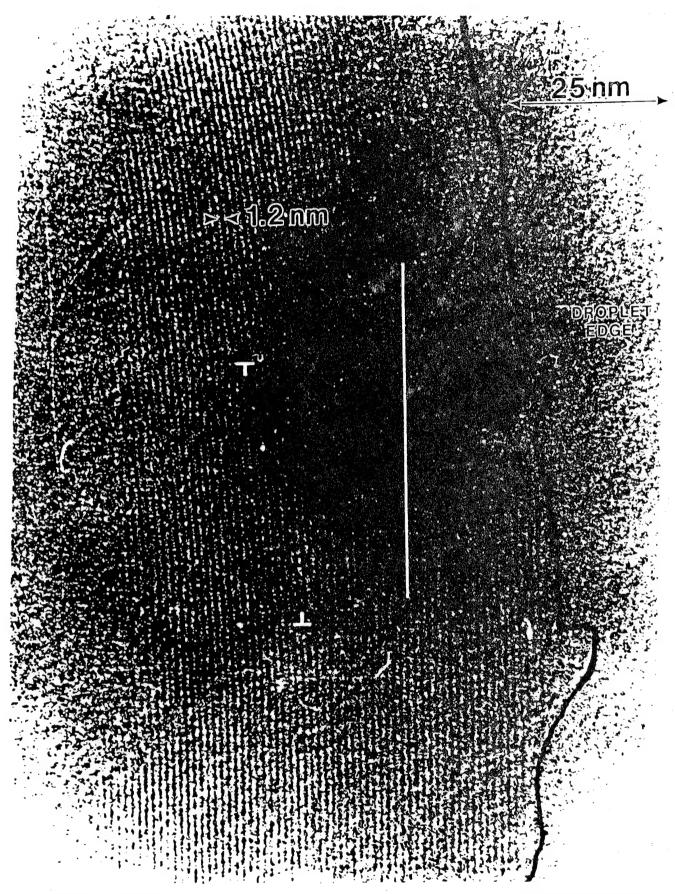
Figure 7: HREM image of DCHD droplet edge where the chain axis is parallel to the edge. The lattice fringes from the (010) plane can be seen to bend to conform to the droplet surface. Several edge dislocations with a Burgers vector in the [010] direction can be seen.

374

25 nm
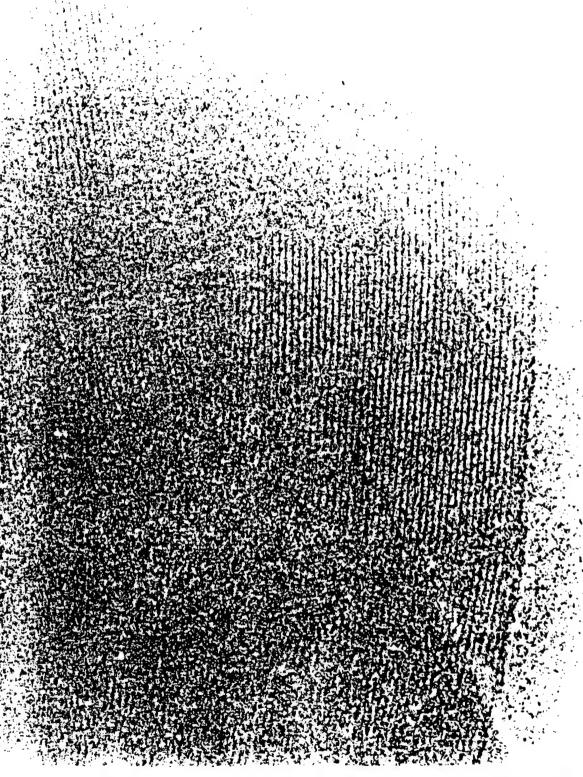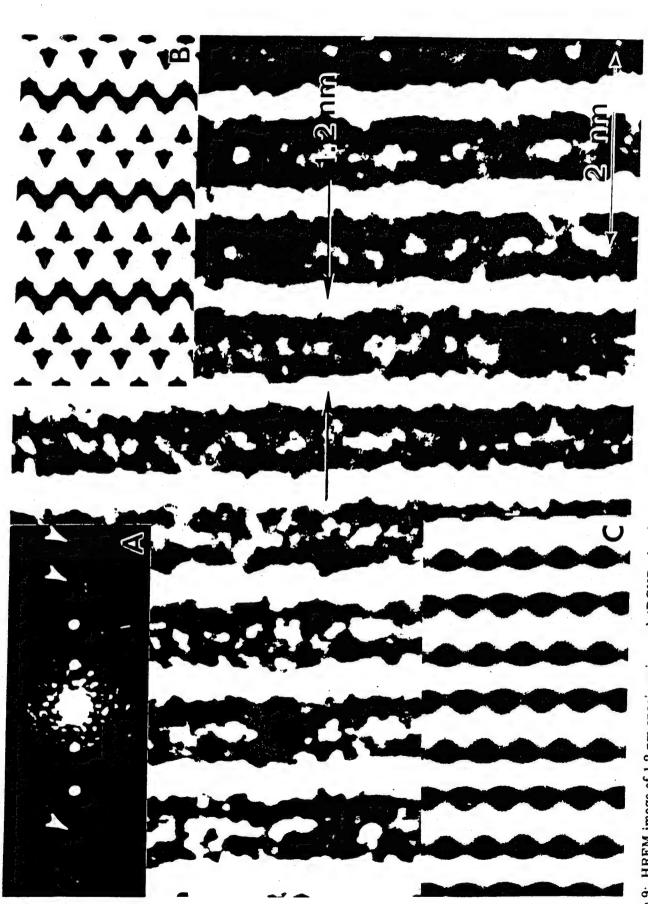
Figure 8: HREM image of poly(DCHD) droplet edge with fringes from (010) planes bent. On close inspection the bending is actually a series of tilt boundaries possible formed by the polygonalization of defects.

Figure 9: HREM image of 1.2 nm spacings in a poly(DCHD) droplet showing detail about the chain backbone and its side groups. Inset a) is the optical transform of the image showing the 4th order spots indicating a resolution of 0.3 nm. Inset b) is a simulated image of the projected electron potential for the (010) plane calculated using the multislice technique (MacTempas). Inset c) shows a simulated image of the planes using multislice transforms for the JEOL 4000 EX using $C_s = 1.0$ mm, an aperture of 0.25 Å^{-1}, -1000 nm defocus, defocus spread of $\Delta f = 8$ nm, and a sample thickness of 10 nm.

376
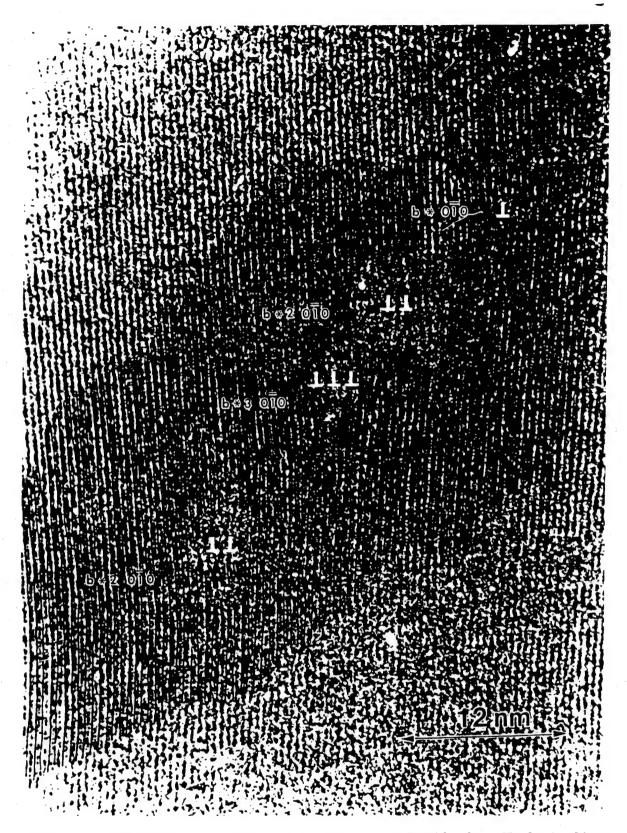
Figure 10: HREM image of a low angle tilt boundary in a DCHD droplet. The lattice fringes being imaged are the (010) planes with a spacing of 1.2 nm and correspond to the spacing between chains. The image has lines drawn to highlight the dislocations along the tilt boundary. The Burgers vector is [010] with a magnitude of 1.2 nm. Around the dislocations there is a region of crystal that the contrast does not give rise to lattice fringes, these areas measure from approximately 6nm to 36 nm. The angle of the tilt changes from 4° to 6° along the boundary. The distance between the imaged dislocations is approximately 7.0 to 12.0 nm.

377
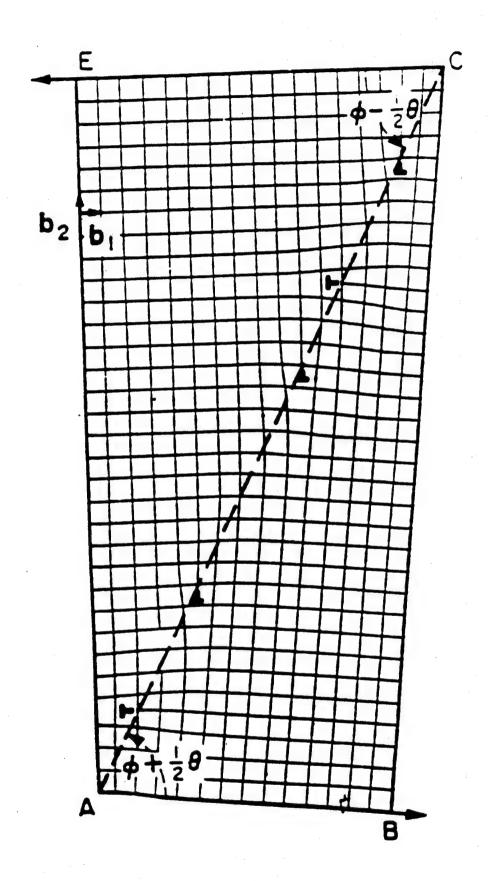
Figure 11: A graphical representation of a low angle tilt boundary of the type in figure 10 showing the inclusion of several dislocations located D from each other to incorporate the tilt. For figure 10, D is calculated to be 11.5 nm. [27]

378
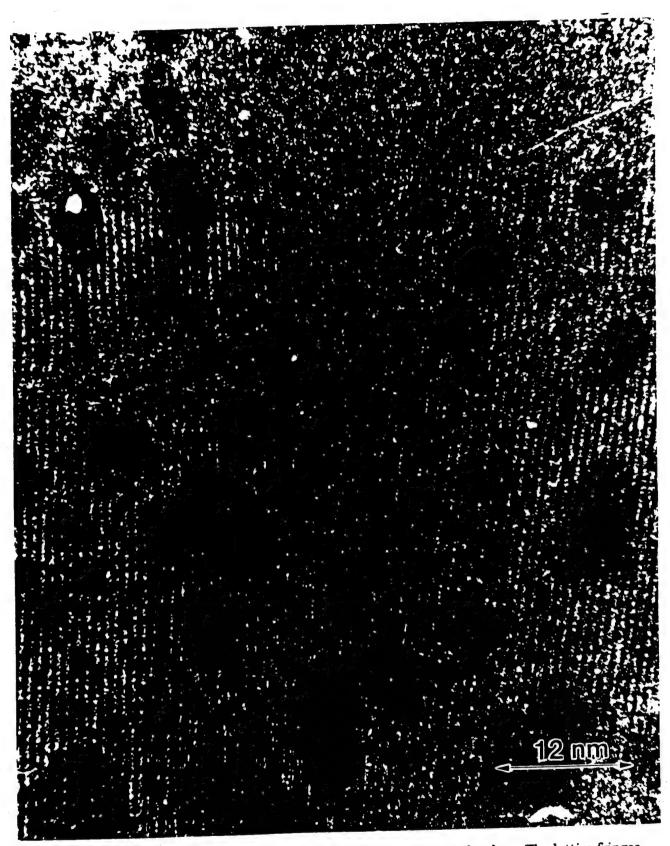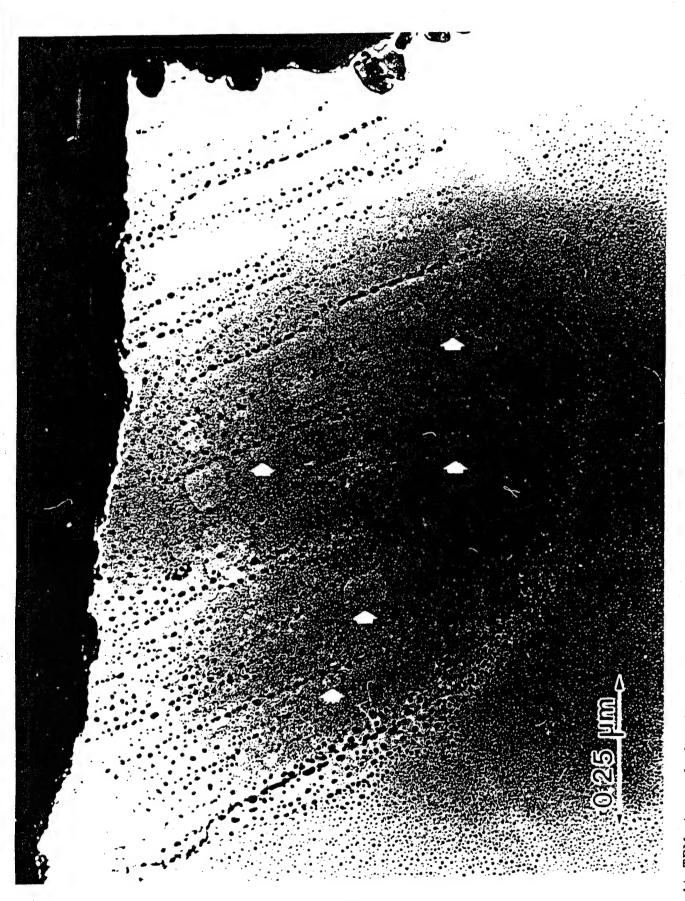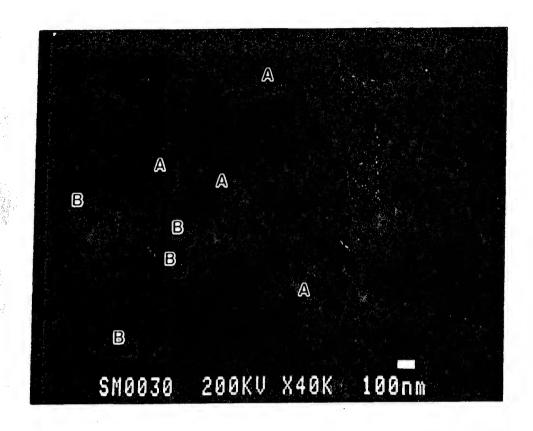
Figure 12: HREM image of a low angle tilt boundary in a DCHD droplet. The lattice fringes being imaged are the (010) planes with a spacing of 1.2 nm and correspond to the spacing between chains. The image has lines drawn to clarify the tilt of the crystals and the location of the dislocations needed to give the orientation. The angle of the boundary, θ, is 6°. The Burgers vector is the (010) spacing of the DCHD crystal, 1.2 nm, and the distance between dislocations, D, is measured to be approximately 12.5 nm.

Figure 14: TEM micrograph of a polymerized droplet of DCHD shadowed with gold and etched with a chloroform solution. The arrows point out holes that may be pits formed around a dislocation.

Figure 15: TEM micrograph of a polymerized DCHD droplet that was etched with a chloroform solution. The micrograph was taken in diffraction mode as a defocused (000) spot in order to increase the contrast. Arrows point out lines of possible etch pits that have polygonalized as a result of bending of the lattice at the edges.
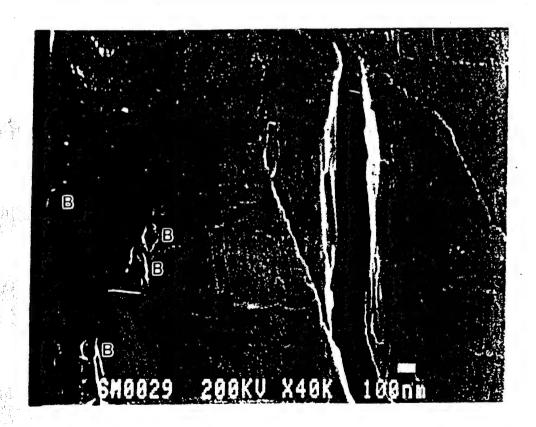
Figure 16: a) STEM image of etched poly(DCHD) droplet showing regions of low light contrast that correspond to voids (A) or surface holes (B) b) SEM image of same area of droplet that shows corresponding holes (B) in surface versus other areas that have no surface holes.
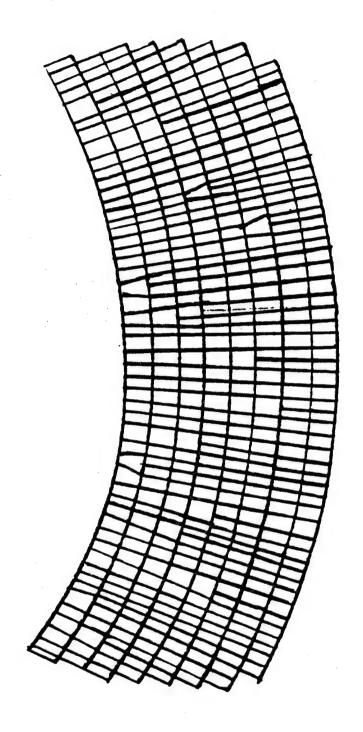
Figure 17: Schematic of a bent crystal with edge dislocations of the type **b**=[001] to incorporate the bending.
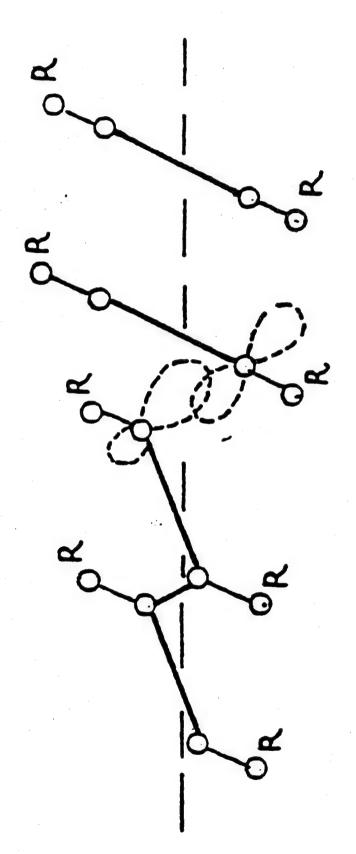
Figure 18: Scheme of the compressed growing chain in a DCHD crystal showing poor overlap of orbitals [24].
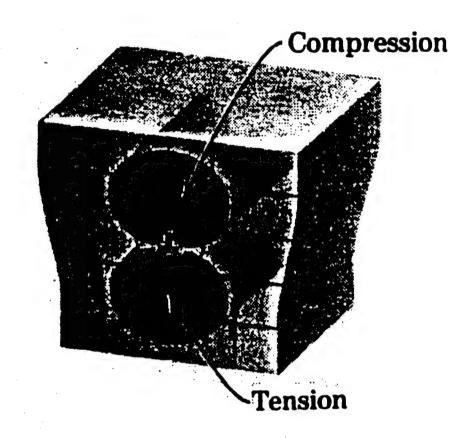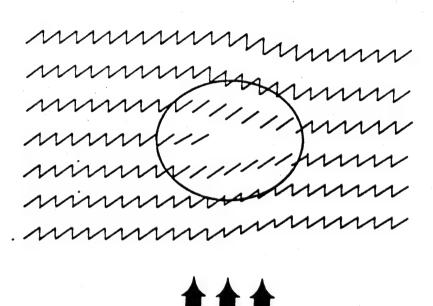
Figure 19: A schematic showing the strain fields surrounding an edge dislocation in an isotropic material [25].
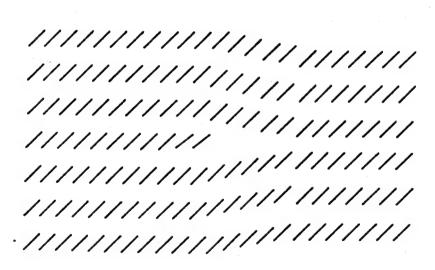
Figure 20: A schematic showing a edge dislocation in the monomer lattice of type b=[010] and the resulting transition to polymer with a region of unreacted monomer near the dislocation as a result of misorientation of the monomer units outside of the necessary polymerization parameters.
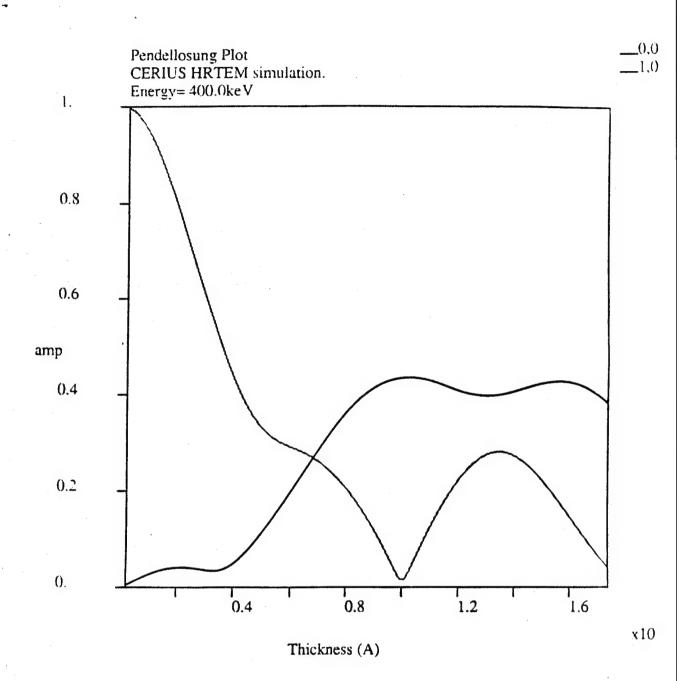
Figure 21: Pendellosung plot for poly(DCHD) showing the amplitude of the transmitted beam (
and the diffracted beam (010) versus sample thickness.
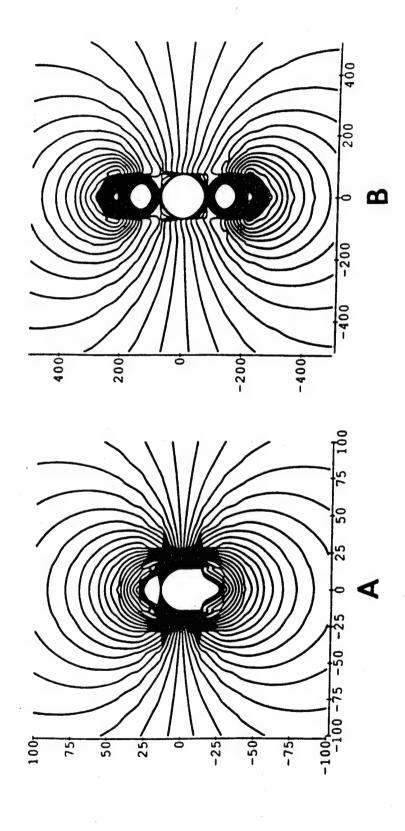
Figure 22: A) A plot of the hydrostatic pressure around an edge dislocation in DCHD monomer of type **b**=[010] using G =10 GPa, b = 1.37 nm, and n = 0.3. The shear modulus used is an average value found for a similar diacetylene [12], the magnitude of the Burgars vector is the (010) spacing of the DCHD monomer, and we assumed that for a first approximation we could model the system as an isotropic material although the monomer lattice is actually anisotropic. B) A plot of the hydrostatic pressure around a grain boundary made up three dislocations using the same assumptions.

STRUCTURAL CHARACTERIZATION OF MODULARLY CONSTRUCTED POLYAROMATIC MACROCYCLES
Patricia M. Wilson

Structural Characterization of Modularly Constructed Polyaromatic Macrocycles

Patricia M. Wilson and David C. Martin
Materials Science and Engineering Department

Jinghan Zhang and Jeffrey S. Moore
Chemistry Department

University of Michigan

Determination of the Structure of Polyaromatic Macrocycles

Patricia M. Wilson and David C. Martin
Department of Materials Science and Engineering

Jinghan Zhang and Jeffrey S. Moore
Department of Chemistry

The University of Michigan, Ann Arbor, MI   48109
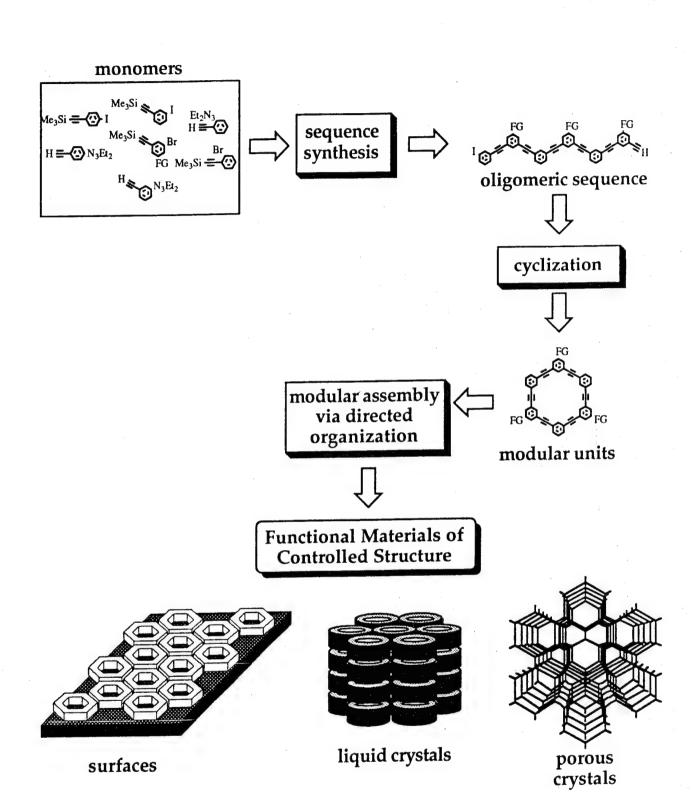
A novel family of cyclic molecules has been synthesized opening up the possibility of many tailored microstructures based on washer shaped building blocks.   Several of the family of molecules have been investigated using different structural probes to determine the organization of the crystals. Powder X-ray diffraction patterns show a decrease in crystallinity as the length of the side groups are increased. Molecular mechanics simulations using PolyGraf software indicate that the cyclic "backbone" ($C_{60}H_{48}$) of the molecule is rigid allowing the molecules to pack in a face to face manner. The steric distance between molecules is estimated to be 0.35 nm. This spacings is predominate in many of the electron diffraction patterns, X-ray diffraction patterns, and Scanning Tunneling Microscopy images.

Using Selected Area Electron Diffraction (SAED) patterns taken with low dose techniques, the crystal structure of one molecule (C-60) has been estimated to be a hexagonal unit cell. SAED patterns showing six-fold symmetry have also been observed.

Direct imaging of 2.2 nm fringes from C-60-B has been performed showing small crystallites which correspond with the SAED and X-ray diffraction information.

Engineered Microstructures

The ability to engineer the structure and conversely the properties of a material is important for future applications. A new class of polyaromatic macrocycles have been synthesized. These molecules are unique in their cyclic "backbone" and the ability to tailor the length of side groups. The intention is to use these molecules to build useful microstructures as seen in the schematics. The possibility exists to develop porous films with well defined pore sizes for filtration or polymer tubes with one dimensional transport properties. By varying the side group length, these materials could also be used to investigate the onset of liquid crystalline behavior and the nature of ordering. The structure of several of the family of polyaromatic macrocycles have been investigated.

monomers

sequence synthesis

oligomeric sequence

cyclization

modular assembly via directed organization

modular units

Functional Materials of Controlled Structure

surfaces

liquid crystals

porous crystals

Modular Construction -Some Hypothetical(?) Examples

a)

trimerization

b)

Polyaromatic Macrocycles
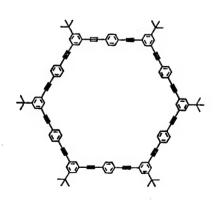
C-60

C-60-B

C-60-ET

C-60-BET

C-120
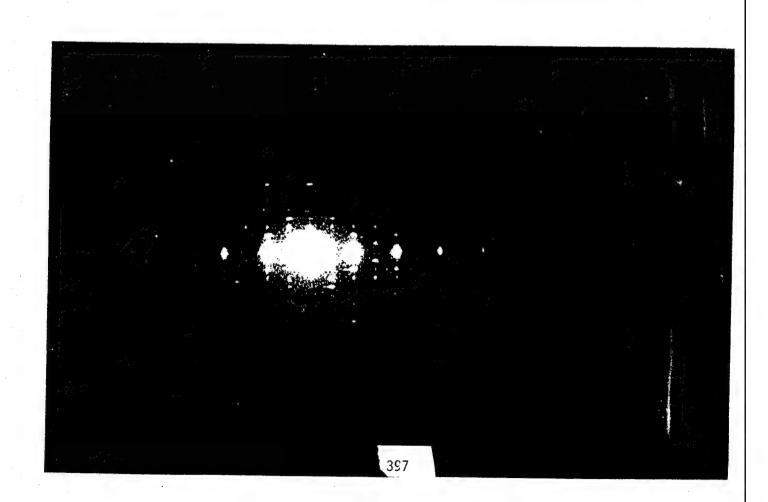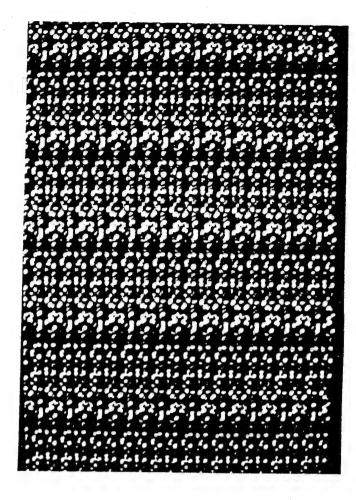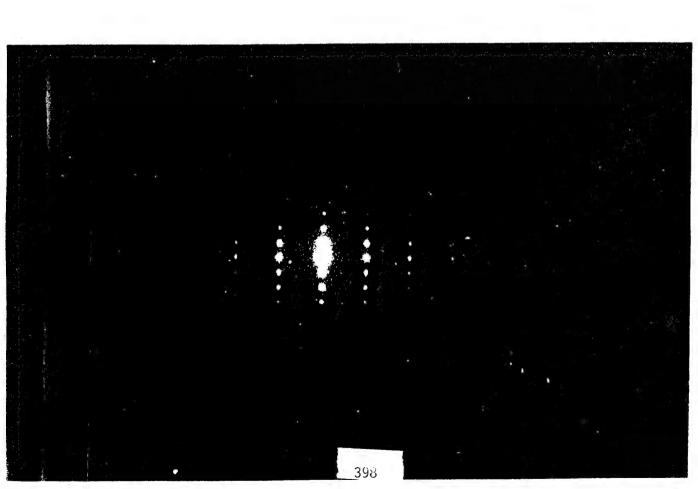
Figure 1: a) SAED of C-60 crystal. Spacings are 0.774 and 1.983 nm. **b)** (100) projection of proposed crystal structure. SAED patterns calculated for zone axises [100] and [010] match the experimentally observed pattern in a).

Figure 2: **a)** SAED of C-60 crystal. Spacings are 0.383 and 10.90 nm. **b)** Tilted orientation of proposed crystal structure. SAED patterns calculated for zone axises [310] and higher [h10] match the experimentally observed pattern in a).
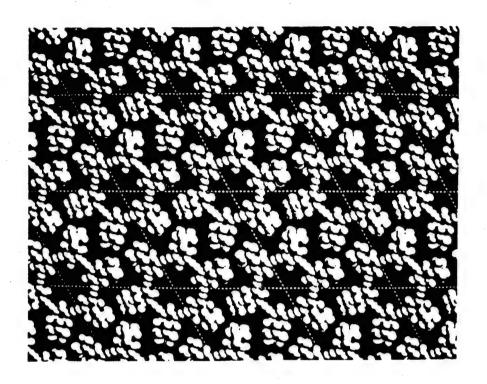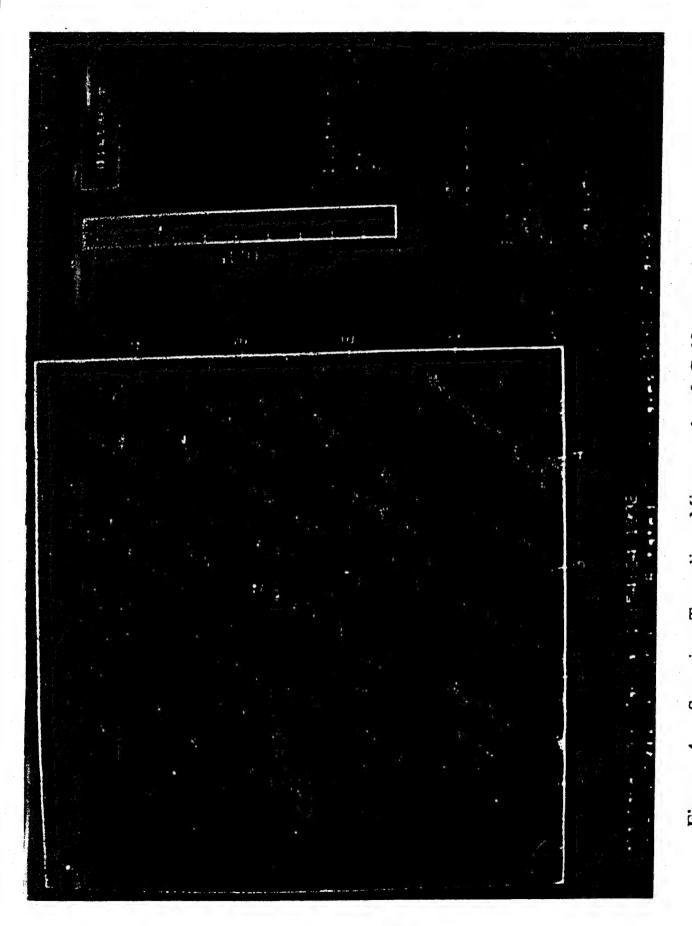
Figure 3: (001) projection of proposed crystal
structure.

Figure 4: Scanning Tunneling Micrograph of C-60 crystal surface showing 0.3-0.4 nm spacings and 1.5 nm spacings. (John Pochan, Polymer Research Labs, Eastman Kodak Research Laboratory, Rochester, NY).

Structure Information of Similar Macrocycles
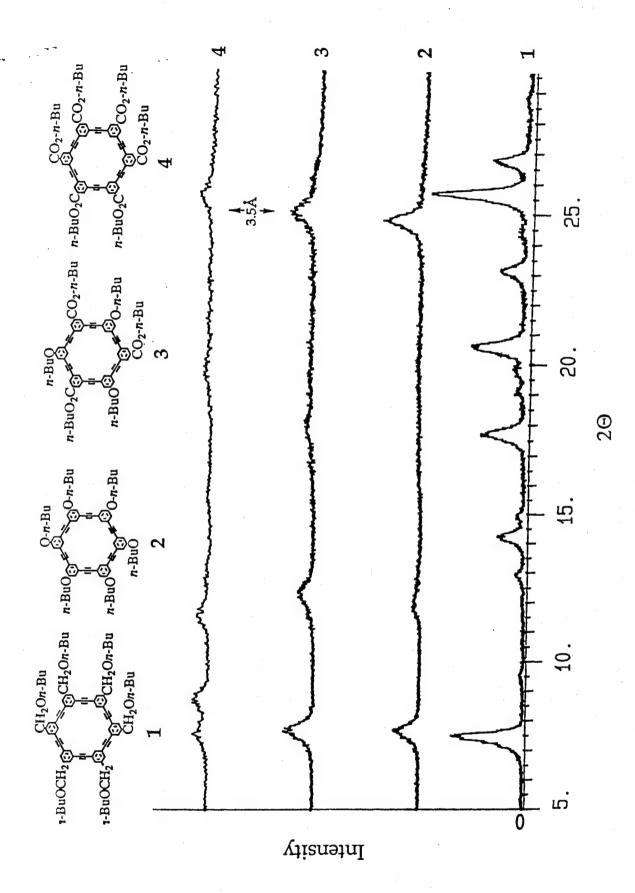
Several generations of related polyaromatic molecules have been synthesized. Since they all have the same cyclic "backbone" with different side groups, we can use information from all the molecules to help in structure determination.

Powder X-ray Diffraction has been performed on four derivatives showing a loss in order as the length of side groups are increased. All molecules show similar characteristic spacings of approximately 3.5 Å and 11 Å.

Scanning Tunneling Microscopy of C-60 and C-120 molecules show approximate 3.5 Å spacings. Molecular Mechanics using PolyGraf software have shown the cyclic "backbone" of these molecules to be planar due to electron delocalization and an approximate thickness of 3.5 - 4 Å. This would suggest that the molecules pack together face to face like "washers".

Transmission Electron Microscopy of crystals of C-60-ET have shown faceted crystals with angles close to 120°. Selected Area Electron Diffraction Patterns of these crystals show six fold symmetry as would be expected if looking down on basal planes of a hexagonal unit cell. The presence of a twinned crystal is seen both in the TEM image and in the SAED as two superimposed patterns.

401

Figure 5: Powder X-ray diffraction patterns for four polyaromatic macrocycle molecules. As the length of the side chains increase, the crystallinity decreases. All the patterns exhibit spacings at approximately 0.35 nm.

Figure 6: Scanning Tunneling Micrograph of C-120 crystal surface showing 0.3-0.4 nm spacings. (John Pochan, Polymer Research Labs, Eastman Kodak Research Laboratory, Rochester, NY).
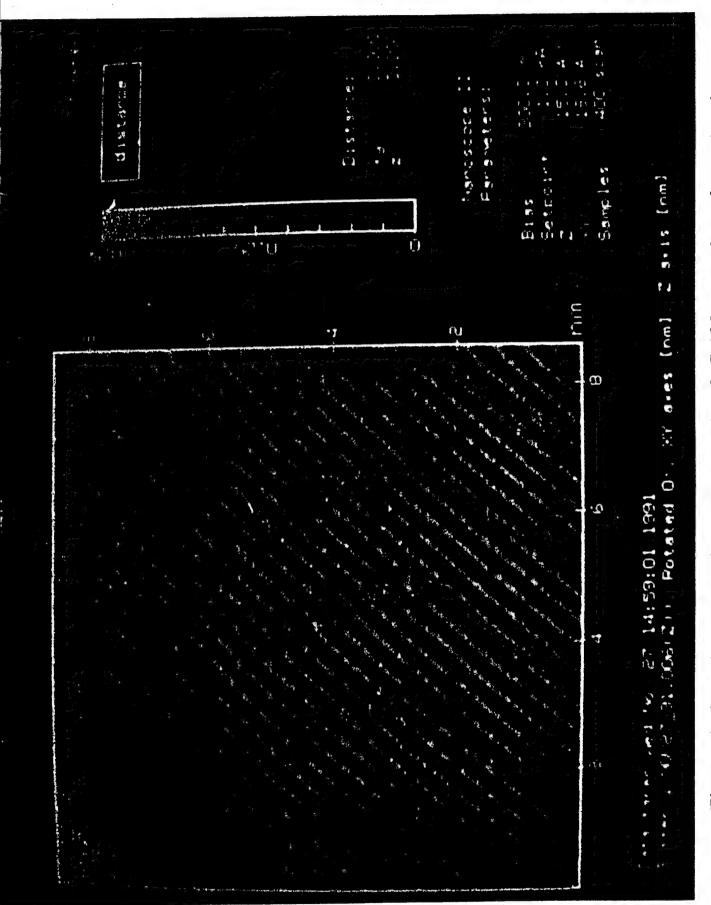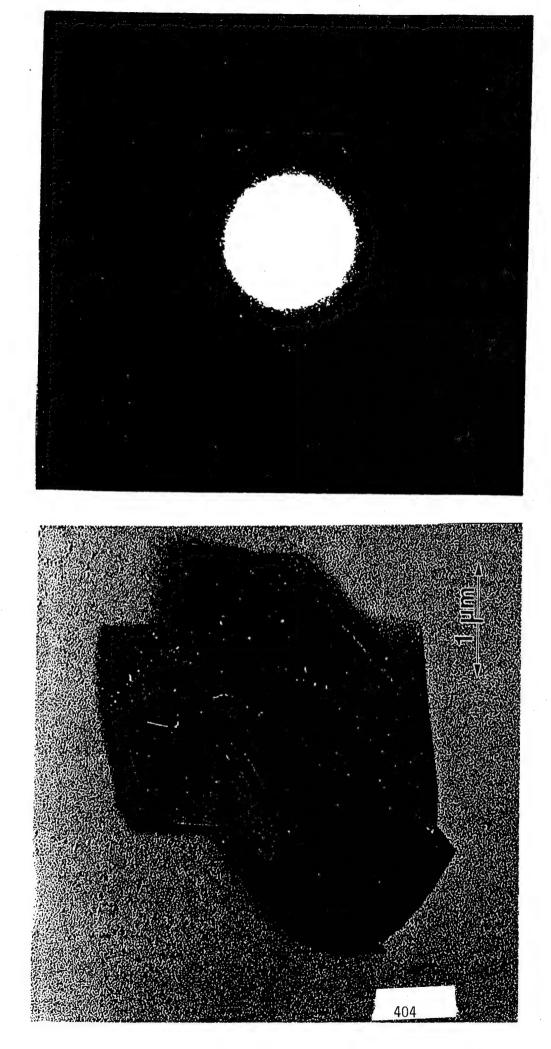
Figure 7: a) TEM micrograph of C-60-ET crystal. The crystal appears to be twinned and several facets are at an angle of 120°. b) SAED of a twinned C-60-ET crystal. The pattern shows six-fold symmetry and spacings are 0.21 and 0.12 nm.

404

Lattice Imaging

High Resolution Electron Microscopy (HREM) can be used to image the lattice of organic crystals but has had limited application because of the sensitivity of organic molecules to beam damage. Using innovative extremely-low dose procedures, developed in our lab, ordered organic materials which had previously eluded direct lattice imaging can now be investigated to provide information on their structure.

HREM samples were prepared by evaporating a dilute solution on amorphous carbon and collecting the film with copper grids. Imaging was performed on a JEOL 4000 EX at 400 kV using low dose procedures and a YAG-video system. The total end point dose (TEPD) was measured for all materials and imaging was kept below 75% of the TEPD.

405

Electron Damage Sensitivity

Molecule	TEPD (C/cm^2)
C-60	4.5×10^{-2}
C-60-BET	1.8×10^{-2}
C-60-ET	1.4×10^{-2}
C-60-B	8.6×10^{-3}

The TEPD increases as a function of crystallinity

406
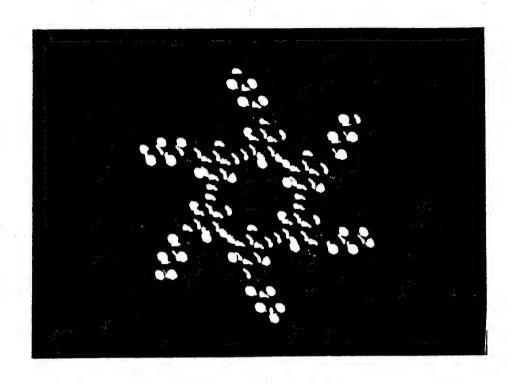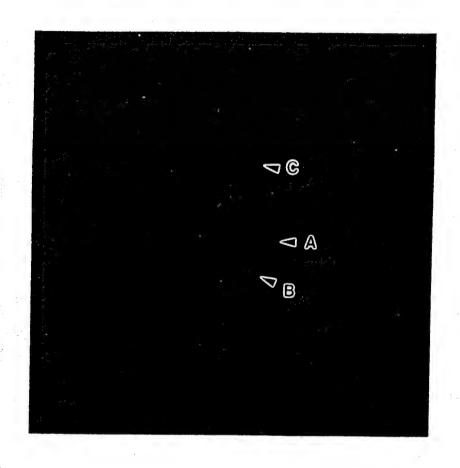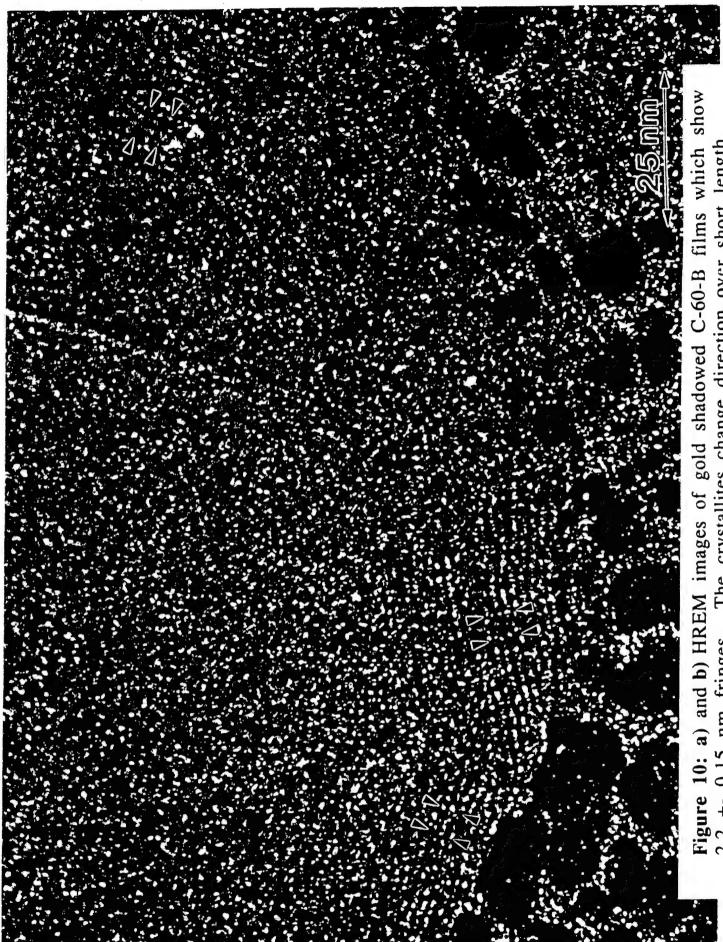
Figure 8: C-60-B molecule.

Figure 9: SAED of C-60-B molecule. The pattern shows misorientation of crystallites as seen in the HREM images. Spacings are A=0.362 nm, B=0.356 nm, and C=0.195 nm.

Figure 10: a) and b) HREM images of gold shadowed C-60-B films which show 2.2 +- 0.15 nm fringes. The crystallites change direction over short length scales and are pointed out with arrows.
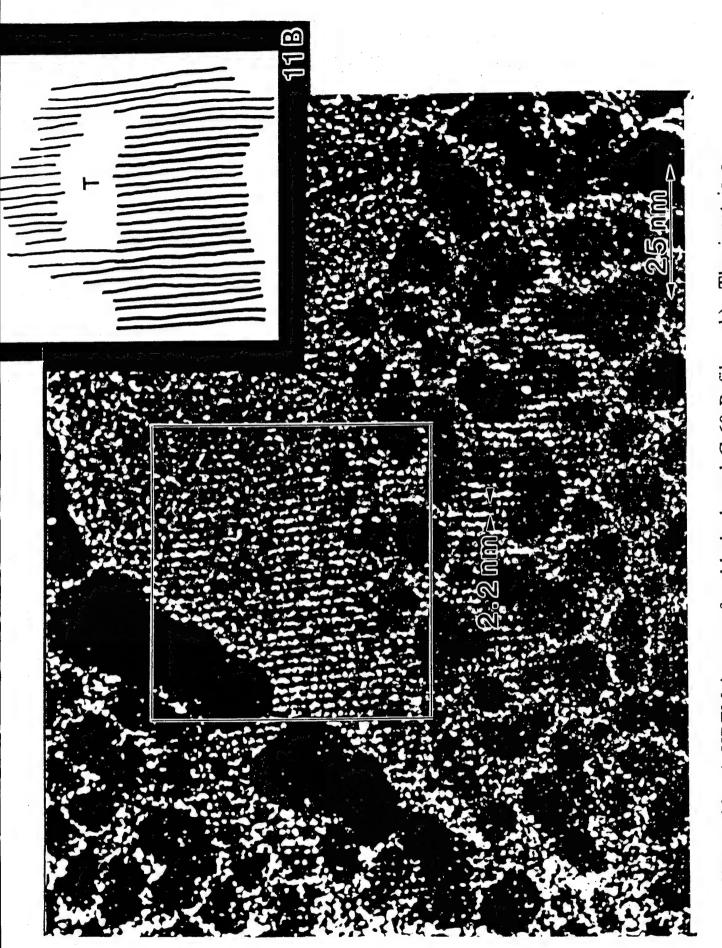
Figure 11: a) HREM image of gold shadowed C-60-B film. b) The inset is a tracing of the lattice fringes in box showing an edge dislocation defect.

411

Conclusions

The data obtained by several structural probes suggests that the family of polyaromatic macrocycles organize in a face to face manner. The data also suggests that the unit cell may have three- or six-fold symmetry.

The amount of crystallinity as illuminated by HREM and SAED is consistent with X-ray diffraction experiments, as longer side groups are added to the cyclic "backbone", the crystallinity decreases.

As we continue to directly image the materials, more information will provide us with a better understanding of the structure.

412

Future Work

Future work will include Small Angle X-Ray Diffraction on powder samples to measure larger spacings and HREM of the entire family of molecules.

Acknowledgments

Crystal Structure Determination

Due to the limited supply of newly synthesized materials, the normal procedure of using single crystals to perform structure determination by X-ray diffraction is problematic. Using low dose electron diffraction, information about the crystal structure can be obtained using extremely small amounts of material. The limited information available from many means together with molecular simulation can provide an approximation to the structure that can be refined further as new data is obtained.

C-60 has been investigated in this manner. Low dose electron diffraction patterns were obtained from this material which has a TEPD of 4.5×10^{-2} C/cm^2. Using the systematic absences that are apparent in the electron diffraction patterns a limited number of space groups were available to simulate. The structure obtained is a hexagonal unit cell. The three fold symmetry of the molecule fits neatly into the cell thereby maximizing the density. Using the hexagonal unit cell supposition, electron diffraction patterns of basal planes would have six fold symmetry and have been observed. Further refinement of the unit cell is anticipated as more information becomes available.

C-60 Unit Cell

space group	P6$_3$
a	2.235 nm
b	2.235 nm
c	0.774 nm
α=β	90°
γ	120°

COMPUTATIONAL MODELING OF PBZT CRYSTALS
K. S. Macturk

COMPUTATIONAL MODELING OF PBZT CRYSTALS

K. S. Macturk and R. K. Eby
Dept. & Inst. of Polymer Science, The University of Akron
Akron, OH 44325-3909, USA

B.L. Farmer
Dept. of Materials Science, The University of Virginia
Charlottesville, VA 22901, USA

ABSTRACT:

Molecular dynamics simulations were performed in an attempt to elucidate the molecular mechanism of a relaxation measured experimentally in PBZT fibers. Results for the coefficient of thermal expansion parallel to the molecular axis and tensile modulus agreed favorably with published experimental values. The x-ray peak intensity ratio of (200)/(010) versus temperature obtained from the simulations showed a variation qualitatively similar to that from experiments. The torsion angle between the benzobisthiazole and phenyl moieties increased with temperature. A distortion of the phenyl and benzobisthiazole moieties also occurred and the molecules were observed to undergo increased oscillatory ribbon-like motions perpendicular to the (010) plane as the temperature increased. Finally, translational oscillations of the molecules parallel to the c-axis occurred. These molecular motions are coupled to the tensile stress and could play a role in the relaxation.

INTRODUCTION:

PBZT fibers are well known for their high specific tensile strength and specific modulus. They also have potential for use in high temperature applications. Therefore, it is necessary to understand their behavior in these environments. Use of ultrasound to investigate the modulus-

temperature relationship of these fibers produced evidence of a relaxation in the $300\text{-}400^{\circ}$ C temperature range[1]. A change in the ratio of the wide angle x-ray diffraction peak intensity of (100) (one molecule per unit cell) relative to (010) was also found in this temperature range. In addition, a peak in attenuation of the ultrasonic waves used to make the modulus measurements was found and TGA measurements showed a small weight loss. The combined data suggest a relaxation is occurring. The authors noted that there must be a coupling between the applied stress and the molecular mechanism of the relaxation. A change in the torsion angle between the benzobisthiazole and phenyl moieties was proposed as a possible mechanism. A similar change has been observed in *para*-phenylenes[2]. It was also noted that there is evidence of a mechanical relaxation in other polymers which contain heterocyclic moieties in the backbone[3,4]. The purpose of this note is to report results from a modeling investigation of the molecular mechanisms that might be involved in the relaxation.

COMPUTATIONAL METHOD:

Molecular dynamics simulations were performed using the Sybyl® software package from Tripos Associates. The force fields were modified according to published work[5]. The non-primitive unit cell[6] was minimized using a grid search. The experimental unit cell and minimized unit cell dimensions are shown in Table 1. The value of γ was 94.0°. An array of chains arranged as shown in Figure 1 was used for the simulations. The molecules were five monomers in length. Alternating rows of molecules in the array were shifted one-third of a repeat unit in the z-direction. Thus, a unit cell consists of molecules 1-6 in Figure 1, with molecules 2,5 and 8 shifted one-third of a repeat unit in the z-direction relative to the others. During the dynamics

runs, molecules 2,4,5,6 and 8 were allowed to move. The rest of the molecules were held fixed due to memory and speed limitations of the computer. Dynamics simulations 10,000 fs in length were run at temperatures of 27, 197, 277, 347, 427, 497, and 577° C. Time steps of 1 fs were used with data being saved every 25 fs. Since the autocorrelation functions of the properties of interest showed the data were not yet uncorrelated, the simulation at 27°C was extended to 100,000 fs. Even this extended simulation time did not result in uncorrelated data. Since the size of the dynamics history file was very large, the calculation could not be extended. The dimensions of the arrays were expanded with temperature to match experimental values of the unit cell dimensions and γ was held constant[1].

In order to test the validity of the simulations the coefficient of thermal expansion and the tensile modulus were calculated. The tensile modulus for the array run at 27° C was found using a published approach[7]:

$$E = 4v^2L^2\rho$$

where E is the tensile modulus, v is the frequency of the longitudinal acoustic mode, L is the length of the molecule and ρ is the density of the unit cell. The frequency of the mode was found by doing a Fourier transform of the length of the central molecule versus time. The coefficient of thermal expansion was calculated with the time average lengths at 27, 347 and 427°C.

The x-ray intensity of the relevant peaks were calculated using the following formula:

$$I_{(hkl)} \sim [\{\Sigma\ f_j\ e^{-Mj}\ \cos 2\pi(hu_j + kv_j + lw_j)\}^2 + \{\Sigma\ f_j\ e^{-Mj}\ \sin 2\pi(hu_j + kv_j + lw_j)\}^2]$$

where f_j is the atomic scattering factor for atom j; u_j, v_j and w_j are the fractional coordinates of atom j; $M_j = 8\pi^2\mu^2[(\sin\theta)/\lambda]^2$; μ^2 is the mean squared displacement of atom j normal to the plane with Miller Indices (hkl); θ is one-half the scattering angle and λ is the wavelength of radiation

used. Molecules 5 and 6 from Figure 1, both of which were allowed to move during the simulations, were used to calculate the time average x-ray intensities. Theoretically it is difficult to accurately estimate μ^2 in anisotropic materials. Using molecular modeling it is a fairly straightforward task.

RESULTS AND DISCUSSION:

The thermal expansion coefficient and tensile modulus are given in Table 2 along with experimental results from the literature. The modeling results compare favorably with the experimental values. In addition the computed coefficient for 27 to 347°C matched that determined for a modeling time of 3,000fs[8]. Finally, the results for 27°C changed little during the extended simulation time. Thus, the model appears to be reasonably valid.

The modeling analog of the experimental x-ray results is given in Figure 2. In this figure, as in all others, the errors are less than or equal to the size of the symbols themselves. The curve exhibits an increase in the peak intensity ratio in the 300-400°C range which is qualitatively similar to the experimental curve. In addition the magnitude of the curve is correct. Examination of the change in intensity ratio in further detail shows that the intensity of the (200) peak remains essentially constant over the temperature range (Figure 3) while the intensity of the (010) peak decreases as the temperature increases (Figure 4). This accounts for the increase in the ratio of the peak intensities (200)/(010). Thus, the molecular mechanism responsible for this decrease must increase the displacement of the atoms relative to the (010) planes while leaving the distance from the (200) planes relatively unchanged. Figure 4 also shows that the decrease in (010) intensity is due mainly to the motion of the aromatic carbon and sulphur atoms. The labels

422

in Figures 3 and 4 indicate the atom types which were considered to be moving in the calculation, i.e. the atom types for which the e^{-M} term was included. Thus, the curves labeled by atom type in Figures 3 and 4 must be examined mainly for changes in intensity since the magnitude of the intensity has been altered due to the fact that motion of only the specified types of atoms was taken into account.

A further investigation of the aromatic carbon atoms shows that the decrease in (010) intensity is due mainly to a decrease in the intensity contributions from the aromatic carbons in the benzobisthiazole moieties (Figure 5). Thus, the molecular mechanism of the increase in the peak intensity ratio would seem to be an increase in the displacement of the aromatic carbon and sulphur atoms with the aromatic carbon atoms in the benzobisthiazole moieties experiencing a larger increase in displacement than do those in the phenyl moieties.

The exact nature of the molecular mechanism is difficult to discern. The increase in rms torsion angle between the phenyl and benzobisthiazole moieties was mentioned earlier. In addition, examination of the molecules during dynamics playbacks showed another displacement mechanism to be a combination of an increase in ribbon-like oscillatory motion of the molecules as a whole perpendicular to the (010) plane as well as a puckering of the phenyl and benzobisthiazole moieties as the temperature increases. Figure 6 shows an example of this for a simulation at 277°C. In general, the shape of the molecules at any given moment appears similar to that reported previously to account for the negative coefficient of thermal expansion parallel to the molecular axis[8]. The effects of the torsion angle and ribbon-like motions are hard to separate.

In addition, mean square displacements of ~ 0.1 Å^2 along the c-axis were found at room

423

temperature. The mean square displacements increased with temperature. These displacements would be affected by the finite size of the model. For example, the magnitude of the barrier that must be surmounted for a given translation would be reduced. Therefore, the magnitude should be viewed qualitatively. Nevertheless, the array is ordered at the start of the simulation and the c-axis displacements can be thought of as axial translational disorders. These disorders will have the effect of reducing intensities of spots on the upper layer lines of a fiber diffraction pattern[9] and, thus, help to explain the limited number of reflections seen on the upper layer lines in PBZT.

It is possible that the above motions are involved in the relaxation. The axial translations will be coupled to tensile stress applied along the fiber axis. Since the ribbon-like motion shortens the molecule, it too will be coupled to the tensile stress. Finally, the torsional oscillations of the moieties are also coupled to the tensile stress[10]. Provided that the molecules rearrange with a resulting strain at a relaxation time τ under an applied stress and that the frequency of the applied stress is equal to $1/(2\pi\tau)$, a relaxation will be observed. For the experimental frequency used, the relaxation time in the 300-400°C range would be on the order of 3×10^{-7} sec, which is considerably longer than the simulation time. However, the motions are coupled to the stress and could be involved in the relaxation. This possibility is strengthened by the good agreement between experimental and modeled results for x-ray, modulus and thermal expansion data.

CONCLUSION:

The results of the dynamics simulations show the same general behavior for the x-ray

intensity ratio versus temperature as does experiment. The mechanism appears to be due an increase in displacement relative to the (010) planes of the aromatic carbons, mainly those in the benzobisthiazole moieties, and the sulphur atoms. The displacement results from a combination of torsional oscillations between the phenyl and benzobisthiazole moieties, a ribbon-like motion of the molecule as a whole perpendicular to the (010) plane and out of plane distortions of the phenyl and benzobisthiazole moieties themselves. Finally, translational motions of the molecules parallel to the c-axis were observed. These motions might play a role in the mechanical relaxation which has been observed.

Unit Cell Dimension	Experimental Unit Cell[6] ($\mathring{A}$)	Minimized Unit Cell ($\mathring{A}$)
a	11.790	13.150
b	3.539	3.189
c	12.514	12.711

Table 1. Experimental and Minimized Unit Cell Dimensions.

Property	Experimental	Modeling
CTE ($\times 10^{-6}$ K^{-1}) (27-427 °C)	-7[11] (oriented film)	-6
Tensile Modulus(GPa)	450[1]	370

Table 2. Comparison of Experimental and Modeling Results.

Figure Captions:

Figure 1. Molecular array used for dynamics simulations. Molecules are five monomers long. The (200) plane is vertical and the (010) plane is horizontal. Benzobisthiazole moieties are parallel to (010) and phenyl moieties are approximately 20° from (010). Molecules 2,5 & 8 are shifted one-third of a repeat unit into the page.

Figure 2. Modeled x-ray intensity ratio (200)/(010) vs. temperature.

Figure 3. Modeled x-ray contributions from various atom types to (200) intensity vs. temperature.

Figure 4. Modeled x-ray contributions from various atom types to (010) intensity vs. temperature.

Figure 5. Modeled x-ray contributions from aromatic carbons for (010) intensity vs. temperature.

Figure 6. Ribbon-like distortion of molecule at 277° C. The bottom molecule is undistorted.

REFERENCES:

1. Jiang, H.; Eby, R.K.; Adams, W.W.; Lenhart, P.G. "Nonlinear Elasticity of Poly(p-phenylene Benzobisthiazole) Fibers" in The Materials Science and Engineering of Rigid-Rod Polymers. W.W. Adams, R.K. Eby and D.E. McLemore, eds., MRS, Pittsburgh, PA, 341-350 (1989).

2. Baudour, J.L.; Delugeard, Y.; Rivet, P. *Acta Cryst.* **B34**, 625 (1978).

3. Ii, T.; Tashiro, K.; Kobayashi, M.; Tadokoro, H. *Macromolecules*, **19**, 1809 (1986).

4. Tashiro, K.; Nakata, Y.; Ii, T.; Kobayashi, M.; Chatani, Y.; Tadokoro, H. *Sen-i-Gakkaishi*, **44**(1), 7 (1988).

5. Farmer, B.L.; Chapman, B.R.; Dudis, D.S.; Adams, W.W. *Polymer*, **34**, 1588 (1993).

6. Fratini, A.V.; Lenhart, P.G.; Resch, T.J.; Adams, W.W. "Molecular Packing and Crystalline Order in Polybenzobisoxazole and Polybenzobisthiazole Fibers" in The Materials Science and Engineering of Rigid-Rod Polymers. W.W. Adams, R.K. Eby and D.E. McLemore, eds. MRS, Pittsburgh, PA, 431-435 (1989).

7. Tadokoro, H. Structure of Crystalline Polymers. John Wiley & Sons, New York, 309 (1979).

8. Klunzinger, P.E.; Green, K.A.; Eby, R.K.; Farmer, B.L.; Adams, W.W.; Czornyj, G. Tech. Papers XXXVII. Society of Plastics Engineers, Brookfield, CT, 1532-1536 (1991).

9. Clark, E.S.; Muus, L.T. *Zeit. Krist.* **117**, 108-118 (1962). see also Vainshtein, B.K. *Diffraction of X-rays by Chain Molecules*; Elsevier: New York, 1966; pp. 277-282.

10. Wierschke, S.G. "Computational Predictions of the Tensile and Compressive Properties of Rigid-Rod Polymers" in The Materials Science and Engineering of Rigid-Rod Polymers. W.W. Adams, R.K. Eby and D.E. McLemore, eds., MRS, Pittsburgh, PA, 313-327 (1989).

11. Lusignea, R.W.; Foster-Miller Inc. "Film Processing and Applications for Rigid-Rod Polymers" in The Materials Science and Engineering of Rigid-Rod Polymers. W.W. Adams, R.K. Eby, and D.E. McLemore, eds., MRS, Pittsburgh, PA, 265-276 (1989).

428

Figure 1
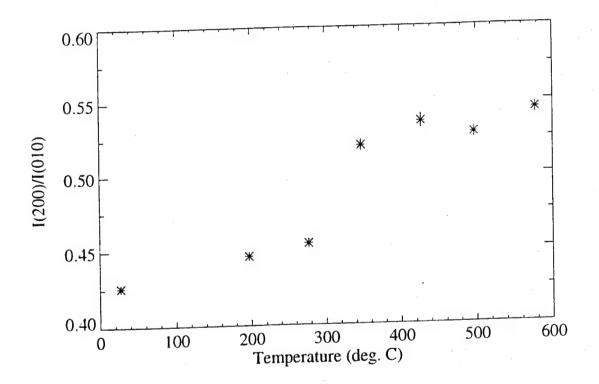
Figure 2
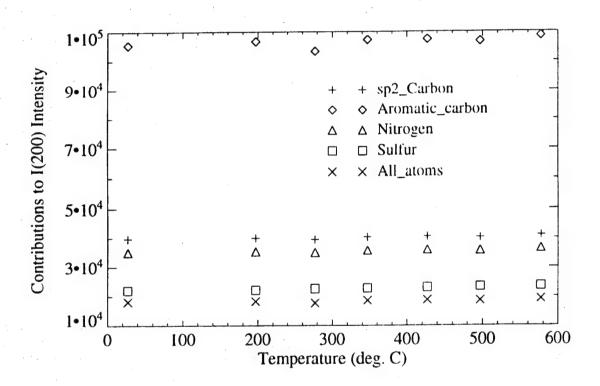
Figure 3
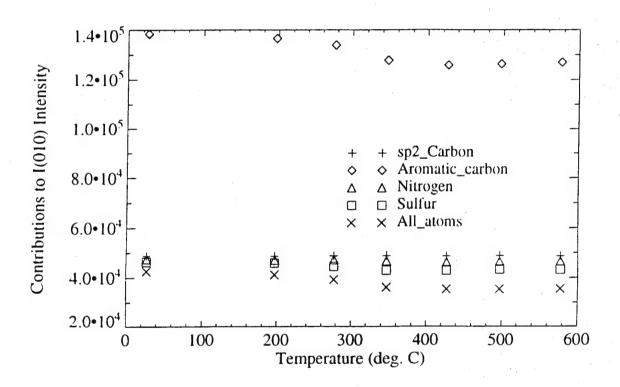
Figure 4
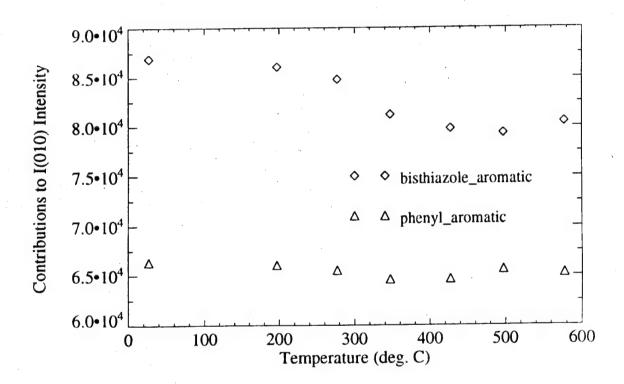
Figure 5
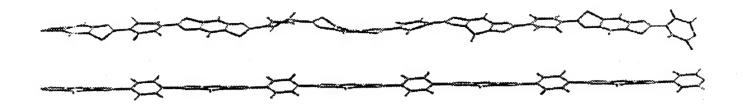
Figure 6

RUGATE FILTER MODELING
Walter E. Johnson

Rugate Filter Modeling

Walter E. Johnson

Wright Laboratory

Materials Directorate

WL/MLPJ

Wright-Patterson Air Force Base, OH 45433-6533

(513) 255-2110

Abstract

Fundamental concepts which define a rugate filter as an optical interference filter are covered. A historical perspective highlighting the leadership role of WL/MLPJ in the technical development of rugate filters is shown. A comparison of the spectral modeling for fabricated single and multi-band filters are presented. A modeling technique for enhancing the laser damage threshold probability of these filters is included. Nonconventional applications for rugate filters (i.e. broadband reflectors and bandpass filters) are also presented. General considerations for incorporating rugate filter technology into Air Force optical systems are identified.

Rugate Filter Modeling

Walter E. Johnson

Wright Laboratory

Materials Directorate

WL/MLPJ

Wright-Patterson Air Force Base,
OH 45433-6533

(513) 255-2110

Abstract

Fundamental concepts which define a rugate filter as an optical interference filter are covered. A historical perspective highlighting the leadership role of WL/MLPJ in the technical development of rugate filters is shown. A comparison of the spectral modeling for fabricated single and multi-band filters are presented. A modeling technique for enhancing the laser damage threshold probability of these filters is included. Nonconventional applications for rugate filters (i.e. broadband reflectors and bandpass filters) are also presented. General considerations for incorporating rugate filter technology into Air Force optical systems are identified.

Reducing the Standing-wave Field Profile within High Reflection Interference Coatings

Walter E. Johnson and Robert L. Crane
Wright Laboratory
Materials Directorate
WL/MLPJ
Wright-Patterson Air Force Base, OH 45433-6533
(513) 255-2110

Research to identify methods for increasing the laser damage threshold probability of high reflection interference coatings dates to the early 1970's. Particular emphasis has been placed on the wavelength(s) coinciding with the laser line(s) being reflected by these coatings. This work typically addressed multi-layer stack coatings. Our work has examined a sine-wave refractive index profile, commonly called a rugate filter (Ref 1). A single sine-wave refractive index profile having numerous identical cycles produces one well defined reflection band. This reflection band can be spectrally tailored and positioned anywhere within the passband of the filter with no associated higher order reflection bands present. The spectral location of this reflection band is twice the optical thickness of one of the cycles comprising the sine-wave refractive index profile. The refractive index at any point along this sine-wave profile is:

$$n(x) = n_a + \frac{n_{pv}}{2} \sin \left\{ \frac{2\pi \ x}{n_a P} + \theta \right\} \quad (1)$$

where,

n_a = the average refractive index
n_{pv} = the peak to valley excursion in the refractive index
P = the period of the sine-wave in physical thickness
θ = the phase angle of the sine-wave at the coating/substrate interface

The reflection band of a rugate filter reflects an incident laser line via the well known interference phenomenon, also exhibited by multi-layer stack coatings. This phenomenon can be visualized as the interaction of "two kinds" of traveling waves of coherent light which are distinguished from each other by the direction of travel. One travels within the coating in the direction of the incident wave and the second is reflected by the coating, traveling

in the opposite direction. These "two" traveling waves interfere with each other to produce a standing-wave field within the coating. The laser damage in multi-layer stack coatings has been linked to the peaks in this standing-wave field profile (Ref 2). Our model for rugate coatings reveals a useful relationship between the air/coating boundary and the standing-wave field profile.

The model assumes a normally incident traveling plane wave impinging the air/coating boundary with a flux density of 1 watt/cm^2. The fractional number of sine-wave cycles comprising the coating, N, (which defines the phase angle of the sine-wave refractive index profile at the air/coating boundary) and the phase angles at the coating/substrate interface, θ, are the only parameters varied in the current study. The other parameters describing the sine-wave refractive index profile of the rugate coating are $n_a=2$, $n_{pv}=0.2$ and P=0.266μm (the reflection band will reflect a 1.064μm laser line). In addition, the substrate is assumed to be a glass with a refractive index of n=1.52.

The standing-wave field profile within the rugate coating diminishes in magnitude as a function of optical thickness (Fig 1a). The dashed line in the figure denotes a sine-wave refractive index profile having N=19.5 cycles and θ=0 radians. The solid line in the figure denotes the standing-wave field profile within the coating while the "x" locates the maximum flux density present in the coating. The maximum flux density has a value of 0.89 watts/cm^2 that occurs at the nineteenth cycle. This location in the rugate coating is where the sine-wave refractive index profile has a value of n(x)=2, the average refractive index.

The relationship between the maximum flux density within a rugate coating and the fractional number of sine-wave cycles, N, was determined by the following procedure. The maximum flux density was calculated in each coating as a function of an increasing number of fractional sine-wave cycles, incremented by tenths of a cycle from 0.1$\leq$ N$\geq$40 cycles. The maximum flux density exhibits a cyclic variation as a function of the number of fractional cycles comprising the sine-wave refractive index profile of the coating (Fig 1b). Note that the "x" in this figure occurs at N=19.5 and has a value of 0.89 watts/cm^2, the maximum flux density within the coating depicted in Figure 1a. As the rugate coating increases in the number of cycles the maximum flux density varies asymptotically between both 1 and 4 watts/cm^2. The minimum values in the maximum flux

density occur when the refractive index profile of the rugate coatings end with a downward slope on a half cycle at the average refractive index, n(x)=2.

This variation in the maximum flux density exhibited by rugate coatings is best understood by using the general equation describing the interference between two coherent waves of light .

$$I = I_1 + I_2 + 2\sqrt{I_1 I_2}\cos\alpha$$

In this equation I is the flux density resulting from the interference of two coherent traveling waves of light I_1 and I_2. The interference of these two waves is not simply the sum of I_1 and I_2 but, also includes an interference term, $2\sqrt{I_1 I_2}$ cos α. If the interference term is a positive, then constructive interference results between I_1 and I_2. However, if this term is negative then there is destructive interference between I_1 and I_2. For the condition, $I_1=I_2=1$ watt/cm^2, flux densities $\geq$2 watts/cm^2 result from the constructive interference between I_1 and I_2, while flux densities <2 watts/cm^2 result from the destructive interference between I_1 and I_2. Total constructive interference exists when I=4 watts/cm^2 and total destructive interference exists when I=0 watts/cm^2. As the number of sine-wave cycles comprising a rugate coating increase, the flux density of the "reflected wave, I_2," approaches but, never equals that of the incident wave, I_1. Figure 1b shows that a rugate coating can exhibit either constructive or destructive interference as a function of the fractional number of sine-wave cycles comprising the refractive index profile.

The influence of the phase angle at the coating/substrate interface, θ, on the flux density within a rugate coating was examined. This was accomplished by specifying a filter with a phase angle at the coating/substrate interface of θ=0.5π radians and a fractional cycle number of N=19.25 cycles. In all other aspects the filter was identical to the one modeled in the previous calculations. The flux density profile for this filter also diminishes in magnitude as a function of coating thickness (Fig 1c). All flux density peaks occur at three-fourths of an integer number of cycles, where the sine-wave refractive index profile has a refractive index of n(x)=2.

This rugate filter also exhibits a cyclic variation in the maximum flux density as a function of the number of cycles comprising the coating (Fig 1d). Again as the rugate filter increases in the number of fractional cycles the maximum flux density varies asymptotically between 1 and 4 watts/cm^2. Also the minimum values in the maximum flux density occur when the sine-wave refractive index profile ends with a downward slope on a half cycle at the average refractive index.

For completeness, a third rugate filter is modeled. The coating is similar in design to the previous two, except values of $\theta=1.4\pi$ radians and N=19.8 cycles were used (Fig 1e). The maximum flux density has a value of 0.88 watts/cm^2 and occurs at 19.3 cycles, where the sine-wave refractive index profile has a value of the average refractive index n(x)=2. This third rugate filter also exhibits a cyclic variation in the maximum flux similar in description to the previous ones (Fig 1f).

In conclusion, rugate filters can be designed to reduce the standing-wave field profile within the coating for the wavelength coinciding with a laser line which the coating was designed to reflect. This should result in increasing the laser damage threshold probability of a rugate coating.

REFERENCES

1). Rugate Filter Session, K. L. Lewis and R. M. A. Azzam Presiders, Optical Interference Coatings, 1988 Technical Digest Series, Volume 6, (Optical Society of America, Washington, D. C. 1988) pp. 117-157.

2) J. H. Apfel, J. S. Matteucci, B. E. Newnam and D. H. Gill, "The Role of Electric Field Strength in Laser Damage of Dielectric Multilayers," A. J. Glass and A. H. Guenther, Editors, National Bureau of Standards Special Publication 462 (Boulder, Colorado, 13-15 July 1976), December 1976, pp. 301-309.

Figure 1a Standing-wave profile in a rugate coating (—). Refractive index profile (----) N = 19.5 cycles and $\theta=0$ radians.

Figure 1c Standing-wave profile in a rugate coating (—). Refractive index profile (----) N = 19.25 cycles and $\theta=0.5\pi$ radians.

Figure 1e Standing-wave profile in a rugate coating (—). Refractive index profile (----) N = 19.8 cycles and $\theta=1.4\pi$ radians.

Reducing the Standing-wave Field Profile within High Reflection Interference Coatings

Walter E. Johnson and Robert L. Crane
Wright Laboratory
Materials Directorate
WL/MLPJ
Wright-Patterson Air Force Base, OH 45433-6533
(513) 255-2110

Research to identify methods for increasing the laser damage threshold probability of high reflection interference coatings dates to the early 1970's. Particular emphasis has been placed on the wavelength(s) coinciding with the laser line(s) being reflected by these coatings. This work typically addressed multi-layer stack coatings. Our work has examined a sine-wave refractive index profile, commonly called a rugate filter (Ref 1). A single sine-wave refractive index profile having numerous identical cycles produces one well defined reflection band. This reflection band can be spectrally tailored and positioned anywhere within the passband of the filter with no associated higher order reflection bands present. The spectral location of this reflection band is twice the optical thickness of one of the cycles comprising the sine-wave refractive index profile. The refractive index at any point along this sine-wave profile is:

$$n(x) = n_a + \frac{n_{pv}}{2} \sin\left\{\frac{2\pi \, x}{n_a P} + \theta\right\}$$
(1)

where,

n_a = the average refractive index

n_{pv} = the peak to valley excursion in the refractive index

P = the period of the sine-wave in physical thickness

θ = the phase angle of the sine-wave at the coating/substrate interface

The reflection band of a rugate filter reflects an incident laser line via the well known interference phenomenon, also exhibited by multi-layer stack coatings. This phenomenon can be visualized as the interaction of "two kinds" of traveling waves of coherent light which are distinguished from each other by the direction of travel. One travels within the coating in the direction of the incident wave and the second is reflected by the coating, traveling in the opposite direction. These "two" traveling waves interfere with each other to produce a standing-wave field within the coating. The laser damage in multi-layer stack coatings has been linked to the peaks in this standing-wave field profile (Ref 2). Our model for rugate coatings reveals a useful relationship between the air/coating boundary and the standing-wave field profile.

The model assumes a normally incident traveling plane wave impinging the air/coating boundary with a flux density of 1 watt/cm^2. The fractional number of sine-wave cycles comprising the coating, N, (which defines the phase angle of the sine-wave refractive index profile at the air/coating boundary) and the phase angles at the coating/substrate interface, θ, are the only parameters varied in the current study. The other parameters describing the sine-wave refractive index profile of the rugate coating are n_a=2, n_{pv}=0.2 and P=0.266µm (the reflection band will reflect a 1.064µm laser line). In addition, the substrate is assumed to be a glass with a refractive index of n=1.52.

The standing-wave field profile within the rugate coating diminishes in magnitude as a function of optical thickness (Fig 1a). The dashed line in the figure denotes a sine-wave refractive index profile having N=19.5 cycles and θ=0 radians. The solid line in the figure denotes the standing-wave field profile within the coating while the "x" locates the maximum flux density present in the coating. The maximum flux density has a value of 0.89 watts/cm^2 that occurs at the nineteenth cycle. This location in the rugate coating is where the sine-wave refractive index profile has a value of n(x)=2, the average refractive index.

The relationship between the maximum flux density within a rugate coating and the fractional number of sine-wave cycles, N, was determined by the following procedure. The maximum flux density was calculated in each coating as a function of an increasing number of fractional sine-wave cycles, incremented by tenths of a cycle from 0.1 ≤ N ≥ 40 cycles. The maximum flux density exhibits a cyclic variation as a function of the number of fractional cycles comprising the sine-wave refractive index profile

441

of the coating (Fig 1b). Note that the "x" in this figure occurs at N=19.5 and has a value of 0.89 watts/cm^2, the maximum flux density within the coating depicted in Figure 1a. As the rugate coating increases in the number of cycles the maximum flux density varies asymptotically between both 1 and 4 watts/cm^2. The minimum values in the maximum flux density occur when the refractive index profile of the rugate coatings end with a downward slope on a half cycle at the average refractive index, n(x)=2.

This variation in the maximum flux density exhibited by rugate coatings is best understood by using the general equation describing the interference between two coherent waves of light .

$$I = I_1 + I_2 + 2\sqrt{I_1 I_2}\cos\alpha \qquad (2)$$

In this equation I is the flux density resulting from the interference of two coherent traveling waves of light I_1 and I_2. The interference of these two waves is not simply the sum of I_1 and I_2 but, also includes an interference term, $2\sqrt{I_1 I_2}\cos\alpha$. If the interference term is a positive, then constructive interference results between I_1 and I_2. However, if this term is negative then there is destructive interference between I_1 and I_2. For the condition, $I_1=I_2=1$ watt/cm^2 , flux densities ≥ 2 watts/cm^2 result from the constructive interference between I_1 and I_2, while flux densities <2 watts/cm^2 result from the destructive interference between I_1 and I_2. Total constructive interference exists when I=4 watts/cm^2 and total destructive interference exists when I=0 watts/cm^2. As the number of sine-wave cycles comprising a rugate coating increase, the flux density of the "reflected wave, I_2," approaches but, never equals that of the incident wave, I_1. Figure 1b shows that a rugate coating can exhibit either constructive or destructive interference as a function of the fractional number of sine-wave cycles comprising the refractive index profile.

The influence of the phase angle at the coating/substrate interface, θ, on the flux density within a rugate coating was examined. This was accomplished by specifying a filter with a phase angle at the coating/substrate interface of $\theta=0.5\pi$ radians and a fractional cycle number of N=19.25 cycles. In all other aspects the filter was identical to the one modeled in the previous calculations. The flux density profile for this filter also diminishes in magnitude as a function of coating thickness (Fig 1c). All flux density peaks occur at three-fourths of an integer number of cycles, where the sine-wave refractive index profile has a refractive index of n(x)=2.

This rugate filter also exhibits a cyclic variation in the maximum flux density as a function of the number of cycles comprising the coating (Fig 1d). Again as the rugate filter increases in the number of fractional cycles the maximum flux density varies asymptotically between 1 and 4 watts/cm^2. Also the minimum values in the maximum flux density occur when the sine-wave refractive index profile ends with a downward slope on a half cycle at the average refractive index.

For completeness, a third rugate filter is modeled. The coating is similar in design to the previous two, except values of $\theta=1.4\pi$ radians and N=19.8 cycles were used (Fig 1e). The maximum flux density has a value of 0.88 watts/cm^2 and occurs at 19.3 cycles, where the sine-wave refractive index profile has a value of the average refractive index n(x)=2. This third rugate filter also exhibits a cyclic variation in the maximum flux similar in description to the previous ones (Fig 1f).

In conclusion, rugate filters can be designed to reduce the standing-wave field profile within the coating for the wavelength coinciding with a laser line which the coating was designed to reflect. This should result in increasing the laser damage threshold probability of a rugate coating.

REFERENCES

1). Rugate Filter Session, K. L. Lewis and R. M. A. Azzam Presiders, Optical Interference Coatings, 1988 Technical Digest Series, Volume 6, (Optical Society of America, Washington, D. C. 1988) pp. 117-157.

2) J. H. Apfel, J. S. Matteucci, B. E. Newnam and D. H. Gill, "The Role of Electric Field Strength in Laser Damage of Dielectric Multilayers," A. J. Glass and A. H. Guenther, Editors, National Bureau of Standards Special Publication 462 (Boulder, Colorado, 13-15 July 1976), December 1976, pp. 301-309.

NANOCRYSTALLINE SILICONE: SIMULATION AND VISUALIZATION
Dr. James A. Lupo

Nanocrystalline Silicon: Simulation and Visualization

James A. Lupo

16 July 1992

Nanocrystalline materials are novel substances constructed of randomly oriented, perfectly crystalline grains compressed under high pressure until their density approaches that of the normal bulk material. X-ray diffraction studies have shown neither long or short range order in nanocrystalline materials, and physical properties, such as diffusion rates, differ markedly from those of the bulk material. Atomistic simulations of nanocrystalline copper and silicon have been conducted. A method for speeding up the numerical simulation via coordinated parallel computation on a conventional UNIX multiprocessor system will be discussed. The difficulties of analyzing 3-D data results will be addressed, and several techniques for dealing with perception problems will be presented, including interactive perspective display. Volume visualization results from applying the "marching cubes" surface tracing algorithm and an artificial opacity volume rendering alogrithm will also be discussed.

PARALLEL COMPUTING CONCEPTS, PROBLEMS, AND ARCHITECTURES
Dr. Gary B. Lamont

447

Parallel Computing Concepts, Problems and Architectures

Gary B. Lamont
Department of Electrical and Computer Engineering
Graduate School of Engineering
Air Force Institute of Technology
Wright-Patterson AFB, Ohio 45433-7765
lamont@afit.af.mil

1   Introduction

Over the years, technological advances have dramatically increased the performance of sequential computer architectures; however, the laws of physics ultimately limit the achievable performance of these architectures [7, 2]. Parallel computer architectures offer a complementary approach to sequential architectures in solving problems of ever increasing complexity. The main thrust behind parallel computing is the explicit use of multiple processing elements (often computers in themselves), to solve complex problems many times faster than on a comparable sequential architecture [1]. Many computer scientists foresee standard computer designs of the future employing massive parallelism; that is, computers containing an arbitrarily large number of processing elements.

As attractive as parallel computing sounds, there are still many issues to be addressed before massively parallel computers can be used to solve complex problems efficiently. This chapter explores the concepts of parallel program design and the architectures currently available for parallel processing in an effort to give the reader some feel for the existing problems inherent in parallel computing.

2   Essential Concerns in Parallel Computing

The essential concerns in designing programs for parallel computer architectures fall into two categories: correctness and performance. A program design must be correct in order to guarantee solution of the problem. As one might expect, ensuring the correctness of a parallel program design is generally more difficult than for a sequential design, primarily due to the existence of multiple threads of control.

Besides being correct, the parallel program design should make the most effective use of the computational resources of the parallel computer architecture. Recent advances in semiconductor memory and microprocessor technology have eased the requirement for space efficiency; consequently, more emphasis is currently being placed on time efficiency. While poor time-efficiency gradually degrades the performance of a program, generally space-efficiency produces an abrupt cutoff: either it fits in memory or it doesn't.

Although parallel architectures constitute a potentially tremendous increase in computational power, difficulties with correctness or performance can limit their usefulness. The following section discusses correctness and performance of parallel program design and how they relate to the development of "successful" applications on parallel computers.

---

[1] By "comparable" we mean the single processor of the sequential architecture possesses the same computational power as each processing element of the parallel architecture

3 Design and Development of Correct Parallel Programs

Most of the literature on programming parallel computers begins with the assumption of program correctness. As a result, discussion of program correctness is often left out entirely. The omission of program correctness concepts is dangerous in light of the complexities of parallel program design. Developing programs for parallel computers is nearly always a more difficult task than developing programs for sequential architectures [3, 5]. The existence of multiple processing elements compounds the task of isolating and correcting program mistakes significantly. Incorrect parallel program design may yield implementations that encounter problems related to: deadlock, starvation, termination detection and race conditions. Any of these problems may cause a computer to halt execution abnormally, continue execution indefinitely, or produce incorrect answers [13, 593]. Our goal is a correct program -one that produces correct results in a predictable and repeatable manner.

Chapter [3, 4] is a supplemental reference for the UNITY [2] approach to developing parallel programs. The chief source of information for this "foundation for parallel program design"[3, 4] is the Chandy and Misra text. The UNITY approach isolates the program designer from the specifics of a given parallel architecture in the same way that modern compilers isolate programmers from the machine specific characteristics. UNITY combines the use of temporal predicate logic combined with a simple, but powerful state transition model [3, 9].

Other methods for parallel program development include Communicating Sequential Processes (CSP) by C. A. R. Hoare [9], the Parallation model defined by Gary Sabot [15], and the Actors model formalized by Gul Agha [1].

The power of the UNITY approach is that a proof of program correctness can be extracted from the high-level specification of the program design using a combination of standard logic operators (reductions) and special temporal logic operators. Once the high level design is proven correct, the UNITY approach provides a method for transforming high level designs into intermediate forms using correctness-preserving *mappings*. These intermediate forms maintain the correctness of the original UNITY program, while provide a structure for developing implementations on specific parallel architectures. Once this is achieved, source code for the executable program can be written based on the intermediate form.

4 Parallel Program Performance

A correct program design does not guarantee an efficient implementation. An efficient parallel program design enables the maximum use of all processing elements of the computer architecture toward a solution. An efficient parallel program runs many times faster than a comparable sequential program. There are significant obstacles to development of efficient parallel program designs. Stone describes how these obstacles manifest themselves as overhead costs [16, 280]:

- *Communication overhead*, or delays introduced by communicating data between processing elements in the parallel architecture.

- *Synchronization delays* introduced when one processor must wait for another to complete a given task before it can proceed.

- *Load imbalances*, which cause lost efficiency when one or more processors runs out of useful work (tasks) and becomes idle.

- Efficiency lost through computations not required for a sequential implementation:

    - The cost of using non-optimal sequential algorithms and data structures.

    - The cost associated with such control functions as task ordering and task scheduling.

---

[2] Unbounded Non-deterministic Iterative Transform

– The cost of computations not required by equivalent sequential implementations.

A parallel program design is either correct or incorrect, but parallel program performance is not so "black and white". Because performance is not as definite, some means of quantifying the likely performance of a given design. Many tools exist for determining the performance of an actual implementation.

The two fundamental measures of parallel program performance are parallel program speedup (S) and parallel program efficiency[3] (ε). Parallel program speedup is a measure of how much faster a given problem can be solved on a specific parallel architecture than on a comparable sequential architecture. Parallel program efficiency is a measure of how efficiently the parallel program design uses the parallel processing elements in solving the problem, **not** how much faster the design is.

Speedup (S), one of the most important and widely used measures of parallel program performance is:

$$S = \frac{T_{sequential}}{T_{parallel}}$$

where ($T_{parallel}$) is the time required to solve the problem on a parallel architecture and ($T_{sequential}$) is the time required to solve the same problem on a comparable sequential architecture using the best sequential algorithm [7, 55]. $T_{parallel}$ is a combination of the time required to compute a solution to the problem plus the overhead costs mentioned above. Thus $T_{parallel}$ can be written as:

$$T_{parallel} = \overbrace{\frac{T_{sequential}}{N}}^{computation} + \overbrace{T_{comm} + T_{synch} + T_{imbalance} + T_{comp}}^{overhead}$$

The above equation assumes all overhead costs can be independently quantified and the problem can be divided into N independently executable tasks. Although the equation provides a starting point for a discussion of parallel program performance, later examples show neither of these assumptions hold for all problems.

The definition of parallel program efficiency follows from the definition of speedup; efficiency is:

$$\varepsilon = \frac{S_N}{N}$$

where S_N is the speedup achieved using N processing elements.

A primary goal of using a parallel architecture is to reduce the time required to solve the problem. When this happens, we have a speedup greater than one. Ideally, a given parallel architecture with N processors would solve a problem N times faster than a comparable sequential architecture. This is known as *linear speedup* and results in "perfect" efficiency of 1.00. Linear speedup implies the overhead of parallelization is essentially 0 (this is very hard to achieve). Techniques for minimizing overhead and dividing (balancing) the problem evenly between available processors vary based on three major concerns [7, 3]:

- Characteristics of the problem to be solved.

- The program design and decomposition techniques employed.

- The chosen parallel architecture and its characteristics.

5   Decomposing a Problem/Composing a Design

As with the problem solving process on sequential architectures, algorithms are typically the starting point for any parallel program design. Many problems have highly efficient sequential algorithms but have become

---

[3]This metric is different than the measure of time and space complexity of a sequential or parallel program design with the same name

too large or complex to be solved on standard sequential architectures [7, 26]. Sometimes the optimal sequential algorithm can be easily extended to support a parallel design. But if the optimal algorithm represents an inherently sequential process or is incompatible with the target architecture, the designer must consider either adapting non-optimal algorithms or developing entirely new parallel algorithms.

Problem *decomposition* is the breaking down of a high-level algorithm into independently executable tasks. Since a program is composed of both control structure and data structure [17], a parallel program can be decomposed in terms of its data structure, control structure or both [2, 4-1]. Most highly parallel programs use data decomposition, and indeed, data decomposition is what comes to mind most easily for the typical software engineer. True functional (control) decomposition techniques often yield only small amounts of effective parallelism [8, 900]. However, for the sake of completeness, both data decomposition and control decomposition techniques are presented.

Problem decomposition introduces three important problem characteristics that are major issues when attempting to design efficient programs for specific parallel architectures:

- problem granularity

- problem connectivity

- problem homogeneity

Granularity is the relative size of independent tasks to be completed in solving a given problem. The relative size of tasks can be measured in terms of worst case order-of, average order-of, or actual profiler line execution counts. Problem connectivity describes interdependence of the tasks that make up the problem. Connectivity concerns how many tasks affect a given task and how often they do so. Granularity and connectivity are related since large grain problems tend to have low connectivity and small grain problems tend to have high connectivity. Problem homogeneity is the difference in the size of tasks to be completed in solving the problem. Homogeneity is a more abstract characteristic and is harder to measure than the others.

Parallel programs fit across a spectrum of synchronicity. The three chief categories along the spectrum are [8, 903]:

- *Synchronous* - Problems with a known number of roughly equal sized tasks requiring global synchronization at various points during execution.

- *Loosely Synchronous* - Problems with a roughly defined number of tasks of approximately predictable sizes requiring infrequent local and/or global synchronization.

- *Asynchronous* - Problems with a very approximate number of unevenly sized tasks which have synchronization requirements that are determined dynamically (during execution).

5.1 Data Decomposition

Data (or domain) decomposition breaks large sets of data into a number of smaller sets of data, each of which can be operated on in parallel. A number of processing elements then apply an essentially identical control structure (algorithm) to each of these data subsets independently. A problem is *perfectly* parallel if the final problem solution can be computed by a number of independent processors with no communication between processors and no redundant computation during program execution. Large-sized perfectly parallel problems can be effectively and efficiently implemented many different parallel architectures [8, 905]. However, these "embarrassingly parallel" problems constitute only a small portion of all problems [8, 927]. Typically, a problem introduces one or more of the parallel overhead components discussed earlier.

452
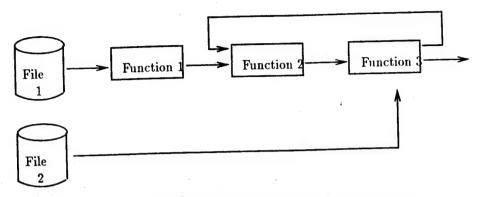
Figure 1: A Generic Static Control Decomposition Example
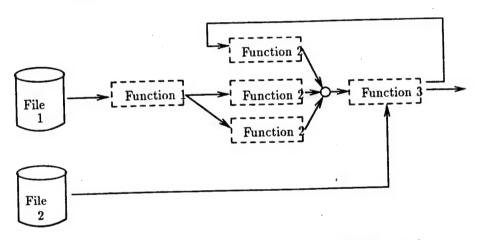
Figure 2: A Generic Dynamic Control Decomposition Example

5.2 Control Decomposition

In control decomposition, a problem is decomposed into a number of separate functional units. The control structure of a program, the algorithm, can often be viewed as a series of functional modules as shown in Figure 1 [2, 6-1]. In a sequential application the modules are typically executed in sequence once for every distinct piece of data to be processed. In a parallel implementation, each processor performs a separate function on one or more input data stream(s) and outputs one or more streams. This process of communicating data between a series of independent processes is similar to instruction pipelining done in modern microprocessors and pipelining of vector operations done in supercomputers such as the Cray-1 [7, 25]. Operations in instruction and vector pipelines are typically only a very few computer clock cycles and therefore constitute very small grain synchronous tasks. On the other hand, control decomposition typically concentrates on problems that can be decomposed into a number of larger grain functions that can be performed asynchronously [2, 6-3].

It is often difficult to divide a complex algorithm into a number of functions that require approximately the same amount of time. Further, the "chunks" of data passing through the pipeline may be of widely different sizes, or may require different amounts of processing time at each functional unit. For instance, in Figure 1, function 1 must wait for function 2 to complete processing on its current "chunk" of data before it can begin processing on more of input file 1. Alternately, it can put the data in a queue that function 2 can access later. In either case, additional overhead is added to the system.

We often want to decompose a problem apriori, but in many cases, it is most efficient to do the decom-

453

position "on the fly." Dynamic load balancing can often significantly increase parallel program performance. Figure 2 shows a generic example of dynamic load balancing applied to a control decomposition problem. In this model, logical processes are created and assigned to physical processors as the need for a given function is detected. For example, when the processor executing function 1 finishes processing input file data, it may begin running another process, say function 2. The use of task queues between processes allows execution of the parallel program as a whole to continue with little synchronization overhead. The drawback here is the cost of creating, terminating and scheduling logical processes, and the cost of piping (communicating) data between processes [14, 385]. Problems using dynamic logical processes must possess large grain functional blocks. If the operating system is not able to manipulate logical processes efficiently, control and communication overheads significantly reduce available speedup.

5.3 Object-Oriented Design and Development

An object-oriented approach to program development seems to have a natural affinity for parallel hardware architectures. Individual objects could be put on different processors. Since an object-oriented approach localizes data with the functions performed on that data, this model would seem to map well to parallel process. Communications between processes can be simple messages of the form "do X to D."

This paradigm runs into difficulty when there are only one or two major objects, and it is desired to spread the system over a large number of nodes. Any attempt to spread objects over multiple processors is likely to result in a lot of communications on a distributed memory architecture. It would seem that any given object-oriented design would map well to a specific number of processors, but poorly to any number of processors greater than that. A shared memory architecture would not have as much difficulty.

For a good discussion of OOD and parallel programming, see chapter 6 of Lewis and El-Rewini [11].

6 Parallel Computer Architectures

This section is a brief overview of parallel computer architectures. This is not the appropriate place for presenting a description of every available parallel architecture. Instead we concentrate on general characteristics of commercially available, general purpose parallel architectures. The concepts of granularity, connectivity and homogeneity play a significant role in classifying parallel computer architectures.

6.1 Choosing a Useful Subset of Parallel Architectures

In 1966, Flynn proposed a taxonomy which, based on instruction and data streams, give four basic classes of computer [6, 1901]:

- *Single-Instruction-Single-Data-Stream (SISD)* - a computer with one central processor unit that operates on only one stream of data at a time. This is the architecture of a typical sequential computer.

- *Multiple-Instruction-Single-Data-Stream (MISD)* - a computer capable of performing multiple operations on the same data stream at the same time. This architecture is generally considered infeasible.

- *Single-Instruction-Multiple-Data-Stream (SIMD)* - a computer that perform the same operation on a number of different data streams at the same time (synchronously). This is the class into which vector machines fall.

- *Multiple-Instruction-Multiple-Data-Stream (MIMD)* - a computer with multiple processing elements, each capable of performing different operations on different sets of data at the same time (asynchronously).

This taxonomy provides a useful method for classifying parallel architectures, but it is incapable of effectively classifying the recent diversity of parallel architectures [5, 6]. As a result, an extended taxonomy (Figure 3) of parallel architectures is presented which extends Flynn's taxonomy to cover the new diversity
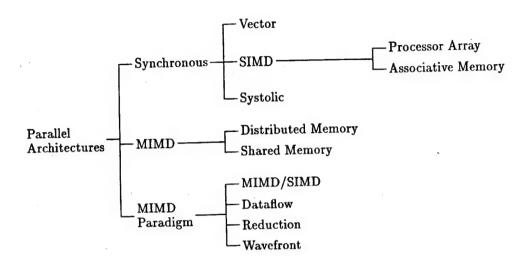
Figure 3: High-Level Taxonomy of Parallel Architectures [5, 6]
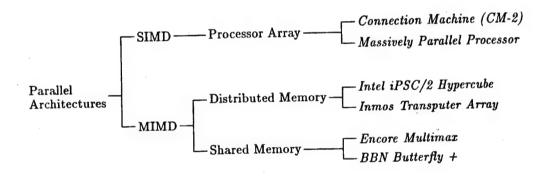
Figure 4: A Useful Subset of Parallel Architectures

of architectures. Other taxonomies for classifying parallel architectures exist, but this one was chosen for its elegance and simplicity. The extended taxonomy incorporates some recent (and sometimes exotic) parallel architectures.

The remainder of our discussion is limited to a subset of this taxonomy based on the following criteria:

- *General Purpose* - Architectures capable of solving a wide variety of problems. This eliminates machines specifically designed to solve a single class of problems.

- *Generally Available* - Commercially available architectures or experimental architectures widely available to researchers.

- *Known Performance* - Architectures for which important measures of performance (processor and interprocessor communications speeds) are available.

Restricting the overall taxonomy to architectures meeting the criteria yields a the subset of parallel architectures shown in Figure 4. The elements in *italics* are specific examples of actual machines. This taxonomy excludes new and promising parallel architectures for which there is insufficient information about critical
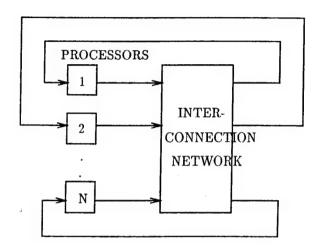
Figure 5: Architecture of a Generic Multi-computer [16, 280]

performance factors and problem solving capabilities. The UNITY approach for designing parallel programs does not directly support mappings to these architectures [3, 82] in any event. A recent article by Ralph Duncan [5] provides a concise overview of the parallel architectures not addressed here (such as Cluster and Single Bus, Systolic Arrays, Switch Lattice, Tree, Pyramid and Prism).

6.2 MIMD Architectures
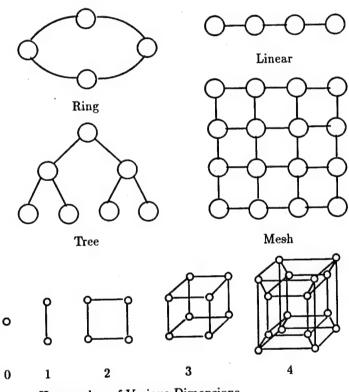
MIMD architectures are probably the most natural extension of the sequential computer architecture. MIMD architectures are collections of independent computing elements capable of communicating with each other in some manner. Each MIMD computational element can execute different sets of instructions (programs) on different sets of data. Processing elements are typically very powerful microprocessors with access to significant program and data memory [7, 23]. Collections of MIMD processors can be combined to solve problems through interprocessor communications. The structure of the communications network is the main differentia of the two classes of MIMD architectures. The two subclasses are distributed memory computers (multi-computers) and shared memory computers (multi-processors). Hybrid architectures exist.

6.2.1 Distributed Memory MIMD Architectures

Figure 5 shows the basic design of a distributed memory MIMD (DMM) architecture. Each independent processor (node) contains local memory that only it can access. Communication between nodes takes the form of message passing, similar to passing data packets between computers over a local area network. The node interconnection network can take many forms and the selected form determines the *topology* of the particular DMM implementation. Figure 6 shows several popular choices of topology. The current philosophy of multi-computer design is to hide the details of the topology from the programmer by giving the illusion that every node is directly connected to every other node in the computer [12, 651].

In practice, complete connection networks are infeasible for large numbers of processing elements [5, 12], so multi-computer designers concentrate on efficient and scalable architectures. A major disadvantage of using a DMM architecture is the significant communication overhead time (typically tens of milliseconds) required to pass data between nodes. The communication overhead would appear to make DMM architectures incompatible with small grain problems, but research to alleviate this problem is under way [4, 2].

Use of efficient topologies and message passing techniques can reduce the large communication overheads suffered by DMM architectures. The binary N-cube (Hypercube) architecture shown in Figure 6 is a very popular multicomputer topology. However, hypercubes with a large number of nodes have problems with

456

Ring

Linear

Tree

Mesh

0 1 2 3 4

Hypercubes of Various Dimensions

Figure 6: Distributed Memory MIMD Topologies [7, 23] [5, 10]
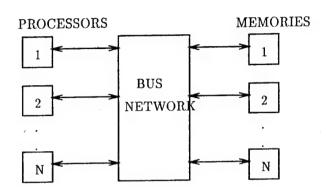
Figure 7: Architecture of a Generic Multi-Processor [16, 280]

large communication overhead, inefficient message routing and a multitude of routing wires [4, 4]. A newer network design based on a torroidal (end-connected) mesh attempts to address these problems. MIT's torroidal routing chip (TRC) design uses shared memory, bidirectional parallel data paths and adaptive routing techniques to route a 150 bit message between nodes on a 1024 node processor in an average time of 7.5 microseconds [4, 6]. The TRC represents a several order of magnitude decrease in communication time over current (second) generation multi-computers. The next (third) generation of multi-computer is likely to be much more compatible with smaller grain tasks.

6.2.2 Shared Memory MIMD Architectures

Figure 7 shows the basic layout of the shared memory MIMD (SMM) architecture. SMMs are similar to DMMs except that communication between processors takes place through shared memory instead of message passing. In the SMM approach, each processor typically possesses some local memory as well as having access to a significant amount of global (shared) memory through some interconnection network. Figure 8 presents some shared memory interconnection topologies used in commercially available multi-processor implementations. These networks require large bandwidths to minimize the overhead of CPUs accessing instructions and data. As a result, data passing between processors via shared memory is very fast (on the order of a few memory access cycles).

A fairly standard name for the synchronous shared-memory model is the *parallel random-access machine* model, or PRAM [10]. There are several variations of the PRAM model based on the assumptions regarding the handling of simultaneous access to global memory. *Exclusive read exclusive write* EREW PRAM does not allow any simultaneous access to a memory location. *Concurrent read exclusive write* CREW PRAM permits simultaneous access for read, but any write must have exclusive access. *Concurrent read concurrent write* CRCW PRAM is further differentiated as follows: *common* CRCW PRAM permits concurrent writes only if all processors are trying to write the same value; *arbitrary* CRCW PRAM permits an arbitrary processor to succeed; and *priority* CRCW PRAM permits the highest priority processor to succeed.

The more processors, the greater the contention for access to shared memory. Shared memory contention is typically greatest for a bus interconnection network [16, 302]. The problems with SMAs is not so much communication time as scalability of the interconnection topology used.

Each topology in Figure 8 has advantages and disadvantages with respect to variable access time and scalability. The bus interconnection network allows very fast access to shared variables, but 20 processors is the upper limit for a single shared bus system [16, 283]. Multiple busses connected by cache memories are an alternative to single bus designs, but this concept is still in the experimentation stages. Crossbar switches allow complete connection of processors and memories, but this approach is very costly. Crossbar
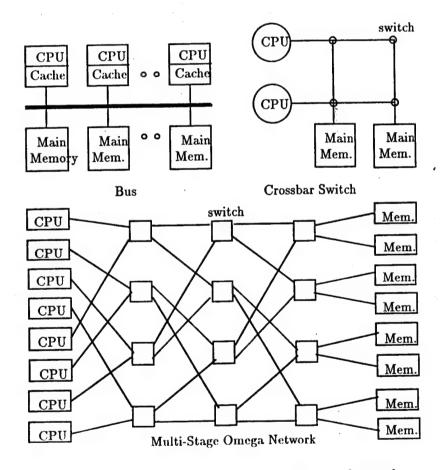
458

Figure 8: Common Interconnection Architectures [16, 158]
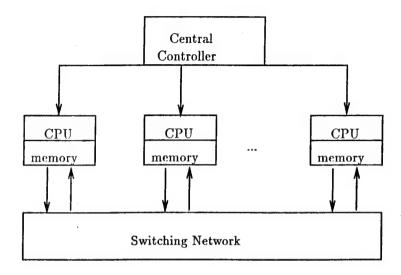
Figure 9: General Structure of a SIMD Array Architecture

switches are not feasible for highly parallel architectures because the number of switching elements required is $O(N^2)$, where N is the number of processors in the parallel architecture [5, 12].

Multistage switches, like the Omega network, requiring $O(Nlog_2 N)$ switches, provide scalability and suffer relatively small increases in memory access time as the number of stages increases. Using a six stage network, BBN's Butterfly+ requires only slightly more time to access a remote memory location ($\approx$ 6 microseconds), than to access a local memory location ($\approx$ 2 microseconds). Considering the scalability of the multistage networks and their relatively fast access times, this increase in access time to add many more processors might appear cheap.

6.3 SIMD Processor Array Architectures

SIMD architectures are usually implemented on a scale more massive than other parallel architectures, using multitudes of efficiently connected, simple (but fast) processing elements [7, 22]. Figure 9 illustrates the basic architectural components of a SIMD array architecture and the connections between the components. In addition to a simple ALU and control circuitry, each processing element typically possesses a small amount of local memory (less than 1000 bytes), and facilities for communicating with neighboring processing elements. The limited memory on each processing element is not sufficient to contain a computer program, so instructions must be provided by the control computer.

In the SIMD mode of operation, each processor executes the instruction broadcast by the central control computer. All processing elements are connected to the same system clock, therefore the operation of all processors is completely synchronous. The large number of processing elements provide the potential for massive parallelism if the problem being solved "cooperates" by being homogeneous on an equally massive scale.

MIMD based architectures often have a difficult time achieving speed-ups when executing small grain tasks due to communication overheads, but SIMD machines are capable of producing significant speed-ups with small grain tasks because of their efficient processor to processor communication structures. The interconnection topologies used for multi-computers (Figure 6) can also be used to connect SIMD processing elements. On many SIMD machines, communicating data between neighboring processing elements often requires only one instruction cycle. Some SIMD implementations restrict data exchanges to nearest neighbors, but others (such as the CM-2) allow for communication between processors that are separated by some power of 2 other processing elements. A "remote" communication typically requires more than one machine cycle,

460

	small grain	medium grain	large grain
Problem			
Synchronous			
	MIMD & SIMD		MIMD & SIMD
Loosely Synchronous	SMM	MIMD	MIMD
		SMM	MIMD
Asynchronous			
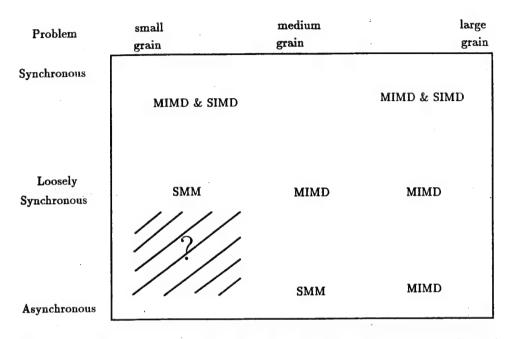
Figure 10: A General Common Framework for Problems and Architectures [8, 953]

but is much faster than passing the message through 2^N nearest neighbor processors. Efficient passing of data between processing elements means very few operations on each piece of data is required to "amortize" communication cost. Consequently, significant speed-ups for small grain size messages can be achieved much more easily than with most MIMD machines if the problem contains sufficient homogeneity.

Most SIMD architectures are inherently capable of solving very small grain problems efficiently [7, 23], but are not equipped to effectively deal with nonhomogeneous problems. Because only one instruction can be executed at a time, "left over" processors cannot be used to perform other tasks. A particular problem does not require complete homogeneity because SIMD architectures can use certain techniques to "generalize" the effects of global instructions. The data contained on each processing element can affect how a given instruction is actually executed: Each processor node typically has its own status registers. Local processor flags can be used to modify the node's response to subsequent instructions [7, 22]. For example, a *skip-on-zero* instruction causes any processing element with a set zero flag to skip execution of the next instruction.

Another approach to generalizing the affect of global instructions is through the use of *very long instruction words* (VLIWs). Each VLIW instruction actually contains a number of instructions that can be used to control different partitions of SIMD processing elements. Under the VLIW concept, each instruction is executed synchronously, but subsets of SIMD processing elements can execute different instructions.

7 Summary: Problems and Architectures, A Common Framework

Given a specific problem and a specific means for solving it, there is almost always one parallel architecture that produces the best performance in terms of speedup; however, this same architecture may not produce the best performance in terms of efficiency or execution time. As with other engineering fields, tradeoff decisions are necessary when "mating" a problem to an architecture. Figure 10 presents a general common framework for problems and architectures based on research by Geoffrey Fox [8]. The positioning of the architectures on the problem space background indicates a given architecture provides efficient solutions for problems of a particular type.

References

[1] Agha, Gul. *Actors: A Model of Concurrent Computation in Distributed Systems*. Cambridge MA: MIT Press, 1986.

[2] Asbury, et al. *Parallel Programming Primer*. Technical Report, Beaverton, OR: Intel Corporation, 1990.

[3] Chandy, K. Mani and Jayadev Misra. *Parallel Program Design: A Foundation*. Reading, Massachusetts: Addison-Wesley, 1988.

[4] Dally, William J. "Fine-Grain Message-Passing Concurrent Computers." *Third Conference on Hypercube Concurrent Computers and Applications*. 2–12. 1988.

[5] Duncan, Ralph. "A Survey of Parallel Computer Architectures," *IEEE Computer*, *23*(5):16 (February 1990).

[6] Flynn, M. J. "Very High Speed Computing Systems." *Proceedings of the IEEE*. 1901–1909. December 1966.

[7] Fox, G., et al. *Solving Problems on Concurrent Processors*. Englewood Cliffs, New Jersey: Prentice-Hall, 1988.

[8] Fox, Geoffrey C. "What Have We Learnt from Using Real Parallel Machines to Solve Real Problems?." *Proceedings of the Third Conference on Hypercube Concurrent Computers and Applications*. 897–955. ACM, 1988.

[9] Hoare, C. A. R. *Communicating Sequential Processes*. Englewood Cliffs, NJ: Prentice-Hall, 1985.

[10] JaJa, Joseph. *An Introduction to Parallel Algorithms*. Addison-Wesley, 1992.

[11] Lewis, Theodore G. and Heshem El-Rewini. *Introduction to Parallel Computing*. Englewood Cliffs, NJ: Prentice-Hall, 1992.

[12] Lillevik, Sigurd. "Touchstone Program Overview." *Proceedings of the Fifth Conference on Distributed Memory Computing*. 647–657. ACM, May 1990.

[13] McDowell, Charles E. and David Helmbold. "Debugging Concurrent Programs," *ACM Computing Surveys*, *21*(4):593–622 (December 1989).

[14] Riley, Gary. *Implementation of an Expert System Shell on a Parallel Computer*. Technical Report, Houston, TX: NASA/Johnson Space Center, 1988.

[15] Sabot, Gary W. *The Parallelation Model: Architecture Independent Programming*. Cambridge, MA: MIT Press, 1988.

[16] Stone, Harold S. *High-Performance Compter Architecture*. Reading, Massachusetts: Addison-Wesley, 1987.

[17] Wirth, Niklaus. *Algorithms + Data Structures = Programs*. Englewood Cliffs, NJ: Prentice-Hall, 1976.

MANIPULATING MOLECULAR MODELS IN "INNER SPACE" USING A FORCE-REFLECTING CONTROL ARM
Lt Christopher J. Hasser

Manipulating Molecular Models in "Inner Space" Using a Force-Reflecting Control Arm

Lt Christopher J. Hasser, Armstrong Laboratory, AL/CFBA

RELEVANT HISTORY

The idea of manipulating molecular models on a three-dimensional computer screen, using a force-reflecting control arm as an input and feedback device, has existed for over 20 years. Within the last 10 years, increasing computational power has enabled Brooks and Wright at the University of North Carolina (UNC) to pioneer a working system using a surplus control arm from Argonne National Lab. This system is used to study the docking of drug molecules onto protein molecules. With the help of UNC and the Armstrong Laboratory, the Wright Laboratory is developing an enhanced system that will use a modern force-reflecting controller and handle much larger polymer molecules for the study of thin films.

The force feedback controllers for molecular docking are based on teleoperation technology developed for use with nuclear materials beginning in the late 1940's. In 1948, Ray Goertz developed the first master-slave manipulator system at the Argonne National Laboratory. It consisted of a mechanical manipulator arm with a set of tongs at the end of the wrist, controlled by a nearly identical master arm. The master and slave were connected by mechanical linkages and separated by a leaded glass shield. The technology evolved to use electric motors to power the slave arm, with a purely electrical connection between master and slave. This obviated the need for a direct mechanical linkage, but made operation more clumsy and less efficient, since the operator (moving a control arm with position sensors only) could not feel the forces involved in the task.

Goertz enhanced teleoperation significantly in 1954 when he added motors to the master arm so that forces in the remote work environment could be reflected back to the operator. The nuclear industry continued to drive the development of teleoperation in the 1950's and 60's, but teleoperation was also being developed for underwater use by organizations like Woods Hole Oceanographic Institute, French researchers, and the U.S. Navy. In April of 1966, an underwater teleoperated manipulator arm was used to retrieve a U.S. Air Force nuclear weapon that had been lost in over 2500 feet of water during an aerial refueling accident near Palomares, Spain. The teleoperator system allowed its operator, safe on the surface of the water, to extend human reach down to a level not otherwise possible. Teleoperations are still preferred for unstructured tasks such as this, where automation is not possible or not practical due to the limitations of artificial intelligence or the need for direct human involvement.

Late in the 1970's and during the 1980's, teleoperator technology began to be pushed by NASA. The long boom-like Remote Manipulator System on the Space Shuttles is an example of a space-based teleoperator at work. In the 1990's, new drivers of teleoperation will include virtual environment (synthetic reality) applications, and possibly construction equipment control applications. Teleoperation has relevance to any situation requiring the unique capabilities of a human, but with direct human involvement prevented by hazard (nuclear, biological, chemical, or explosive threat) or inaccessibility (underwater or in outer space). Emerging applications in simulation and real microdevices will also extend scientists' reach to the previously untouchable "inner space."

MOLECULAR DOCKING APPLICATION

Extension of telepresence to "inner space" allows scientists to directly grasp things on a scale normally inaccessible to their senses, and to match intuition with these sensory impressions. Such a matching can provide insight to problems like the docking of two large molecules, proving superior to brute force iterative solution searches. In the molecular docking task, scientists control the motion

465

of one of two molecules on a computer screen. The situation compares to a teleoperation task where the master is a real device and the slave exists in a simulated world. The operator manipulates one molecule with respect to the stationary molecule in order to find the minimum energy docking position. The system reflects the sum of all interatomic forces back to the operator through the master controller. A bar graph readout of total force aids the operator. The operator may switch modes so that the master manipulates the entire scene; this latter mode allows the operator to reorient both molecules and change the viewing angle.

SERIAL LINK MANIPULATORS

Force-reflecting master controllers are essentially serial link robotic arms, so a very brief mention of manipulators will contribute to an understanding of force display in molecular docking. Most manipulator arms possess between three and seven degrees of freedom, where each degree of freedom represents a different way that the arm can bend or move. A joint connecting two mechanical links allows either a rotational or a linear degree of freedom. Links are cascaded in a serial fashion ("The shoulder bone's connected to the arm bone," etc.), with either a linear or rotational degree of freedom at each joint. Six degrees of freedom can describe any point and orientation in space (x, y, z, pitch, roll, and yaw), so most teleoperated slaves and masters have at least six degrees of freedom. Like the human arm, some systems have seven degrees of freedom-- the seventh motion adding the redundancy that allows you to reach around the bowl of green beans to grab the salt shaker at dinner. Redundancy can be crucial to some real-world tasks.

Manipulators have position sensors at the joints themselves, or attached to the joint actuators (the actuators usually being connected to the joints through a transmission or gear train). Force sensors are either placed at the joints or in one package at the end of the manipulator. One matrix describes the position (kinematic) relationship between two links, and another describes the force (Jacobian) relationship. These matrices, cascaded to provide the forward kinematic and Jacobian solutions, will yield a resultant endpoint position and force, given all joint positions and torques. The inverse kinematic and Jacobian solutions are more difficult; they determine the combination of joint positions (torques) required to result in a desired end- point position (force). The output of the master forward kinematics determines the position of the molecule being manipulated, and the inverse Jacobian solution of the master determines joint torques needed to feed given forces back to the operator. Both the master forward kinematic and inverse Jacobian solutions must be calculated in real time by a molecular docking force display. The computational load of these calculations is small relative to the load of the molecular modeling, but the rate of the inverse Jacobian outputs depends on the frequency of the force inputs from the molecular modeling program.

IMPLEMENTATIONS

The Argonne ARM manipulator used in the UNC system is a six degree-of-freedom (six-jointed), ceiling-mounted system with a joystick handgrip. It is over 20 years old, and was designed for identical master-slave operation with analog controls and direct master-to-slave sensor comparison (i.e. no A/D conversion). Backlash, friction, and other nonidealities severely restrict system performance. To insure stability, position gain must be set low, requiring the operator to use a very large workspace. The UNC system is elegant considering the equipment used, but many improvements could be made by simply using modern teleoperation hardware.

Telerobotic masters can be divided broadly into two classes: joystick and exoskeleton. Joystick masters are serial link arms with six or fewer degrees of freedom and a joystick or other handgrip at the endpoint; they may or may not resemble their slave. The structure of the joystick master usually lies in front of the operator and only contacts him or her at the handgrip. In contrast, the operator wears an exoskeleton as a framework surrounding the arm and shoulder, usually contacting his or her arm at least at the hand and forearm. Two contact points allow the operator to control a seventh, redundant, degree of freedom. Both joystick and exoskeleton masters may be either passive or force-reflecting.

Exoskeletons offer the advantage of a redundant degree of freedom and may be easier to integrate with a force-reflecting hand controller (human fingers controlling slave fingers) than a joystick. Joystick masters are cheaper, simpler, and usually more compact than exoskeletons. With only six degrees of freedom, their kinematics and inverse Jacobian solutions are also less complicated. Present molecular force display systems need none of the advantages of exoskeleton masters but would suffer from the disadvantages-- joystick masters seem the most appropriate choice at this time.

One improvement on current molecular force display masters would be velocity control. With position control, operators must drag the molecule through large trajectories by moving the master from one end of its workspace to the other, letting go of the molecule and moving back in the other direction, then repeating. Imagine using "click and drag" to move an icon across your computer screen if you only had a 3"x3" mousepad. Velocity control will allow the operator to control a molecule's velocity in a given direction (rotation) with proportional displacements from (rotations about) a given center point. The operator can then "fly" the molecule over larger trajectories. This approach would be indispensable for compact masters with smaller workspaces.

PERFORMANCE

A number of factors affect force-feedback master performance relevant to molecular docking. Friction in the machine must be overcome by the actuators; it raises the minimum force that can be reflected back to the operator. It is difficult to adequately compensate for friction in the motor controller. Although friction contributes to operator fatigue, operators appear to be assisted by a small amount of friction (Jacobus, et al.). Backlash, experienced by many people as "play" in their car's steering wheel, contributes to instability, causes jitter, and limits the operator's sense of "presence" in the virtual world. Since some of the interatomic forces vary on the order of 10^6 or 10^{12} with position, position sensor precision and noise resistance is very important Force feedback would ideally be monitored by force sensors at every joint, although some systems infer a force from motor winding currents. One significant factor affecting any master manipulator is the force-feedback update rate. Computing molecular forces generated by each atom in a long polymer chain (hundreds of atoms) presents a staggering computational load; all forces must be computed each time a new force signal is sent to the master. The best rate UNC has attained with molecules approaching the size of the Wright Laboratory's polymer molecules is 10 Hz. This performance is not acceptable . A figure of 60-200 Hz has been cited (Jacobus) as a minimum rate .. To maintain these update rates, a molecular docking system must possess massive computational power commiserate with the complexity of the molecular model.

CONCLUSION

Low backlash and high position accuracy should be two of the highest criteria for a molecular docking (MoDoc) master. A well-designed machine with good sensors and tight tolerances should be selected. With a better system, position gain should be raised. Velocity control should also be added to allow the operator to control the molecules' motion more effectively, complementing the sometimes tedious "click and drag" of position control. More than anything, increased computation rates will allow a molecular docking force display system to succeed with modern telerobotic equipment. These high update rates are an operational requirement of manipulator controllers. The rates needed exceed those typically sufficient for visual display only; the increased computational demand is perhaps the only drawback of adding force display to a dynamic molecular modeling system. Advancing technology has recently made possible the relatively old idea of force display in molecular docking. As the system at UNC matures and one at Wright Laboratory is born, force display will be applied to more complex molecular models with increasing fidelity; giving more power to an intuitive tool that speeds the work of molecular scientists.

USING A GENETIC ALGORITHM TO EXPLAIN PROTEIN BINDING AND FOLDING
Dr. Steven R. LeClair

USING A GENETIC ALGORITHM TO EXPLAIN PROTEIN BINDING AND FOLDING

Steven R. LeClair

Materials Directorate
Wright Laboratory
Wright Patterson AFB, OH

Jack Park
&
Dan Wood

ThinkAlong Software, Inc.
Brownsville, CA

Abstract A genetic algorithm is a method for global optimization. Given some data set associated with an observed result, the task is to either find some function which best predicts or explains the results of the data or, in other cases, optimizes the behavior of a system (search strategy) based on observations of past behavior. In protein binding and folding, both tasks are of interest. Each is discussed in terms of building a qualitative representation of polypeptide chains which is used to explain the function (conditions) which best predict the formation of secondary structures in proteins. Of particular interest is the formation of structures referred to as helices.

Keywords genetic algorithms, artificial intelligence, knowledge-based systems, polymer chemistry, biotechnology

INTRODUCTION

A recurrent theme in research involving "intelligent systems" is the application of biological metaphors to computers, e.g., the so-called Genetic Algorithm (GA) [Holland, 1989], [Goldberg, 1989], [Farmer et al., 1986], [Judson and Rabitz, 1992]. GAs are a family of iterative search algorithms, and therefore comparable to conventional optimization techniques. From this perspective, it is important to understand what distinguishes GAs from conventional techniques.

A universal problem associated with optimization techniques is, when applied they are typically over-constrained by the numerous assumptions made to transform a dynamic real-world problem into a static contrived formalization. In addition, conventional optimization techniques such as linear programming, dynamic programming, branch and bound techniques, etc. inherently have three difficulties: 1) depending on their search strategy they are sensitive to large or erratic noise in the data, 2) they are easily misled by local peaks that may be unrelated to the overall

maximum, and 3) their search strategy uses the slope of the function to select the next step in the search process. These difficulties are further compounded by computation of the slope at each evaluation (slopes are often expensive to calculate) and for a large problem total enumeration may be a more attractive, possibly more efficient, alternative. For the more complex problems, the local slope does not provide adequate information about the location of the maximum. This is particularly the case for nonlinear functions.

A GA is a unique computational method because it employs and combines qualitative operators with quantitative goals, i.e., to maximize or minimize some specified parameter. In comparison with other conventional optimization techniques, a genetic algorithm has several advantages: 1) GAs encode the parameters which they have to optimize and base their procedure on the codes - not on the parameters themselves, 2) GAs work in parallel on a number of search points (potential solutions) and not on a unique solution, which means that the search method is not local in scope but rather looks globally at the search space, 3) GAs require from the environment only an objective function measuring the fitness score of each individual, and 4) both selection and recombination steps are performed by using probabilistic rules rather than deterministic ones. [Renders & Nordvik, 1992].

As per their biological roots, GAs imply the use of *mutation* as a fundamental mechanism, but instead of the usual genetic material, i.e., DNA in biology, problems encoded in the form of IF-THEN rules are addressed. In addition to mutation, GAs have two (2) other operators called *reproduction* and *crossover*.

Reproduction provides a natural selection process based on the principle of "survival-of-the-fittest". Each cycle of the GA requires the generation of a new population of genetic material (rules) formed by randomly selecting rules from the existing population according to their fitness. This process results in rules with higher fitness values obtaining one or more copies in the next generation while lower fitness individuals may have none. [Linkens & Nyongesa, 1992]

In order to add new rules to population, GAs employ the crossover operator. Crossover is regarded as the dominant operator when compared to reproduction and mutation. Using crossover, two rules are selected to produce an "off-spring" by exchanging a portion of their rules: IF

(antecedent) subjects, objects and relations; and/or THEN (consequent) subjects, objects and relations (analogous to gene splicing as depicted in **Figure 1**). The intent is for the offspring to replace weaker rules in the population. Crossover serves two (2) complementary functions. First, it provides new points for further testing within the existing problem "subspaces" (represented by the parent rules). Secondly, it introduces representative members of "subspaces" not already existing through prior crossover.
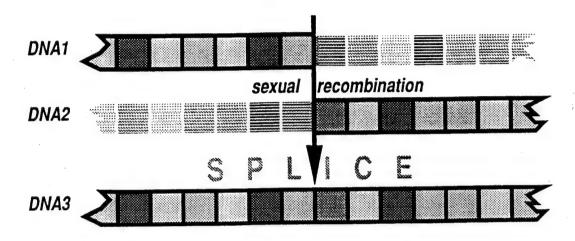
Figure 1. Crossover of Genetic Components

Mutation is a secondary operator, and is applied with very low probability of occurence, typically less than .01. It operation is to alter the value of a random position (point) on a string. When used in this way, together with the reproduction and crossover operators, mutation acts as an insurance against total loss of any bit value in a particular position in the population. Thus, an analog "point mutation" of the computational mechanism would be insertion, deletion, or change of some rule component, as illustrated using a biological example in **Figure 2**.

Point mutation to a gene
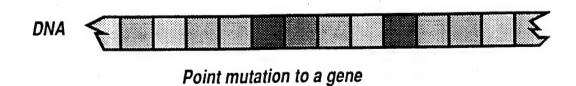
Figure 2. Point Mutations from a Biological Metaphor

In the computational domain, components of "if-then" rules serve as the genome (biological domain), and the rules themselves serve as the phenotypes. An adaptation of the genetic algorithm developed by the second author is referred to as **directed evolution** (after [Abelson, 1990]) — is applied to a population of rules to evolve a more successful population. In the example below, directed evolution develops a population of rules intended to predict the presence of helical structures in a protein when given the amino acid sequence of the protein.

DISCOVERY ON PROTEINS

The problem is to predict the presence of helical structures in a protein when given its amino acid sequence. TSC's approach is to build a population of rules when given a "genome". The genome is built from three "chromosomes", the working components of an observer rule. A pair of observer rules follows:

```
c: OBS.1
    worth               100
    if.actors           ( ( ala ( *x ) true ) ( glu ( *y ) true ) )
    if.relations        ( ( abuts ( *x *y ) true ) )
    then.predict        ( ( helix ( window ) true ) )

c: OBS.2
    worth               100
    if.actors           ( ( leu ( *x ) true ) ( glu ( *y ) true ) )
    if.relations        ( ( abuts ( *x *y ) true ) )
    then.predict        ( ( helix ( window ) true ) )
```

The three chromosomes are:

- actors
- relations
- predictions

The syntax of a typical TSC message is based on a sentence with a subject, predicate, and truth; a message can also involve a sentence with a subject, predicate, object, and truth. Variables are words which begin with an asterisk (*). These sentences are read as illustrated:

```
( predicate ( subject ) truth )
       ( ala ( *x ) true )
```

$$(\text{predicate} \ (\text{subject object} \ ) \ \text{truth} \ )$$
$$(\text{abuts} \ (\ *x \ *y \ ) \ \text{true} \ )$$

Actors are comprised of the twenty natural amino acids:

Alanine	Arginine	Asparagine	Aspartate
Cystine	Glutamine	Glutamate	Glycine
Histidine	Isoleucine	Leucine	Lysine
Methionine	Phenylalanine	Proline	Serine
Threonine	Tryptophan	Tyrosine	Valine

Relations are primarily structural or spatial in this example:

abuts	A•B	(abuts (A B) true)
precedes.1	A•X•B	(precedes.1 (A B) true)
precedes.2	A•X•Y•B	(precedes.2 (A B) true)

The two predictions, used as *votes* by a population of rules, are:

$$(\text{helix} \ (\text{window} \ ) \ \text{true} \ )$$
$$(\text{helix} \ (\text{window} \ ) \ \text{false} \ )$$

An example sequence for the protein *ACYLTRANSFERASE* (after [Gibbs & Leslie, 1990]) is comprised of the following amino acids:

```
MET ASN TYR THR LYS PHE ASP VAL LYS ASN TRP VAL ARG
ARG GLU HIS PHE GLU PHE TYR ARG HIS ARG LEU PRO CYS
GLY PHE SER LEU THR SER LYS ILE ASP ILE THR THR LEU
LYS LYS SER LEU ASP ASP SER ALA TYR LYS PHE TYR PRO
VAL MET ILE TYR LEU ILE ALA GLN ALA VAL ASN GLN PHE
ASP GLU LEU ARG MET ALA ILE LYS ASP ASP GLU LEU ILE
VAL TRP ASP SER VAL ASP PRO GLN PHE THR VAL PHE HIS
GLN GLU THR GLU THR PHE SER ALA LEU SER CYS PRO TYR
SER SER ASP ILE ASP GLN PHE MET VAL ASN TYR LEU SER
VAL MET GLU ARG TYR LYS SER ASP THR LYS LEU PHE PRO
GLN GLY VAL THR PRO GLU ASN HIS LEU ASN ILE ALA ALA
LEU PRO TRP VAL ASN PHE ASP SER PHE ASN LEU ASN VAL
ALA ASN PHE THR ASP TYR PHE ALA PRO ILE ILE THR MET
ALA LYS TYR GLN GLN GLU GLY ASP ARG LEU LEU LEU PRO
```

477

LEU SER VAL GLN VAL HIS HIS ALA VAL CYS ASP GLY PHE
HIS VAL ALA ARG PHE ILE ASN ARG LEU GLN GLU LEU CYS
ASN SER LYS LEU LYS

Observer rules are exercised on segments of a natural system as read
from a data base (such as the Brookhaven National Laboratories Protein
Database). These segments are called *windows* of sequence data. During
learning, the window is shifted along the data. An example window of
data, with a window size of five (5) amino acids, looks like:

[ALA ARG GLY ALA PRO]

TSC encoders write a body of statements about the window:

(ala (ala.1) true) (arg (arg.1) true) (gly (gly.1) true)
(ala (ala.2) true) (pro (pro.1) true)
(abuts (ala.1 arg.1) true) (abuts-1 (ala.1 gly.1) true)
(abuts-2 (ala.1 ala.2) true) (abuts (arg.1 gly.1) true)
...

All rules are then exercised (allowed to vote) on this encoded window.
This voting is repeated as the window is "slid" along the entire data set. A
reward/punishment algorithm — part of the directed evolution component
of TSC — then examines the performance of the individual rules which cast
a vote. Following the "bucket brigade" algorithm of John Holland [Holland,
1986], those rules which participate in the vote, and which vote correctly,
get a reward (their *worth* is increased). Thinking of a given rule and the
source (parents) of that rule as a "bloodline," additional reward is
bestowed upon the source of the successful rules.

Once rewards have been passed to appropriate rules, a small decay
(reduction of worth) of *all* rules is computed. This has the effect of
punishing those rules which do not participate in the vote, or which vote
incorrectly. Rules whose worth falls below a specified value are
eliminated.

At this point the directed evolution component, with its genetic
algorithm, mutates the rule population and conducts a search for the
optimum rule set. For example, using as parents OBS.1 and OBS.2 listed

above, "sexual recombination" builds a child or constructed (CON) rule that looks like the following:

```
c: CON.3
    my.source        obs.1  obs.2
    my.creator       crossover.1
    worth            100
    if.actors        ( ( leu ( *x ) true ) ( ala ( *y ) true ) )
    if.relations     ( ( abuts ( *x *y ) true ) )
    then.predict     ( ( helix ( window ) true ) )
```

This "child" rule is added to the population of rules and given a starting worth value. Now, consider the effect of a point mutation on the rule CON.3 to make a new rule CON.4.

```
c: CON.4
    my.source        con.3
    my.creator       point.mutate.2
    worth            100
    if.actors        ( ( leu ( *x ) true ) ( ala ( *y ) true ) )
    if.relations     ( ( abuts ( *x *y ) true ) )
    then.predict     ( ( helix ( window ) false ) )
```

This rule is essentially the same rule as its source, OBS.3, except that it votes a different way. If the rule is successful, it will eventually replace its source in the rule population.

To summarize directed evolution, using a biological metaphor, we see that:

the strongest rules get to breed,
successful rules get fed well,
parents of successful rules get treats,
and all rules age

INITIAL PERFORMANCE OF DISCOVERY SYSTEM

The authors have developed a test knowledge base comprised of observation rules (rules from the literature regarding amino acids which have been observed to contribute to forming helices) and exercised the

479

discovery system (TSC) on this knowledge base. Results of these trial runs are illustrated in the following figures but represent only the performance of the system, not the product of the exercise, i.e., the discovery of rules which successfully predict helices in proteins with better than 90% accuracy.
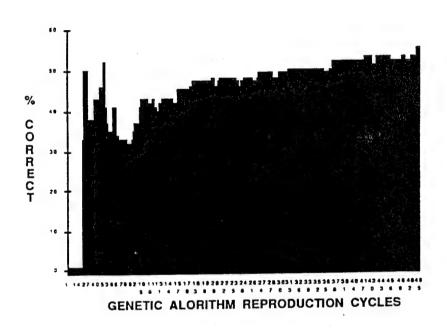

Figure 3. System Performance (trial KB) 11 Jul 92

The next step is to begin the integration of the GA with deep knowledge about protein structure to both guide the GA and begin to explain why certain rules predict helices in proteins. The deep knowledge will focus on collecting and representing information from the literature on protein structure together with heuristics which will prioritize meaningful inquiries about this knowledge and hypotheses. The hypotheses will be both human and machine generated, i.e., the discovery system will construct its own hypotheses. The objective is to enable TSC to discover rules and explanations whereby the GA begins to conduct experiments which either prove or disprove hypotheses.

REFERENCES

Abbas, Abul K., Andrew H. Lichtman, and Jordan S. Pober, *Cellular and Molecular Immunology*, 1991, Philadelphia, W.B. Saunders Company.

Abelson, John, "Directed Evolution of Nucleic Acids by Independent Replication and Selection," *Science*, 249, 3 August 1990, pp 488-489.

Abrams, F., P. Garrett, T. Lagnese, S. LeClair, C. W. Lee, and J. Park, "Qualitative Process Automation for Autoclave Curing of Composites," AFWAL-TR-87-4083, 1987 Wright-Patterson AFB, Ohio.

Casti, John L., *Alternate Realities: Mathematical Models of Nature and Man*, 1989, New York, John Wiley & Sons.

Chou, P.Y., & Fasman, G.D., Prediction of the Secondary Structure of Proteins from their Amino Acid Sequence, *Journal of Advanced Enzymology*, 47, 45-148 (1978).

Dress, W.B., "On Doing Science by Computer—Part I: Philosophical Underpinnings," 1992a, ThinkAlong Technical Report, Brownsville, ThinkAlong Software Inc.

_____, "On Doing Science by Computer—Part III: Modelling the Model," 1992b, ThinkAlong Technical Report, Brownsville, ThinkAlong Software Inc.

Erickson, Michael D., and Jan M. Zytkow, "Utilizing Experience for Improving the Tactical Manager," in *Proceedings of the Fifth International Conference on Machine Learning*, 1989, San Mateo, Morgan Kaufmann Publishers, pp 444-450.

Farmer, J. D., N. H. Packard, and A. S. Perelson, "The Immune System, Adaptation, and Machine Learning," in Doyne Farmer, Alan Lapedes, Norman Packard, and Burton Wendroff, editors: *Evolution, Games, and Learning: Models for Adaption in Machines and Nature*, Amsterdam, North-Holland, 1986, pp 187-204.

Forbus, Kenneth D., *Qualitative Process Theory*, 1984, Ph.D. Thesis, MIT Technical Report 789.

Franks, Nigel R. "Army Ants: a Collective Intelligence," *American Scientist*, 77, March-April 1989, pp 139-145.

Gardner, M., *Wheels, Life and Other Mathematical Amusements*, 1983, San Francisco, Freeman.

Gibbs, M.R., and A.G.W. Leslie, 1990, in the Brookhaven Protein Data Base.

Goldberg, David E., *Genetic Algorithms in Search, Optimization & Machine Learning*, 1989, Menlo Park, Addison-Wesley Publishing Company.

```
C:  OBS.56
     LEVEL                    BASIC
     SUB.OF                   OBS.PROCESS
     INSTANCE.OF     RULE
     WORTH            5218
     #TRIED           10167
     RECENT.COUNT     0
     #SUCCEED         150
     MY.CREATOR       SAK
     ATTACH.TO        OBSERVERS
     IF.ACTORS        ( ( VAL ( *AC ) TRUE ) ( ASN ( *AB ) TRUE )
                            ( PHE ( *AA TRUE ) )
     MY.LHS           IF.ACTORS  IF.RELATES
     IF.RELATES       ( ( PRECEEDS.1.SRL ( *AA *AC ) TRUE )
                            ( ABUTS.SRL ( *AA *AB ) TRUE ) )
     THEN.PREDICT     ( ( HELIX ( WINDOW ) TRUE ) )
     MY.RHS           THEN.PREDICT
```

Figure 4. Observation Rule (trial KB) after 500 cycles

```
C:  CON_FH
     LEVEL            BASIC
     SUB.OF           OBS.PROCESS
     INSTANCE.OF      RULE
     WORTH            1822
     #TRIED           8403
     RECENT.COUNT     0
     #SUCCEED         123
     MY.CREATOR       SAK
     ATTACH.TO        OBSERVERS
     IF.ACTORS        ( ( PHE ( *AA ) TRUE ) ( ASN ( *AB ) TRUE )
                            ( VAL ( *AC ) TRUE ) )
     MY.LHS           IF.ACTORS IF.RELATES
     IF.RELATES       ( ( ABUTS.SRL ( *AB *AC ) TRUE )
                            ( PRECEEDS.1.SRL ( *AA *AC ) TRUE )
                       ( ABUTS.SRL ( *AA *AB ) TRUE ) )
     THEN.PREDICT     ( ( HELIX ( WINDOW ) TRUE ) )
     MY.RHS           THEN.PREDICT
     MY.SOURCE        ( OBS.56 )
```

Figure 5. Construction Rule (trial KB) after 500 cycles

Holland, John H., "Escaping Brittleness: The Possibilities of General-Purpose Learning Algorithms Applied to Parallel Rule-Based Systems," 1986, in [Michalski et al., 1986] pp 593-624.

_____, "Using Classifier Systems to Study Adaptive Nonlinear Networks," 1989, in [Stein, 1989], pp 463-500.

Jackson, A.G., "The Role of Genetic and Self-Learning Algorithms in Research from a User Scientist's Viewpoint," 1992, ThinkAlong Technical Report, Brownsville, ThinkAlong Software Inc.

Jen, Erica, "Limit Cycles in One-Dimensional Cellular Automata," 1989, in [Stein, 1989], pp 743-758.

Jerne, N. K., "The Immune System," *Scientific American*, **229**, 1973, pp 52-60.

Judson, Richard S. andHerschel Rabitz, "Teaching Lasers to Control Molecules," 1992, *Phys. Rev. Letters*, **68**, Number 10, pp 1500-1503.

Karr, C. Lucas, An Adaptive System for Process Control Using Genetic Algorithms, *Proceedings of 1992 IFAC/IFIP/IMACS International Symposium on Artificial Intelligence in Real-Time Control*, Delft University, Delft, the Netherlands, June 16-18, pp 585-590.

Karp, Peter D., *Hypothesis Formation and Qualitative Reasoning in Molecular Biology*, 1989, Ph.D. Thesis, STAN-CS-89-1263, Stanford University.

Kougias, Ch. F., and J. Schulte, "Simulating the Immune Response to the HIV-1 Virus with Cellular Automata," *J. Statistical Physics*, **60**, Nos. 1/2, 1990, pp 263-273.

Lenat, Douglas B., "The Role of Heuristics in Learning by Discovery: Three Case Studies," in Michalski, R. S., J. G. Carbonell, and T. M. Mitchell, editors: *Machine Learning, an Artificial Intelligence Approach*, 1983, Palo Alto, Tioga Publishing Company.

Linkens, Derek A., and Nyongesa H. Okola, Real-Time Acquisition of Fuzzy Rules Using Genetic Algorithms, *Proceedings of 1992 IFAC/IFIP/IMACS International Symposium on Artificial Intelligence in Real-Time Control*, Delft University, Delft, the Netherlands, June 16-18, pp 599-603.

Lucasius, C.B., Bloomers, M.J.J., Buydens, L.M.C., & Kateman G., A Genetic Algorithm for Conformational Analysis of DNA, *Handbook of Genetic Algorithms*, Ed. Lawrence Davis, Van Nostrand Reinhold, New York, 1991.

Michalski, Ryszard S., Jaime G. Carbonell, and Tom M. Mitchell, editors:*Machine Learning: Volume II*, 1986, Los Altos, Morgan Kaufmann Publishers, Inc.

Park, Jack, and Dan Wood, *User's Manual for The Scholar's Companion*, 1992, Brownsville CA, ThinkAlong Software, Inc.

Renders, J.M., and Norvik, J. P., Genetic Algoritms for Process Control: A Survey, *Proceedings of 1992 IFAC/IFIP/IMACS International Symposium on Artificial Intelligence in Real-Time Control*, Delft University, Delft, the Netherlands, June 16-18, pp 579-584.

Rosen, Robert, *Anticipatory Systems*, 1985, New York, Pergamon Press.

Sieburg, H., H. McCutchan, O. Clay, L. Caballero, and J. Ostlund, "Simulation of HIV-infection in Artificial Immune Systems," in Howard Gutowitz, Ed.: *Cellular Automata: Theory and Experience*, Cambridge, MA, MIT Press, 1991, pp 208-228.

Stein, Daniel L., Editor, *Lectures in the Sciences of Complexity*, 1989, Redwood City, Addison-Wesley Publishing Company.

Thagard, Paul, *Computational Philosophy of Science*, 1988, Cambridge, The MIT Press.
Wood, Dan, and Jack Park, *Qualitative Process Discovery: The Next Step Toward Intelligent Systems*, 1990, AFWAL TR, Dayton, Wright Research Laboratories—United States Air Force.

484